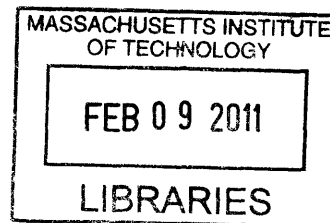


Engineering Electroresponsive Layer-by-Layer Thin Films

By

Daniel J. Schmidt

B.S.E. Chemical Engineering
University of Michigan – Ann Arbor, 2005



SUBMITTED TO THE DEPARTMENT OF CHEMICAL ENGINEERING IN PARTIAL
FULFILLMENT OF THE REQUIREMENTS FOR THE DEGREE OF

DOCTORATE OF PHILOSOPHY IN CHEMICAL ENGINEERING
AT THE
MASSACHUSETTS INSTITUTE OF TECHNOLOGY

ARCHIVES

FEBRUARY 2011

© 2011 Massachusetts Institute of Technology. All rights reserved.

Signature of Author: _____

Dept. of Chemical Engineering
December 8, 2010

Certified by: _____

Paula T. Hammond
Bayer Chair Professor of Chemical Engineering
Thesis Supervisor

Accepted by: _____

William M. Deen
Professor of Chemical Engineering
Chairman, Committee for Graduate Students

Engineering Electroresponsive Layer-by-Layer Thin Films

By

Daniel J. Schmidt

Submitted to the Department of Chemical Engineering
On December 8, 2010 in Partial Fulfillment of the Requirements for the Degree of
Doctor of Philosophy in Chemical Engineering
At the Massachusetts Institute of Technology

Abstract

Electroresponsive layer-by-layer (LbL) polymer films and polymer nanocomposite films were investigated as model systems for electrically triggered drug delivery applications and “mechanomutable” surface coating applications. Two strategies were implemented in the design of these electroresponsive films: the use of redox-active, charge-shifting nanoparticles and the control over local pH utilizing the electrochemical reduction of dissolved oxygen. These strategies and the multiple materials systems explored are described below.

Redox-active Prussian Blue (PB) nanoparticles exhibit multiple, stable oxidation states and can shift their charge in response to mild electric potentials. The inherently negatively charged particles may be self-assembled into LbL films along with positively charged polyelectrolytes. When the PB in an LbL film is oxidized to its neutral state, dissolution of the film occurs as cohesive ionic crosslinks are broken and excess charge in the film brings in ions and water for electroneutrality, which solubilize the film components. The release of the polyanion dextran sulfate and the small molecule antibiotic gentamicin sulfate were precisely controlled with an electric potential. When PB is reduced, the negative charge on the particle is doubled, which results in film swelling and a decrease in stiffness. In films comprising PB and linear polyethyleneimine, reversible thickness changes on the order of 5-10% and reversible elastic modulus changes on the order of 50% (between 3.40 GPa and 1.75 GPa) were observed.

Employing the second strategy mentioned above, the local pH near an electrode surface may be increased to more basic values when dissolved oxygen is electrochemically reduced to hydroxide ions. In the first model system explored, hydrogen bonded (H-bonded) films comprising polyvinylpyrrolidone (PVPON) and tannic acid (TA), were dissolved at constant bulk pH by applying mild potentials (-0.25 V to -1.00 V vs. Ag/AgCl). The dissolution mechanism and kinetics could be tuned with the magnitude of the applied voltage and the concentration of dissolved oxygen. In the second model system explored, films comprising polyallylamine hydrochloride (PAH) and sulfonated polystyrene (SPS) were found to undergo reversible and dramatic swelling/deswelling transitions on the order of roughly 300 vol% and mechanical transitions on the order of 600-800% (shear modulus between 230 kPa and 1.9 MPa and loss modulus between 90 kPa and 620 kPa).

This thesis contributes to the applied materials science branch of chemical engineering. New polymer and polymer nanocomposite thin films were developed that can be further engineered and incorporated into implantable drug delivery devices for electrically triggered drug delivery or incorporated into MEMS and microfluidic systems for flow control or biomedical applications. Furthermore, the model systems presented here open doors for fundamental work on the transport of electrons, ions, and water through these electroresponsive films and the implications of transport phenomena on the control over film dissolution and swelling responses.

Thesis Supervisor: Paula T. Hammond
Bayer Chair Professor of Chemical Engineering

Table of Contents

Abstract.....	3
Table of Contents.....	5
List of Figures.....	8
List of Tables.....	15
Acknowledgements.....	16
Chapter 1: Introduction and Background.....	17
1.1 Introductory Remarks and Technical Summary.....	17
1.2 Layer-by-Layer Assembly.....	21
1.3 Electroresponsive Layer-by-Layer Films.....	24
1.3.1 Redox-Active, Charge-Shifting Materials.....	26
1.3.1.1 Transition metal ions and complexes.....	27
1.3.1.2 Polymer-tethered transition metal complexes.....	29
1.3.1.3 Supramolecular transition metal complexes and clusters.....	31
1.3.1.4 Conjugated polymers.....	36
1.3.2 Local pH Control.....	37
1.4 Electrically Triggered Drug Delivery.....	41
1.5 Mechanomutable Materials.....	43
1.6 Thesis Overview.....	45
1.7 References.....	47
Chapter 2: Macromolecule Drug Delivery Utilizing Prussian Blue.....	61
2.1 Introduction.....	61
2.2 Materials and Methods.....	63
2.3 Results and Discussion.....	68
2.4 Conclusions.....	77
2.5 References.....	78
Chapter 3: Small Molecule Drug Delivery Utilizing Prussian Blue.....	81
3.1 Introduction.....	81
3.1.1 Micelles.....	82
3.1.2 Cyclodextrins.....	84
3.1.3 Electrostatic Complexation.....	86
3.2 Materials and Methods.....	87
3.2.1 Micelles.....	87
3.2.2 Cyclodextrins.....	90
3.2.3 Electrostatic Complexation.....	92
3.3 Results and Discussion.....	96
3.3.1 Micelles.....	96
3.3.1.1 Micelle and Film Characterization.....	97
3.3.1.2 Electrochemical Analysis.....	99
3.3.1.3 Drug Loading and Release.....	100
3.3.2 Cyclodextrins.....	105
3.3.3 Electrostatic Complexation.....	109
3.3.3.1 Film Growth and Surface Morphology.....	109
3.3.3.2 Electrochemical Analysis.....	113

3.3.3.3	Electrodissolution and Drug Release	115
3.3.3.4	Efficacy of Released Drug	126
3.4	Conclusions.....	128
3.4.1	Micelles.....	128
3.4.2	Cyclodextrins	129
3.4.3	Electrostatic Complexation.....	130
3.5	References.....	131
Chapter 4: Mechanomutable Layer-by-Layer Polymer Nanocomposite Thin Films Utilizing Prussian Blue		137
4.1	Introduction.....	137
4.2	Materials and Methods.....	140
4.3	Results and Discussion	148
4.3.1	Dry Film Characterization	148
4.3.2	Passive Swelling	149
4.3.3	Active Swelling.....	151
4.3.4	Mechanical Measurements.....	155
4.3.5	Mechanistic Discussion	159
4.4	Conclusions.....	161
4.5	References.....	163
Chapter 5: Electrochemically Erasable Hydrogen-Bonded Thin Films		165
5.1	Introduction.....	165
5.2	Materials and Methods.....	167
5.3	Results and Discussion	171
5.3.1	Electrochemical Response of a Gold-Coated Silicon Electrode.....	171
5.3.2	Electrochemical Dissolution – Effect of Applied Voltage	173
5.3.3	Electrochemical Dissolution – Effect of Oxygen Concentration.....	177
5.3.4	Surface Morphology during Dissolution	178
5.3.5	Ultrathin Free-Standing Film Release	183
5.3.6	Control – Bulk pH-Triggered Dissolution	185
5.4	Conclusions.....	187
5.5	References.....	188
Chapter 6: Mechanomutable Polyelectrolyte Thin Films Controlled by Electrochemically Induced pH Gradients		191
6.1	Introduction.....	191
6.2	Materials and Methods.....	192
6.3	Results and Discussion	196
6.3.1	Film Assembly and Swelling	196
6.3.2	Electrochemically Triggered Deswelling	198
6.3.3	Effect of Film Thickness on Deswelling Kinetics	200
6.3.4	Effect of Magnitude of Applied Potential on Deswell Kinetics	203
6.3.5	Effect of Bulk pH on Deswell Kinetics	205
6.3.6	QCM-D	208
6.4	Conclusions.....	212
6.5	References.....	214
Chapter 7: Layer-by-Layer Films for Education – Assembly of a pH-Responsive and Electrochromic Thin Film.....		216

7.1	Introduction.....	216
7.2	Materials and Methods.....	219
7.3	Results and Discussion	222
	7.3.1. Module #1 - Fabrication and characterization of (SPS/PANi) _n thin film growth.	222
	7.3.1. Module #2 - Electrochromic properties of (SPS/PANi) ₈ films.....	225
7.4	Conclusions.....	227
7.5	References.....	228
Chapter 8: Conclusions and Recommendations		231
Appendix 1: Supplemental Materials for Chapter 2		237
Appendix 2: Supplemental Materials for Chapter 3		242
Appendix 3: Supplemental Materials for Chapter 4		249

List of Figures

Figure 1.1. Schematic representation of the layer-by-layer assembly of a polycation and a polyanion to form a polyelectrolyte multilayer thin film.

Figure 1.2. Schematic representation of the electrically triggered dissolution and swelling of a layer-by-layer film. Swelling to an equilibrium state occurs when the elastic forces in the film (from cohesive interactions and/or crosslinks) balance the osmotic pressure forces. Dissolution results when the osmotic pressure forces exceed the elastic forces.

Figure 1.3. Molecular structure of iron phthalocyanine tetrasulfonic acid (FePcTs) (left) and a generic, charged metalloporphyrin (right).

Figure 1.4. Molecular structure of ferrocene-modified polyallylamine (PAH-Fc) (left) and osmium pyridine/bipyridine-modified polyallylamine (PAH-Os).

Figure 1.5. Molecular structure of a poly(ferrocenylsilane) (PFS). PFS polyelectrolytes are made using various charged groups for the R unit, as shown by Ma et al.

Figure 1.6. Crystal structure of Prussian Blue. Potassium ions, which are not shown for clarity, are the counterions for the negatively charged sites on the crystal surface and interior sites.

Figure 2.1. Fabrication of LbL nanocomposite thin films based on PB. (a) Generalized schematic detailing the deconstruction of PB-based films containing drugs or other chemical species (blue circles represent PB nanoparticles and red lines represent drugs or chemical species (with or without a second encapsulating species)). (b) Absorbance (700 nm) versus number of deposited tetralayers for the (LPEI/PB/LPEI/¹⁴C-DS)₃₀ system as determined by UV-Visual spectroscopy. Absorbance values are normalized to the absorbance of a 25 tetralayer film. (Inset: Thickness (nm) versus number of deposited tetralayers in the same system as determined by profilometry. Measurements were performed at six predetermined spots on the surface of the films, and error bars represent one standard deviation in measured values.)

Figure 2.2. Electrochemical deconstruction of (LPEI/PB/LPEI/¹⁴C-DS)₃₀ films. (A) Absorbance spectrum showing decreasing PB absorbance with increasing time at 1.25 V. (B) Normalized absorbance (700 nm) versus time for films with (filled triangles) and without (open triangles) an applied potential.

Figure 2.3. Release of a model compound, ¹⁴C-DS, from PB-containing films held at a constant potential of 1.25 V. All films are (LPEI/PB/LPEI/¹⁴C-DS)₃₀. (A) Films held constant at 1.25 V (closed diamonds) or no applied potential (open diamonds) are shown. (B) Serial ¹⁴C-DS release from two (LPEI/PB/LPEI/¹⁴C-DS)₃₀ films in a single solution. One film was held at the oxidizing potential for 10 min, followed by 10 min below the oxidizing potential. Next, the process was repeated with a second film in the same degradation bath. Periods during which an oxidizing potential was applied are shaded. (C) Release rate versus time for the films in part (b). In all cases, error bars represent one standard deviation in measured values.

Figure 2.4. On-off switchable destabilization of PB-containing (LPEI/PB/LPEI/¹⁴C-DS)₃₀ films. (A) Total ¹⁴C-DS release from equivalent samples held at the oxidizing potential of 1.25 V for varying times (normalized to total release at 30 min). (B) ¹⁴C-DS release from a single film held at 1.25 V for 1 min intervals at t = 0 and t = 15 min⁻¹. (C) Release rate from film shown in (B)². In all cases, error bars indicate one standard deviation in measured values.

Figure 2.5. MTT assay for cellular toxicity indicates that PB nanoparticles exhibit no toxicity on three different cell lines at concentrations up to 1.0 mg/mL. Error bars represent one standard deviation in measured values.

Figure 3.1. General schematic of a micelle comprising a hydrophilic, charged corona (blue) and a hydrophobic interior (green), where hydrophobic molecules may be sequestered.

Figure 3.2. Molecular structure of β -cyclodextrin.

Figure 3.3. Molecular structure of Coumarin 30.

Figure 3.4. Molecular structures of POPOP (left) and DPA (right).

Figure 3.5. Molecular structure of Flurbiprofen.

Figure 3.6. Molecular structure of gentamicin sulfate. The primary and secondary amines are shown as charged, and the sulfate counterions are eliminated for clarity.

Figure 3.7. Thickness of (PS-b-P4VP “crew cut” micelle / PB)_n and (PS-b-P4VP “hairy” micelle / PB)_n films determined via profilometry. Error bars represent \pm one standard deviation from at least $n = 5$ spots on each film. The solid lines represent best fits from linear regression. R^2 values greater than 0.99 were achieved for both linear fits.

Figure 3.8. Photographs of (PS-b-P4VP “crew cut” micelle / PB)_n (left) and (PS-b-P4VP “hairy” micelle / PB)_n (right) films.

Figure 3.9. Cyclic voltammograms of (PS-b-P4VP “crew cut” micelle / PB)_n (left) and (PS-b-P4VP “hairy” micelle / PB)_n (right) films for $n = 10, 20, 30,$ and 40 . The electrolyte was 0.1 M KHPH (pH 4) and the scan rate was 50 mV/s.

Figure 3.10. Fluorescence spectra of (PS-b-P4VP “crew cut” micelle / PB)₃₀ and (PS-b-P4VP “hairy” micelle / PB)₃₀ films loaded with Coumarin 30 dye. The “crew cut” micelle-containing film loads substantially more dye than the “hairy” micelle-containing film.

Figure 3.11. Release of Coumarin 30 at the open circuit potential (OCP) and during application of +1.25 V (vs. SCE) in 10 mM KHPH (pH 4) from (A) (PS-b-P4VP “crew cut” micelle / PB)₃₀ and (B) LPEI(PB/LPEI/PB/PS-b-P4VP “crew cut” micelle)₂₀ films loaded with Coumarin 30 dye. In both cases, the Coumarin 30 leaks out of the film passively within the first 30 min. The applied potential of +1.25 V does not release any further dye from the bilayer film, but does release a small amount of additional dye from the tetralyer film.

Figure 3.12. Fluorescence spectrum of a LPEI(PB/LPEI/PB/PS-b-P4VP “crew cut” micelle)₂₀ films loaded with POPOP fluorescent dye (left) and DPA fluorescent dye (right).

Figure 3.13. Release of POPOP at the open circuit potential (OCP) and during application of +1.25 V (vs. SCE) in 10 mM KHPH (pH 4) from an LPEI(PB/LPEI/PB/PS-b-P4VP “crew cut” micelle)₂₀ films loaded with POPOP dye. The POPOP leaks out of the film passively within the first 30 min. The applied potential of +1.25 V does not release any further significant amount of dye from the film.

Figure 3.14. Thickness of LPEI(CM β CD/Chi)_n films determined via ellipsometry. Error bars represent \pm one standard deviation from at least $n = 5$ spots on each film. The solid lines represent best fits from linear regression. R^2 values greater than 0.99 were achieved for both linear fits.

Figure 3.15. Fluorescence spectra of of LPEI(CM β CD/Chi)_n films assembled at pH 5.0/5.0 loaded with Flurbiprofen. The films assembled with 0.50 M NaCl in the polymer dipping baths were thicker and loaded a substantially greater amount of the drug.

Figure 3.16. Cyclic voltammograms of LPEI(Chi/PB)₁₀ and LPEI(Chi/PB/Chi/CM β CD)₁₀ films in a 0.1 M KCl electrolyte at a scan rate of 10 mV/s. The oxidation of Prussian Blue to the Prussian Yellow oxidation state is apparently stifled by the presence of CM β CD.

Figure 3.17. A) Growth curve, determined via profilometry, for Chi(PB/Chi)₅(PB/GS)_n and Chi(PB/Chi)_n film architectures, revealing accelerated film growth when adhesion layers are

deposited. The lines are best fit lines for exponential and linear growth models for films with and without adhesion layers, respectively. Error bars represent \pm one standard deviation in measured thickness values at $n = 5-7$ locations on each film. B) Photographs of $\text{Chi}(\text{PB}/\text{Chi})_5(\text{PB}/\text{GS})_n$ films for $n = 0, 25, 50,$ and 75 .

Figure 3.18. Atomic force microscopy 3D height images of A) $n = 25$, B) $n = 50$, and C) $n = 75$ bilayer films and D) an optical micrograph of an $n = 75$ film. Film surface roughness increases and clusters form on the film surface with the deposition of an increasing number of bilayers.

Figure 3.19. Cyclic voltammograms of a $\text{Chi}(\text{PB}/\text{Chi})_5(\text{PB}/\text{GS})_{25}$ film subjected to multiple cycles at a scan rate of 50 mV/s in a PBS, pH 7.4 electrolyte. A decrease in peak height (and peak area) with subsequent scans reveals a loss of the electroactive Prussian Blue from the film.

Figure 3.20. A) Absolute and B) normalized thickness of $\text{Chi}(\text{PB}/\text{Chi})_5(\text{PB}/\text{GS})_n$ films over time at an applied potential of $+1.25 \text{ V}$ vs. Ag/AgCl in a PBS, pH 7.4 electrolyte. The thickest films dissolve more slowly, and all film thicknesses plateau to approximately 25-45% of initial thickness. The lines represent the best fit to a first order exponential decay model. Error bars represent \pm one standard deviation in measured thickness values at $n = 5-10$ locations on each film.

Figure 3.21. (A) Drug release profiles from $\text{Chi}(\text{PB}/\text{Chi})_5(\text{PB}/\text{GS})_n$ films at an applied potential of $+1.25 \text{ V}$ vs. Ag/AgCl and at the open circuit potential (OCP). The total amount of released drug, or the drug dosage, can be set by tuning the number of deposited layers, n . Error bars represent \pm one standard deviation in measured values from $n = 3$ films. (B) Linear regression best fits for a pseudo-second order drug release kinetics model for $n = 25, 50,$ and 75 films.

Figure 3.22. A) Total amount of gentamicin released from a $\text{Chi}(\text{PB}/\text{Chi})_5(\text{PB}/\text{GS})_{50}$ film over time at different applied potentials. B) Total amount of gentamicin released from a $\text{Chi}(\text{PB}/\text{Chi})_5(\text{PB}/\text{GS})_{50}$ film in 1 hr at different applied potentials. The smallest amount of drug is released at the open circuit potential of $+0.25 \text{ V}$, while increasing amounts of drug are released at both anodic and cathodic potentials, with the greatest amount released during oxidation of the PB. Error bars represent \pm one standard deviation in measured values from $n = 3$ films. All means are statistically different from each other with $p < 0.05$ except for those at $+1.00$ and $+1.25 \text{ V}$, for which $p = 0.15$.

Figure 3.23. Drug release profile from a $\text{Chi}(\text{PB}/\text{Chi})_5(\text{PB}/\text{GS})_{75}$ film with 2 sec pulses of $+1.25 \text{ V}$ to turn drug release 'on', followed by 30 sec pulses at $+0.25 \text{ V}$ to turn drug release 'off'. The films are sufficiently stable to allow for on/off, or pulsatile, drug release controlled by the applied potential. Error bars represent \pm one standard deviation in measured values from $n = 3$ films.

Figure 3.24. Results of a microdilution assay of gentamicin released from a $\text{Chi}(\text{PB}/\text{Chi})_5(\text{PB}/\text{GS})_{75}$ film against *S. aureus* bacteria. The MIC of the drug released from the film corresponds well with that of the free drug. Error bars represent \pm one standard deviation in measured values from $n = 3$ samples.

Figure 4.1. (A) Redox states of Prussian Blue. (B) Schematic of an $(\text{LPEI}/\text{PB})_{30}$ film swelling under the influence of an electric potential. Water molecules and positive charges on the polymer are omitted for clarity. The degree of swelling represented in the figure is exaggerated for the reader's convenience.

Figure 4.2. Photograph of an electrochemical cell interfaced with a spectroscopic ellipsometer. The three-electrode cell comprises a Ag/AgCl reference electrode, a Pt coil counter electrode,

and a gold-coated silicon wafer modified with a (LPEI/PB)_n film as the working electrode. The gold working electrode is connected to the external circuit by a contact connection with a Pt wire. **Figure 4.3.** Photograph of an electrochemical cell interfaced with a nanoindenter. The three-electrode cell comprises Ag pseudo-reference electrode, a Pt wire counter electrode, and an ITO-coated glass slide modified with a (LPEI/PB)₅₀ film as the working electrode. The substrate, mounted on the aluminum support, is only partially submerged in the liquid, allowing for direct connection to the external circuit with an alligator clip.

Figure 4.4. AFM height image of an (LPEI/PB)₃₀ film surface assembled on ITO-glass, acquired via contact-mode imaging in an aqueous 0.1 M potassium hydrogen phthalate solution. RMS roughness is 3.48 ± 0.16 nm.

Figure 4.5. (A) Passive swelling of an (LPEI/PB)₃₀ film in a 0.1 M KHPH electrolyte solution over one hour. All of the error bars represent 95% confidence intervals based on the ellipsometry model fit. (B) Active swelling of two (LPEI/PB)₃₀ films subjected to ten redox cycles. Error bars representing 95% confidence intervals based on the ellipsometry model fit are approximately the size of the data points. Selected swelling percentage values (calculated relative to thickness in the preceding redox state) are next to the corresponding data points; negative values represent shrinking.

Figure 4.6. (A) Surface profile of an (LPEI/PB)₃₀ film measured with EC-AFM at applied potentials of -0.2 V and +0.6 V. The inset shows a height image of the film/substrate boundary with a demarcation denoting the location of the surface profile measurement. (B) Evolution of film thickness with successive potential cycling. The error bars represent the standard deviation from n=5 measurements taken at different locations on the film. Swelling percentage values (calculated relative to thickness in the preceding redox state) are next to the data points; negative values represent shrinking.

Figure 4.7. Instrumented nanoindentation results for an (LPEI/PB)₅₀ film immersed in aqueous 0.1 M KHPH. (A) Loading portion of the load-depth response for a film in the oxidized (black, +0.6 V) and reduced (red, -0.2 V) state. (B) Effective Young's elastic moduli E_i of the film subjected to two redox cycles, corrected for finite thickness as described in Methods. O.C.P. stands for open circuit potential. Error bars represent the standard deviation from n=6 measurements at different locations on the film for each condition.

Figure 4.8. Change in frequency and dissipation (13th overtone) of a Au-coated QCM crystal modified with an (LPEI/PB)₃₀ film upon alternate application of -0.2 V and +0.6 V (versus Ag/AgCl). Signal-to-noise of dissipation at the lower frequency overtones was insufficient to identify changes upon voltage switching.

Figure 4.9. Overlay of a cyclic voltammogram and EQCM frequency data (3rd overtone) for an (LPEI/PB)₃₀ film. Scan rate is 10 mV/s. The inflection in frequency (mass change) corresponds with the potential of the Prussian Blue-Prussian White redox couple.

Figure 5.1. Schematic of electrochemically induced oxygen reduction at a film-coated gold electrode inducing dissolution of the film.

Figure 5.2. Linear scan voltammograms (A) including the reduction of water (below -1 V) and (B) including only the oxygen reduction region (0 V to -1 V) of a gold-coated Si substrate at a scan rate of 50 mV/s in 10 mM Na₂SO₄ with different concentrations of dissolved oxygen.

Figure 5.3. Effect of different applied voltages (at ~8 ppm dissolved O₂) on the thickness of (PVPON/TA)₂₀ films over time in 10 mM Na₂SO₄. Error bars represent \pm one standard deviation from measurements taken at five different locations on each film.

Fig. 5.4. Cumulative charge injected over time into gold electrodes coated with (PVPON/TA)₂₀ films at different applied voltages. The slope of each line corresponds to the current, that is, the rate of reaction (O₂ and/or H₂O reduction to OH⁻).

Figure 5.5. Effect of different oxygen concentrations (at -0.50 V vs. SCE) on the thickness of (PVPON/TA)₂₀ films over time in 10 mM Na₂SO₄. Error bars represent ± one standard deviation from measurements taken at five different locations on each film.

Fig. 5.6. AFM height images with scale 20 μm x 20 μm x 20 nm (left) and 20 μm x 20 μm x 200 nm (right) of bare, freshly cleaned gold-coated silicon slides in the dry state. The normalized film thickness (*h*) and RMS roughness (*Rq*) are reported with ± one standard deviation from n = 5-7 measurements.

Fig. 5.7. AFM height images with scale 20 μm x 20 μm x 20 nm (left) and 20 μm x 20 μm x 200 nm (right) of initial (PVPON/TA)₂₀ films in the dry state. The normalized film thickness (*h*) and RMS roughness (*Rq*) are reported with ± one standard deviation from n = 5-7 measurements.

Fig. 5.8. AFM height images (scale 20 μm x 20 μm x 20 nm) of (PVPON/TA)₂₀ films in the dry state after application of -0.25 V (top row) and -0.50 V (bottom row) in a 10 mM Na₂SO₄ solution (8 ppm O₂) for the specified amounts of time. The normalized film thickness (*h*) and RMS roughness (*Rq*) are reported for each image. Values are reported with ± one standard deviation from n = 5-7 measurements. At these mild voltages, the films appear to degrade by a homogeneous, top-down surface erosion mechanism.

Fig. 5.9. AFM height images (scale 20 μm x 20 μm x 200 nm) of (PVPON/TA)₂₀ films in the dry state after application of -1.00 V in a 10 mM Na₂SO₄ solution (8 ppm O₂) for the specified amounts of time. The normalized film thickness (*h*) and RMS roughness (*Rq*) are reported for each image. Values are reported with ± one standard deviation from n = 5-7 measurements. At this more negative voltage, the films develop a porous morphology indicative of a phase separation and they appear to degrade by a heterogeneous bulk erosion mechanism. At t = 20 sec, the films were not spatially homogenous; thus, images from different locations on the film are provided.

Fig. 5.10. AFM height images (scale 20 μm x 20 μm x 200 nm) of (PVPON/TA)₂₀ films in the dry state after application of -0.50 V in a 10 mM Na₂SO₄ solution (30 ppm O₂) for the specified amounts of time. The normalized film thickness (*h*) and RMS roughness (*Rq*) are reported for each image. Values are reported with ± one standard deviation from n = 5-7 measurements. At this elevated concentration of dissolved oxygen, a potential of -0.50 V more rapidly increases local pH and leads to a different film erosion mechanism. As at -1.00 V with 8 ppm O₂, the films develop a porous morphology indicative of a phase separation and they appear to degrade by a heterogeneous bulk erosion mechanism. At t = 10 sec, the films were not spatially homogenous; thus, images from different locations on the film are provided.

Fig. 5.11. Profilometry scan of a free-standing ultrathin (PAH/SPS)₈₀ film detached from a gold-coated silicon substrate through electrochemical dissolution of an underlying sacrificial (PVPON/TA)₂₀ film at -1.0 V (vs. SCE). Regions of a single sheet (~250 nm thick) and regions of the film folded upon itself giving integral multiples of the single sheet thickness were observed. The inset shows a photograph of the film partially detached from the substrate.

Figure 5.12. Normalized thickness of three identical (PVPON/TA)₂₀ films exposed to different bulk pH conditions over time. Error bars represent ± one standard deviation from measurements taken at five different locations on each film.

Figure 6.1. Schematic of electrochemically induced deswelling of a (PAH/SPS)_n film through an increase in local pH.

Figure 6.2. Thickness of (PAH/SPS)_n films in the dry state, immersed in DI water for 1 min, and immersed in pH 4 water for 15 min, as determined with spectroscopic ellipsometry.

Figure 6.3. (A) Thickness of (PAH/SPS)_{5.5} swollen at pH 4, deswollen at -0.50 V, and reswollen at the open circuit potential (OCP). (B) Thickness of (PAH/SPS)_{5.5} after multiple swell (at pH 4) and deswell (-0.50 V) cycles. Odd numbered cycle numbers correspond to the OCP, while even numbered cycles correspond to application of -0.50 V.

Figure 6.4. (A) Thickness of (PAH/SPS)_n at an applied potential of -0.50 V in a pH 4 electrolyte solution. The thickness was normalized to the initial swollen thickness in pH 4, which can be found in Fig. 1. The data shown are for the first deswell cycle. (B) Linear relationship between the initial film thickness and the square root of the deswelling time indicates that diffusion of water out of the film controls the rate of film deswelling.

Figure 6.5. Normalized thickness versus time of (PAH/SPS)_{5.5} films at bulk pH values of (A) 3.0, (B) 3.5, and (C) 4.0. The minimum electric potential required to deswell the film depends strongly on the bulk pH. Thickness is normalized to the swollen film thickness at the open circuit potential after the first swell/deswell cycle. Data for multiple cycles are reported to show reproducibility.

Figure 6.6. Normalized thickness versus time of (PAH/SPS)_{5.5} films at (A) -0.25 V, (B) -0.50 V, and (C) -1.0 V. Thickness is normalized to the swollen film thickness at the open circuit potential after the first swell/deswell cycle. Data for multiple cycles are reported to show reproducibility.

Figure 6.7. Thickness of a (PAH/SPS)_{5.5} film initially immersed in DI water, swollen after immersion in pH 3.5 solution, transferred to a pH 7.4 solution, electrochemically deswollen during application of -0.25 V (vs. Ag/AgCl (3 M NaCl)), and then reswollen after re-immersion in a pH 3.5 solution. Returning to the open circuit potential (OCP) alone does not cause the film to reswell in the pH 7.4 solution, since that pH is above the critical pH for film swelling.

Figure 6.8. Change in frequency (F) and dissipation (D) of a QCM crystal during *in situ* build up of a (PAH/SPS)_{5.5} film at pH 9.3/9.3, film swelling at pH 4, electrochemically triggered deswelling at -0.50 V, and reswelling at the open circuit potential (OCP). Dashed arrows indicate injection of the PAH, while solid arrows indicate injection of the SPS. The blue arrows indicate application of -0.50 V, and the orange arrows indicate a return to the OCP. Data are presented for the 3rd (F3, D3), 5th (F5, D5), and 7th (F5, D7) overtones corresponding to resonance frequencies of approximately 15 MHz, 25 MHz, and 35 MHz, respectively.

Figure 6.9. (A) Thickness of a (PAH/SPS)_{5.5} film swollen upon exposure to pH 4 water, deswollen upon application of -0.50 V, and reswollen at the open circuit potential. (B) Shear (storage) modulus and (C) loss modulus of (PAH/SPS)_{5.5} films during multiple swell (at pH 4, OCP) / deswell (-0.50 V) cycles.

Figure 7.1. Schematic representation of the layer-by-layer assembly of a polycation and a polyanion to form a polyelectrolyte multilayer thin film.

Figure 7.2. Molecular structures of polyaniline (acid-doped, conducting emeraldine salt form) (left) and sulfonated polystyrene (right).

Figure 7.3. Photograph of (SPS/PANi)_{n=0, 2, 4, 6, 8} films in the acid-doped emeraldine salt form (top) and de-doped emeraldine base form (bottom) on glass microscope slides (1 cm x 2 cm).

Figure 7.4. (A) UV/Vis absorbance spectrum of (SPS/PANi)_n films for $n = 2, 4, 6, 8, 10$ and (B) linear regression of absorbance at 620 nm versus the number of deposited bilayers, n .

Figure 7.5. (A) Photograph showing measurement of in-plane conductivity using a handheld multimeter. (B) Student-collected data showing conductivity versus number of bilayers for (SPS/PANi)_n films.

Figure 7.6 (A) A cyclic voltammogram and photos showing the electrochromism of a (SPS/PANi)₈ film on ITO-glass. The colors of three PANi oxidation states, leucoemeraldine, emeraldine salt, and pernigraniline, are apparent in the photographs from right to left. (B) Student-collected data showing spectroelectrochemistry of (SPS/PANi)₈ subject to square waves at -0.2 V and 0.9 V (with respect to a Ag/AgCl reference electrode).

List of Tables

Table 3.1. The fraction of total gentamicin released from Chi(PB/Chi)₅(PB/GS)₅₀ films with different pulse lengths at +1.25 V vs. Ag/AgCl. The pulse length may be used to control the total amount of released drug. The standard deviations were determined from n = 3 films.

Table 5.1: Comparison of the time to 50% dissolution and the total cumulative charge injected up to that time for (PVPON/TA)₂₀ films subjected to different voltages.

Table 6.1. Percent swelling (relative to dry thickness) of (PAH/SPS)_n films in DI water and in pH 4 water.

Table 7.1. The four oxidation states of polyaniline.

Acknowledgements

This thesis is dedicated to my fiancée Erin Bell, who has provided me with constant encouragement and support throughout my Ph.D.

I thank my advisor Prof. Paula T. Hammond for giving me the opportunity to work in her lab and for helping me to grow as a scientist. She has been continually supportive and understanding and I am especially thankful for the freedom she gave me to explore many of my own interests and side projects during my thesis work.

I thank Prof. Chris Love for mentoring me during my teaching assistantship, for his encouragement to write a paper in the Journal of Chemical Education, and for his close scrutiny and improvement of my writing skills.

I thank Prof. Krystyn Van Vliet and her students Ilke Kalcioglu, Irene Chen, and Adam Zeiger for their very helpful collaborations and lending me their expertise on the measurement of thin film mechanical properties.

I am grateful to my thesis committee members Prof. Michael Rubner, Prof. Darrell Irvine, and Prof. Patrick Doyle for all of their helpful suggestions.

I thank former fellow graduate students Kris Wood, Nicole Zacharia, and Jodie Lutkenhaus for being my mentors in the early years of my Ph.D. Also, I thank Fevzi Cebeci for collaborating closely with me during the final few years of my thesis and for providing electrochemical and AFM expertise. In addition, I thank Josh Moskowitz for his assistance working with bacteria cells, Jinkee Hong for lending his expertise with micelles, Renee Smith for lending her expertise with cyclodextrins, and Younjin Min for collaborating and assisting me with AFM nanoindentation and ellipsometry swelling experiments.

For their friendship and for helping to foster an enjoyable lab camaraderie I thank former and present Hammond group members Nathan Ashcraft, Avni Argun, Dan Bonner, Fevzi Cebeci, Eunice Costa, Nicole Davis, Peter DeMuth, Amanda Engler, Kevin Huang, Nasim Hyder, Yong Hoon Kim, Jason Kovacs, Kevin Krogman, Becky Ladewsky, Jung-Ah Lee, David Liu, Jodie Lutkenhaus, Rebekah Miller, Younjin Min, Isa Montiero, Josh Moskowitz, Grinia Nogueira, Megan O'Grady, Nick Orf, Juhyun Park, Mike Petr, Zhiyong Poon, Kittipong Saetia, Ray Samuel, Anita Shukla, Kris Stokes, Marianne Terrot, Eric Verploegen, Ryan Waletzko, Jessie Wong, Kris Wood, Pil Yoo, and Nicole Zacharia.

I also thank the undergraduate students who have worked with me over the years, including Adrian Li, Sammi Wyman, Thu Duong, Chris Love, and Sean Rogers.

I thank Christine Preston and Linda Mousseau for helping me with innumerable administrative matters.

Finally, I thank my parents Deborah and Darrell Schmidt and my grandparents Jean Fine and the late Sidney Fine for their constant support and encouragement.

This work was supported primarily by the MRSEC Program of the National Science Foundation and made use of the MRSEC Shared Experimental Facilities under award number DMR – 0819762. We thank the Center for Materials Science and Engineering, the Institute for Soldier Nanotechnologies, and the Langer Lab for access to their facilities.

Chapter 1: Introduction and Background

*Portions reproduced from “Electroresponsive Layer-by-Layer Thin Films” by Daniel J. Schmidt and Paula T. Hammond, *In preparation*.

1.1 Introductory Remarks and Technical Summary

The field of stimuli-responsive, or “smart”, materials has taken off in recent years toward innumerable applications, including controlled drug delivery, biological and chemical sensing, separations, flow control in microfluidic devices, and artificial muscles, among many other others.¹⁻⁹ Layer-by-layer (LbL) self assembly of thin film coatings¹⁰ provides a compelling strategy for the engineering of stimuli-responsive surface coatings in particular on account of the simplicity and versatility of the technique and the capability to conformally coat complicated geometries. While much work has been done on LbL films responsive to stimuli such as pH, ionic strength, and temperature,¹¹ relatively fewer works have focused on electroresponsive LbL films. Of the various available stimuli, electrochemical stimuli are particularly advantageous since they can be applied rapidly, reversibly, locally (i.e., at an electrode instead of throughout the bulk), remotely, and under mild conditions at constant bulk pH and temperature. This thesis investigates the manipulation of LbL film stability, structure, and mechanical properties through the use of electrochemical stimuli, in particular toward applications in electrically triggered drug delivery and “mechanomutable” surface coatings.

Since LbL films are typically held together by non-permanent crosslinks, such as ionic bonds or hydrogen bonds, there exists the possibility to manipulate the film structure and stability by disrupting the crosslinks in the film and/or dynamically changing the degree of functionality of the film constituents. Two strategies are employed to electrochemically manipulate LbL films in this thesis: the use of charge-shifting redox-active nanoparticles to

directly manipulate charge density within a film and the control over local/interfacial pH, which can effect changes in charge-shifting, pH-responsive materials.

The redox-active, charge-shifting nanoparticle material used in this work was Prussian Blue (PB), which is described in depth in section 1.3.1.3 below. PB, a well-known dye and electrochromic and electrocatalytic material, may be synthesized as negatively charged nanoparticles which can be assembled into LbL films. While PB-containing thin films have been studied for electrochromic devices¹² and sensing applications,¹³ the use of PB charge-shifting had been explored only briefly before this thesis.¹⁴ In the first model system explored in this thesis, PB was incorporated into LbL films along with positively charged, linear polyethyleneimine (LPEI) and a model polyanionic agent, dextran sulfate (DS). Application of +1.25 V (vs. SCE) oxidizes the PB and “erases” its negative charge, resulting in the controlled dissolution of the film and release of the model agent. Burst release profiles (with release completed within ~10 min) and “on-off” switchable release were achieved. Subsequently, films comprising PB and a small molecule antibiotic, gentamicin sulfate (GS), were developed. It was found that the drug loading into films could be precisely controlled with the number of deposited layers and that release amount (i.e., dosage) and kinetics could be controlled by the applied potential (in the range +0.50 to +1.25 V (vs. Ag/AgCl)) and the potential profile. The released drug was found to maintain its efficacy *in vitro* against *Staphylococcus aureus* bacteria. Furthermore, this material system is the first example of an LbL film comprised primarily of nanoparticles and small molecules, which may raise interesting fundamental questions regarding the self-assembly between these materials. Also, this body of work is among the first examples of electrically triggered dissolution of LbL films at very low electric potentials that do not change the local pH or generate gas bubbles.

PB was also utilized to induce reversible swelling and mechanical changes in thin film coatings. PB was incorporated into LbL films along with LPEI and upon application of -0.2 V (vs. Ag/AgCl), the negative charge on the PB surface doubled, causing an influx of ions and water into the film. Upon application of +0.6 V to re-oxidize the PB, the surface charge returned to the original level and ions and water were expelled from the film. Electrochemical cells were integrated with an ellipsometer, atomic force microscope (AFM), quartz crystal microbalance with dissipation monitoring (QCM-D), and nanoindenter to follow film thickness and mechanical stiffness in real-time during application of an electric potential. Reversible thickness changes on the order of 2-10% and reversible elastic modulus changes on the order of 50% (between 3.40 GPa and 1.75 GPa) were observed. This work set the stage for the design and study of other “mechanomutable” coatings that could exhibit even more dramatic changes.

Manipulation of local/interfacial pH was next utilized to both dissolve and swell/deswell LbL films. The first class of films explored was hydrogen-bonded LbL films. These films are known to dissolve at elevated pH above the pKa of the H-bond donor where it becomes substantially ionized;¹⁵ however, for biomedical applications, raising the bulk pH may not be a feasible option. Therefore, an electrochemically triggered increase in the *local* pH was induced by reducing dissolved oxygen to hydroxide ions. Films comprising polyvinylpyrrolidone (PVPON) and tannic acid (TA), which may be assembled under mild, physiological conditions, could also be dissolved at these conditions at rates dependent upon the applied voltage (in the range -0.25 V to -1.25 V vs. Ag/AgCl) and oxygen concentration. Since a number of groups have demonstrated encapsulation and controlled release of drugs from H-bonded films utilizing bulk pH or temperature changes,¹⁶⁻¹⁸ the technique developed here could serve as a promising

platform technology for actively triggered release of drugs from such films under mild conditions.

Besides film dissolution, a number of other materials systems may undergo swelling/deswelling transitions with changes in pH; however, large swings in bulk pH may be detrimental for sensitive biological materials such as cells and proteins. Therefore, this thesis aimed to extend the strategy mentioned above to actuate dramatic swelling and mechanical transitions in classically pH-responsive materials by controlling only the local/interfacial pH with electrochemistry. Films comprising polyallylamine hydrochloride (PAH) and sulfonated polystyrene (SPS) assembled at high pH (>9.0) are known to exhibit a superswelling transition (400-800 vol%) when pH is decreased below 4.0.^{19,20} The system exhibits hysteresis such that the pH must be raised above 10.5 to induce deswelling. Here, again utilizing electrochemical reduction of dissolved oxygen, we achieved reversible 300% volume changes and nearly order-of-magnitude changes in film viscoelasticity (i.e., shear modulus between 1.9 MPa and 230 kPa and loss modulus between 620 kPa and 90 kPa) at a constant bulk pH in the range of 3.0-4.0. The deswelling transition could also be carried out one time in a mild pH (i.e., 7.4) if the film is initially preswollen under acidic conditions. The effects of the applied voltage, the bulk pH, and initial film thickness on film deswelling kinetics were systematically investigated. The effect of thickness specifically allowed for the application of scaling arguments to estimate the diffusivity of water within the LbL films.

Together, these various model systems and the two strategies for manipulating charge density within LbL films highlight how electroresponsive LbL films may be engineered for desired applications. The LbL assembly technique is a promising method for the design of “smart”, electroresponsive surfaces.

1.2 Layer-by-Layer Assembly

Layer-by-layer (LbL) assembly is a simple and versatile, surface-mediated self assembly technique for the fabrication of nano- and microscale thin films.²¹⁻²⁷ The technique is based upon the alternating adsorption of materials with complementary functional groups (Fig. 1.1) in which the adsorption of each layer both compensates for the existing functionality on the surface and reverses the functionality on the film surface allowing for the deposition of subsequent layers.²⁸ The concept of LbL assembly was first introduced in the 1960s by Iler for the assembly of charged colloids (e.g., silica and alumina),²⁹ and then in the 1990s it was rediscovered and extended to charged polymers (i.e., polyelectrolytes) by Decher.^{10,30} While films are typically constructed on the basis of electrostatic attraction between oppositely charged materials, many examples in the literature exist of LbL films fabricated based on hydrogen bonding,^{31,32} covalent bonding,^{33,34} and specific biochemical interactions, among others.³⁵

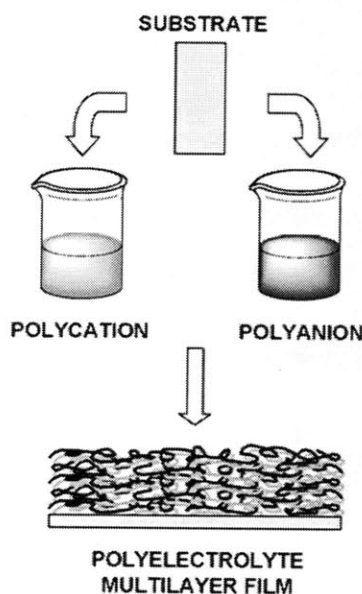


Figure 1.1. Schematic representation of the layer-by-layer assembly of a polycation and a polyanion to form a polyelectrolyte multilayer thin film.

Given the many interactions that can permit LbL assembly, a wide array of different types of materials have been incorporated into these films. The primary requirement is that the material must be polyvalent, such that it can cooperatively bind to a surface and reverse the surface functionality. The pioneering work by Decher demonstrated the incorporation of synthetic polyelectrolytes.¹⁰ Since then, many naturally occurring polyelectrolytes including nucleic acids (e.g., DNA and RNA), proteins and enzymes,³⁶ and polysaccharides, as well as many organic, inorganic, and metallic nano-objects have been incorporated.^{21,22,24-27} The myriad available functional materials have resulted in the development of LbL coatings for many applications including biomedical uses such as drug delivery and antibacterial surfaces,³⁷⁻⁴² electrochemical applications such as fuel cell membranes, sensors, and electrochromic devices,⁴³⁻⁴⁵ and surface wetting and optical applications such as antireflective, superwetting, and anti-fog coatings,^{46,47} among many others.

The LbL assembly approach is especially versatile because of the number of parameters that can be used to control and tune film properties.^{27,48} Since the films are generally deposited one molecular layer at a time, film thickness can be precisely tuned on the nanoscale simply by adjusting the number of deposited layers or adjusting the coating parameters. Furthermore, the film thickness as well as morphology (e.g., porosity, roughness, etc.) are greatly affected by the concentration, degree of charge (or other functionality), and the shape/morphology of the material being deposited. Besides controlling the components of the film, many researchers have demonstrated the influence of concentration, pH, ionic strength, deposition time, temperature, and deposition process type on the LbL process.

LbL films are typically fabricated via dip coating, but may also be assembled via alternate spin coating⁴⁹ or spray coating/misting (spray-LbL).^{50,51} The latter two techniques significantly

decrease the processing time, making these films more applicable for high throughput industrial applications. While self-assembly via dip coating generally proceeds only through diffusion of the polymers toward a substrate under the influence of electrostatic or other interactions, spin assembly and spray assembly provide an additional convective driving force. A twist on dip coating that allows for continuous manufacturing on a larger scale is roll-to-roll processing, which was previously applied to LbL coatings by the company Avery Dennison.²⁵ The spray-LbL technique is also very applicable to industrial applications where uniform coating of very large area surfaces is required. Two companies, Svaya Nanotechnologies, Inc. and Agiltron, Inc., are currently developing commercial spray-LbL coaters. Lastly, for smaller scale applications, it has also been shown that LbL films may be assembled under continuous flow in a microfluidic device.⁵² The work in this thesis involves coating by dip coating only, but the reader should take notice of the plethora of coating options.

In addition to the various LbL coating processing options, LbL assembly may be carried out on substrates of virtually any size, shape, or chemical composition. While traditional “top-down” coating techniques (e.g., spin coating and spray coating) and lithographic techniques are restricted to planar substrates, LbL assembly can be used to conformally coat virtually any 3-D geometry such as an endovascular stent.⁵³ Furthermore, spray-LbL has been shown to conformally coat fibrous mats and other porous materials.⁵⁴ The use of colloidal templates has further allowed LbL assembly to be used for the fabrication of polymeric micro- and nanometer-sized capsules⁵⁵ and nanotubes.⁵⁶ In some cases, one may fabricate free-standing LbL films that are peeled off of a substrate or triggered to release from a substrate.⁵⁷ Lastly, while LbL assembly is most classically carried out based on electrostatics, films may even be deposited on non-charged substrates. Our group and others have demonstrated film assembly on such low

surface energy polymers as Teflon® and PDMS, where weak van der Waals and hydrophobic interactions are sufficient to initiate film growth.⁵⁸ Various surface treatments such as plasma/corona treatment⁵⁹ or silanization⁶⁰ may also be applied to prime substrates for LbL assembly. While the work in this thesis involves coating of planar substrates only, the reader should again appreciate the diversity of applicable substrates for the LbL process.

1.3 Electroresponsive Layer-by-Layer Films

While many coating applications require that the properties of a coating remain constant over time, other applications arise from coatings engineered to respond to various external stimuli such as changes in pH, ionic strength, or temperature, or exposure to light or electric/magnetic fields. Indeed, the field of stimuli-responsive materials has taken off in recent years as multiple applications have arisen, including drug delivery, biological and chemical sensing, separations, and mechanical actuation, among others.¹⁻⁹ Stimuli-responsive LbL films represent an especially attractive platform given their versatility, simplicity of fabrication, and wide variety of incorporable functional and responsive materials.¹¹ This thesis focuses exclusively on LbL films that are responsive to electrochemical stimuli.

Two strategies are utilized to engineer the electrochemical response of LbL films: the use of redox-active, charge-shifting materials and the control over local pH. In the case of redox-active materials, the charge density within a film is changed directly through the injection or withdrawal of electrons from the material. In the case of local pH control, the charge density within the film is changed indirectly when generated H^+ or OH^- ions protonate or deprotonate film components, respectively. When there is a change in charge density within a film, nature requires that electroneutrality be maintained in the film; consequently, counterions and water of

solvation (i.e. through electroosmotic flux) will rush into the film. Further, the difference in concentration of the counterion in the film versus the surrounding solution will generate an ionic contribution to osmotic pressure, π_{ion} (Equation 1.1) that will bring additional water into the film. The film will swell to an equilibrium state when the total osmotic pressure in the film equals zero, which occurs when the other contributions to osmotic pressure balance the ionic contributions (Equation 1.2) (Fig. 1.2).⁶¹⁻⁶⁴ These other contributions include the elastic (entropic) restoring force from the polymer chains, π_{el} , repulsion between fixed charged groups in the film, π_{coul} , and contributions from mixing between the polymer and solvent, π_{mix} , which is typically calculated from Flory-Huggins theory. When the film does not have sufficient cohesive interactions (i.e., electrostatic crosslinks, H-bonds, or covalent crosslinks) to generate an elastic restoring force to counter film swelling, the film will dissolve (Fig. 1.2).

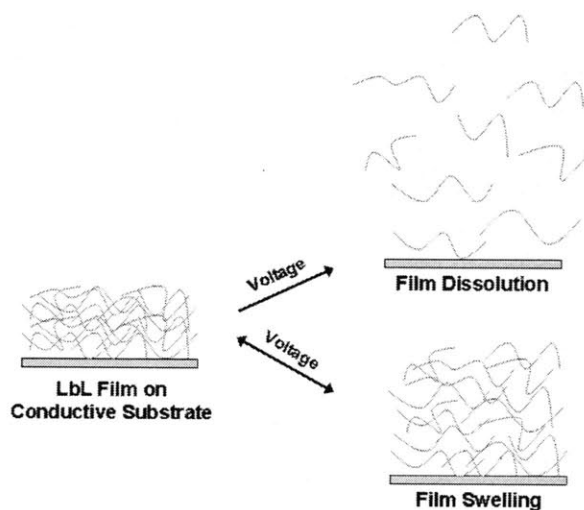


Figure 1.2. Schematic representation of the electrically triggered dissolution and swelling of a layer-by-layer film. Swelling to an equilibrium state occurs when the elastic forces in the film (from cohesive interactions and/or crosslinks) balance the osmotic pressure forces. Dissolution results when the osmotic pressure forces exceed the elastic forces.

$$\pi_{ion} = RT \sum_i (C_i - C_i')$$
 (1.1)

$$\pi_{total} = \pi_{el} + \pi_{coul} + \pi_{mix} + \pi_{ion} = - \left. \frac{\partial G}{\partial V} \right|_T = 0$$
 (1.2)

The two strategies that were utilized to engineer the electrochemical response of LbL films are reviewed in the sections below.

1.3.1 Redox-Active, Charge-Shifting Materials

Redox reactions, or those that involve the transfer of electrons and the change in the oxidation state of one or more atoms, are ubiquitous in nature in biological systems, for example in the processes of cell signaling and cellular respiration,⁶⁵ and in non-biological systems, such as the rusting of iron. In addition, mankind has harnessed the potential of redox reactions for energy storage and generation, such as in batteries and fuel cells, as well as for chemical synthesis and the smelting of metals. A number of redox-active materials exhibit multiple, stable redox sites, which allow the molecules to shift their charge reversibly in response to an electric potential or chemical oxidation/reduction. These materials fall into two general classes. The first class includes transition metal atoms, which have been incorporated into films as individual ions/coordination complexes, polymer-tethered complexes, and supramolecular complexes and clusters. The second class of materials, conjugated polymers, does not contain transition metal atoms, rather they are purely organic. Below I review the area of dynamically responsive LbL films based on redox-active charge shifting materials.

1.3.1.1 Transition metal ions and complexes

Many transition metal atoms, either unbound or part of a coordination complex, may exhibit multiple different oxidation states with different corresponding charge states. While some researchers have neglected the charge-shifting nature of these materials in LbL films since their applications of interest were relatively unaffected by this phenomenon, others, including our group, have explicitly utilized this phenomenon to induce swelling, mechanical, or dissolution responses in LbL films.

Zr⁴⁺ ions

The first class of transition metal materials reviewed here are individual ions or coordination complexes. Wang et al. fabricated LbL films containing DNA and inorganic zirconium ions (Zr⁴⁺) on gold electrodes.⁶⁶ The authors found that application of negative electric potentials in the range of -0.50 V to -1.1 V (vs. Ag/AgCl) to the gold electrode induced film dissolution and the controlled release of DNA.⁶⁶ They proposed that reduction of the Zr⁴⁺ to a Zr³⁺ species is the stimulating factor for film dissolution through either DNA decondensation, movement of Zr ions or other ions within the film that disrupt the film stability, or reductive formation of polynuclear zirconium complexes.⁶⁶ They also acknowledge that a local pH increase near the electrode surface may trigger dissolution as the citric acid in the electrolyte is deprotonated and competes with DNA for binding to Zr⁴⁺.⁶⁶ Electrochemical surface plasmon resonance was used to track film dissolution.

Metalloporphyrins and metallophthalocyanines

Metalloporphyrins and metallophthalocyanines (Figure 1.3) represent another class of transition metal complexes that have been incorporated into LbL films. Many porphyrins are naturally occurring, including heme and chlorophyll, while phthalocyanines are structurally similar, synthetic analogues. The properties of porphyrins and phthalocyanines have been reviewed in books by Kadish et al.⁶⁷ and Leznoff et al.,⁶⁸ respectively. Interestingly, redox reactions involving the π -conjugated ring system alone are observed in addition to transition metal redox reactions.⁶⁹ A number of different researchers have investigated the assembly of LbL films including these materials⁷⁰⁻⁹⁰ and have explored their potential for applications in optoelectronic/photovoltaic devices,^{78,83,86,89} thin film transistors,⁷⁹ data storage,⁷² photocatalysis and electrocatalysis,^{71,74} electrochromism,⁸⁴ non-linear optical devices,⁸⁸ biological and chemical sensing,⁸⁵ and gas sensing.⁷⁵ To our knowledge, the effect of metalloporphyrin and metallophthalocyanine charge shifting on the structure of LbL films has yet to be investigated.

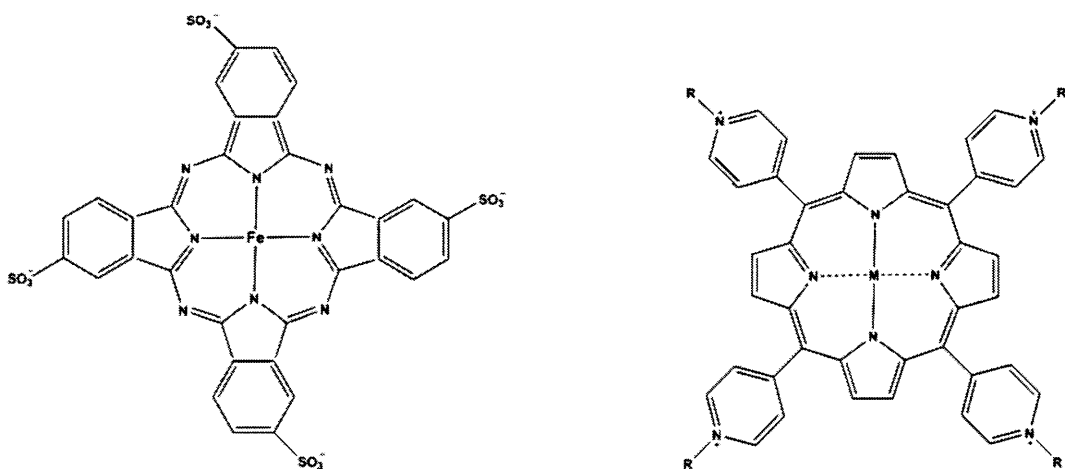


Figure 1.3. Molecular structure of iron phthalocyanine tetrasulfonic acid (FePcTs) (left) and a generic, charged metalloporphyrin (right).

Ferrocyanide complexes

Instead of building films with a transition metal complex as a structural film component, Grieshaber et al. incorporated ferrocyanide ions ($\text{Fe}^{\text{II}}(\text{CN}_6)^{4-}$) into poly(L-glutamic acid)/poly(allylamine hydrochloride) (PGA/PAH) LbL films after film assembly.⁹¹ They proposed that the polyvalent ferrocyanide ion forms ionic bridges between the PAH polymer chains. When the $\text{Fe}^{\text{II}}(\text{CN}_6)^{4-}$ is oxidized to $\text{Fe}^{\text{III}}(\text{CN}_6)^{3-}$, a charge imbalance is created in the film; to compensate for the excess positive charge present in the film, anions and water from solution will swell the film. Using QCM-D, they observed 5-10% reversible volume changes when applying mild voltages between 0 and +0.6 V (vs. Ag/AgCl).

1.3.1.2 Polymer-tethered transition metal complexes

Ferrocene- and osmium(II)-modified poly(allylamine hydrochloride)

A number of other authors have also synthesized transition metal-containing organic and inorganic polymers. Calvo et al. synthesized poly(allylamine hydrochloride) (PAH) modified by ferrocene (PAH-Fc) (Fig. 1.2),⁹² and Danilowicz et al. synthesized PAH modified by an osmium bipyridine-pyridine complex (PAH-Os) (Fig. 1.4).⁹³ The modified polymers were synthesized by a condensation coupling reaction between aldehyde groups on the metal complexes and primary amines on the PAH to form imine bonds. Initially, Calvo and coworkers crosslinked the PAH-Fc and PAH-Os with themselves to make surface-bound, redox-active hydrogels.^{94,95} Subsequently, they fabricated LbL films utilizing PAH-Fc and PAH-Os as the polycations and various other

polymers, including glucose oxidase, polystyrene sulfonate, and polyvinyl sulfonate, as the polyanions.^{64,96-102} In the films containing PAH-Fc, the oxidation state of the iron in ferrocene could be shifted from the Fe(0) state in ferrocene to the Fe(I) state in ferrocenium at a mild electric potential between +0.1 V and +0.7 V vs. SCE. In the films containing PAH-Os, the oxidation state of the osmium could be shifted between Os^{II} and Os^{III} at a mild electric potential between 0 V and +0.5 V vs. SCE. Using ellipsometry as well as electroacoustic impedance measurements acquired with a quartz crystal microbalance (QCM) to assess film thickness and viscoelastic changes upon application of electric potentials, they observed maximum changes in both quantities on the order of 10%. The proposed mechanism of film swelling involved the generation of a charge imbalance within the LbL films when the charge of the transition metal was altered.

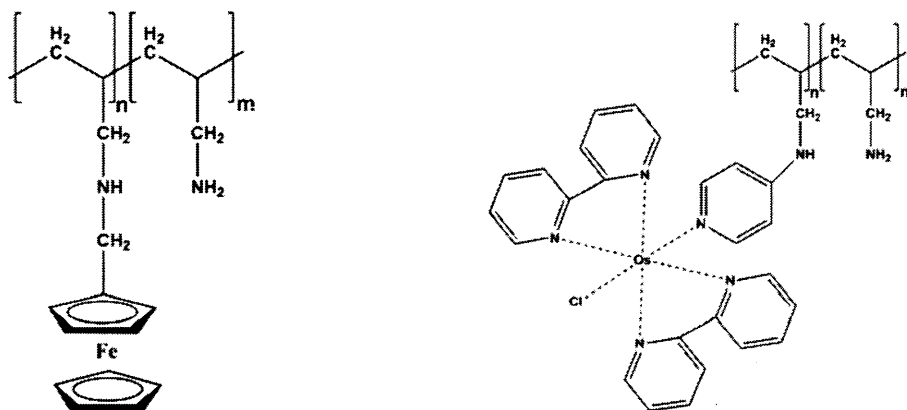


Figure 1.4. Molecular structure of ferrocene-modified polyallylamine (PAH-Fc) (left) and osmium pyridine/bipyridine-modified polyallylamine (PAH-Os).^{92,93}

Polyferrocenylsilanes

A second class of redox-active polyelectrolytes that have been incorporated into LbL films are polyferrocenylsilanes (PFS).¹⁰³ The synthesis of these polymers, which

was pioneered by the Manners and Vancso groups, involves the ring opening polymerization of a silicon-bridged ferrocenophane, which results in ferrocene units within the polymer backbone (Figure 1.5).¹⁰⁴⁻¹⁰⁹ As in the case of the ferrocene-modified polyallylamine studied by the Calvo group, the redox state of the iron in ferrocene may be reversibly modulated either electrochemically or chemically. Vancso and co-workers have assembled both thin film coatings and multilayer capsules containing ionically charged PFS.¹¹⁰ When the Fc is oxidized to Fc^+ , the polymer chains stretch due to an increase in charge density; in addition, counterions (along with water) will enter the system to maintain electroneutrality. These phenomenon lead to swelling of both PFS thin films¹¹¹ and PFS-containing LbL microcapsules.¹¹² The authors studied redox-responsive capsule wall permeability utilizing fluorescent probe molecules and *in situ* confocal laser scanning microscopy (CLSM), and they propose potential biomedical applications for these materials.

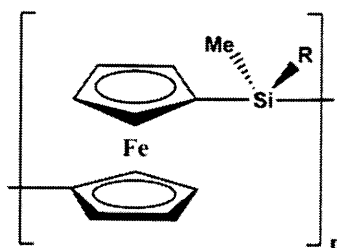


Figure 1.5. Molecular structure of a poly(ferrocenylsilane) (PFS). PFS polyelectrolytes are made using various charged groups for the R unit, as shown by Ma et al.¹⁰³

1.3.1.3 Supramolecular transition metal complexes and clusters

The final class of transition metal-based, redox-active materials reviewed here are those that exist as polynuclear clusters or supramolecular constructs. The two

compounds that fall into this category that have been incorporated into LbL films are polyoxometalates and Prussian Blue and its analogues.

Polyoxometalates

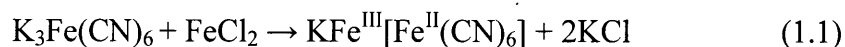
A number of authors have incorporated polyoxometalates (POMs)¹¹³ into LbL films.¹¹⁴ POMs are a diverse class of inorganic transition metal oxygen clusters with unique electronic properties, making them useful for applications including electrochromic windows, sensors, and catalysts.^{113,114} In addition, some POMs are biologically active and exhibit anti-tumor, antiviral, and antibacterial activity.¹¹⁵ The synthesis of POMs was recently reviewed by Long et al.,¹¹³ while the incorporation of POMs into LbL films was reviewed by Liu et al.¹¹⁴ A number of different types of POMs have been developed, including, for example, Keggin ($[\text{XM}_{12}\text{O}_{40}]^{3-4-}$ where X=P, Si, M = W, Mo), Dawson ($[\text{P}_2\text{M}_{18}\text{O}_{62}]^{6-}$ where M = W, Mo), Preyssler ($[\text{M}(\text{H}_2\text{O})\text{P}_5\text{W}_{30}\text{O}_{110}]^{14-/12-}$ where M = Na, Eu), Co-POM ($[\text{Co}_4^{\text{II}}(\text{H}_2\text{O})_2\text{P}_4\text{W}_{30}\text{O}_{112}]^{16-}$), and Mo132 Giant Keplerate ($[\text{Mo}_{132}\text{O}_{372}(\text{CH}_3\text{COO})_{30}(\text{H}_2\text{O})_{72}]^{42-}$) types. These clusters exhibit multiple different geometries and have diameters ranging from <1 nm to roughly 5 nm.¹¹³ While a number of groups have investigated the fundamentals of POM self assembly in LbL films, the electrochemical behavior of POM in LbL films, and the use of POM-containing LbL films for applications as electrochromic/photochromic materials and as pH-sensitive probes,¹¹⁶⁻¹²² the effects of POM charge-shifting have yet to be explored.

Prussian Blue

The final supramolecular transition metal compound reviewed here is Prussian Blue (PB), which is the charge-shifting material used predominantly in this thesis. PB,

which has been termed the “artists’ pigment and chemists’ sponge” by Ware¹²³ due to its intense color and zeolitic structure, is the colloquial name for iron (III) hexacyanoferrate (II). PB exists in a face centered cubic (FCC) crystal structure in which low spin Fe(II) atoms are coordinated to the C atoms in the CN ligand and the high spin Fe(III) atoms are coordinated to the N atoms in the CN ligand (Figure 1.6).¹²⁴ There are two different forms of PB, the so-called “soluble” and “insoluble” forms, which have molecular formulas of $\text{KFe}^{\text{III}}[\text{Fe}^{\text{II}}(\text{CN})_6]$ and $\text{Fe}^{\text{III}}_4[\text{Fe}^{\text{II}}(\text{CN})_6]_3$, respectively. Both forms are truly insoluble, however, the “soluble” form may form electrostatically stable dispersions in water when the potassium ions dissociate.¹²⁴ Synthesis takes place through a step growth mechanism in three dimensions, involving alternating complexation between an Fe(II) salt (e.g. FeCl_2) and an Fe(III) cyano salt (e.g. $\text{K}_3\text{Fe}(\text{CN})_6$) (Reaction 1.1).¹⁴

Delongchamp and Hammond showed that nanoparticles of “soluble” PB with controlled size may be synthesized by controlling the ratio between the two iron salts.¹⁴ Analogous to polymer step growth, in which a large excess of one monomer results in polymers with smaller molecular weight, a large excess of one iron salt results in smaller nanoparticles. Furthermore, the monomer (or iron salt) in excess will cap the ends of the polymer (nanoparticle). Therefore, the “soluble” form of PB results when the $\text{K}_3\text{Fe}(\text{CN})_6$ is added in excess. PB exhibits multiple, stable redox states (Table 1.1), with the colloquial names Prussian White (PW), Prussian Blue (PB), Berlin Green (BG), and Prussian Yellow (PX), in order of increasing oxidation state.¹²⁴



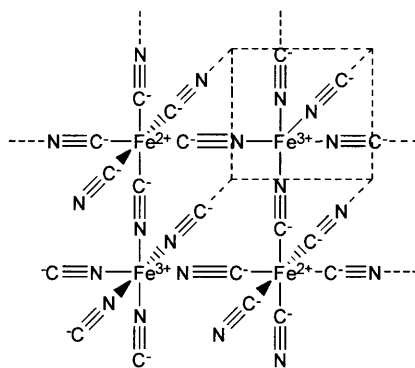


Figure 1.6. Crystal structure of Prussian Blue. Potassium ions, which are not shown for clarity, are the counterions for the negatively charged sites on the crystal surface and interior sites.

Table 1.1. Oxidation states of Prussian Blue

Common Name	Formula Unit	Charge per Formula Unit
Prussian White (PW)	$K_2Fe^{II}[Fe^{II}(CN)_6]$	-2
Prussian Blue (PB)	$KFe^{III}[Fe^{II}(CN)_6]$	-1
Berlin Green (BG)	1:2 ratio of PB and PX	-1/3
Prussian Yellow (PX)	$Fe^{III}[Fe^{III}(CN)_6]$	0

PB has a long history, as it was originally discovered by accident in 1704 by a German artist attempting to make a red pigment.¹²³ Since then it has been used extensively as a dye by artists and in the textile industry, as well as in the blueprinting process.¹²³ Besides its intense blue color, the zeolitic structure and ion-exchange capabilities of PB have resulted in its use as an antidote for thallium and radioactive cesium poisoning. Normally, the internal lattice sites are occupied by potassium ions (K^+); however, in the presence of Th^{1+} and Cs^{1+} ions (or the Cs^{137} radioisotope), which possess similar ionic radii to potassium, an ion exchange will take place.¹²³ In fact, PB was approved by the FDA in an oral dosage form as an antidote to these toxins,¹²⁵ and has been shown to be safe for use in humans.¹²⁶ It was administered after the Chernobyl

disaster, and the U.S. government maintains PB in its Strategic National Stockpile in case of a “dirty bomb” attack or other related emergency.

More recently, PB has been investigated due to its interesting electrical, magnetic, and catalytic properties. Lezna and coworkers recently reviewed the synthesis, characterization, and emerging applications of PB and its analogues (i.e., metal hexacyanoferrates).¹²⁷ In 1978, Neff was the first to immobilize PB on a conductive substrate using electrodeposition.¹²⁸ Since then, PB thin films have been fabricated through both Langmuir-Blodgett assembly¹²⁹ and LbL assembly.^{14,130-139} PB is a mixed valence transition metal material since it contains iron in both its +3 and +2 oxidation states. Electron hopping between the iron atoms results in a strong absorption band centered at 680 nm, corresponding to a blue color. PB is electrochromic since the modulation of the oxidation state of the iron atoms by an applied electric potential changes the color of the material. Researchers have investigated the potential of PB for use in electrochromic devices in both LbL^{14,131} and non-LbL assemblies.^{12,140-143} PB also exhibits ferromagnetic ordering below 5.6 K;¹⁴⁴ however, there has been increased interest in practical applications since certain PB analogues exhibit Curie temperatures much closer to room temperature.¹⁴⁵ Finally, since PB can electrocatalyze the oxidation of hydrogen peroxide, which is produced during the oxidation of glucose by glucose oxidase, many researchers have developed PB-based glucose sensors, as well as other biosensors.^{13,146}

The Hammond group was the first to explore the effects of PB charge-shifting on the stability and structure of LbL films. Delongchamp and Hammond synthesized an electrostatically stabilized colloidal suspension of PB nanoparticles with a median

diameter of 4-5 nm and assembled them into LbL films with the polycation linear polyethyleneimine (LPEI). The main thrust of that study was for applications in electrochromic displays and “smart” windows, however, they found that oxidation of the PB to its fully oxidized state (i.e., Prussian Yellow, or Prussian Brown), resulted in the controlled dissolution of the thin film. They proposed that neutralization of the charge on PB broke the cohesive ionic crosslinks between PB and LPEI. This phenomenon was exploited in Chapters 2 and 3 of this thesis for the study of electrically triggered drug delivery. The electrochemical reduction of PB to the fully reduced state (i.e., PW) doubles the charge on the PB surface. This phenomenon was used in Chapter 4 of this thesis for the study of electrically triggered swelling and mechanical changes in LbL films.

1.3.1.4 Conjugated polymers

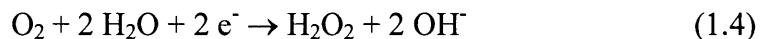
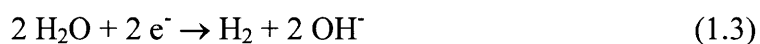
Conjugated polymers were discovered in 1970 by Heeger, McDiarmid, and Shirakawa, all of whom received the Nobel Prize for their discovery. These polymers continue to be an area of great interest as electroactive and responsive materials.¹⁴⁷⁻¹⁴⁹ Typically, these polymers must be “doped” through partial oxidation or reduction of the polymer backbone to generate a delocalized π -electron network with free charge carriers. Conjugated polymers can possess an interesting combination of properties: the conductivity of metals along with the processability of polymers.¹⁴⁸ This combination makes them useful for biological and chemical sensors, displays, batteries, antistatic coatings, and artificial muscles, among other applications.¹⁵⁰⁻¹⁵³

Conjugated polymer thin films may be fabricated via electropolymerization or self-assembly techniques, such as LbL assembly. A number of authors have developed responsive, electropolymerized films of polyaniline and polypyrrole, and studied thickness and mechanical changes in response to applied electric potentials.¹⁵⁴⁻¹⁶⁰ Similarly, many authors have developed conjugated polymer actuators through deposition on a flexible electrode for applications as artificial muscles, as well as for use in catheters and bioMEMS devices.¹⁶¹ Rubner and co-workers were the first to incorporate a conjugated polymer (i.e., polyaniline) into LbL films, which was done on the basis of both electrostatics¹⁶² and H-bonding.¹⁶³ Subsequently, Schlenoff et al. incorporated a polyviologen into an LbL film and reported that electrochemical reduction of the polymer, which increased the negative charge density, resulted in an influx of cations to compensate the excess charge in the film.¹⁶⁴ More recently, a number of other groups, including the Hammond group, have assembled conjugated polymers into LbL films for applications in electrochromism,^{131,165-167} drug delivery,¹⁶⁸ and pH sensing, among others.¹⁶⁹ To our knowledge no one has explored the swelling and mechanical response of LbL films containing conjugated polymers.

1.3.2 Local pH Control

In addition to modulating the oxidation state of materials adsorbed to an electrode surface, it is also possible to initiate redox reactions with molecules dissolved in the bulk solution. In this latter case, molecules will diffuse to an electrode surface, undergo reduction or oxidation, and then the reaction products will diffuse away from the electrode. In an aqueous electrolyte solution containing water, dissolved oxygen, and an

electroinert salt, Reactions 1.2-1.5 are possible. These reactions are the oxidative and reductive hydrolysis of water, respectively, and the two-electron and four-electron reduction of dissolved oxygen, respectively. The reader may recognize that Reactions 1.2 and 1.3 in reverse are the cathode and anode reactions of a hydrogen fuel cell. In a fuel cell, O₂ and H₂ are the fuels that spontaneously combine to form water and release energy. For local pH control using these reactions, one must supply energy (i.e., in an electrolytic cell) to split water. The use of local pH control to manipulate polymeric materials, with a focus on LbL films, is reviewed in the sections below.



There has been a large body of work on electroactive polymers (EAPs) and hydrogels that swell, shrink, or bend in response to an electric field.¹⁷⁰ While there are many mechanisms for actuation, many EAPs are polyelectrolyte hydrogels that respond to the motion of ions, and especially to pH gradients generated by applied electric potentials or currents. Typically, the polymer material will be sandwiched between two flexible electrodes, and Reactions 1.2 and 1.3 above will occur at the anode and cathode, respectively. The resulting pH gradients will then cause a gradient in the degree of ionization across the gel, and therefore a deformation as ions and water enter or leave the gel to maintain electroneutrality. Such electroactive polymers have been explored for multiple biomedical applications and various soft robotic applications;^{6,171,172} however,

typically they require the applications of large electric potentials, and the generation of hydrogen and oxygen gas may be detrimental for a desired application.

A local decrease in pH (i.e., local acidification) may be induced by the oxidative hydrolysis of water (Reaction 1.2). Gabi et al. measured local pH profiles near an ITO substrate with an applied current density of 1 A/m^2 , and found that the pH at the electrode reaches a value of around 4.0 in a non-buffered 0.15 M NaCl solution at neutral bulk pH.¹⁷³ In the field of LbL assembly, there have been reports of thin film dissolution for drug delivery applications based on this local acidification phenomenon.¹⁷⁴⁻¹⁷⁶

Boulmedais et al. fabricated LbL films with poly(L-lysine) (PLL) and heparin, both of which are weak polyelectrolytes, which exhibit a pH-sensitive degree of ionization.¹⁷⁴

They propose that local acidification via application of +1.8 V (vs. Ag wire pseudoreference electrode) protonates the carboxylic, sulfate, and sulfamide groups on heparin, resulting in breakage of ionic crosslinks and film dissolution.¹⁷⁴ Similarly, Dieguez et al. fabricated LbL films comprising PLL and DNA, and they triggered film dissolution by application of +1.9 V (vs. Ag/AgCl). They refer to work from Blättler et al. who showed that PLL desorbs from a substrate at a pH below the substrate isoelectric point.¹⁷⁷ Gabi et al. found PLL desorption to occur at roughly pH 3.8-4.2 at an indium tin oxide (ITO) substrate.¹⁷³ Further, they propose that production of Cl_2 at the electrode (from oxidation of Cl^- ions), which reacts with water to form HClO , may crosslink PLL chains causing them to lose their charge. Lastly, Sato et al. fabricated LbL films composed of 2-iminobiotin-labeled polyethyleneimine and avidin based upon the well known biotin-avidin complexation.¹⁷⁶ The 2-iminobiotin-avidin complex is only stable at basic pH values.¹⁷⁸ Therefore, films were assembled at pH 9, and when an electric

potential of +0.6 to +1.0 V (vs. AgCl) was applied to a Pt electrode coated with the film, the film dissolved on account of local acidification.¹⁷⁶ Sato et al. used the same local acidification mechanism to control the release of a charged porphyrin molecule from LbL films.¹⁷⁹

A local increase in pH (i.e., local basification) may be induced by the reductive hydrolysis of water (Reaction 1.3) and/or the reduction of dissolved oxygen (Reactions 1.4 and 1.5). Deslouis et al. developed an experimental device to measure interfacial pH during oxygen reduction at a submerged impinging jet electrode.¹⁸⁰ They found that the interfacial pH reaches a value of 10.4-10.7 in a non-buffering solution at neutral bulk pH. There has been a substantial amount of work on the use of a local pH decrease to precipitate metal salts and oxides for various applications including desalination of water, scale removal from water streams, and synthesis of corrosion-resistant coatings.¹⁸¹⁻¹⁸⁶ The use of a local pH decrease to manipulate soft materials was pioneered by Kwon et al. in 1991 who applied reducing potentials to hydrogen-bonded hydrogels to control the release of insulin.¹⁸⁷ Subsequently, Kwon et al. controlled the release of heparin from a polyelectrolyte complex using the same mechanism.¹⁸⁸ More recently, Tam et al. utilized the reduction of dissolved oxygen to “open” and “close” an electrode interface modified with a pH-sensitive polyelectrolyte brush. Despite these precedents, there have been no reports on the use of an electrochemically triggered increase in local pH to manipulate LbL films. In this thesis, I utilize that strategy to induce the dissolution of hydrogen-bonded thin films in Chapter 5 and to trigger swelling/deswelling and mechanical transitions in pH-responsive LbL films in Chapter 6.

1.4 Electrically Triggered Drug Delivery

Electrically triggered drug delivery is a primary application area of much of the work presented in this thesis. Traditionally, medications have been administered orally or intravenously. These routes of entry generally result in systemic exposure of the body to the drug, which may be undesired due to unwanted side effects and higher dosage requirements. Therefore, many different localized and controlled release technologies have been explored. Many of these technologies rely on the encapsulation of drug molecules in a polymer matrix or reservoir, which can be implanted in the body. Drug release is then typically mediated either through passive diffusion and/or through erosion of the polymer. These types of “passive” release systems are ideal for many applications and have been commercialized in multiple products including the Gliadel® wafer to treat brain tumors and the Taxus® and Endeavor® drug-eluting endovascular stents; however, there are other applications which could benefit from actively triggered drug delivery.

The ability to actively trigger drug delivery from an implant could allow for better temporal control over drug release through remote-controlled drug release or pre-programmed drug release. Further, biosensing and drug delivery units can be integrated to allow for real-time drug release in response to physiological cues.^{189,190} Triggered drug delivery is also especially relevant for therapies or treatments that require pulsatile release profiles with potentially long durations between doses, such as in the case of many hormone therapies and vaccines.^{191,192} Given all of these benefits, many researchers have developed stimuli-responsive drug delivery systems.^{2,3,193-196} As mentioned previously, few stimuli have the advantages of electrical stimuli. There are two notable examples of electrically triggered drug delivery devices. Santini et al. and the company MicroCHIPS, Inc. have developed a microreservoir-based “pharmacy-on-a-chip”.

The first version of the device utilized thin gold caps to sequester drug in micromachined wells in a silicon wafer.¹⁹⁷ A potential of roughly +1V (vs. SCE) was applied to the gold, causing it to dissolve into soluble gold chloride complexes, thereby releasing drug from the uncapped well.¹⁹⁷ More recent versions of the device utilize gold or titanium capped wells to which a large current pulse is applied to thermally heat and melt the reservoir cap.^{198,199} MicroCHIPS has demonstrated actively triggered drug release via telemetry to successfully release a polypeptide in dogs over a 6 month period.¹⁹⁹ Current clinical trials in humans involve the delivery of parathyroid hormone to treat osteoporosis. A second notable example is the electro-osmotic pump developed by MicroLin LLC.²⁰⁰ It is a miniaturized implantable pump that operates without an external power source, using an electro-osmotic engine, and has shown promising results in three animal studies. The reader should refer to Grayson et al. for a review of electronic MEMS for drug delivery.²⁰¹

While there has been great success thus far both in academic and industrial setting for the design of electrically-triggered drug delivery devices, there are some limitations to the existing technologies. First, microfabrication techniques are typically limited to planar substrates, making integration with nonplanar medical implants challenging. Second, the lithographic and micromachining processes required to fabricate Si-based devices are time-consuming and expensive. The work in this thesis sought to overcome some of these limitations by developing a simple and easy-to-fabricate layer-by-layer coating that can be dissolved upon application of an electric potential. While there have been previous reports of electrically-triggered dissolution and drug delivery from LbL films, most of those reports use high voltages that hydrolyze water and thus change local pH and generate gas bubbles, which may be undesirable for *in vivo* applications. The work in this thesis utilizes a redox-active, biocompatible nanoparticle which

can shift its charge at very mild potentials, and therefore may be particularly promising for biomedical applications.

1.5 Mechanomutable Materials

The other primary application of the work in this thesis lies in the area of “mechanomutable” materials. These materials are those that change their mechanical properties in a response to external stimuli, a feature which could be useful for control over cellular behavior on surfaces, protein adsorption, tunable vibration absorption/damping, motors that perform mechanical work, responsive coatings in nanoscale devices, and ballistic protection for soldiers, among others. Interestingly, many examples of mechanomutable materials can be found in nature. For instance, a number of echinoderms (e.g., sea urchins, sea cucumbers, and starfish) can rapidly alter the stiffness of their tissue to squeeze through gaps in rocks.^{202,203} Another example is the female cervix, which becomes more compliant during childbirth.²⁰⁴ In both of these examples, the mechanical response relies upon reversible crosslinking and complex structural remodeling processes in the material.

Researchers have explored multiple strategies for developing synthetic, mechanically response materials, some of which are based on examples from nature. A recent biomimetic, mechanomutable material system, which mimics the sea cucumber dermis, was designed by Capadona et al.²⁰⁵ In that work and those that followed,²⁰⁵⁻²⁰⁸ cellulose nanowhisker composites were fabricated, and interactions between the whiskers were turned “on” and “off” by exposure of the composite to a competitive H-bonding solvent. Through this strategy, which breaks the mechanical percolation between fibers, they achieved over three order-of-magnitude changes in the material elastic modulus. A second notable example based upon the formation/disruption of

a percolative network was reported by Loveless et al. where they fabricated supramolecular gels based upon the coordination between poly(4-vinylpyridine) and bimetallic crosslinkers.²⁰⁹ Dramatic changes (up to five orders of magnitude) in the viscoelastic properties of the gel were observed over a narrow range of crosslinker concentration (i.e., at the percolation threshold).²⁰⁹ Other examples of reversibly tunable stiffness and damping in macroscopic materials have been reported for magnetorheological elastomers,²¹⁰ poly(dimethylsiloxane) elastomers with ionic and H-bonding constituents,²¹¹ and salt-triggered peptide folding.²¹²

Mechanomutable phenomena on the nanoscale, which are particularly relevant to applications in bionanotechnology, have been less explored. This field has thus far focused on polyelectrolyte brushes responsive to pH and ionic strength²¹³ as well as homopolymer and block-copolymer films and brushes sensitive to the solvent.²¹⁴⁻²¹⁶ Layer-by-layer films represent a particularly compelling system to study stimuli-responsive behavior on the nanoscale. It is well-known that LbL film mechanical properties may be controlled by post-assembly crosslinking²¹⁷⁻²²² as well as assembly pH and choice of polymer.^{223,224} These films can also be stimuli-responsive; in particular, it has been shown that changes in humidity²²⁵ and ionic strength²²⁶ can reversibly alter the stiffness of LbL films. More recent work has demonstrated reversibly swellable LbL films and nanotubes with change in pH²²⁷ and temperature,²²⁸ but without quantification of mechanical changes. There have also been a number of electrically swellable LbL systems mentioned in sections 1.3.1.1 and 1.3.1.2, but with little to no mechanical characterization.

This thesis examines two material systems that exhibit electrochemically triggered, reversible swelling and mechanical transitions utilizing both charge-shifting of redox-active, Prussian Blue nanoparticles and local pH changes. The work that utilizes Prussian Blue

nanoparticles opens up avenues for controlling mechanical percolation in thin polymer films, in which interactions between nanoscale filler particles could be turned “on” and “off” by an electrical stimulus to achieve drastic mechanical changes. The work that utilizes local pH changes achieves much more dramatic swelling and mechanical changes and opens up avenues for the control of mechanical percolation based upon forming and disrupting dynamic crosslinks above and below the critical crosslink density for network percolation.

1.6 Thesis Overview

In this thesis, electrochemical stimuli are utilized to either dissolve or swell/deswell LbL polymer and polymer nanocomposite thin films. Multiple materials systems are investigated to demonstrate the versatility, tunability, and potential applications of these electroresponsive coatings.

Chapters 2-4 examine the use of redox-active, charge-shifting, Prussian Blue nanoparticles to manipulate LbL nanocomposite films. **Chapter 2-3** focus on controlled film dissolution and drug delivery. Film growth and dissolution are followed with profilometry and UV/Vis spectroscopy, while film surface morphology is studied with atomic force microscopy (AFM). The release of radiolabeled drug molecules is quantified via scintillation counting and the loading and release of non-radiolabeled drugs is followed with fluorescence spectroscopy. Electrochemical behavior of the films is assessed with cyclic voltammetry and chronoamperometry. Cell viability assays were carried out to confirm the biocompatibility of PB, and microdilution assays were carried out to confirm the *in vitro* efficacy of an antibiotic released from a film. Together, the data reveal that PB-containing LbL films are sufficiently versatile to load and release diverse classes of molecules (e.g., polyanions and small molecules

that are both hydrophilic and hydrophobic). Release of an active small molecule antibiotic drug may be precisely controlled by an electrochemical stimulus.

Chapter 4 focuses on controlled film swelling/deswelling and mechanomutability. Film swelling/deswelling during the application of an applied potential is followed with spectroscopic ellipsometry, AFM, and a quartz crystal microbalance with dissipation monitoring (QCM-D). Mechanical properties of the films are assessed with both nanoindentation and QCM-D. The data confirm our hypothesis that an increase in charge density within an LbL film will result in film swelling and an increase in compliance. While the mutability of the system is relatively modest, this work is the first to demonstrate electrically controlled mechanomutability of an LbL nanocomposite system, opening up multiple possible applications and also avenues for the investigation of mechanical percolation phenomenon.

Chapters 5-7 examine the use of electrochemically induced local/interfacial pH gradients for the manipulation of LbL polymer films. **Chapter 5** focuses on controlled dissolution of hydrogen-bonded films for both controlled release applications and ultrathin free-standing film generation. Spectroscopic ellipsometry is used to follow changes in film thickness over time, while AFM is used to study film surface morphology. The data reveal that film dissolution kinetics may be controlled by both the magnitude of the applied potential and the concentration of dissolved oxygen. Interesting morphological changes, involving the formation of microporous films, were observed during film dissolution. Besides controlled release applications, the films may also be used as sacrificial layers to trigger the release of overlying ultrathin films that don't respond to the electric potential.

Chapters 6 focuses on controlled film swelling/deswelling and mechanomutability of an all-polymer LbL film. Again, spectroscopic ellipsometry and QCM-D were used to follow film

thickness and mechanical properties under the influence of applied electric potential. The effects of film thickness, the magnitude of the applied voltage, and the bulk pH on film deswelling kinetics were systematically investigated. The data revealed that deswelling kinetics were faster for greater voltages, higher bulk pH, and thinner films as expected. The magnitude of the swelling and mechanical transitions were much greater than those for the PB-based films making this film system especially promising for applications and further fundamental study.

Chapter 7 is a reproduction of a manuscript published in the Journal of Chemical Education based upon a layer-by-layer experiment designed for undergraduate polymer science courses. The experiment exposes students to the concepts of functional and responsive polymer coatings and to LbL assembly, a versatile and relatively new thin film fabrication technique. The students dip coat substrates by hand to make films containing the conducting polymer polyaniline. Film growth is followed with UV/Vis spectroscopy and film conductivity is measured with a multimeter. The optical pH-response of the films is assessed with UV/Vis spectroscopy and the electrochromic properties (i.e., switching speed and contrast) are measured in a spectroelectrochemical cell. Given the simplicity of LbL assembly, it provides a perfect platform for undergraduate polymer courses to study both the fundamentals of self-assembly and applications thereof.

1.7 References

1. Ahn, S. K.; Kasi, R. M.; Kim, S. C.; Sharma, N.; Zhou, Y. X. Stimuli-Responsive Polymer Gels. *Soft Matter* **2008**, *4*, 1151-1157.
2. Ganta, S.; Devalapally, H.; Shahiwala, A.; Amiji, M. A Review of Stimuli-Responsive Nanocarriers for Drug and Gene Delivery. *J. Controlled Release* **2008**, *126*, 187-204.
3. Mano, J. F. Stimuli-Responsive Polymeric Systems for Biomedical Applications. *Advanced Engineering Materials* **2008**, *10*, 515-527.
4. Mendes, P. M. Stimuli-Responsive Surfaces for Bio-Applications. *Chem. Soc. Rev.* **2008**, *37*, 2512-2529.

5. Nelson, A. Stimuli-Responsive Polymers - Engineering Interactions. *Nat. Mater.* **2008**, *7*, 523-525.
6. Roy, D.; Cambre, J. N.; Sumerlin, B. S. Future Perspectives and Recent Advances in Stimuli-Responsive Materials. *Prog. Polym. Sci.* **2010**, *35*, 278-301.
7. Stuart, M. A. C.; Huck, W. T. S.; Genzer, J.; Muller, M.; Ober, C.; Stamm, M.; Sukhorukov, G. B.; Szleifer, I.; Tsukruk, V. V.; Urban, M.; Winnik, F.; Zauscher, S.; Luzinov, I.; Minko, S. Emerging Applications of Stimuli-Responsive Polymer Materials. *Nat. Mater.* **2010**, *9*, 101-113.
8. Tokarev, I.; Minko, S. Stimuli-Responsive Hydrogel Thin Films. *Soft Matter* **2009**, *5*, 511-524.
9. Tokarev, I.; Minko, S. Multiresponsive, Hierarchically Structured Membranes: New, Challenging, Biomimetic Materials for Biosensors, Controlled Release, Biochemical Gates, and Nanoreactors. *Adv. Mater.* **2009**, *21*, 241-247.
10. Decher, G. Fuzzy Nanoassemblies: Toward Layered Polymeric Multicomposites. *Science* **1997**, *277*, 1232-1237.
11. Sukhishvili, S. A. Responsive Polymer Films and Capsules Via Layer-by-Layer Assembly. *Curr. Opin. Colloid Interface Sci.* **2005**, *10*, 37-44.
12. Mortimer, R. J. Electrochromic Materials. *Chem Soc Rev* **1997**, *26*, 147-156.
13. Ricci, F.; Palleschi, G. Sensor and Biosensor Preparation, Optimisation and Applications of Prussian Blue Modified Electrodes. *Biosens Bioelectron* **2005**, *21*, 389-407.
14. DeLongchamp, D. M.; Hammond, P. T. High-Contrast Electrochromism and Controllable Dissolution of Assembled Prussian Blue/Polymer Nanocomposites. *Adv Funct Mater* **2004**, *14*, 224-232.
15. Sukhishvili, S. A.; Granick, S. Layered, Erasable, Ultrathin Polymer Films. *J. Am. Chem. Soc.* **2000**, *122*, 9550-9551.
16. Kharlampieva, E.; Erel-Unal, I.; Sukhishvili, S. A. Amphoteric Surface Hydrogels Derived from Hydrogen-Bonded Multilayers: Reversible Loading of Dyes and Macromolecules. *Langmuir* **2007**, *23*, 175-181.
17. Kim, B. S.; Park, S. W.; Hammond, P. T. Hydrogen-Bonding Layer-by-Layer Assembled Biodegradable Polymeric Micelles as Drug Delivery Vehicles from Surfaces. *ACS Nano* **2008**, *2*, 386-392.
18. Quinn, J. F.; Caruso, F. Facile Tailoring of Film Morphology and Release Properties Using Layer-by-Layer Assembly of Thermoresponsive Materials. *Langmuir* **2004**, *20*, 20-22.
19. Hiller, J.; Rubner, M. F. Reversible Molecular Memory and pH-Switchable Swelling Transitions in Polyelectrolyte Multilayers. *Macromolecules* **2003**, *36*, 4078-4083.
20. Itano, K.; Choi, J. Y.; Rubner, M. F. Mechanism of the pH-Induced Discontinuous Swelling/Deswelling Transitions of Poly(Allylamine Hydrochloride)-Containing Polyelectrolyte Multilayer Films. *Macromolecules* **2005**, *38*, 3450-3460.
21. Ariga, K.; Hill, J. P.; Ji, Q. M. Layer-by-Layer Assembly as a Versatile Bottom-up Nanofabrication Technique for Exploratory Research and Realistic Application. *Phys. Chem. Chem. Phys.* **2007**, *9*, 2319-2340.
22. Bertrand, P.; Jonas, A.; Laschewsky, A.; Legras, R. Ultrathin Polymer Coatings by Complexation of Polyelectrolytes at Interfaces: Suitable Materials, Structure and Properties. *Macromol. Rapid Commun.* **2000**, *21*, 319-348.

23. *Multilayer Thin Films: Sequential Assembly of Nanocomposite Materials*; Decher, G.; Schlenoff, J. B., Eds.; Wiley-VCH: Weinheim, 2003.
24. Hammond, P. T. Recent Explorations in Electrostatic Multilayer Thin Film Assembly. *Curr. Opin. Colloid Interface Sci.* **1999**, *4*, 430-442.
25. Hammond, P. T. Form and Function in Multilayer Assembly: New Applications at the Nanoscale. *Adv. Mater.* **2004**, *16*, 1271-1293.
26. Jaber, J. A.; Schlenoff, J. B. Recent Developments in the Properties and Applications of Polyelectrolyte Multilayers. *Curr. Opin. Colloid Interface Sci.* **2006**, *11*, 324-329.
27. Schonhoff, M. Self-Assembled Polyelectrolyte Multilayers. *Curr. Opin. Colloid Interface Sci.* **2003**, *8*, 86-95.
28. Schlenoff, J. B.; Dubas, S. T. Mechanism of Polyelectrolyte Multilayer Growth: Charge Overcompensation and Distribution. *Macromolecules* **2001**, *34*, 592-598.
29. Iler, R. K. Multilayers of Colloidal Particles. *J. Colloid Interface Sci.* **1966**, *21*, 569-&.
30. Decher, G.; Hong, J. D.; Schmitt, J. Buildup of Ultrathin Multilayer Films by a Self-Assembly Process .3. Consecutively Alternating Adsorption of Anionic and Cationic Polyelectrolytes on Charged Surfaces. *Thin Solid Films* **1992**, *210*, 831-835.
31. Kharlampieva, E.; Kozlovskaya, V.; Sukhishvili, S. A. Layer-by-Layer Hydrogen-Bonded Polymer Films: From Fundamentals to Applications. *Adv. Mater.* **2009**, *21*, 3053-3065.
32. Kharlampieva, E.; Sukhishvili, S. A. Hydrogen-Bonded Layer-by-Layer Polymer Films. *Polymer Reviews* **2006**, *46*, 377-395.
33. Kohli, P.; Blanchard, G. J. Applying Polymer Chemistry to Interfaces: Layer-by-Layer and Spontaneous Growth of Covalently Bound Multilayers. *Langmuir* **2000**, *16*, 4655-4661.
34. Such, G. K.; Quinn, J. F.; Quinn, A.; Tjijto, E.; Caruso, F. Assembly of Ultrathin Polymer Multilayer Films by Click Chemistry. *J. Am. Chem. Soc.* **2006**, *128*, 9318-9319.
35. Quinn, J. F.; Johnston, A. P. R.; Such, G. K.; Zelikin, A. N.; Caruso, F. Next Generation, Sequentially Assembled Ultrathin Films: Beyond Electrostatics. *Chem. Soc. Rev.* **2007**, *36*, 707-718.
36. Ariga, K.; Ji, Q. M.; Hill, J. P. Enzyme-Encapsulated Layer-by-Layer Assemblies: Current Status and Challenges toward Ultimate Nanodevices. *Modern Techniques for Nano- and Microreactors/-Reactions* **2010**, *229*, 51-87.
37. Boudou, T.; Crouzier, T.; Ren, K. F.; Blin, G.; Picart, C. Multiple Functionalities of Polyelectrolyte Multilayer Films: New Biomedical Applications. *Adv. Mater.* **2010**, *22*, 441-467.
38. Jewell, C. A.; Lynn, D. M. Multilayered Polyelectrolyte Assemblies as Platforms for the Delivery of DNA and Other Nucleic Acid-Based Therapeutics. *Adv. Drug Delivery Rev.* **2008**, *60*, 979-999.
39. Lichter, J. A.; Van Vliet, K. J.; Rubner, M. F. Design of Antibacterial Surfaces and Interfaces: Polyelectrolyte Multilayers as a Multifunctional Platform. *Macromolecules* **2009**, *42*, 8573-8586.
40. Lynn, D. M. Layers of Opportunity: Nanostructured Polymer Assemblies for the Delivery of Macromolecular Therapeutics. *Soft Matter* **2006**, *2*, 269-273.
41. Lynn, D. M. Peeling Back the Layers: Controlled Erosion and Triggered Disassembly of Multilayered Polyelectrolyte Thin Films. *Adv. Mater.* **2007**, *19*, 4118-4130.

42. Tang, Z. Y.; Wang, Y.; Podsiadlo, P.; Kotov, N. A. Biomedical Applications of Layer-by-Layer Assembly: From Biomimetics to Tissue Engineering. *Adv. Mater.* **2006**, *18*, 3203-3224.
43. Bucur, C. B.; Sui, Z.; Schlenoff, J. B. Ideal Mixing in Polyelectrolyte Complexes and Multilayers: Entropy Driven Assembly. *J. Am. Chem. Soc.* **2006**, *128*, 13690-13691.
44. Crespilho, F. N.; Zucolotto, V.; Oliveira, O. N.; Nart, F. C. Electrochemistry of Layer-by-Layer Films: A Review. *Int. J. Electrochem. Sci.* **2006**, *1*, 194-214.
45. Lutkenhaus, J. L.; Hammond, P. T. Electrochemically Enabled Polyelectrolyte Multilayer Devices: From Fuel Cells to Sensors. *Soft Matter* **2007**, *3*, 804-816.
46. Cebeci, F. C.; Wu, Z. Z.; Zhai, L.; Cohen, R. E.; Rubner, M. F. Nanoporosity-Driven Superhydrophilicity: A Means to Create Multifunctional Antifogging Coatings. *Langmuir* **2006**, *22*, 2856-2862.
47. Wu, Z. Z.; Walish, J.; Nolte, A.; Zhai, L.; Cohen, R. E.; Rubner, M. F. Deformable Antireflection Coatings from Polymer and Nanoparticle Multilayers. *Adv. Mater.* **2006**, *18*, 2699-+.
48. Dubas, S. T.; Schlenoff, J. B. Factors Controlling the Growth of Polyelectrolyte Multilayers. *Macromolecules* **1999**, *32*, 8153-8160.
49. Cho, J.; Char, K.; Hong, J. D.; Lee, K. B. Fabrication of Highly Ordered Multilayer Films Using a Spin Self-Assembly Method. *Adv. Mater.* **2001**, *13*, 1076-+.
50. Krogman, K. C.; Zacharia, N. S.; Schroeder, S.; Hammond, P. T. Automated Process for Improved Uniformity and Versatility of Layer-by-Layer Deposition. *Langmuir* **2007**, *23*, 3137-3141.
51. Schlenoff, J. B.; Dubas, S. T.; Farhat, T. Sprayed Polyelectrolyte Multilayers. *Langmuir* **2000**, *16*, 9968-9969.
52. Lefaux, C. J.; Mather, P. T. Build-up of Multilayered Thin Lines Using Sequential Adsorption of Polymers in Microfluidic Channels. *Mater. Res. Soc. Symp. Proc.* **2004**, *EXS-2*, M4.5.1-M4.6.3.
53. Thierry, B.; Winnik, F. M.; Merhi, Y.; Silver, J.; Tabrizian, M. Bioactive Coatings of Endovascular Stents Based on Polyelectrolyte Multilayers. *Biomacromolecules* **2003**, *4*, 1564-1571.
54. Krogman, K. C.; Lowery, J. L.; Zacharia, N. S.; Rutledge, G. C.; Hammond, P. T. Spraying Asymmetry into Functional Membranes Layer-by-Layer. *Nat. Mater.* **2009**, *8*, 512-518.
55. Johnston, A. P. R.; Cortez, C.; Angelatos, A. S.; Caruso, F. Layer-by-Layer Engineered Capsules and Their Applications. *Curr. Opin. Colloid Interface Sci.* **2006**, *11*, 203-209.
56. Wang, Y.; Angelatos, A. S.; Caruso, F. Template Synthesis of Nanostructured Materials Via Layer-by-Layer Assembly. *Chem. Mater.* **2008**, *20*, 848-858.
57. Jiang, C. Y.; Tsukruk, V. V. Freestanding Nanostructures Via Layer-by-Layer Assembly. *Adv. Mater.* **2006**, *18*, 829-840.
58. Park, J.; Hammond, P. T. Polyelectrolyte Multilayer Formation on Neutral Hydrophobic Surfaces. *Macromolecules* **2005**, *38*, 10542-10550.
59. Liston, E. M. Plasma Treatment for Improved Bonding - a Review. *J. Adhes.* **1989**, *30*, 199-218.
60. VanDerVoort, P.; Vansant, E. F. Silylation of the Silica Surface a Review. *J. Liq. Chromatogr. Relat. Technol.* **1996**, *19*, 2723-2752.

61. Barenbrug, T. M. A. O. M.; Bedeaux, D.; Smit, J. A. M. Conformational Free Energy of Lattice Polyelectrolytes with Fixed End Points. 2. The Swelling Behavior of a Permanent Network of Lattice Polyelectrolytes. *Macromolecules* **1999**, *32*, 199-209.
62. English, A. E.; Mafe, S.; Manzanares, J. A.; Yu, X. H.; Grosberg, A. Y.; Tanaka, T. Equilibrium Swelling Properties of Polyampholytic Hydrogels. *J. Chem. Phys.* **1996**, *104*, 8713-8720.
63. Ricka, J.; Tanaka, T. Swelling of Ionic Gels - Quantitative Performance of the Donnan Theory. *Macromolecules* **1984**, *17*, 2916-2921.
64. Tagliazucchi, M.; Grumelli, D.; Calvo, E. J. Nanostructured Modified Electrodes: Role of Ions and Solvent Flux in Redox Active Polyelectrolyte Multilayer Films. *Phys. Chem. Chem. Phys.* **2006**, *8*, 5086-5095.
65. Jacob, C.; Winyard, P. G.; Wiley InterScience (Online service); Wiley-VCH: Weinheim, 2009, p 1 online resource (xxxiii, 481 p.).
66. Wang, F.; Li, D.; Li, G. P.; Liu, X. Q.; Dong, S. J. Electrodissolution of Inorganic Ions/DNA Multilayer Film for Tunable DNA Release. *Biomacromolecules* **2008**, *9*, 2645-2652.
67. Kadish, K. M.; Smith, K. M.; Guillard, R. *The Porphyrin Handbook*; Academic Press: San Diego, 2000.
68. Leznoff, C. C.; Lever, A. B. P. *Phthalocyanines : Properties and Applications*; VCH: New York, NY, 1989.
69. Kadish, M.; Van Caemelbecke, E. Electrochemistry of Porphyrins and Related Macrocycles. *J Solid State Electr* **2003**, *7*, 254-258.
70. Alencar, W. S.; Crespilho, F. N.; Santos, M. R. M. C.; Zucolotto, V.; Oliveira, O. N.; Silva, W. C. Influence of Film Architecture on the Charge-Transfer Reactions of Metallophthalocyanine Layer-by-Layer Films. *J Phys Chem C* **2007**, *111*, 12817-12821.
71. Araki, K.; Wagner, M. J.; Wrighton, M. S. Layer-by-Layer Growth of Electrostatically Assembled Multilayer Porphyrin Films. *Langmuir* **1996**, *12*, 5393-5398.
72. Baba, A.; Locklin, J.; Xu, R. S.; Advincula, R. Nanopatterning and Nanocharge Writing in Layer-by-Layer Quinquethiophene/Phthalocyanine Ultrathin Films. *J Phys Chem B* **2006**, *110*, 42-45.
73. Doherty, W. J.; Friedlein, R.; Salaneck, W. R. Layer-by-Layer Deposition of Copper Phthalocyanine from Aqueous Solution: Molecular Orientation, Ordering Parameters, and Electronic Structure. *J Phys Chem C* **2007**, *111*, 2724-2729.
74. Jin, Y. N.; Xu, L.; Zhu, L. D.; An, W. J.; Gao, G. G. Nanocomposite Multilayer Films Containing Dawson-Type Polyoxometalate and Cationic Phthalocyanine: Fabrication, Characterization and Bifunctional Electrocatalytic Properties. *Thin Solid Films* **2007**, *515*, 5490-5497.
75. Kato, K.; Watanabe, N.; Katagiri, S.; Shinbo, K.; Kaneko, F.; Locklin, J.; Baba, A.; Advincula, R. C. Electrical Properties and Gas Response in Alternate Layer-by-Layer Films of Copper Phthalocyanine Dyes. *Jpn J Appl Phys* **2004**, *43*, 2311-2314.
76. Li, D. Q.; Lutt, M.; Fitzsimmons, M. R.; Synowicki, R.; Hawley, M. E.; Brown, G. W. Preparation, Characterization, and Properties of Mixed Organic and Polymeric Self-Assembled Multilayers. *J Am Chem Soc* **1998**, *120*, 8797-8804.
77. Li, L. S.; Jia, Q. X.; Li, A. D. Q. Effects of Organic Self-Assembled Polymer and Metal Phthalocyanine Multilayers on the Surface Photovoltaic Properties of Indium Tin Oxide and Titanium Oxide. *Chem Mater* **2002**, *14*, 1159-1165.

78. Garjonyte, R.; Malinauskas, A. Amperometric Glucose Biosensors Based on Prussian Blue- and Polyaniline-Glucose Oxidase Modified Electrodes. *Biosens Bioelectron* **2000**, *15*, 445-451.
79. Locklin, J.; Shinbo, K.; Onishi, K.; Kaneko, F.; Bao, Z. N.; Advincula, R. C. Ambipolar Organic Thin Film Transistor-Like Behavior of Cationic and Anionic Phthalocyanines Fabricated Using Layer-by-Layer Deposition from Aqueous Solution. *Chem Mater* **2003**, *15*, 1404-1412.
80. Lutt, M.; Fitzsimmons, M. R.; Li, D. Q. X-Ray Reflectivity Study of Self-Assembled Thin Films of Macrocycles and Macromolecules. *J Phys Chem B* **1998**, *102*, 400-405.
81. Lvov, Y. M.; Kamau, G. N.; Zhou, D. L.; Rusling, J. F. Assembly of Electroactive Ordered Multilayer Films of Cobalt Phthalocyanine Tetrasulfonate and Polycations. *J Colloid Interf Sci* **1999**, *212*, 570-575.
82. Mao, H. F.; Sun, Y. P.; Li, H. W.; Zhou, Q. F.; Zhang, X.; Shen, J. C.; Xu, H. J. Molecular Deposition Film of Porphyrin and Phthalocyanine Bearing Oppositely Charged Substituents. *Sci China Ser B* **1998**, *41*, 449-454.
83. Pradhan, B.; Bandyopadhyay, A.; Pal, A. J. Molecular Level Control of Donor/Acceptor Heterostructures in Organic Photovoltaic Devices. *Appl Phys Lett* **2004**, *85*, 663-665.
84. Shinbo, K.; Onishi, K.; Miyabayashi, S.; Takahashi, K.; Takahashi, K.; Kato, K.; Kaneko, F.; Advincula, R. C. Fabrication and Electrochemical Properties of Layer-by-Layer Deposited Films Containing Phthalocyanine Dyes. *Thin Solid Films* **2003**, *438*, 177-181.
85. Siqueira, J. R.; Gasparotto, L. H. S.; Crespilho, F. N.; Carvalho, A. J. F.; Zucolotto, V.; Oliveira, O. N. Physicochemical Properties and Sensing Ability of Metallophthalocyanines/Chitosan Nanocomposites. *J Phys Chem B* **2006**, *110*, 22690-22694.
86. Sun, Y. P.; Zhang, X.; Sun, C. Q.; Wang, Z. Q.; Shen, J. C.; Wang, D. J.; Li, T. J. Supramolecular Assembly of Alternating Porphyrin and Phthalocyanine Layers Based on Electrostatic Interactions. *Chem Commun* **1996**, 2379-2380.
87. Tao, X.; Li, J. B.; Hartmann, J.; Mohwald, H. Self-Assembly and Properties of Phthalocyanine and Polyelectrolytes onto Melamine Resin Particles. *New J Chem* **2004**, *28*, 1579-1583.
88. Xu, L.; Wang, E. B.; Li, Z.; Kurth, D. G.; Du, X. G.; Zhang, H. Y.; Qin, C. Preparation and Nonlinear Optical Properties of Ultrathin Composite Films Containing Both a Polyoxometalate Anion and a Binuclear Phthalocyanine. *New J Chem* **2002**, *26*, 782-786.
89. Zhao, S.; Li, X. F.; Yang, M.; Sun, C. Q. Fabrication and Characterization of Covalently Attached Multilayer Films Containing Iron Phthalocyanine and Diazo-Resins. *J Mater Chem* **2004**, *14*, 840-844.
90. Zucolotto, V.; Ferreira, M.; Cordeiro, M. R.; Constantino, C. J. L.; Balogh, D. T.; Zanatta, A. R.; Moreira, W. C.; Oliveira, O. N. Unusual Interactions Binding Iron Tetrasulfonated Phthalocyanine and Poly(Allylamine Hydrochloride) in Layer-by-Layer Films. *J Phys Chem B* **2003**, *107*, 3733-3737.
91. Grieshaber, D.; Voros, J.; Zambelli, T.; Ball, V.; Schaaf, P.; Voegel, J. C.; Boulmedais, F. Swelling and Contraction of Ferrocyanide-Containing Polyelectrolyte Multilayers Upon Application of an Electric Potential. *Langmuir* **2008**, *24*, 13668-13676.
92. Calvo, E. J.; Danilowicz, C.; Diaz, L. A New Polycationic Hydrogel for 3-Dimensional Enzyme Wired Modified Electrodes. *J Electroanal. Chem.* **1994**, *369*, 279-282.

93. Danilowicz, C.; Corton, E.; Battaglini, F. Osmium Complexes Bearing Functional Groups: Building Blocks for Integrated Chemical Systems. *J. Electroanal. Chem.* **1998**, *445*, 89-94.
94. Calvo, E. J.; Danilowicz, C.; Etchenique, R. Measurement of Viscoelastic Changes at Electrodes Modified with Redox Hydrogels with a Quartz-Crystal Device. *Journal of the Chemical Society-Faraday Transactions* **1995**, *91*, 4083-4091.
95. Calvo, E. J.; Etchenique, R. Viscoelastic Changes in Os-Containing Poly(Allylamine) Based Redox Hydrogels for Amperometric Enzyme Electrodes: An EQCM Study. *J. Phys. Chem. B* **1999**, *103*, 8944-8950.
96. Forzani, E. S.; Otero, M.; Perez, M. A.; Teijelo, M. L.; Calvo, E. J. The Structure of Layer-by-Layer Self-Assembled Glucose Oxidase and Os(Bpy)(2)CIPyCH₂NH-Poly(Allylamine) Multilayers: Ellipsometric and Quartz Crystal Microbalance Studies. *Langmuir* **2002**, *18*, 4020-4029.
97. Forzani, E. S.; Perez, M. A.; Teijelo, M. L.; Calvo, E. J. Redox Driven Swelling of Layer-by-Layer Enzyme-Polyelectrolyte Multilayers. *Langmuir* **2002**, *18*, 9867-9873.
98. Grumelli, D.; Bonazzola, C.; Calvo, E. J. Hydration Cycling in Redox Active LBL Self-Assembled Polyelectrolyte Multilayers. *Electrochem. Commun.* **2006**, *8*, 1353-1357.
99. Hodak, J.; Etchenique, R.; Calvo, E. J.; Singhal, K.; Bartlett, P. N. Layer-by-Layer Self-Assembly of Glucose Oxidase with a Poly(Allylamine)Ferrocene Redox Mediator. *Langmuir* **1997**, *13*, 2708-2716.
100. Tagliazucchi, M.; Grumelli, D.; Bonazzola, C.; Calvo, E. J. Oxidation-Reduction Dynamics in Layer-by-Layer Self-Assembled Redox Polyelectrolyte Multilayer Modified Electrodes. *J. Nanosci. Nanotechnol.* **2006**, *6*, 1731-1740.
101. Tagliazucchi, M.; Williams, F. J.; Calvo, E. J. Effect of Acid-Base Equilibria on the Donnan Potential of Layer-by-Layer Redox Polyelectrolyte Multilayers. *J. Phys. Chem. B* **2007**, *111*, 8105-8113.
102. Tagliazucchi, M. E.; Calvo, E. J. Surface Charge Effects on the Redox Switching of LbL Self-Assembled Redox Polyelectrolyte Multilayers. *J. Electroanal. Chem.* **2007**, *599*, 249-259.
103. Ma, Y. J.; Hempenius, M. A.; Vancso, G. J. Electrostatic Assembly with Poly(Ferrocenylsilanes). *J. Inorg. Organomet. Polym. Mater.* **2007**, *17*, 3-18.
104. Power-Billard, K. N.; Manners, I. Hydrophilic and Water-Soluble Poly(Ferrocenylsilanes). *Macromolecules* **2000**, *33*, 26-31.
105. Hempenius, M. A.; Peter, M.; Robins, N. S.; Kooij, E. S.; Vancso, G. J. Water-Soluble Poly(Ferrocenylsilanes) for Supramolecular Assemblies by Layer-by-Layer Deposition. *Langmuir* **2002**, *18*, 7629-7634.
106. Hempenius, M. A.; Vancso, G. J. Synthesis of a Polyanionic Water-Soluble Poly(Ferrocenylsilane). *Macromolecules* **2002**, *35*, 2445-2447.
107. Wang, Z.; Lough, A.; Manners, I. Synthesis and Characterization of Water-Soluble Cationic and Anionic Polyferrocenylsilane Polyelectrolytes. *Macromolecules* **2002**, *35*, 7669-7677.
108. Hempenius, M. A.; Robins, N. S.; Lammertink, R. G. H.; Vancso, G. J. Organometallic Polyelectrolytes: Synthesis, Characterization and Layer-by-Layer Deposition of Cationic Poly(Ferrocenyl(3-Ammoniumpropyl)Methylsilane). *Macromol. Rapid Commun.* **2001**, *22*, 30-33.

109. Hempenius, M. A.; Brito, F. F.; Vancso, G. J. Synthesis and Characterization of Anionic and Cationic Poly(Ferrocenylsilane) Polyelectrolytes. *Macromolecules* **2003**, *36*, 6683-6688.
110. Ma, Y. J.; Dong, W. F.; Kooij, E. S.; Hempenius, M. A.; Mohwald, H.; Vancso, G. J. Supramolecular Assembly of Water-Soluble Poly(Ferrocenylsilanes): Multilayer Structures on Flat Interfaces and Permeability of Microcapsules. *Soft Matter* **2007**, *3*, 889-895.
111. Peter, M.; Hempenius, M. A.; Kooij, E. S.; Jenkins, T. A.; Roser, S. J.; Knoll, W.; Vancso, G. J. Electrochemically Induced Morphology and Volume Changes in Surface-Grafted Poly(Ferrocenyldimethylsilane) Monolayers. *Langmuir* **2004**, *20*, 891-897.
112. Ma, Y. J.; Dong, W. F.; Hempenius, M. A.; Mohwald, H.; Vancso, G. J. Redox-Controlled Molecular Permeability of Composite-Wall Microcapsules. *Nat. Mater.* **2006**, *5*, 724-729.
113. Long, D. L.; Burkholder, E.; Cronin, L. Polyoxometalate Clusters, Nanostructures and Materials: From Self Assembly to Designer Materials and Devices. *Chem Soc Rev* **2007**, *36*, 105-121.
114. Liu, S. Q.; Volkmer, D.; Kurth, D. G. Functional Polyoxometalate Thin Films Via Electrostatic Layer-by-Layer Self-Assembly. *J Clust Sci* **2003**, *14*, 405-419.
115. Yamase, T. Anti-Tumor, -Viral, and -Bacterial Activities of Polyoxometalates for Realizing an Inorganic Drug. *J Mater Chem* **2005**, *15*, 4773-4782.
116. Caruso, F.; Kurth, D. G.; Volkmer, D.; Koop, M. J.; Muller, A. Ultrathin Molybdenum Polyoxometalate-Polyelectrolyte Multilayer Films. *Langmuir* **1998**, *14*, 3462-3465.
117. Ichinose, I.; Tagawa, H.; Mizuki, S.; Lvov, Y.; Kunitake, T. Formation Process of Ultrathin Multilayer Films of Molybdenum Oxide by Alternate Adsorption of Octamolybdate and Linear Polycations. *Langmuir* **1998**, *14*, 187-192.
118. Kurth, D. G.; Volkmer, D.; Ruttorf, M.; Richter, B.; Muller, A. Ultrathin Composite Films Incorporating the Nanoporous Isopolyoxomolybdate "Keplerate" $(\text{NH}_4)_{42}[\text{Mo}_{132}\text{O}_{372}(\text{CH}_3\text{COO})_{30}(\text{H}_2\text{O})_{72}]$. *Chem Mater* **2000**, *12*, 2829-+.
119. Liu, S. Q.; Kurth, D. G.; Bredenkotter, B.; Volkmer, D. The Structure of Self-Assembled Multilayers with Polyoxometalate Nanoclusters. *J Am Chem Soc* **2002**, *124*, 12279-12287.
120. Liu, S. Q.; Kurth, D. G.; Mohwald, H.; Volkmer, D. A Thin-Film Electrochromic Device Based on a Polyoxometalate Cluster. *Adv Mater* **2002**, *14*, 225-+.
121. Liu, S. Q.; Kurth, D. G.; Volkmer, D. Polyoxometalates as pH-Sensitive Probes in Self-Assembled Multilayers. *Chem Commun* **2002**, 976-977.
122. Moriguchi, I.; Fendler, J. H. Characterization and Electrochromic Properties of Ultrathin Films Self-Assembled from Poly(Diallyldimethylammonium) Chloride and Sodium Decatungstate. *Chem Mater* **1998**, *10*, 2205-2211.
123. Ware, M. Prussian Blue: Artists' Pigment and Chemists' Sponge. *J Chem Educ* **2008**, *85*, 612-+.
124. Ware, M. *Cyanotype: The History, Science and Art of Photographic Printing in Prussian Blue*; Science Museum: London, 1999.
125. In P03-75; Food and Drug Administration: 2003.
126. Pearce, J. Studies of Any Toxicological Effects of Prussian-Blue Compounds in Mammals - a Review. *Food Chem Toxicol* **1994**, *32*, 577-582.

127. de Tacconi, N. R.; Rajeshwar, K.; Lezna, R. O. Metal Hexacyanoferrates: Electrolysis, in Situ Characterization, and Applications. *Chem Mater* **2003**, *15*, 3046-3062.
128. Neff, V. D. Electrochemical Oxidation and Reduction of Thin-Films of Prussian Blue. *J Electrochem Soc* **1978**, *125*, 886-887.
129. Mingotaud, C.; Lafuente, C.; Amiell, J.; Delhaes, P. Ferromagnetic Langmuir-Blodgett Film Based on Prussian Blue. *Langmuir* **1999**, *15*, 289-292.
130. Del Villar, I.; Matias, I. R.; Arregui, F. J.; Claus, R. O. Esa-Based in-Fiber Nanocavity for Hydrogen-Peroxide Detection. *Ieee T Nanotechnol* **2005**, *4*, 187-193.
131. DeLongchamp, D. M.; Hammond, P. T. Multiple-Color Electrochromism from Layer-by-Layer-Assembled Polyaniline/Prussian Blue Nanocomposite Thin Films. *Chem Mater* **2004**, *16*, 4799-4805.
132. Fiorito, P. A.; Goncales, V. R.; Ponzio, E. A.; de Torresi, S. I. C. Synthesis, Characterization and Immobilization of Prussian Blue Nanoparticles. A Potential Tool for Biosensing Devices. *Chem Commun* **2005**, 366-368.
133. Hornok, V.; Dekany, I. Synthesis and Stabilization of Prussian Blue Nanoparticles and Application for Sensors. *J Colloid Interf Sci* **2007**, *309*, 176-182.
134. Jaiswal, A.; Colins, J.; Agricole, B.; Delhaes, P.; Ravaine, S. Layer-by-Layer Self-Assembly of Prussian Blue Colloids. *J Colloid Interf Sci* **2003**, *261*, 330-335.
135. Li, F. H.; Shan, C. S.; Bu, X. Y.; Shen, Y. F.; Yang, G. F.; Niu, L. Fabrication and Electrochemical Characterization of Electrostatic Assembly of Polyelectrolyte-Functionalized Ionic Liquid and Prussian Blue Ultrathin Films. *J Electroanal Chem* **2008**, *616*, 1-6.
136. Pyrasch, M.; Toutianoush, A.; Jin, W. Q.; Schnepf, J.; Tieke, B. Self-Assembled Films of Prussian Blue and Analogues: Optical and Electrochemical Properties and Application as Ion-Sieving Membranes. *Chem Mater* **2003**, *15*, 245-254.
137. Wang, L.; Guo, S. J.; Hu, X. O.; Dong, S. J. Layer-by-Layer Assembly of Carbon Nanotubes and Prussian Blue Nanoparticles: A Potential Tool for Biosensing Devices. *Colloid Surface A* **2008**, *317*, 394-399.
138. Wang, Q. F.; Zhang, L.; Qiu, L. Y.; Sun, J. Q.; Shen, J. C. Fabrication and Electrochemical Investigation of Layer-by-Layer Deposited Titanium Phosphate/Prussian Blue Composite Films. *Langmuir* **2007**, *23*, 6084-6090.
139. Zhao, W.; Xu, J. J.; Shi, C. G.; Chen, H. Y. Multilayer Membranes Via Layer-by-Layer Deposition of Organic Polymer Protected Prussian Blue Nanoparticles and Glucose Oxidase for Glucose Biosensing. *Langmuir* **2005**, *21*, 9630-9634.
140. Mortimer, R. J.; Rosseinsky, D. R. Iron Hexacyanoferrate Films - Spectroelectrochemical Distinction and Electrodeposition Sequence of Soluble (K⁺-Containing) and Insoluble (K⁺-Free) Prussian Blue, and Composition Changes in Polyelectrochromic Switching. *J Chem Soc Dalton* **1984**, 2059-2061.
141. Shiozaki, H.; Kawamoto, T.; Tanaka, H.; Hara, S.; Tokumoto, M.; Gotoh, A.; Satoh, T.; Ishizaki, M.; Kurihara, M.; Sakamoto, M. Electrochromic Thin Film Fabricated Using a Water-Dispersible Ink of Prussian Blue Nanoparticles. *Jpn J Appl Phys* **2008**, *47*, 1242-1244.
142. Somani, P. R.; Radhakrishnan, S. Electrochromic Materials and Devices: Present and Future. *Mater Chem Phys* **2003**, *77*, 117-133.

143. Sone, Y.; Kishimoto, A.; Kudo, T.; Ikeda, K. Reversible Electrochromic Performance of Prussian Blue Coated with Proton Conductive Ta₂O₅ Center Dot Nb(2)O Film. *Solid State Ionics* **1996**, *83*, 135-143.
144. Ito, A.; Suenaga, M.; Ono, K. Mossbauer Study of Soluble Prussian Blue Insoluble Prussian Blue and Turnbells Blue. *J Chem Phys* **1968**, *48*, 3597-&.
145. Ferlay, S.; Mallah, T.; Ouahes, R.; Veillet, P.; Verdaguer, M. A Room-Temperature Organometallic Magnet Based on Prussian Blue. *Nature* **1995**, *378*, 701-703.
146. Karyakin, A. A. Prussian Blue and Its Analogues: Electrochemistry and Analytical Applications. *Electroanal* **2001**, *13*, 813-819.
147. Heeger, A. J. Semiconducting and Metallic Polymers: The Fourth Generation of Polymeric Materials (Nobel Lecture). *Angew. Chem., Int. Ed.* **2001**, *40*, 2591-2611.
148. MacDiarmid, A. G. "Synthetic Metals": A Novel Role for Organic Polymers (Nobel Lecture). *Angew. Chem., Int. Ed.* **2001**, *40*, 2581-2590.
149. Shirakawa, H. The Discovery of Polyacetylene Film: The Dawning of an Era of Conducting Polymers (Nobel Lecture). *Angew. Chem., Int. Ed.* **2001**, *40*, 2575-2580.
150. Kumar, D.; Sharma, R. C. Advances in Conductive Polymers. *Eur. Polym. J.* **1998**, *34*, 1053-1060.
151. *Handbook of Conducting Polymers*; 3rd ed. ed.; Skotheim, T. A.; Reynolds, J. R., Eds.; CRC: Boca Raton, Fla., 2007.
152. Entezami, A. A.; Massoumi, B. Artificial Muscles, Biosensors and Drug Delivery Systems Based on Conducting Polymers: A Review. *Iran Polym J* **2006**, *15*, 13-30.
153. Guimard, N. K.; Gomez, N.; Schmidt, C. E. Conducting Polymers in Biomedical Engineering. *Prog Polym Sci* **2007**, *32*, 876-921.
154. Barbero, C.; Kotz, R. Nanoscale Dimensional Changes and Optical-Properties of Polyaniline Measured by in-Situ Spectroscopic Ellipsometry. *J Electrochem Soc* **1994**, *141*, 859-865.
155. Lizarraga, L.; Andrade, E. M.; Molina, F. V. Swelling and Volume Changes of Polyaniline Upon Redox Switching. *J Electroanal Chem* **2004**, *561*, 127-135.
156. Mohamoud, M. A.; Hillman, A. R. The Effect of Anion Identity on the Viscoelastic Properties of Polyaniline Films During Electrochemical Film Deposition and Redox Cycling. *Electrochim Acta* **2007**, *53*, 1206-1216.
157. Nyffenegger, R.; Ammann, E.; Siegenthaler, H.; Kotz, R.; Haas, O. In-Situ Scanning Probe Microscopy for the Measurement of Thickness Changes in an Electroactive Polymer. *Electrochim Acta* **1995**, *40*, 1411-1415.
158. Pytel, R. Z.; Thomas, E. L.; Hunter, I. W. In Situ Observation of Dynamic Elastic Modulus in Polypyrrole Actuators. *Polymer* **2008**, *49*, 2008-2013.
159. Singh, P. R.; Mahajan, S.; Raiwadec, S.; Contractor, A. Q. EC-AFM Investigation of Reversible Volume Changes with Electrode Potential in Polyaniline. *J Electroanal Chem* **2009**, *625*, 16-26.
160. Smela, E.; Gadegaard, N. Volume Change in Polypyrrole Studied by Atomic Force Microscopy. *J Phys Chem B* **2001**, *105*, 9395-9405.
161. Smela, E. Conjugated Polymer Actuators. *Mrs Bull* **2008**, *33*, 197-204.
162. Cheung, J. H.; Stockton, W. B.; Rubner, M. F. Molecular-Level Processing of Conjugated Polymers .3. Layer-by-Layer Manipulation of Polyaniline Via Electrostatic Interactions. *Macromolecules* **1997**, *30*, 2712-2716.

163. Stockton, W. B.; Rubner, M. F. Molecular-Level Processing of Conjugated Polymers .4. Layer-by-Layer Manipulation of Polyaniline Via Hydrogen-Bonding Interactions. *Macromolecules* **1997**, *30*, 2717-2725.
164. Schlenoff, J. B.; Ly, H.; Li, M. Charge and Mass Balance in Polyelectrolyte Multilayers. *J Am Chem Soc* **1998**, *120*, 7626-7634.
165. DeLongchamp, D.; Hammond, P. T. Layer-by-Layer Assembly of PEDOT/Polyaniline Electrochromic Devices. *Adv Mater* **2001**, *13*, 1455-+.
166. DeLongchamp, D. M.; Hammond, P. T. Electrochromic Polyaniline Films from Layer-by-Layer Assembly. *Acs Sym Ser* **2005**, *888*, 18-33.
167. DeLongchamp, D. M.; Kastantin, M.; Hammond, P. T. High-Contrast Electrochromism from Layer-by-Layer Polymer Films. *Chem Mater* **2003**, *15*, 1575-1586.
168. Recksiedler, C. L.; Deore, B. A.; Freund, M. S. A Novel Layer-by-Layer Approach for the Fabrication of Conducting Polymer/RNA Multilayer Films for Controlled Release. *Langmuir* **2006**, *22*, 2811-2815.
169. Ge, C. H.; Armstrong, N. R.; Saavedra, S. S. Ph-Sensing Properties of Poly(Aniline) Ultrathin Films Self-Assembled on Indium-Tin Oxide. *Anal Chem* **2007**, *79*, 1401-1410.
170. Bar-Cohen, Y. *Electroactive Polymer (Eap) Actuators as Artificial Muscles : Reality, Potential, and Challenges*; SPIE Press: Bellingham, Wash., 2001.
171. Kulkarni, R. V.; Biswanath, S. Electrically Responsive Smart Hydrogels in Drug Delivery: A Review. *Journal of Applied Biomaterials & Biomechanics* **2007**, *5*, 125-139.
172. Murdan, S. Electro-Responsive Drug Delivery from Hydrogels. *J. Controlled Release* **2003**, *92*, 1-17.
173. Gabi, M.; Sannomiya, T.; Larmagnac, A.; Puttaswamy, M.; Voros, J. Influence of Applied Currents on the Viability of Cells Close to Microelectrodes. *Integrative Biology* **2009**, *1*, 108-115.
174. Boulmedais, F.; Tang, C. S.; Keller, B.; Vörös, J. Controlled Electrodissolution of Polyelectrolyte Multilayers: A Platform Technology Towards the Surface-Initiated Delivery of Drugs. *Adv. Funct. Mater.* **2006**, *16*, 63-70.
175. Dieguez, L.; Darwish, N.; Graf, N.; Voros, J.; Zambelli, T. Electrochemical Tuning of the Stability of PLL/DNA Multilayers. *Soft Matter* **2009**, *5*, 2415-2421.
176. Sato, K.; Kodama, D.; Naka, Y.; Anzai, J. Electrochemically Induced Disintegration of Layer-by-Layer-Assembled Thin Films Composed of 2-Iminobiotin-Labeled Poly(Ethyleneimine) and Avidin. *Biomacromolecules* **2006**, *7*, 3302-3305.
177. Blattler, T. M.; Pasche, S.; Textor, M.; Griesser, H. J. High Salt Stability and Protein Resistance of Poly(L-Lysine)-G-Poly(Ethylene Glycol) Copolymers Covalently Immobilized Via Aldehyde Plasma Polymer Interlayers on Inorganic and Polymeric Substrates. *Langmuir* **2006**, *22*, 5760-5769.
178. Hofmann, K.; Titus, G.; Montibeller, J. A.; Finn, F. M. Avidin Binding of Carboxyl-Substituted Biotin and Analogs. *Biochemistry* **1982**, *21*, 978-984.
179. Sato, H.; Takano, Y.; Sato, K.; Anzai, J. Electrochemically Controlled Release of Alpha,Beta,Gamma,Delta-Tetrakis(4-N-Methylpyridyl)Porphine from Layer-by-Layer Thin Films. *J. Colloid Interface Sci.* **2009**, *333*, 141-144.
180. Deslouis, C.; Frateur, I.; Maurin, G.; Tribollet, B. Interfacial pH Measurement During the Reduction of Dissolved Oxygen in a Submerged Impinging Jet Cell. *J Appl Electrochem* **1997**, *27*, 482-492.

181. Gabrielli, C.; Maurin, G.; Francy-Chausson, H.; They, P.; Tran, T. T. M.; Tlili, M. Electrochemical Water Softening: Principle and Application. *Desalination* **2006**, *201*, 150-163.
182. Hasson, D.; Lumelsky, V.; Greenberg, G.; Pinhas, Y.; Semiat, R. Development of the Electrochemical Scale Removal Technique for Desalination Applications. *Desalination* **2008**, *230*, 329-342.
183. Peulon, S.; Lincot, D. Mechanistic Study of Cathodic Electrodeposition of Zinc Oxide and Zinc Hydroxychloride Films from Oxygenated Aqueous Zinc Chloride Solutions. *J Electrochem Soc* **1998**, *145*, 864-874.
184. Tlili, M. M.; Benamor, M.; Gabrielli, C.; Perrot, H.; Tribollet, B. Influence of the Interfacial pH on Electrochemical CaCO₃ Precipitation. *J Electrochem Soc* **2003**, *150*, C765-C771.
185. Decroly, A.; Petitjean, J. P. Study of the Deposition of Cerium Oxide by Conversion on to Aluminium Alloys. *Surf Coat Tech* **2005**, *194*, 1-9.
186. Ben Moussa, S.; Maurin, G.; Gabrielli, C.; Ben Amor, M. Electrochemical Precipitation of Struvite. *Electrochem Solid St* **2006**, *9*, C97-C101.
187. Kwon, I. C.; Bae, Y. H.; Kim, S. W. Electrically Erodible Polymer Gel for Controlled Release of Drugs. *Nature* **1991**, *354*, 291-293.
188. Kwon, I. C.; Bae, Y. H.; Kim, S. W. Heparin Release from Polymer Complex. *J Controlled Release* **1994**, *30*, 155-159.
189. Razzacki, S. Z.; Thwar, P. K.; Yang, M.; Ugaz, V. M.; Burns, M. A. Integrated Microsystems for Controlled Drug Delivery. *Adv. Drug Delivery Rev.* **2004**, *56*, 185-198.
190. Tsai, H. K. A.; Moschou, E. A.; Daunert, S.; Madou, M.; Kulinsky, L. Integrating Biosensors and Drug Delivery: A Step Closer toward Scalable Responsive Drug-Delivery Systems. *Adv. Mater.* **2009**, *21*, 656-+.
191. Brabant, G.; Prank, K.; Schofl, C. Pulsatile Patterns in Hormone-Secretion. *Trends Endocrinol. Metab.* **1992**, *3*, 183-190.
192. Gammon, C. M.; Freeman, G. M.; Xie, W. H.; Petersen, S. L.; Wetsel, W. C. Regulation of Gonadotropin-Releasing Hormone Secretion by Cannabinoids. *Endocrinology* **2005**, *146*, 4491-4499.
193. Alarcon, C. D. H.; Pennadam, S.; Alexander, C. Stimuli Responsive Polymers for Biomedical Applications. *Chem. Soc. Rev.* **2005**, *34*, 276-285.
194. Bajpai, A. K.; Shukla, S. K.; Bhanu, S.; Kankane, S. Responsive Polymers in Controlled Drug Delivery. *Prog. Polym. Sci.* **2008**, *33*, 1088-1118.
195. Bawa, P.; Pillay, V.; Choonara, Y. E.; du Toit, L. C. Stimuli-Responsive Polymers and Their Applications in Drug Delivery. *Biomedical Materials* **2009**, *4*, -.
196. Roy, I.; Gupta, M. N. Smart Polymeric Materials: Emerging Biochemical Applications. *Chem. Biol.* **2003**, *10*, 1161-1171.
197. Santini, J. T.; Cima, M. J.; Langer, R. A Controlled-Release Microchip. *Nature* **1999**, *397*, 335-338.
198. Maloney, J. M.; Uhlend, S. A.; Polito, B. F.; Sheppard, N. F.; Pelta, C. M.; Santini, J. T. Electrothermally Activated Microchips for Implantable Drug Delivery and Biosensing. *J Controlled Release* **2005**, *109*, 244-255.
199. Prescott, J. H.; Lipka, S.; Baldwin, S.; Sheppard, N. F.; Maloney, J. M.; Coppeta, J.; Yomtov, B.; Staples, M. A.; Santini, J. T. Chronic, Programmed Polypeptide Delivery from an Implanted, Multireservoir Microchip Device. *Nat. Biotechnol.* **2006**, *24*, 437-438.

200. Bhavaraju, S.; Gordon, J.; Joshi, A. A Compact, Controllable, Implantable Delivery Device Driven by Electro-Osmosis. In *Drug Delivery Technology*; Ralph Vitaro: Montville, NJ, **2010**, *10*, 5 24-31.
201. Grayson, A. C. R.; Shawgo, R. S.; Li, Y. W.; Cima, M. J. Electronic MEMS for Triggered Delivery. *Adv. Drug Delivery Rev.* **2004**, *56*, 173-184.
202. Trotter, J. A.; Tipper, J.; Lyons-Levy, G.; Chino, K.; Heuer, A. H.; Liu, Z.; Mrksich, M.; Hodneland, C.; Dillmore, W. S.; Koob, T. J.; Koob-Emunds, M. M.; Kadler, K.; Holmes, D. Towards a Fibrous Composite with Dynamically Controlled Stiffness: Lessons from Echinoderms. *Biochem. Soc. Trans.* **2000**, *28*, 357-362.
203. Motokawa, T.; Tsuchi, A. Dynamic Mechanical Properties of Body-Wall Dermis in Various Mechanical States and Their Implications for the Behavior of Sea Cucumbers. *Biological Bulletin* **2003**, *205*, 261-275.
204. Conrad, J. T.; Ueland, K. Stretch Modulus of Human Cervical Tissue in Spontaneous, Oxytocin-Induced, and Prostaglandin E2-Induced Labor. *Am. J. Obstet. Gynecol.* **1979**, *133*, 11-14.
205. Capadona, J. R.; Shanmuganathan, K.; Tyler, D. J.; Rowan, S. J.; Weder, C. Stimuli-Responsive Polymer Nanocomposites Inspired by the Sea Cucumber Dermis. *Science* **2008**, *319*, 1370-1374.
206. Shanmuganathan, K.; Capadona, J. R.; Rowan, S. J.; Weder, C. Biomimetic Mechanically Adaptive Nanocomposites. *Prog. Polym. Sci.* **2010**, *35*, 212-222.
207. Shanmuganathan, K.; Capadona, J. R.; Rowan, S. J.; Weder, C. Stimuli-Responsive Mechanically Adaptive Polymer Nanocomposites. *Acs Applied Materials & Interfaces* **2010**, *2*, 165-174.
208. Shanmuganathan, K.; Capadona, J. R.; Rowan, S. J.; Weder, C. Bio-Inspired Mechanically-Adaptive Nanocomposites Derived from Cotton Cellulose Whiskers. *J. Mater. Chem.* **2010**, *20*, 180-186.
209. Loveless, D. M.; Jeon, S. L.; Craig, S. L. Chemoresponsive Viscosity Switching of a Metallo-Supramolecular Polymer Network near the Percolation Threshold. *J. Mater. Chem.* **2007**, *17*, 56-61.
210. von Lockette, P. R.; Lofland, S. E.; Koo, J. H.; Kadlowec, J.; Dermond, M. Dynamic Characterization of Bimodal Particle Mixtures in Silicone Rubber Magnetorheological Materials. *Polym. Test.* **2008**, *27*, 931-935.
211. Klok, H. A.; Rebrov, E. A.; Muzafarov, A. M.; Michelberger, W.; Moller, M. Reversible Gelation of Poly(Dimethylsiloxane) with Ionic and Hydrogen-Bonding Substituents. *Journal of Polymer Science Part B-Polymer Physics* **1999**, *37*, 485-495.
212. Ozbas, B.; Kretsinger, J.; Rajagopal, K.; Schneider, J. P.; Pochan, D. J. Salt-Triggered Peptide Folding and Consequent Self-Assembly into Hydrogels with Tunable Modulus. *Macromolecules* **2004**, *37*, 7331-7337.
213. Hayashi, S.; Abe, T.; Higashi, N.; Niwa, M.; Kurihara, K. Polyelectrolyte Brush Layers Studied by Surface Forces Measurement: Dependence on pH and Salt Concentrations and Scaling. *Langmuir* **2002**, *18*, 3932-3944.
214. Hadziioannou, G.; Patel, S.; Granick, S.; Tirrell, M. Forces between Surfaces of Block Copolymers Adsorbed on Mica. *J. Am. Chem. Soc.* **1986**, *108*, 2869-2876.
215. Kaholek, M.; Lee, W. K.; Ahn, S. J.; Ma, H. W.; Caster, K. C.; LaMattina, B.; Zauscher, S. Stimulus-Responsive Poly(N-Isopropylacrylamide) Brushes and Nanopatterns Prepared by Surface-Initiated Polymerization. *Chem. Mater.* **2004**, *16*, 3688-3696.

216. Lemieux, M.; Usov, D.; Minko, S.; Stamm, M.; Shulha, H.; Tsukruk, V. V. Reorganization of Binary Polymer Brushes: Reversible Switching of Surface Microstructures and Nanomechanical Properties. *Macromolecules* **2003**, *36*, 7244-7255.
217. Boudou, T.; Crouzier, T.; Auzely-Velty, R.; Glinel, K.; Picart, C. Internal Composition Versus the Mechanical Properties of Polyelectrolyte Multilayer Films: The Influence of Chemical Cross-Linking. *Langmuir* **2009**, *25*, 13809-13819.
218. Francius, G.; Hemmerle, J.; Ohayon, J.; Schaaf, P.; Voegel, J. C.; Picart, C.; Senger, B. Effect of Crosslinking on the Elasticity of Polyelectrolyte Multilayer Films Measured by Colloidal Probe Afm. *Microsc Res Techniq* **2006**, *69*, 84-92.
219. Ren, K. F.; Crouzier, T.; Roy, C.; Picart, C. Polyelectrolyte Multilayer Films of Controlled Stiffness Modulate Myoblast Cell Differentiation. *Adv Funct Mater* **2008**, *18*, 1378-1389.
220. Richert, L.; Engler, A. J.; Discher, D. E.; Picart, C. Elasticity of Native and Cross-Linked Polyelectrolyte Multilayer Films. *Biomacromolecules* **2004**, *5*, 1908-1916.
221. Schneider, A.; Francius, G.; Obeid, R.; Schwinte, P.; Hemmerle, J.; Frisch, B.; Schaaf, P.; Voegel, J. C.; Senger, B.; Picart, C. Polyelectrolyte Multilayers with a Tunable Young's Modulus: Influence of Film Stiffness on Cell Adhesion. *Langmuir* **2006**, *22*, 1193-1200.
222. Vazquez, C. P.; Boudou, T.; Dulong, V.; Nicolas, C.; Picart, C.; Glinel, K. Variation of Polyelectrolyte Film Stiffness by Photo-Cross-Linking: A New Way to Control Cell Adhesion. *Langmuir* **2009**, *25*, 3556-3563.
223. Lichter, J. A.; Thompson, M. T.; Delgadillo, M.; Nishikawa, T.; Rubner, M. F.; Van Vliet, K. J. Substrata Mechanical Stiffness Can Regulate Adhesion of Viable Bacteria. *Biomacromolecules* **2008**, *9*, 1571-1578.
224. Thompson, M. T.; Berg, M. C.; Tobias, I. S.; Rubner, M. F.; Van Vliet, K. J. Tuning Compliance of Nanoscale Polyelectrolyte Multilayers to Modulate Cell Adhesion. *Biomaterials* **2005**, *26*, 6836-6845.
225. Nolte, A. J.; Treat, N. D.; Cohen, R. E.; Rubner, M. F. Effect of Relative Humidity on the Young's Modulus of Polyelectrolyte Multilayer Films and Related Nonionic Polymers. *Macromolecules* **2008**, *41*, 5793-5798.
226. Jaber, J. A.; Schlenoff, J. B. Mechanical Properties of Reversibly Cross-Linked Ultrathin Polyelectrolyte Complexes. *J. Am. Chem. Soc.* **2006**, *128*, 2940-2947.
227. Chia, K. K.; Rubner, M. F.; Cohen, R. E. pH-Responsive Reversibly Swellable Nanotube Arrays. *Langmuir* **2009**, *25*, 14044-14052.
228. Tan, W. S.; Cohen, R. E.; Rubner, M. F.; Sukhishvili, S. A. Temperature-Induced, Reversible Swelling Transitions in Multilayers of a Cationic Triblock Copolymer and a Polyacid. *Macromolecules* **2010**, *43*, 1950-1957.

Chapter 2: Macromolecule Drug Delivery Utilizing Prussian Blue

*Portions reprinted from “Electroactive Controlled Release Thin Films” by Kris C. Wood, Nicole S. Zacharia, Daniel J. Schmidt, Stefani N. Wrightman, Brian J. Andaya, and Paula T. Hammond, *Proc. Natl. Acad. Sci. USA*, 2008, 105(7), 2280-2285. 10.1073/pnas.0706994105, © 2008 National Academy of Sciences of the USA.

2.1 Introduction

Recently, great interest has centered on the development of ‘smart’ controlled release systems capable of administering drugs in response to external stimuli (e.g. electric or magnetic fields) for use in applications such as controlled release implants (‘pharmacy-on-a-chip’).¹⁻³ Toward these goals, microfabricated devices have been developed which make use of micrometer-scale pumps, channels, and wells to deliver drugs on demand.¹⁻⁵ However, while these technologies have resulted in encouraging new treatment possibilities, several challenges still remain. For example, the direct integration of these systems into non-planar, functional, or structural implants such as arterial stents, medical sutures, and bone prostheses is challenging, as photolithographic and micromachining techniques are primarily developed for planar, silicon-based substrates.⁶ Further, the multi-step processing of these systems can be both time-consuming and expensive.⁷ In this thesis, we demonstrate the fabrication of ultrathin films made from nontoxic, FDA-approved materials which can undergo remotely controlled dissolution to release precise quantities of drugs or other agents in response to a small applied voltage (+1.25 V). These nanoscale systems can be used to conformally coat surfaces of virtually any shape, size, or chemical composition, and represent a new class of responsive controlled release systems.

Electroactive thin films are constructed using the layer-by-layer (LbL) directed self-assembly technique, which utilizes the alternating adsorption of materials containing complementary charged or functional groups onto a solid substrate to form thin films.⁸ This method can be used to create highly tunable, conformal thin films with nanometer-scale control over film composition and structure. The only criterion for inclusion in an LbL thin film is that the species of interest either possess, or that it be encapsulated in a ‘carrier’ species (i.e., nanoparticle, micelle, dendrimer, etc.) that possesses the desired complementary functional group. Thus, a wide range of components including polymers, proteins, nucleic acids, small molecules, and nanoparticles have been incorporated into these assemblies, which can further be constructed in a range of geometries and patterns.^{9,10} As a result of this versatility, LbL thin films have been used in a variety of biological applications such as biomimetics, biosensors, functionalized membranes, coatings with antibacterial, anti-inflammatory, and anti-fouling properties, arrays, and materials for directed protein and cell adhesion.¹¹ They have also been used extensively in drug delivery, most notably as films or microcapsules that can release drugs passively¹²⁻¹⁵ or in response to environmental stimuli such as pH, ionic strength, or enzymes.^{11,16-}

25

The electroactive component of our films is Prussian Blue (PB), a non-toxic, FDA-approved inorganic iron hexacyanoferrate compound that is well known for its electrochromic,²⁶ electrochemical,²⁷ and magnetic properties.²⁸ PB exhibits a number of stable oxidation states known colloquially as Prussian White (PW), Prussian Blue (PB), Berlin Green (BG), and Prussian Brown (PX), in order of increasing oxidation state. These states are all negatively charged with the exception of PX, which is neutral.²⁹ PB can be synthesized in the form of polydisperse, anionic nanoparticles (median size 4-5 nm) which are stable in aqueous solution

and can be incorporated into LbL films.³⁰ Applying a potential of +1.25 V (compared to SCE) switches these materials between the PB (negative) and PX (neutral) states.³⁰

Here, we demonstrate that by applying a low voltage to PB nanoparticle-based LbL thin films, and thus changing the PB oxidation state from negative to zero-valent, we can induce rapid film destabilization and controlled release of the film's components. Destabilization leads to the release of the film's components into solution, and we quantify this controlled release using a model, radiolabeled compound (¹⁴C-dextran sulfate, abbreviated as ¹⁴C-DS). We further show that this release is well-controlled; that is, removal of the oxidizing potential results in restabilization of the remaining film, allowing for the release of precise quantities of material from a single film as well as "on-off" switching between stable and unstable states. Finally, as a measure of biocompatibility we demonstrate that PB particles exhibit no measurable toxicity on a panel of mammalian cell lines at concentrations up to 1.0 mg/mL. Together, this technology represents a new, robust, inexpensive, and versatile platform for the fabrication of field-activated (remote-controlled) controlled release systems.

2.2 Materials and Methods

¹⁴C-dextran sulfate sodium salt (¹⁴C-DS, 100 μ Ci, 1.5 μ Ci/mg, $M_n = 8000$) was obtained from American Radiolabeled Chemicals, Inc (St. Louis, MO). Linear poly(ethylenimine) (LPEI, $M_n = 25000$ or $M_n = 250000$) was received from Polysciences, Inc. (Warrington, PA). FeCl₂, potassium ferricyanide (K₃Fe(CN)₆), potassium hydrogen phthalate (KHPH), and potassium chloride (KCl) were purchased from Sigma Aldrich (St. Louis, MO). All materials and solvents were used as received without further purification.

Synthesis of PB nanoparticles proceeded as follows. Briefly, 35 mL of 10 mM aqueous FeCl_2 was added dropwise to an equivalent volume of 50 mM $\text{K}_3\text{Fe}(\text{CN})_6$ and 50 mM KCl, agitated for 1 min, and dialyzed in deionized water (with magnetic stirring) against a 3500 Da MWCO regenerated cellulose membrane. Permeate solutions (containing ten or more equivalent volumes) were yellow, suggesting that only the excess potassium ferricyanide along with a trivial amount of PB may have passed through the membrane. The retentate solution was collected, pH adjusted to 4 by addition of KHP buffer, and used immediately in LbL assembly.³⁰ The final concentration of PB in the dipping solution was approximately 1.5 mg/mL.

LbL films were assembled on conducting ITO-coated glass substrates (Delta Technologies, 750.7 mm cuvette slide, 8-12 ohms resistance) for profilometry, spectroscopic, deconstruction, and release studies. ITO-glass substrates were cleaned via ultrasonication in dichloromethane, acetone, methanol, and deionized water for 15 min each, followed by a 5 min oxygen plasma etch (Harrick PCD 32G) to ensure that the surfaces were clean and abundant in hydroxyl groups. Dextran sulfate and LPEI dipping solutions were prepared at concentrations of 10 mM with respect to the polymer repeat unit in acetate buffer (100 mM, pH 5.1) and deionized water (pH 4.0 by addition of HCl), respectively. Deionized water ($>18.2 \text{ M}\Omega\cdot\text{cm}$ resistivity), obtained using a Milli-Q Plus system (Millipore, Bedford, MA), was used to make all solutions.

LbL films were constructed as follows according to the alternate dipping method using an automated Carl Zeiss HMS Series Programmable Slide Stainer.⁸ Briefly, pretreated substrates were submerged in an LPEI dipping solution for 10 minutes followed by a cascade rinse cycle consisting of three deionized water rinsing baths at pH 4.0 (15, 30, and 45 seconds, respectively). Substrates were then submerged in a PB dispersion for 10 minutes followed by the same cascade

rinsing cycle, and the entire process was repeated as desired to construct (LPEI/PB) films with desired numbers of layer pairs. Tetralayer films containing LPEI/PB/LPEI/¹⁴C-DS were constructed using the same general protocol; however, in this case, the PB dipping step alternated with a DS dipping step (10 min with cascade rinse cycle). Tetralayer systems were capped with a single layer of LPEI following the last deposition step. Following deposition, films were immediately removed from the final rinsing bath and dried thoroughly under a stream of dry nitrogen gas. Film thickness and deconstruction experiments on conducting ITO-glass substrates were conducted using a Tencor P10 profilometer by scoring the film and profiling the score. A tip force of 5 mg was used to avoid penetrating the underlying ITO film.

Electrochemical deconstruction studies and chronoamperometry were performed using an EG&G 263 A potentiostat/galvanostat with a three electrode setup in a beaker. The electrolyte was a 10 mM KCl solution in deionized water (40 mL volume). The working electrode was an LbL film assembled on a conducting ITO-glass substrate (Delta Technologies, 750 0.7 mm cuvette slide, 8-12 Ω sheet resistance), the reference electrode was a K-type saturated calomel electrode (SCE), and the counter electrode was a piece of Pt foil (2.5 cm × 2.5 cm). Chronoamperometry was performed by stepping between the open circuit potential (~ +0.27 V) and +1.25 V versus a standard calomel electrode (SCE) with 30 minutes per step and data collection at 0.5 second intervals. Spectroscopic characterization was performed with a StellarNet EPP2000 concave grating UV-Vis-NIR spectrophotometer with a tungsten krypton light source.

For controlled release experiments, films were formed using radiolabeled ¹⁴C-DS (100 μCi, 1.5 μCi/mg) dipping solution at a concentration of approximately 4 μCi/mL. The LbL deposition procedure was then performed as described above. Following deposition, films were

immersed in 40 mL of 10 mM KCl, and electrochemical deconstruction was performed by applying square wave potentials, also as described above. In all cases, films were first immersed for 10 min prior to application of potential, and minimal passive release was observed. A 1 mL sample was extracted at indicated time points and analyzed for radioactive ^{14}C content by adding 5 mL of ScintiSafe Plus 50% (Fisher Scientific, Atlanta, GA) prior to measurement. Raw data (disintegrations per minute per mL, DPM/mL) were converted to micrograms per mL ($\mu\text{g/mL}$) of ^{14}C -DS using the conversion factor $2.2 \times 10^6 \text{ DPM} = 1 \mu\text{Ci} = 0.67 \text{ mg } ^{14}\text{C-DS}$. Finally, the total DS release from a single film was calculated according to the following equation:

$$M_i = C_i \times V_i + (1\text{mL}) \sum_{j=1}^{i-1} C_j \quad (1)$$

where M_i (μg) is the total cumulative mass released from the film as of measurement i , C_i ($\mu\text{g/mL}$) is the concentration of sample i , V_i (mL) is the total volume of the deconstruction bath prior to measurement i , and $(1\text{mL}) \sum_{j=1}^{i-1} C_j$ is the total mass in previously extracted samples.

Cell viability assays were performed in triplicate using the following protocol. All materials, buffers, and reagents were sterilized prior to use. Cell culture reagents were purchased from Invitrogen Corporation (Carlsbad, CA) and MTT viability assay kits were obtained from American Type Culture Collection (Manassas, VA). Focus HCC cells were grown in 96-well plates at an initial seeding density of 5000 cells/well in 150 μL /well of growth medium (90% modified Eagle's medium supplemented with 10% fetal bovine serum, 100 units/mL penicillin, and 100 $\mu\text{g/mL}$ streptomycin, 0.1 mM non-essential amino acids, 1 mM sodium pyruvate, and 2 mM L-glutamine). HeLa cells were grown in 96-well plates at an initial seeding density of 10000 cells/well in 150 μL /well of growth medium (90% modified Eagle's medium supplemented with 10% fetal bovine serum, 100 units/mL penicillin, and 100 $\mu\text{g/mL}$

streptomycin, 0.1 mM non-essential amino acids, 1 mM sodium pyruvate, and 2 mM L-glutamine). Cos-7 cells were grown in 96-well plates at an initial seeding density of 15000 cells/well in 150 μ L/well of growth medium (90% Dulbecco's modified Eagle's medium supplemented with 10% fetal bovine serum, 100 units/mL penicillin, and 100 μ g/mL streptomycin). After seeding, cells were allowed to attach and proliferate for 24 h in an incubator (37° C, 5% CO₂). A sterile, 10X concentrated PBS buffer solution was added to an aqueous suspension of PB nanoparticles to yield a final solution containing 1.125 mg/mL PB, 137 mM NaCl, 2.7 mM KCl, and 10 mM Na₂HPO₄ at pH 7.4. Growth media were removed from cells and replaced with the above suspension of PB particles diluted in Opti-MEM (Invitrogen) at concentrations ranging from 0 mg/mL to 1.0 mg/mL PB. In parallel, cells were also incubated with carrier solutions alone (Opti-MEM plus an equivalent concentration of PBS without PB particles) to account for toxicity associated with the carrier solution only. Cells were incubated with the solutions for 4 h, after which solutions were removed and replaced with growth media. After 72 h, cell metabolic activity was assayed using the MTT cell proliferation assay kit (ATCC, Manassas, VA). Initially, a 10 μ L aliquot of MTT assay reagent was added to each well. After incubating for two hours, 100 μ L of detergent reagent was added. The plate was then covered and left in the dark for 4 h, after which optical absorbance was measured at 570 nm using a SpectraMax 190 microplate reader (Molecular Devices, Sunnyvale, CA). Background (media plus MTT assay reagent plus detergent reagent with no cells present) was subtracted from the value of each well, and all values were normalized to the value of control (untreated) cells. In similar fashion, the toxicity of an equivalent amount of PBS buffer in Opti-MEM (with no PB) was calculated. Values reported in Figure 2.5 represent the normalized

viability of PB-treated cells divided by the normalized viability of cells treated with equivalent amounts of pure PBS (to account for the toxicity of PBS itself).

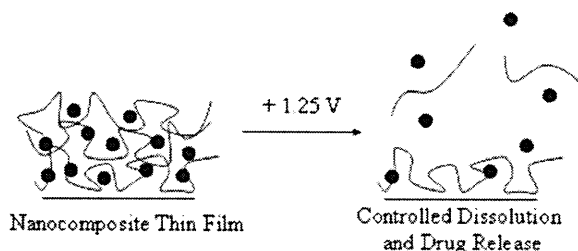
2.3 Results and Discussion

Electroactive LbL thin films are constructed as follows. A glass substrate coated with a conducting film of indium tin oxide (ITO) is first dipped in a solution containing a cationic drug or drug-containing “carrier” species and then rinsed in deionized water. Next, the substrate is dipped into an aqueous PB solution at pH 4 and rinsed again in deionized water. The process is repeated to build up a multilayer nanocomposite film with desired properties. Controlled film deconstruction occurs upon the application of an electrochemical potential of +1.25 V (vs. SCE), “switching” PB to the neutral PX state and destabilizing the film to release its encapsulated components (Fig 2.1A). For details on the synthesis and structure of PB nanoparticles, refer to section 2.2 above.

Fig. 2.1B shows the linear build-up of the tetralayer system containing linear poly(ethylenimine) (LPEI)/PB/LPEI/¹⁴C-DS used in this study (measured by profilometry and UV-Vis spectroscopy). Tetralayer systems, rather than traditional bilayer systems, were used to encapsulate and release ¹⁴C-DS, our negatively charged model compound. The thickness of an average tetralayer was 4.2 ± 0.6 nm. (This value reflects the average of six data points taken at various positions on the surface of the film.) Films were observed to grow linearly in thickness with increasing numbers of layers. The linear growth behavior observed in these systems may have important implications for the controlled delivery of precise quantities of drugs or other agents because the thickness (and mass) of a given layer can be precisely predicted with no

dependence on the thickness of the underlying film, resulting in facile control over release payloads.

(A)



(B)

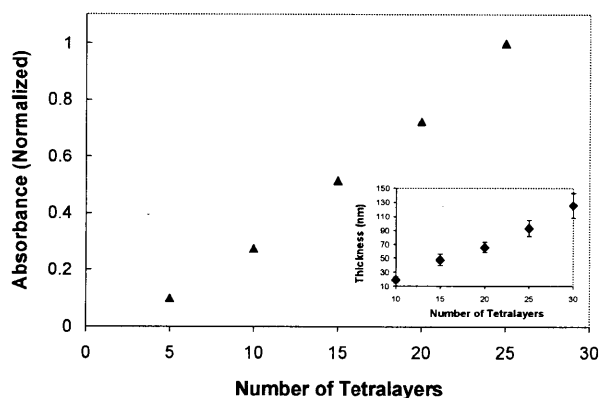


Figure 2.1. Fabrication of LbL nanocomposite thin films based on PB. (a) Generalized schematic detailing the deconstruction of PB-based films containing drugs or other chemical species (blue circles represent PB nanoparticles and red lines represent drugs or chemical species (with or without a second encapsulating species)). (b) Absorbance (700 nm) versus number of deposited tetralayers for the (LPEI/PB/LPEI/¹⁴C-DS)₃₀ system as determined by UV-Visual spectroscopy. Absorbance values are normalized to the absorbance of a 25 tetralayer film. (Inset: Thickness (nm) versus number of deposited tetralayers in the same system as determined by profilometry. Measurements were performed at six predetermined spots on the surface of the films, and error bars represent one standard deviation in measured values.)

Figure 2.2 shows the deconstruction of (LPEI/PB/LPEI/¹⁴C-DS)₃₀ films under the influence of an applied potential held constant at +1.25 V, as monitored by UV-Vis spectroscopy (PB exhibits an absorbance maximum at ~700 nm). Absorbance from PB-containing films was observed to decrease with increasing amounts of time at +1.25 V (Figure 2.2A). Quantitatively, absorbance at 700 nm was observed to decline rapidly during the first 5-10 minutes, reaching a value equal to 54% of that of the original film by 10 minutes (see Figure 2.2B). Thereafter, absorbance continued to decrease, reaching a value of 38.5% of the original film by 20 min, 18.2% by 60 min, and 10.4% by 90 min. Absorbance measurements taken from a control film (no applied potential) showed no decrease in color, suggesting that PB loss is directly related to film instabilities that are stimulated by the applied potential. Total film thickness measurements demonstrate a decrease in film thickness with time (at +1.25 V) that is analogous to PB loss, suggesting that the loss of PB from films is associated with destabilization and deconstruction of the film structure (Figure A1.1 in Appendix 1). The observed film destabilization is likely based on the loss of electroneutrality occurring within the film following the PB to PX transition, which results in the repulsion of adjacent, like-charged layers; similar mechanisms of film destabilization based on interlayer charge repulsion have been cited in the past.^{30,31} Further, the excess positive charge created in the film will cause an influx of anions to maintain electroneutrality, along with an osmotic pressure-induced influx of water, which solubilizes the film components.

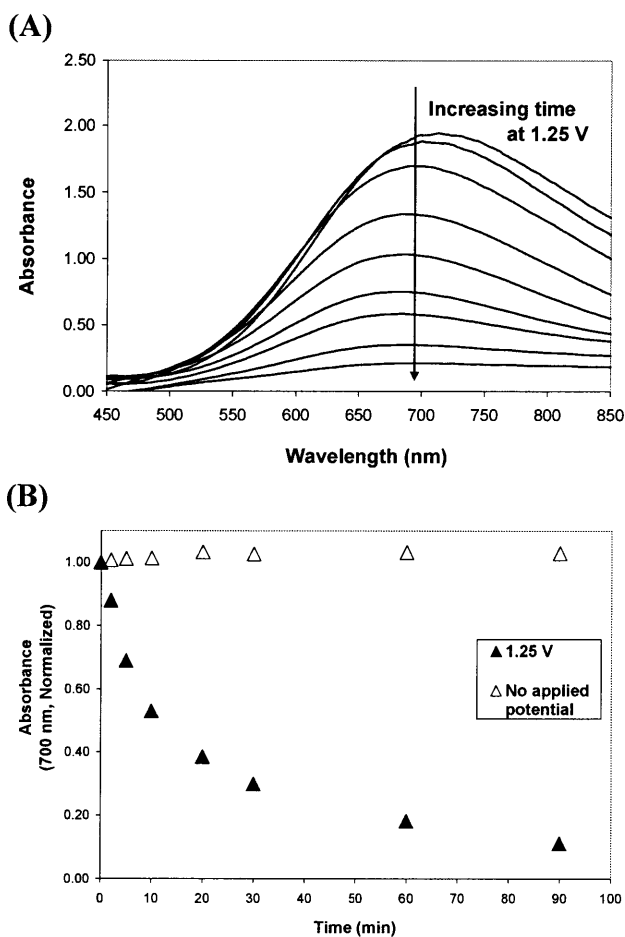


Figure 2.2. Electrochemical deconstruction of $(\text{LPEI/PB/LPEI}/^{14}\text{C-DS})_{30}$ films. (A) Absorbance spectrum showing decreasing PB absorbance with increasing time at +1.25 V. (B) Normalized absorbance (700 nm) versus time for films with (filled triangles) and without (open triangles) an applied potential.

To determine whether the electrochemical destabilization of PB-containing films causes release of the film's components into solution, we built films containing a radiolabeled, model compound, $^{14}\text{C-DS}$. Figure 2.3A shows that these systems release $^{14}\text{C-DS}$ rapidly following the application of +1.25 V (for 30 min), with kinetics occurring over the same time scale as PB loss and total film degradation. To verify that release occurs only in the presence of an applied potential, we soaked films in a solution identical to those used in the deconstruction experiments

(10 mM KCl) and observed no significant passive ^{14}C -DS release. Moreover, (LPEI/ ^{14}C -DS)₃₀ films lacking PB are stable in the presence of an applied potential of +1.25 V, exhibiting negligible ^{14}C -DS release and verifying our hypothesis that film destabilization is mediated by a valency state change in PB. For a description of ^{14}C -DS release from films held at potentials below +1.25 V and analysis of current and power requirements in electroactive thin films, refer to Figures A1.2-A1.4 in Appendix 1.

The ability of PB-containing thin films to release their contents only in response to a small applied potential suggests that these systems might be interesting materials for implantable pharmacy-on-a-chip applications.¹ For example, existing patterning and machining techniques could be used to array multiple films onto individually addressable electrodes on a single substrate, and the application of a potential to individual films could result in the release of an active species from one film at a time. As a simple proof of this concept, we placed two (LPEI/PB/LPEI/ ^{14}C -DS)₃₀ films in a release bath, then applied a potential of +1.25 V to each film individually for 10 min (the time required to release each film's entire contents). As shown in Figure 2.3B and 2.3C, this method results in the release of the contents of the first film followed by the contents of the second film. These results also suggest that the application of voltage to and subsequent degradation of the first film does not affect the release properties of the second film.

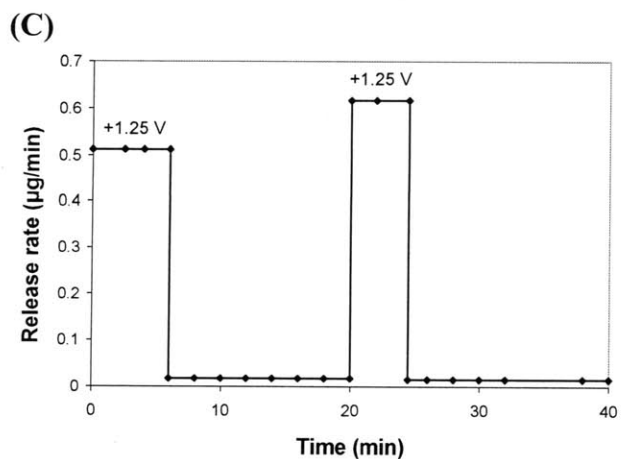
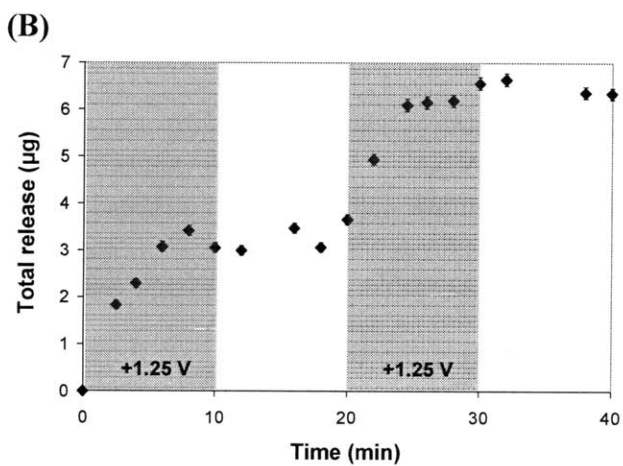
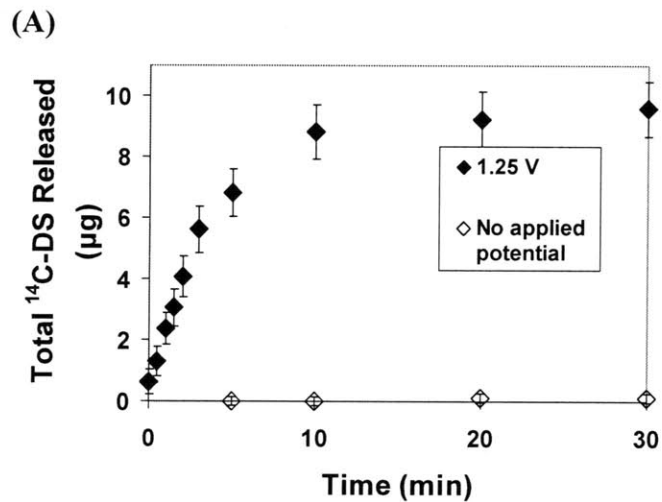
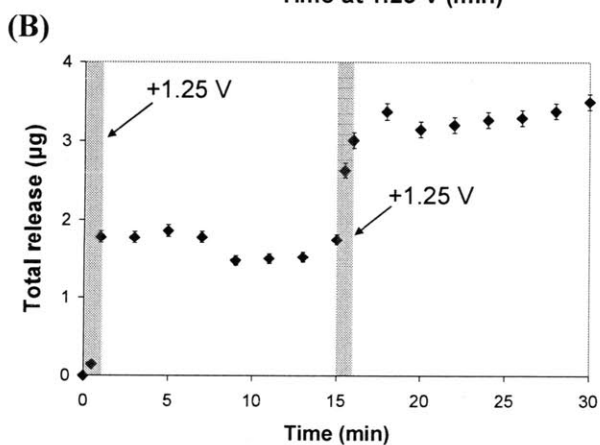
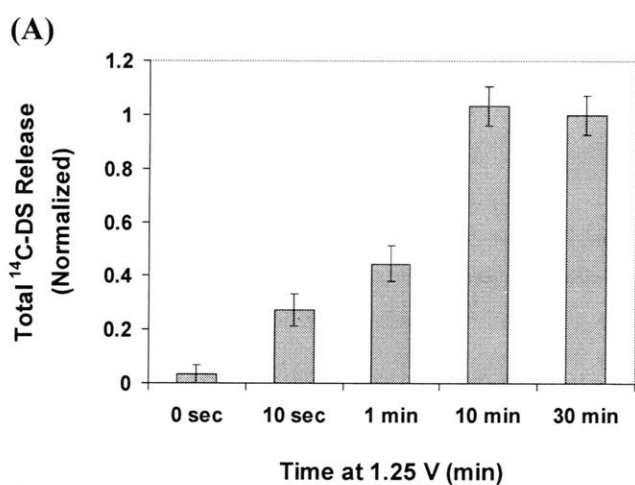


Figure 2.3. Release of a model compound, ¹⁴C-DS, from PB-containing films held at a constant potential of +1.25 V. All films are (LPEI/PB/LPEI/¹⁴C-DS)₃₀. (A) Films held constant at +1.25 V (closed diamonds) or no applied potential (open diamonds) are shown. (B) Serial ¹⁴C-DS

release from two (LPEI/PB/LPEI/¹⁴C-DS)₃₀ films in a single solution. One film was held at the oxidizing potential for 10 min, followed by 10 min below the oxidizing potential. Next, the process was repeated with a second film in the same degradation bath. Periods during which an oxidizing potential was applied are shaded. (C) Release rate versus time for the films in part (b). In all cases, error bars represent one standard deviation in measured values.

To more closely examine the kinetics of film deconstruction, we measured ¹⁴C-DS release from representative 30 tetralayer LPEI/PB/LPEI/¹⁴C-DS systems under the influence of a square wave potentials of +1.25 V for varying amounts of time. In Figure 2.4A the total ¹⁴C-DS release from films held at +1.25 V for differing time intervals is shown. Films release significantly more ¹⁴C-DS following 10 min and 30 min intervals than shorter 10 s or 1 min intervals, an indication of the on-off switchable nature of film destabilization. Further, 10 min and 30 min intervals result in similar quantities of release with similar kinetics (data not shown), suggesting that all of the available ¹⁴C-DS was released within the first 10 min (all films were deposited onto identical ITO-coated glass substrates from the same dipping solutions in order to ensure uniform thickness and ¹⁴C-DS loading). To examine whether films can be switched between stable and unstable states, a single film was exposed to two 1 min intervals at +1.25 V, separated by a 14 min interval without an applied oxidizing potential. (See Figures 2.4B and 2.4C). Release profiles indicate that films are rapidly destabilized in the presence of an oxidizing potential, then restabilized when the potential is removed. This process can be reversed, as reapplication of the oxidizing potential can again destabilize the film. From these data, it is apparent that the stability (and controlled release properties) of PB-based films can be precisely controlled electrochemically. In drug delivery applications, this on-off switchable stability may allow for an additional means of fine-tuned control over doses administered from

implanted films. Together, the data in Figure 2.4 suggests the following: (1) the process of film destabilization can be switched off by removing the oxidizing potential and reactivated by re-applying the potential; (2) diffusion of the film's components out of the destabilized film structure, rather than valency state switching in PB, is the rate-limiting step in film degradation (as PB redox switching times are roughly 10-30 sec) (Fig. A1.3 in Appendix 1); and (3) deconstruction and release from 30 tetralayer systems is completed in less than 10 min when held at constant oxidizing potential.



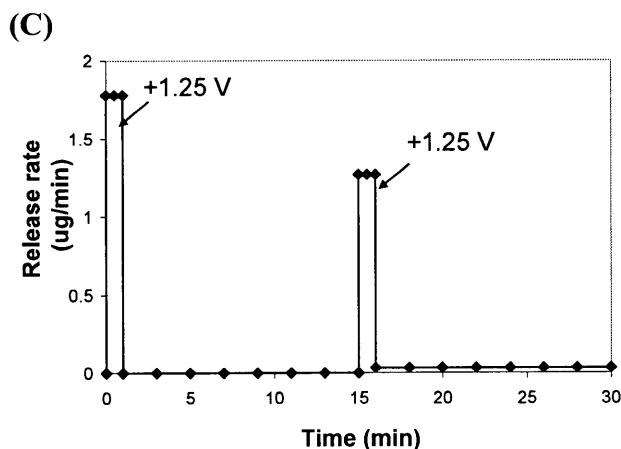


Figure 2.4. On-off switchable destabilization of PB-containing (LPEI/PB/LPEI/ ^{14}C -DS) $_{30}$ films. (A) Total ^{14}C -DS release from equivalent samples held at the oxidizing potential of +1.25 V for varying times (normalized to total release at 30 min). (B) ^{14}C -DS release from a single film held at +1.25 V for 1 min intervals at $t = 0$ and $t = 15$ min³². (C) Release rate from film shown in (B)³³. In all cases, error bars indicate one standard deviation in measured values.

Finally, as a measure of the biocompatibility of PB nanoparticles, we measured their toxicity on a panel of mammalian cell lines, including hepatocellular carcinoma (HCC), ovarian cancer (HeLa), and kidney fibroblast (Cos-7) cells, using a conventional 3-(4,5-dimethylthiazolyl-2)-2,5-diphenyltetrazolium bromide (MTT) assay. The MTT assay measures the effect of added substances on cell growth and metabolism, and is commonly used as an *in vitro* measure of toxicity.³⁴ PB particles caused no observable toxicity at all concentrations tested (up to 1.0 mg/mL) in this assay, which can sensitively detect toxic effects of added substances (Fig. 2.5).³⁵ These findings are not surprising, as PB is known to cause no adverse health effects in humans and was approved by the US FDA in 2003 for the treatment of radiation contamination and

heavy metal poisoning.³⁶ For more information on toxicity studies involving PB-based electroactive thin films, please refer to Appendix 1.

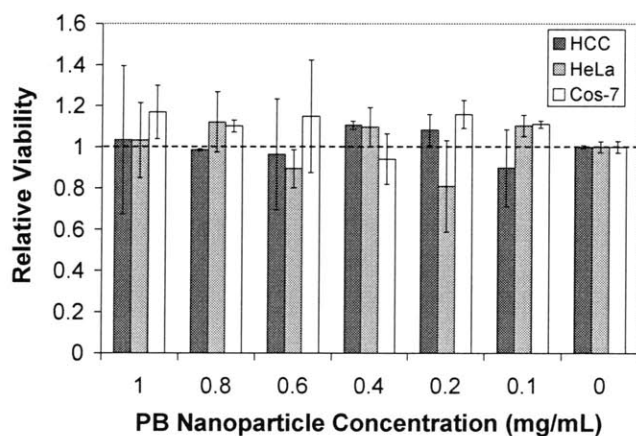


Figure 2.5. MTT assay for cellular toxicity indicates that PB nanoparticles exhibit no toxicity on three different cell lines at concentrations up to 1.0 mg/mL. Error bars represent one standard deviation in measured values.

2.4 Conclusions

We have demonstrated a new approach for constructing nanostructured thin films capable of releasing precise quantities of chemicals on demand in response to small electrochemical potentials. Further, we have shown that the films are stable enough to release a fraction of their contents, then restabilize upon removal of the applied potential. The LbL technique is sufficiently general to allow for the incorporation of chemicals of any structure (small molecules, macromolecules, charged and uncharged species, etc.) into these systems, alone or in conjunction with a ‘carrier’ species.⁸⁻¹⁰ As a simple proof of principle, we have studied the (LPEI/PB/LPEI/¹⁴C-DS) system, in which the biomolecule of interest (dextran sulfate) is alternately deposited (in conjunction with a ‘carrier’ species, LPEI) with the electroactive component, PB. Finally, we

have outlined a mechanistic hypothesis to explain the deconstruction process occurring in these systems, whereby an electrochemical signal oxidizes the nanoparticles to the PX state, resulting in loss of particle charge and destabilization of the film through self-repulsion of the polycation species. We expect that these electroactive controlled release thin films may find interesting applications in fields including drug delivery, tissue engineering, medical diagnostics, analytical chemistry, and chemical detection. Further, using the various thin film patterning techniques developed in recent years, we suggest that these materials may eventually be arrayed to produce multi-drug or multi-dose 'smart' devices.³⁷

2.5 References

1. LaVan, D. A.; McGuire, T.; Langer, R. Small-Scale Systems for in Vivo Drug Delivery. *Nat. Biotechnol.* **2003**, *21*, 1184-1191.
2. Santini, J. T.; Cima, M. J.; Langer, R. A Controlled-Release Microchip. *Nature* **1999**, *397*, 335-338.
3. Santini, J. T.; Richards, A. C.; Scheidt, R.; Cima, M. J.; Langer, R. Microchips as Controlled Drug-Delivery Devices. *Angewandte Chemie-International Edition* **2000**, *39*, 2397-2407.
4. Razzacki, S. Z.; Thwar, P. K.; Yang, M.; Ugaz, V. M.; Burns, M. A. Integrated Microsystems for Controlled Drug Delivery. *Adv. Drug Delivery Rev.* **2004**, *56*, 185-198.
5. Staples, M.; Daniel, K.; Cima, M. J.; Langer, R. Application of Micro- and Nano-Electromechanical Devices to Drug Delivery. *Pharm. Res.* **2006**, *23*, 847-863.
6. Reed, M. L.; Wu, C.; Kneller, J.; Watkins, S.; Vorp, D. A.; Nadeem, A.; Weiss, L. E.; Rebello, K.; Mescher, M.; Smith, A. J. C.; Rosenblum, W.; Feldman, M. D. Micromechanical Devices for Intravascular Drug Delivery. *J. Pharm. Sci.* **1998**, *87*, 1387-1394.
7. Duffy, D. C.; McDonald, J. C.; Schueller, O. J. A.; Whitesides, G. M. Rapid Prototyping of Microfluidic Systems in Poly(Dimethylsiloxane). *Anal. Chem.* **1998**, *70*, 4974-4984.
8. Decher, G. Fuzzy Nanoassemblies: Toward Layered Polymeric Multicomposites. *Science* **1997**, *277*, 1232-1237.
9. Hammond, P. T. Recent Explorations in Electrostatic Multilayer Thin Film Assembly. *Curr. Opin. Colloid Interface Sci.* **1999**, *4*, 430-442.
10. Hammond, P. T. Form and Function in Multilayer Assembly: New Applications at the Nanoscale. *Adv. Mater.* **2004**, *16*, 1271-1293.
11. Tang, Z.; Wang, Y.; Podsiadlo, P.; Kotov, N. A. Biomedical Applications of Layer-by-Layer Assembly: From Biomimetics to Tissue Engineering. *Adv Mater* **2006**, *18*, 3203-3224.

12. Caruso, F.; Schuler, C. Enzyme Multilayers on Colloid Particles: Assembly, Stability, and Enzymatic Activity. *Langmuir* **2000**, *16*, 9595-9603.
13. Shi, X.; Caruso, F. Release Behavior of Thin-Walled Microcapsules Composed of Polyelectrolyte Multilayers. *Langmuir* **2001**, *17*, 2036-2042.
14. Sukhorukov, G. B.; Brumen, M.; Donath, E.; Mohwald, H. Hollow Polyelectrolyte Shells: Exclusion of Polymers and Donnan Equilibrium. *J Phys Chem B* **1999**, *103*, 6434-6440.
15. Sukhorukov, G. B.; Mohwald, H. In *Colloids and Colloid Assemblies*; Caruso, F., Ed.; Wiley-VCH: Weinheim, Germany, 2004.
16. Jewell, C. M.; Zhang, J.; Fredin, N. J.; Lynn, D. M. Multilayered Polyelectrolyte Films Promote the Direct and Localized Delivery of DNA to Cells. *J Control Release* **2005**, *106*, 214-223.
17. Vazquez, E.; DeWitt, D. M.; Hammond, P. T.; Lynn, D. M. Construction of Hydrolytically-Degradable Thin Films Via Layer-by-Layer Deposition of Degradable Polyelectrolytes. *J Am Chem Soc* **2002**, *124*, 13992-13993.
18. Wood, K. C.; Boedicker, J. Q.; Lynn, D. M.; Hammond, P. T. Tunable Drug Release from Hydrolytically Degradable Layer-by-Layer Thin Films. *Langmuir* **2005**, *21*, 1603-1609.
19. Zhang, J.; Chua, L. S.; Lynn, D. M. Multilayered Thin Films That Sustain the Release of Functional DNA under Physiological Conditions. *Langmuir* **2004**, *20*, 8015-8021.
20. Chung, A. J.; Rubner, M. F. Methods of Loading and Releasing Low Molecular Weight Cationic Molecules in Weak Polyelectrolyte Multilayer Films. *Langmuir* **2002**, *18*, 1176-1183.
21. Hiller, J. A.; Rubner, M. F. Reversible Molecular Memory and pH-Switchable Swelling Transitions in Polyelectrolyte Multilayers. *Macromolecules* **2003**, *36*, 4078-4083.
22. Ma, Y.; Dong, W. F.; Hempenius, M. A.; Mohwald, H.; Vancso, G. J. Redox-Controlled Molecular Permeability of Composite-Wall Microcapsules. *Nat Mater* **2006**, *5*, 724-9.
23. Schuler, C.; Caruso, F. Decomposable Hollow Biopolymer-Based Capsules. *Biomacromolecules* **2001**, *2*, 921-926.
24. Wood, K. C.; Chuang, H. F.; Batten, R. D.; Lynn, D. M.; Hammond, P. T. Controlling Interlayer Diffusion to Achieve Sustained, Multiagent Delivery from Layer-by-Layer Thin Films. *Proc Natl Acad Sci USA* **2006**, *103*, 10207-10212.
25. Boulmedais, F.; Tang, C. S.; Keller, B.; Voros, J. Controlled Electrodissolution of Polyelectrolyte Multilayers: A Platform Technology Towards the Surface-Initiated Delivery of Drugs. *Adv. Funct. Mater.* **2006**, *16*, 63-70.
26. Mortimer, R. J. Electrochromic Materials. *Chem Soc Rev* **1993**, *26*, 147-156.
27. Karyakin, A. A.; Gltelmacher, O. V.; Karyakin, E. E. Prussian Blue-Based First-Generation Biosensor - a Sensitive Amperometric Electrode for Glucose. *Anal Chem* **1995**, *67*, 2419-2423.
28. Mingotaud, C.; Lafuente, C.; Amiell, J.; Delhaes, P. Ferromagnetic Langmuir-Blodgett Film Based on Prussian Blue. *Langmuir* **1999**, *15*, 289-292.
29. Neff, V. D. Electrochemical Oxidation and Reduction of Thin-Films of Prussian Blue. *J Electrochem Soc* **1978**, *125*, 886-887.
30. DeLongchamp, D. M.; Hammond, P. T. High-Contrast Electrochromism and Controllable Dissolution of Assembled Prussian Blue/Polymer Nanocomposites. *Adv Func Mater* **2004**, *14*, 224-232.

31. Sukhishvili, S.; Granick, S. Layered, Erasable, Ultrathin Polymer Films. *J Am Chem Soc* **2000**, *122*, 9550-9551.
32. After Holding at the Oxidizing Potential of 1.25 V for the Indicated Time Intervals, a Potential of 0.6 V Was Applied to Accelerate the Reversion of Px Back to Its Fully Charged Pb State. *After holding at the oxidizing potential of 1.25 V for the indicated time intervals, a potential of 0.6 V was applied to accelerate the reversion of PX back to its fully charged PB state.*
33. Release Rates Are Calculated Using a Simple Linear Fit of the Increasing and Plateau Regions of the Release Curve. *Release rates are calculated using a simple linear fit of the increasing and plateau regions of the release curve.*
34. Hansen, M. B.; Nielsen, S. E.; Berg, K. Re-Examination and Further Development of a Precise and Rapid Dye Method for Measuring Cell Growth/Cell Kill. *J Immunol Methods* **1989**, *119*, 203-210.
35. Wood, K. C.; Little, S. R.; Langer, R.; Hammond, P. T. A Family of Hierarchically Self-Assembling Linear-Dendritic Hybrid Polymers for Targeted Efficient Gene Delivery. *Angew Chem Int Ed* **2005**, *44*, 6704-6708.
36. Pearce, J. Studies of Any Toxicological Effects of Prussian Blue Compounds in Mammals - a Review. *Food Chem Toxicol* **1994**, *32*, 577-582.
37. LaVan, D. A.; McGuire, T.; Langer, R. Small-Scale Systems for in Vivo Drug Delivery. *Nat Biotechnol* **2003**, *21*, 1184-91.

Chapter 3: Small Molecule Drug Delivery Utilizing Prussian Blue

*Portions reproduced with permission from “Electrically Triggered Release of a Small Molecule Drug from a Polyelectrolyte Multilayer Coating” by Daniel J. Schmidt, Joshua S. Moskowitz, and Paula T. Hammond, *Chemistry of Materials*, 2010, 22(23), 6416-6425. 10.1021/cm102578j, © 2010 American Chemical Society.

3.1 Introduction

Layer-by-layer (LbL) thin films are a versatile platform for controlling the release of drugs from surfaces¹⁻³ Given the benefits of LbL assembly and the versatility of electrical stimuli, our group and others have previously explored LbL films for electrically controlled release of various molecules.⁴⁻⁹ However, an important challenge toward the engineering of LbL-based drug delivery devices is specifically controlling the release of small molecule therapeutics, which comprise 85% of all FDA-approved drugs between 1981 and 2002.¹⁰ Typically, for electrostatic-based LbL films, water solubility and polyvalency are requirements for direct inclusion of a molecule into the films. To bypass this requirement and to expand the realm of candidate materials, scientists have reported a number of different strategies. Small, uncharged, hydrophobic drugs have been loaded into LbL films via a “pro-drug” approach, in which the drug is covalently bound to a polymer (often with a labile linkage) prior to film assembly.^{11,12} Alternatively, some drugs may be non-specifically absorbed into micro- and nanoporous LbL films from organic solutions.¹³ Lastly, hydrophobic drugs may be sequestered by micelles or cyclodextrins (CDs), both of which possess hydrophobic cores and hydrophilic exteriors, which allow for water solubility and loading into LbL films when the exteriors are charged or otherwise functionalized for LbL assembly. The use of micelles and CDs are reviewed further in sections 3.1.1 and 3.2.2 below, respectively, since both of these strategies were explored in this thesis.

For the case of some small, charged drugs and dyes, incorporation into LbL films can be done directly based on electrostatics. In certain cases, when the small molecule is multivalent it can bind to the surface and reverse surface charge for LbL assembly. When the small molecule is monovalent it may be complexed electrostatically with a polyelectrolyte either prior to or after film assembly. Electrostatic approaches to loading small molecules in LbL films are reviewed in section 3.1.3 below, as this strategy was also explored in this thesis.

The mechanism of electrically triggered film dissolution and drug release is the charge-shifting of Prussian Blue nanoparticles as discussed in the previous chapter. The Hammond group has previously reported on the electrochemically-mediated dissolution of LbL films containing PB and polymer at an applied anodic potential.^{9,14} Electroactive PB nanoparticles, which are negatively charged in the film in the absence of an applied potential, can be switched to neutral at an anodic potential, leading to destabilization of the film. Unlike other works in the literature that rely upon changes in local pH induced by the hydrolysis of water,^{4,5,7} this work uses smaller voltages that will not disrupt the local pH environment, thereby making this system milder and more amenable toward biomedical applications. Further, this work is the first report of electrically-triggered release of a *small molecule drug* from an LbL film and represents a generic platform for controlling the release of any multiply charged, small molecule drug that is not susceptible to degradation by application of a small (< 1.0 V) electric potential. We maintain that such platforms could ultimately be integrated with implantable or transdermal drug delivery devices to address unmet clinical needs.

3.1.1 Micelles

Micelles are self-assembled, macromolecular constructs that may be formed by both small molecule surfactants as well as block copolymers in solution when the molecules are

present above the critical micelle concentration (CMC). In aqueous systems, micelles generally possess a hydrophobic core and a hydrophilic exterior (Fig. 3.1); the hydrophobic core can be used to solubilize in water many different water insoluble, hydrophobic drugs and thereby facilitate their pharmaceutical use. As such, there is a large field of research on the use of micelles as pharmaceutical carriers for the purpose of increasing bioavailability and even for imparting targeting capabilities.¹⁵⁻¹⁷ Multiple micelle-based pharmaceutical formulations are currently in clinical and preclinical trials.

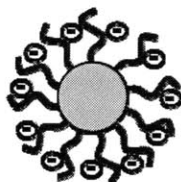


Figure 3.1. General schematic of a micelle comprising a hydrophilic, charged corona (blue) and a hydrophobic interior (green), in which hydrophobic molecules may be sequestered.

Just as micelles may be used to solubilize small hydrophobic drugs in aqueous solutions, they may also be used to encapsulate such drugs in LbL thin films. In this case, the hydrophilic exterior of the micelle must possess charged groups, H-bonding groups, or other functionalities to allow for LbL assembly. Our group recently reported H-bonded LbL films incorporating triclosan-loaded poly(ethyleneoxide)-poly(caprolactone) that release the drug upon exposure to physiological pH.¹⁸ Prior to that we reported electrostatic LbL films incorporating triclosan-loaded poly(propyleneoxide)-poly(amidoamine) micelles that release the drug passively by diffusion.¹⁹ Ma et al.²⁰ and Addison et al.²¹ have reported other block copolymer micelles used to load and release hydrophobic dye molecules from LbL films, while

Liu et al.²² have reported a polyelectrolyte-stabilized surfactant micelle and Jiao et al.²³ have reported a dendronized polymer both of which can load and release pyrene. Guyomard et al. reported an amphiphilic polysaccharide that forms hydrophobic nanoreservoirs used to load and release the dye Nile Red.²⁴ Lastly, Manna et al. have reported the use of micelles comprising sodium dodecyl sulfate for the encapsulation and controlled release of multiple small molecules.^{25,26}

In this thesis, I investigated poly(styrene-block-4-vinylpyridine) (PS-b-P4VP) micelles for the encapsulation of small, hydrophobic molecules and subsequent loading into LbL films containing Prussian Blue. Previously, Cho et al. and Hong et al. successfully fabricated LbL films containing PS-b-P4VP micelles and demonstrated the encapsulation of spiropyran,²⁷ coumarin 30,²⁸ and quantum dots²⁸ for various optical applications. Here we investigated the encapsulation of coumarin 30, 1,4-bis(5-phenyl-2oxazolyl)benzene (POPOP) 9,10-diphenylanthracene (DPA), three small, fluorescent hydrophobic dye molecules. Micelles loaded with these molecules were then layered directly with PB in bilayer architectures (i.e., (PS-b-P4VP micelle/PB)_n) as well as in tetralayer architectures with linear polyethyleneimine (LPEI) (i.e., (LPEI/PB/PS-b-P4VP micelle/PB)_n). We characterized film growth and stability, PB electroactivity, and drug loading and release.

3.1.2 Cyclodextrins

Cyclodextrins (CDs) are cyclic oligosaccharides derived from starch (Fig. 3.2). They possess a hydrophilic exterior and a hydrophobic cavity, which allows them to form inclusion complexes with multiple different small, hydrophobic drugs. Like micelles, CDs have been investigated for solubilizing and increasing the bioavailability of many water insoluble drugs,²⁹⁻

³⁵ as well as for targeting and controlled release applications.³⁶ In fact, multiple CD-containing drug formulations are on the market worldwide.

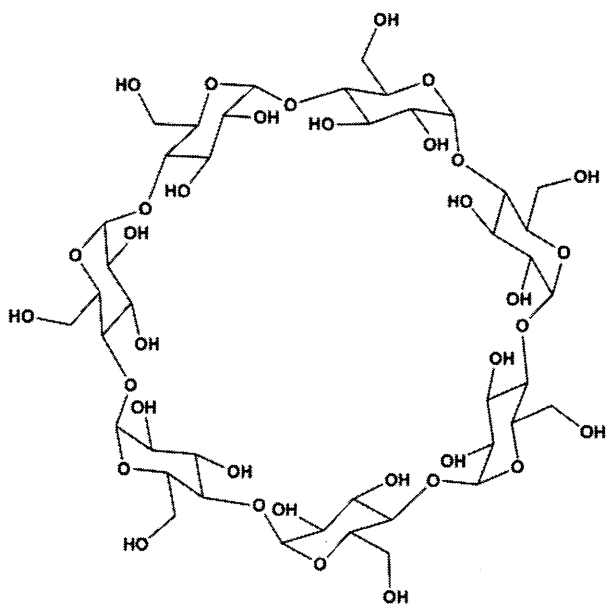


Figure 3.2. Molecular structure of β -cyclodextrin.

A number of authors have included charged CDs in LbL films. Yang et al. were the first to successfully layer CDs into LbL films for use as chemical sensors based on the specificity of the inclusion complexes.³⁷ Fischer et al. then demonstrated the formation of inclusion complexes between CDs and an azoaromatic dye covalently tethered to a polyanion in an LbL film,³⁸ while Sato et al. successfully loaded free small molecule dyes into LbL films via CD-inclusion complexes.^{39,40} They further studied the controlled release of methyl orange from these films as a function of pH and ionic strength.⁴¹ Benkirane-Jessel et al. were the first to incorporate an active small molecule drug into an LbL film using CDs. They complexed the drug piroxicam with a negatively-charged cyclodextrin into an LbL film and demonstrated the anti-inflammatory properties of the film.⁴² More recently, our group demonstrated a platform

technology for the controlled release of small molecule drug-CD complexes from an LbL film based on the hydrolytic degradation of a polymer.⁴³

In this thesis, I have studied the incorporation of polymeric carboxymethyl- β -cyclodextrin (CM β CD) into films along with Prussian Blue (PB) nanoparticles. Since both CM β CD and PB are negatively charged, the biocompatible polycation chitosan (Chi) was used to fabricate films in a tetralayer architecture denoted as (Chi/PB/Chi/CD)_n, where *n* is the number of layers. The small, hydrophobic, anti-inflammatory drug, Flurbiprofen (Flurb) was pre-complexed with the CD before film assembly. Loading and release of the drug were assessed with fluorescence spectroscopy, and electroactivity of the films was assessed with cyclic voltammetry.

3.1.3 Electrostatic Complexation

While small, charged drugs are often water-soluble, encapsulating them in a polymer thin film and controlling their release can be a difficult task. When the small molecule is multivalent it may comprise one of the layers in an LbL film if it has the ability to bind to the surface and reverse the surface charge. Ariga et al. previously demonstrated the assembly of multiple polyelectrolyte multilayer films containing small molecule dye layers.⁴⁴ More recently, our group has shown that the multivalent, positively-charged, aminoglycoside antibiotic gentamicin can be layered into a layer-by-layer film by electrostatics, and the release can be controlled utilizing a hydrolytically degradable polycation.^{45,46} Other small, positively-charged molecules may be complexed with polyanionic species prior to LbL deposition, as shown by Chen et al.,⁴⁷ or loaded into films after assembly through absorption and binding to free negatively charged sites in the film, as shown by Chung et al.⁴⁸ Similarly, many small,

negatively-charged molecules may be complexed with polycationic species before film assembly^{47,49} or bound to free positively charged sites following film assembly.^{50,51}

In this thesis, I present the incorporation of gentamicin sulfate (GS), a small molecule antibiotic, into an LbL assembled thin film coating composed of biocompatible materials. Gentamicin, which is widely used to treat and prevent infections associated with implanted devices, including orthopedic implants,⁵² serves as the cationic component of the LbL film. It possesses up to five positively charged amines below its pKa (~8.2).⁵³ Nanoparticles of Prussian Blue (PB)—approved by the FDA in tablet form in 2003 and shown to have very low cytotoxicity in a previous publication from our group⁹—are the anionic component of the film. Chitosan (Chi), a biocompatible polycation derived from the shells of crustaceans, is used for adhesion layers only. To our knowledge, this is the first report of an LbL film composed primarily of nanoparticles and small molecules, and the first demonstration of systematic electro-activated drug release from such films. These films are assembled with the following architecture: Chi(PB/Chi)₅(PB/GS)_n, where *n* represents the number of deposited bilayers. Drug loading into the film is easily controlled by changing the number of layers, while release of gentamicin can be precisely controlled with an electrochemical stimulus.

3.2 Materials and Methods

3.2.1 Micelles

Materials. Poly(styrene-block-4-vinylpyridine) (PS-*b*-P4VP) (MW: 57.5k-18.5k, “crew cut”; MW: 17k-49k, “hairy”) was purchased from Polymer Source, Inc. (Montreal, Canada). Linear polyethyleneimine (LPEI) (MW 25K) was purchased from PolySciences, Inc. (Warrington, PA). Coumarin 30, 9,10-diphenylanthracene (DPA), iron(II) chloride

tetrahydrate, potassium ferricyanide, potassium chloride (KCl), and potassium hydrogen phthalate (KHPH) were purchased from Sigma Aldrich (St. Louis, MO). Hydrochloric acid and sodium hydroxide solutions for pH adjustments were purchased from VWR Scientific (Edison, NJ). Indium tin oxide (ITO)-coated glass slides (CD-50IN-CUV) were purchased from Delta Technologies, Limited (Stillwater, MN). Glass microscope slides were purchased from VWR Scientific (Edison, NJ). Bandpass and longpass optical filters for solid state fluorescence measurements were purchased from Thor Labs (Newton, NJ). All chemicals were used as received.

Preparation of micelle, nanoparticle, and polyelectrolyte solutions. PS-b-P4VP micelles were made as described by Cho et al.²⁷ PS-b-P4VP was dissolved in dimethylformamide (DMF) at a concentration of 25 mg/mL, and then pH 2.0 water was added dropwise with stirring until a final PS-b-P4VP concentration of 1.0 mg/mL was attained. The micelles have a hydrophobic PS core and a hydrophilic, positively charged P4VP corona. Cho et al. showed that the P4VP is protonated at pH values below roughly 5.5.²⁷ Prussian Blue (PB) nanoparticle solutions were prepared as described previously.¹⁴ Linear polyethyleneimine (LPEI) solutions were prepared at concentration of 10 mM with respect to the repeat unit. Deionized water (18.2 M Ω -cm, Milli-Q Ultrapure Water System, Millipore) was used to prepare all solutions. The pH of all solutions was adjusted to 4.0 with HCl and NaOH.

Zeta potential and particle size. The zeta potential and hydrodynamic diameter of the PS-b-P4VP micelles were determined with a ZetaPALS, Zeta Potential Analyzer (Brookhaven Instruments, Corp.).

Film characterization. Film thickness was determined by profilometry (KLA Tencor P16 surface profiler) using a 2 mg tip force and a stylus with a 2 μ m tip radius. Films were scored

to the substrate surface with a razor blade and step heights were measured at five different locations. Film thickness and optical properties were confirmed with a J.A. Woollam M-2000 spectroscopic ellipsometer. Data were fit using J.A. Woollam WVASE32 software. Electrochemical measurements were carried out with a Princeton Applied Research EG&G 263A potentiostat/galvanostat in a three-electrode cell. The electrolyte was 0.1 M potassium hydrogen phthalate (KHPH). The working electrode was a conducting ITO-glass substrate (7 x 50 x 0.5 mm) coated with the polyelectrolyte thin film, the reference electrode was a Ag/AgCl (3M KCl) electrode (Cypress Systems, Chelmsford, MA), and the counter electrode was a Pt wire.

Small molecule loading and release. To load a small, hydrophobic molecule into the micelle core, the small molecule (Coumarin 30, POPOP, or DPA) was dissolved into the DMF with the PS-b-P4VP before micelle formation. Coumarin 30 (Fig. 3.3) was added in an amount to give a final concentration of 0.05 mg/mL. POPOP and DPA (Fig. 3.4) was added in an amount to give final concentrations in the range of 0.001 mg/mL to 0.05 mg/mL. The loading of the small molecules into the films was confirmed by fluorescence spectroscopy using a Horiba Jobin Yvon Fluorolog-3 spectrofluorometer. Films and solutions containing Coumarin 30 were excited at a wavelength of 413 nm and exhibited an emission peak at roughly 490 nm. Solid state fluorescence measurements were made using a 410 ± 10 nm bandpass filter for the excitation beam and a 435 nm longpass filter for the emission signal to eliminate stray light reflected from the glass substrate. Films and solutions containing POPOP or DPA were excited at a wavelength of 360 nm. Solid state fluorescence measurements were made using a 360 ± 5 nm bandpass filter for the excitation beam and no longpass filter for the emission signal. Release experiments were carried out in 10 mM KHPH (pH 4) instead of physiological

conditions to ensure that dye release did not occur due to a change in micelle ionization when the film assembled at pH 4 is transferred a higher pH above the pKa of the P4VP unit. The water solubility of each of the dye was retrieved from SciFinder (<https://scifinder.cas.org>).

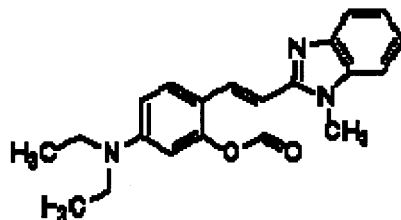


Figure 3.3. Molecular structure of Coumarin 30.

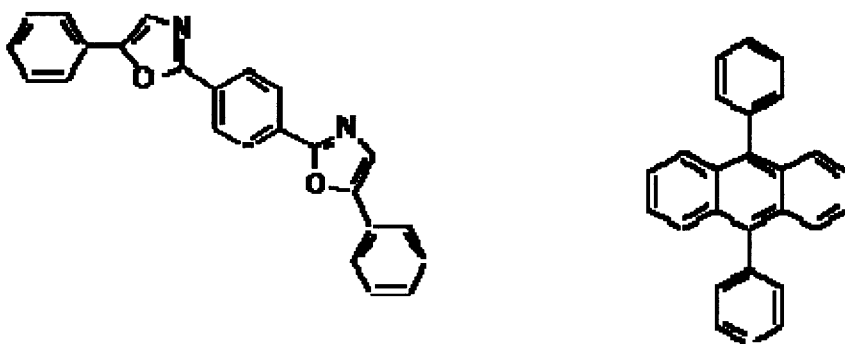


Figure 3.4. Molecular structures of POPOP (left) and DPA (right).

3.2.2 Cyclodextrins

Materials. Carboxymethyl- β -cyclodextrin polymer (CM β CD) (Trappsol[®]), with $M_w = 8000$, $M_n = 5900$, and total carboxy content of 2.8%, was purchased from Cyclodextrin Technologies Development, Inc. (High Springs, FL). Flurbiprofen (Flurb) (Fig. 3.5), iron(II) chloride tetrahydrate, potassium ferricyanide, and potassium hydrogen phthalate (KHPh) were purchased from Sigma Aldrich (St. Louis, MO). Linear polyethyleneimine (LPEI) ($M_n = 25,000$) was purchased from Polysciences, Inc. (Warrington, PA). Potassium chloride was

purchased from Mallinckrodt Baker. All chemicals were used as received. Indium tin oxide (ITO)-coated glass slides (CD-50IN-CUV) were purchased from Delta Technologies, Limited. Quartz slides for solid state fluorescence measurements were purchased from Chemglass (Vineland, NJ)

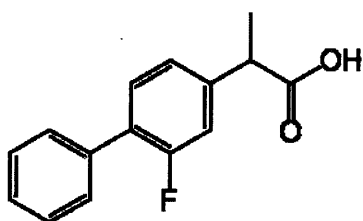


Figure 3.5. Molecular structure of Flurbiprofen.

Preparation of nanoparticle, and polyelectrolyte solutions. Chitosan (Chi) was dissolved at a concentration of 1.5 mg/mL in 0.1 M acetic acid, stirred overnight, and then vacuum filtered through a polyethersulfone membrane with a pore size of 0.45 μm . CM β CD was dissolved in DI water at a concentration of 2-10 mg/mL. To achieve full dissolution, 1 M NaOH was added until the solution pH reached 11-11.5. The pH was then adjusted down to the desired pH (typically 4-6) with 1 M HCl. Prussian Blue (PB) nanoparticle solutions were prepared as described previously.¹⁴ Linear polyethyleneimine (LPEI) solutions were prepared at a concentration of 10 mM with respect to the repeat unit. Deionized water (18.2 M Ω -cm, Milli-Q Ultrapure Water System, Millipore) was used to prepare all solutions. The pH of all solutions was adjusted to 4.0 with HCl and NaOH.

Film characterization. Film thickness was determined by profilometry (KLA Tencor P16 surface profiler) using a 2 mg tip force and a stylus with a 2 μm tip radius. Films were scored to the substrate surface with a razor blade and step heights were measured at five different locations. Film thickness was also determined with a J.A. Woollam M-2000 spectroscopic

ellipsometer. Data were fit using J.A. Woollam WVASE32 software. Electrochemical measurements were carried out with a Princeton Applied Research EG&G 263A potentiostat/galvanostat in a three-electrode cell. The electrolyte was 0.1 M potassium hydrogen phthalate (KHPH). The working electrode was a conducting ITO-glass substrate (7 x 50 x 0.5 mm) coated with the polyelectrolyte thin film, the reference electrode was a Ag/AgCl (3M KCl) electrode (Cypress Systems, Chelmsford, MA), and the counter electrode was a Pt wire

Small molecule loading and release. Small molecule drugs and dyes were precomplexed with the CDs before assembly into films. The maximum amount of Flurbiprofen that could be loaded into the CM β CD was determined from the 1:1 complexation coefficient ($K_{1:1}$) as defined by Loftsson et al.⁵⁴ and calculated for the CM β CD-Flurb complex by Smith et al.⁵⁵ The extent of loading of Flurbiprofen into films and release from films was determined using a spectrofluorometer (Horiba Jobin Yvon Fluorolog-3). Films and solutions containing Flurbiprofen were excited at a wavelength of 280 nm and emission spectra were obtained from 290-400 nm.

3.2.3 Electrostatic Complexation

Materials. Chitosan (Chi, “medium molecular weight”, 75-85% deacetylated), iron(II) chloride tetrahydrate, potassium ferricyanide, potassium chloride (KCl), potassium hydrogen phthalate (KHPH), sodium chloride (NaCl), and acetic acid were purchased from Sigma Aldrich (St. Louis, MO). Gentamicin sulfate (GS), USP Grade was purchased from Teknova (Hollister, CA). ³H-gentamicin sulfate (³H-GS) (0.250 mCi total, 1 mCi/mL in ethanol, 0.200 mCi/g) was purchased from American Radiolabeled Chemicals (St. Louis, MO). Phosphate

buffered saline (PBS), 1X was purchased from Mediatech (Manassas, VA). Hydrochloric acid and sodium hydroxide solutions for pH adjustments were purchased from VWR Scientific (Edison, NJ). Indium tin oxide (ITO)-coated glass slides (CD-50IN-CUV) were purchased from Delta Technologies, Limited (Stillwater, MN). *Staphylococcus aureus*, strain 25923 with no antibiotic resistance, was purchased from ATCC (Manassas, VA), and cation-adjusted Mueller Hinton Broth (CMHB) was purchased from BD (Franklin Lakes, NJ). All chemicals were used as received.

Preparation of polyelectrolyte solutions. Prussian Blue (PB) nanoparticle solutions were prepared as described previously.¹⁴ Gentamicin sulfate (Fig. 3.6) solutions were prepared at a concentration of 1 mg/mL containing 0.1 M sodium chloride (NaCl). Chitosan (Chi) was dissolved at a concentration of 1.5 mg/mL in 0.1 M acetic acid, stirred overnight, and then vacuum filtered through a polyethersulfone membrane with a pore size of 0.45 μm . Deionized water (18.2 M Ω -cm, Milli-Q Ultrapure Water System, Millipore) was used to prepare all solutions. The pH of all solutions was adjusted to 4.0 with HCl and NaOH.

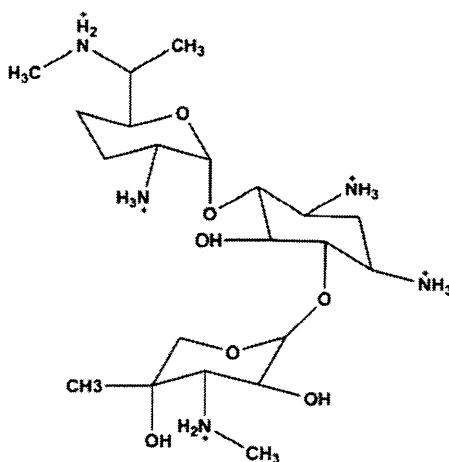


Figure 3.6. Molecular structure of gentamicin sulfate. The primary and secondary amines are shown in their charged state, and the sulfate counterions are eliminated for clarity.

Film assembly. ITO-coated glass slides were sonicated in a 4% solution of Micro-90 cleaning solution (Cole Parmer, Vernon Hills, IL) for 15 min, followed by two 15 min sonication cycles in deionized water. Next, the slides were dried with a stream of nitrogen and subjected to oxygen plasma for 5 min using a Harrick PDC-32G plasma cleaner on high RF power to remove any remaining organic contaminants and increase the negative charge density on the surface. The slides were then immediately immersed in a Chi solution for 1 hr and rinsed in three separate pH 4.0 water baths for a total of 3 min. The LbL assembly technique was employed through dip coating with an automated Zeiss HMS series programmable slide stainer. Films were constructed with the architecture $\text{Chi}(\text{PB}/\text{Chi})_5(\text{PB}/\text{GS})_n$, in which the five (PB/Chi) bilayers served as an adhesion platform for the overlaying (PB/GS)_n layers with $n = 25, 50, \text{ or } 75$. Each individual layer was deposited by a 10 min immersion in the appropriate polyelectrolyte (Chi, PB, or GS) solution, followed by a cascade rinse cycle in three separate pH 4.0 water baths for a total of 3 min to remove weakly bound material. Following deposition, films were dried under a stream of nitrogen.

Film characterization. Film thicknesses were determined by profilometry (KLA Tencor P16 surface profiler) using a 2 mg tip force and a stylus with a 2 μm tip radius. Films were scored to the substrate surface with a razor blade and step heights were measured at five different locations. Surface morphology and roughness were characterized in the dry state via atomic force microscopy (AFM) using a Dimension 3100 Scanning Probe Microscope (Veeco Instruments, Plainview, NY) in tapping mode. PointProbe Plus AFM probes (Nanosensors, Neuchatel, Switzerland) with a nominal tip radius of less than 7 nm were used. Electrochemically triggered film deconstruction studies were carried out with a Princeton Applied Research EG&G 263A potentiostat/galvanostat in a three-electrode cell. The

electrolyte was 15 mL of PBS, 1X at pH 7.4 to mimic physiological conditions. The working electrode was a conducting ITO-glass substrate (7 x 50 x 0.5 mm) coated with the polyelectrolyte thin film, the reference electrode was a Ag/AgCl (3M KCl) electrode (Cypress Systems, Chelmsford, MA), and the counter electrode was a Pt wire. Cyclic voltammetry (CV) and chronoamperometry (CA) were performed in either PBS or a deoxygenated 0.1 M KHPH electrolyte with the same electrodes.

Drug release characterization. To quantify the release of GS, films were assembled with a mixture of radiolabeled ^3H -GS and non-radiolabeled GS (1:600 by mass) through LbL assembly as described above. After film deposition, films were dried under a stream of nitrogen and then immersed in the PBS electrolyte solution at room temperature ($\sim 25\text{ }^\circ\text{C}$). Passive drug release is defined as release in the absence of an applied voltage (i.e., at the open circuit potential), whereas active drug release is in the presence of an applied voltage. During a drug release experiment, 1 mL aliquots were removed from the release bath at indicated time points and were analyzed for radioactive ^3H content through scintillation counting after the addition of 5 mL of ScintiSafe Plus 50% (Fisher Scientific, Atlanta, GA) with a Perkin Elmer Tri-Carb 2810 Liquid Scintillation Counter. Raw data (disintegrations per min per mL, DPM/mL) were converted to $\mu\text{g } ^3\text{H-GS /mL}$ by using the conversion factor $2.2 \times 10^6 \text{ DPM} = 1.0 \text{ } \mu\text{Ci} = 5.0 \text{ } \mu\text{g } ^3\text{H-GS}$. Finally, the total amount of GS released from a single film was calculated according to Equation 3.1,

$$M_i = C_i V_i + (1 \text{ mL}) \sum_{j=1}^{i-1} C_j (600) \quad (3.1)$$

where M_i (μg) is the total cumulative mass released from the film as of measurement i , C_i ($\mu\text{g/mL}$) is the concentration of sample i , V_i (mL) is the total volume of the film dissolution

bath before measurement i , $(1 \text{ mL}) \sum_{j=1}^{i-1} C_j$ is the total mass in previously extracted samples, and 600 is equal to the mass ratio of total GS to $^3\text{H-GS}$ in the solution used for film assembly, which is assumed to be identical to the ratio in the film.

***In vitro* efficacy of released gentamicin.** The *in vitro* efficacy of gentamicin released from the films was tested through a microdilution assay against *Staphylococcus aureus* bacteria following standard methods outlined by the Clinical and Laboratory Standards Institute (M26-A, 1999). The assay was performed in a 96-well plate with 150 μL of liquid culture per well comprising 135 μL of test medium (i.e., PBS containing gentamicin released from an $n = 75$ film (see below), or PBS only for the positive control) and 15 μL of inoculation culture at 10^6 CFU/mL in cation-adjusted Mueller Hinton Broth II (CMHB). All test media were sterile-filtered through 0.2 μm cellulose acetate membranes immediately prior to use. Gentamicin was released from a 75 bilayer film exposed to +1.25 V (vs. Ag/AgCl) for 1 hr in 5 mL of PBS, yielding a gentamicin concentration of approximately 4.0 $\mu\text{g/mL}$. This maximum strength medium was serially diluted into an equal quantity of CMHB eight times in the 96-well plate, yielding a total of nine concentrations down to 0.016 $\mu\text{g/mL}$. A negative control in the absence of inoculated bacteria, and a positive control in the absence of gentamicin were included in the assay. All samples were measured in triplicate. The plate was incubated at 37 $^\circ\text{C}$ for 16 hr. Relative bacterial cell density was determined by recording the optical density (OD) at 600 nm in a BioTek PowerWave XS Microplate spectrophotometer with accompanying Gen5 software.

3.3 Results and Discussion

3.3.1 Micelles

3.3.1.1 Micelle and Film Characterization

Before fabricating films, the size and surface charge of both the “hairy” and “crew cut” micelles were assessed with ZetaPALS. The hydrodynamic diameters were 79.8 ± 31.4 nm and 70.8 ± 16.9 nm for the “hairy” and “crew cut” micelles, respectively. The zeta potentials were $+48.9 \pm 4.2$ mV and $+43.8 \pm 4.6$ mV for the “hairy” and “crew cut” micelles respectively. As expected, the micelles possessed a positive surface charge since the protonated pyridine group is present in the micelle corona. The growth curves of the (PS-b-P4VP “crew cut” micelle / PB)_n and (PS-b-P4VP “hairy” micelle / PB)_n films are shown in Fig. 3.7. Both films exhibit relatively linear growth with the “crew cut” micelle films growing at a faster rate. Photographs of the films are shown in Fig. 3.8. The coatings are relatively uniform in both cases; however the films made with the “crew cut” micelles do possess drip and center-line defects sometimes present during the dip coating process. The film thickness and optical properties of films were also determined with spectroscopic

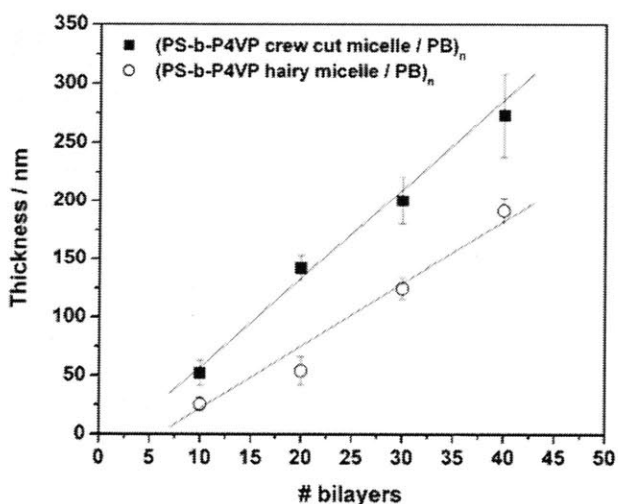


Figure 3.7. Thickness of (PS-b-P4VP “crew cut” micelle / PB)_n and (PS-b-P4VP “hairy” micelle / PB)_n films determined via profilometry. Error bars represent \pm one standard

deviation from at least $n = 5$ spots on each film. The solid lines represent best fits from linear regression. R^2 values greater than 0.99 were achieved for both linear fits.

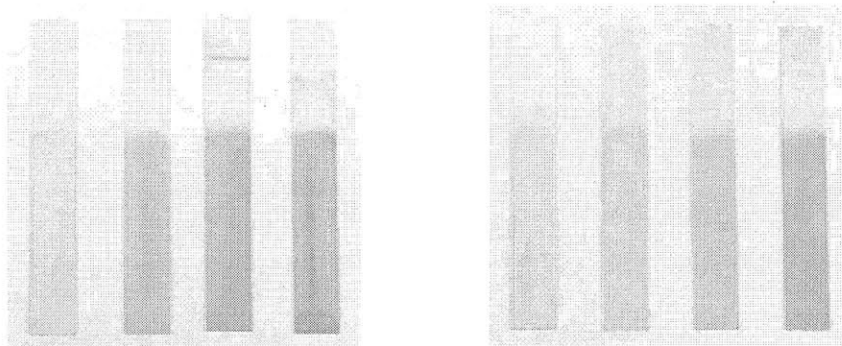


Figure 3.8. Photographs of (PS-b-P4VP “crew cut” micelle / PB)_n (left) and (PS-b-P4VP “hairy” micelle / PB)_n (right) films.

ellipsometry. An optical model for the film that accounts for the strong absorption centered around 700 nm was required. The model, which uses a Gaussian oscillator functional form to model the absorbance, is described in more depth in Appendix 3. The film thicknesses determined from spectroscopic ellipsometry were statistically equivalent ($p = 0.13$ for “crew cut”, 0.34 for “hairy”) to those determined by profilometry for $n = 40$ bilayer films. The refractive indices (in the dry state) at 633 nm were 1.32 for the films made with the “crew cut” micelles and 1.43 for films made with the “hairy micelles”. The fact that the “crew cut” micelle films have a lower refractive index (closer to that of air (1.00)) implies that those films are more porous. This result is in agreement with Cho et al. who also observed greater porosity in films made with “crew cut” versus “hairy” micelles, which they attribute to the lesser ability of the “crew cut” micelles to interpenetrate with adjacent micelles.²⁷ The porosity values for the (PS-b-P4VP micelle /

PB)₄₀ films were calculated using the Lorentz-Lorenz mixing rule (Equation 3.2) as was also used by Cho et al.²⁷ where n_f , n_o , and P are the refractive index of the film, the average refractive index of the film components, and the film porosity, respectively. The refractive index of the PS-b-P4VP was taken to be 1.53²⁷ while the refractive index of the PB was taken to be 1.45, an average of the values reported in the literature (1.42-1.48).⁵⁶⁻⁵⁸ Therefore, the value of n_o was approximated as 1.49. Using all of these values, the porosities of $n = 40$ bilayer “crew cut” and “hairy” micelle-containing films were roughly 29% and 9.4%, respectively. While other authors in the literature have reported micelle/micelle LbL films²⁷ and polymer/micelle LbL films,²⁰ this work is the first report of a micelle/nanoparticle LbL film. Interesting fundamental questions may arise regarding the self-assembly principles between these materials.

$$\frac{n_f^2 - 1}{n_f^2 + 1} = (1 - P) \frac{n_o^2 - 1}{n_o^2 + 1} \quad (3.2)$$

3.3.1.2 Electrochemical Analysis

Cyclic voltammetry was carried out to observe the electrochemical activity of the Prussian Blue within the (PS-b-P4VP micelle / PB)_n films (Fig. 3.9). It is clear that the Prussian Blue within the films is at least partially electrochemically active. Visually, the films underwent full color changes to yellow in the oxidized state and clear in the reduced state. Peak areas and peak heights tended to increase with the deposition of additional layers; however, some deviations from that trend were seen from the $n = 30$ to $n = 40$ films. Those deviations may be explained by either sluggish switching kinetics or incomplete electroactivity of PB nanoparticles in the films. Further fundamental electrochemical experiments were not carried out, since the main concerns here were

whether the oxidation of PB could be used to control film dissolution and release of a small molecule drug.

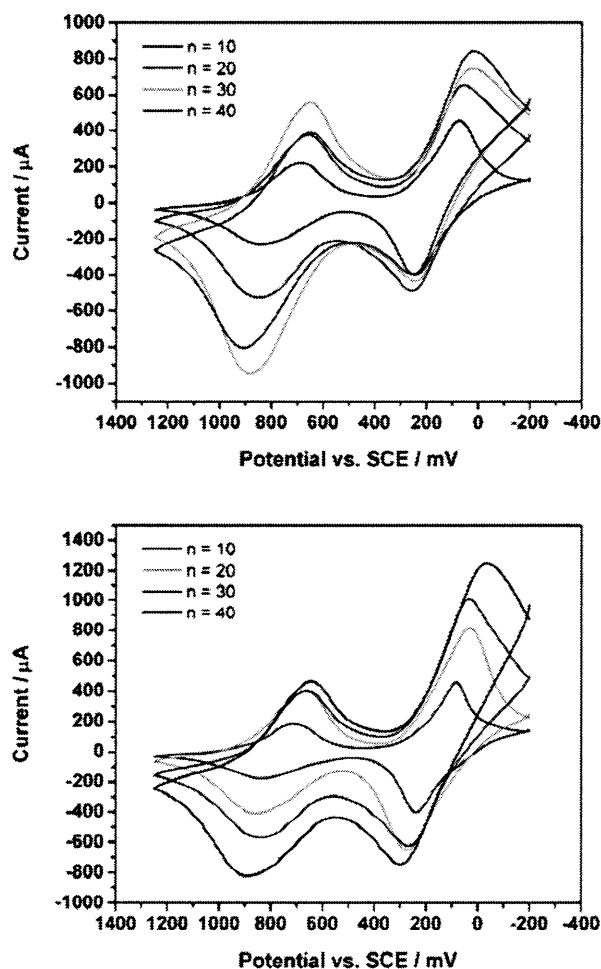


Figure 3.9. Cyclic voltammograms of (PS-b-P4VP "crew cut" micelle / PB)_n (left) and (PS-b-P4VP "hairy" micelle / PB)_n (right) films for n = 10, 20, 30, and 40. The electrolyte was 0.1 M KHPH (pH 4) and the scan rate was 50 mV/s.

3.3.1.3 Drug Loading and Release

The fluorescent, small molecule dye Coumarin 30 was then loaded into the micelles prior to film assembly as described in the Materials and Methods section. Fluorescence spectroscopy was then carried out on films in the dry state on glass

microscope slides to qualitatively assess the dye loading into the films (Fig. 3.10). It is apparent that the “crew cut” micelle-containing film loads substantially more dye than the “hairy” micelle-containing film. Therefore, only “crew cut” micelles were pursued from here on out.

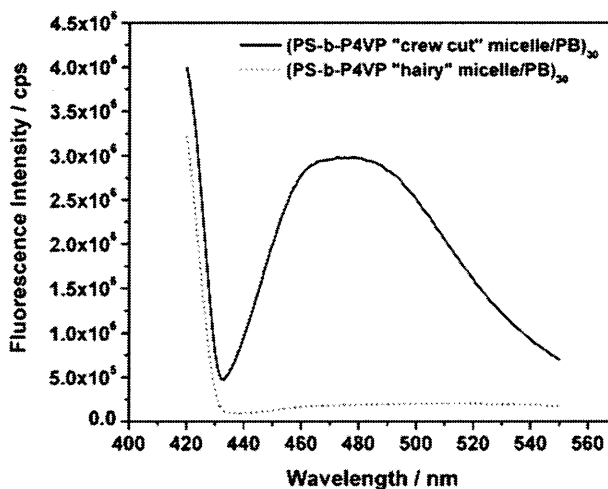


Figure 3.10. Fluorescence spectra of (PS-b-P4VP “crew cut” micelle / PB)₃₀ and (PS-b-P4VP “hairy” micelle / PB)₃₀ films loaded with Coumarin 30 dye. The “crew cut” micelle-containing film loads substantially more dye than the “hairy” micelle-containing film.

The release of the Coumarin 30 from (PS-b-P4VP “crew cut” micelle / PB)₃₀ films was investigated in the absence of an applied potential (i.e., passive release), or at the open circuit potential (OCP), and at an applied potential of +1.25 V (vs. SCE) (i.e., active release) in 10 mM KHPH (pH 4) (Figure 3.11A). We observed that the Coumarin 30 leaks out of the film passively within 30 min when no potential is applied. Application of a potential does not induce any subsequent release of Coumarin 30 from the film. Since the applied voltage does not control the release of the dye, we measured

the thickness of a film simply soaked in the electrolyte solution for 30 min at the OCP compared to a film to which we applied +1.25 V for 30 min. The initial film thickness was 222 ± 15 nm, while the film thicknesses were 205 ± 36 nm and 203 ± 13 nm after soaking at the OCP and at +1.25 V, respectively. Therefore, the films appear to not be completely stable even in the pH 4 solution with low salt concentration (10 mM); further, while the PB in the film is electroactive (Fig. 3.9), the oxidation of PB at +1.25 V does not have any effect on the film thickness. These results are in contrast to the results reported by Delongchamp et al.¹⁴ and Wood et al.⁹ (also see Chapter 2), in which films containing LPEI and PB dissolve only when the PB is oxidized.

A.

B.

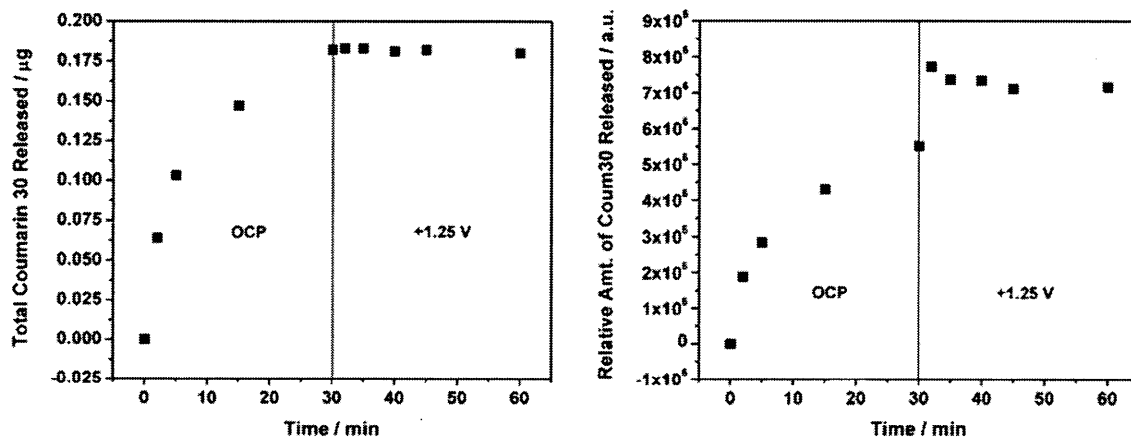


Figure 3.11. Release of Coumarin 30 at the open circuit potential (OCP) and during application of +1.25 V (vs. SCE) in 10 mM KHPH (pH 4) from (A) (PS-b-P4VP “crew cut” micelle / PB)₃₀ and (B) LPEI(PB/LPEI/PB/PS-b-P4VP “crew cut” micelle)₂₀ films loaded with Coumarin 30 dye. In both cases, the Coumarin 30 leaks out of the film passively within the first 30 min. The applied potential of +1.25 V does not release any further dye from the bilayer film, but does release a small amount of additional dye from the tetralyer film.

We hypothesized that switching from a bilayer system (i.e., with micelles and PB only) to a tetralayer system incorporating a polymer may allow for better control over passive drug release and electrodissoolution. Therefore, we assembled an LPEI(PB/LPEI/PB/PS-b-P4VP “crew cut” micelle)₂₀ loaded with Coumarin 30 dye. This film indeed exhibited much better stability when immersed in 10 mM KHPH for 30 min. The initial thickness was 178 ± 11 nm, while the thickness after soaking in the pH 4 solution for 30 min was 179 ± 18 nm. This film architecture also resulted in the ability to induce film dissolution by oxidizing the PB. After 30 min at an applied potential of +1.25 V, the film thickness decreased to 117 ± 7 nm. As can be seen in Fig. 3.11B, however, there is still a substantial amount of passive leakage of the dye out of the film. There is an additional burst of dye released from the film when the potential is applied, indicating that the voltage does have an effect on dye release, however, dye release is not well controlled overall due to the passive diffusion of the dye.

We next hypothesized that switching to a more hydrophobic dye molecule might reduce the level of passive diffusion and allow for better control over dye release profiles. The alternative dyes we chose were 1,4-bis(5-phenyl-2oxazolyl)benzene (POPOP) and 9,10-diphenylanthracene (DPA). While Coumarin 30 has a water solubility of 0.18 mg/mL at pH 4, the water solubilities of POPOP and DPA at pH 4 are 9.5×10^{-5} mg/mL and 6.3×10^{-6} mg/mL, respectively. We assembled separate LPEI(PB/LPEI/PB/PS-b-P4VP “crew cut” micelle)₂₀ films loaded with POPOP or DPA and detected the dye incorporation with fluorescence spectroscopy (Fig. 3.12). As with Coumarin 30, dye release from LPEI(PB/LPEI/PB/PS-b-P4VP “crew cut” micelle)₂₀ films was investigated

in the absence of an applied potential (i.e., at the OCP) and at an applied potential of +1.25 V (vs. SCE) in 10 mM KHPH (pH 4) (Fig. 3.13). We observed that the POPOP leaked out of the films passively and the DPA-containing films did not release any detectable amount of dye into the solution at the OCP or after voltage application. POPOP, despite being significantly less water soluble than Coumarin 30, still diffused passively out of the film. In the case of DPA, it is plausible that too little dye was incorporated into the films initially; alternatively, it is possible that DPA in the film was electrochemically oxidized to a dihydroxy derivative, which is non-fluorescent.⁵⁹ This latter possibility highlights the requirement that only non-electroactive drugs may be explored for release from these coatings.

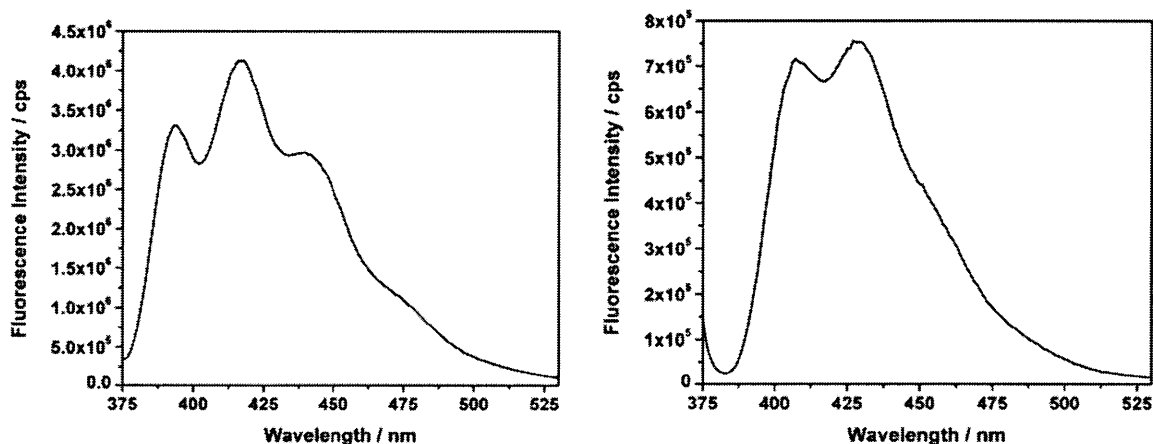


Figure 3.12. Fluorescence spectrum of a LPEI(PB/LPEI/PB/PS-b-P4VP “crew cut” micelle)₂₀ films loaded with POPOP fluorescent dye (left) and DPA fluorescent dye (right).

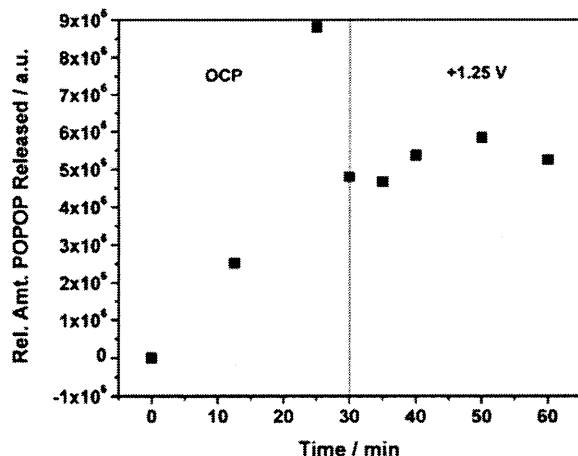


Figure 3.13. Release of POPOP at the open circuit potential (OCP) and during application of +1.25 V (vs. SCE) in 10 mM KHPH (pH 4) from an LPEI(PB/LPEI/PB/PS-b-P4VP “crew cut” micelle)₂₀ films loaded with POPOP dye. The POPOP leaks out of the film passively within the first 30 min. The applied potential of +1.25 V does not release any further significant amount of dye from the film.

3.3.2 Cyclodextrins

To successfully incorporate Chi, PB, and CM β CD into an LbL film, it was necessary to find acceptable pH and ionic strength conditions. In the past, LbL films containing PB were assembled at a pH of 4.^{9,14,60} To assess whether Chi and CM β CD could be layered together at this pH or under different conditions, a number of different conditions were tested. Overall, we found that LPEI(CM β CD/Chi)_n films could not be assembled at pH 4, but could be assembled at pH 5-6 with the growth rate highly dependent upon the salt concentration in the polymer baths (Fig. 3.14). At pH 5.5, the films exhibit linear growth with and without the addition of NaCl to the polymer baths. Without salt, however, the films are ultrathin with a bilayer thickness of only 1-2 nm/bilayer. When 0.5 M NaCl is present in the polymer baths, the films grow with a bilayer thickness in the range of 5.5-6.5 nm/bilayer. At pH 5 (not

shown), films grew at the same rate and exhibited the same trend with salt concentration. At pH 6, the films exhibited non-linear growth for the range of bilayers investigated here; in addition, films made with salt are only marginally thicker than those made without salt. Since LbL films made with Chi are typically assembled at pH 5 and lower⁶¹⁻⁶³ and since the pKa of Chi is roughly 6.2,⁶⁴ it is possible that the decrease in charge density on the Chi may limit its incorporation into LbL films at pH 6. The thickness trends with ionic strength could be rationalized by referring to the reports of Richert et al.⁶³ and Sato et al.³⁹ Richert et al. reported that films comprising chitosan and hyaluronic acid (HA) exhibit faster growth under higher salt conditions (0.15 M NaCl vs. 1×10^{-4} M NaCl). They proposed that, at lower salt conditions, there is a lesser degree of interlayer diffusion of the polyelectrolytes due to the longer persistence length of the polymers. Therefore, the layers build in a thinner, tighter knit fashion, in which deposition of polymer occurs only on the film surface. In addition, they propose that the stronger interactions between the Chi and HA due to a lesser degree of charge screening result in not only polyelectrolyte adsorption, but also stripping of soluble polyelectrolytes from the film to form soluble polyplexes. They observed the stripping behavior with QCM, which revealed a zig-zag type film growth with the number of deposited layers. Sato et al. also observed thicker growth for films comprising polyallylamine hydrochloride (PAH) and sulfated α -cyclodextrin ($s\alpha$ CD) and β -Cyclodextrin ($s\beta$ CD) under elevated salt conditions. Using QCM, they also observed partial stripping of the CDs from the film when the film was immersed in the PAH bath. In addition, they point out that polyelectrolytes adopt a more globular shape under higher salt conditions, and therefore adsorb as thicker layers. Further studies utilizing QCM would be required to elucidate the effect of pH and ionic strength on the growth of the LPEI(CM β CD/Chi)_n investigated here.

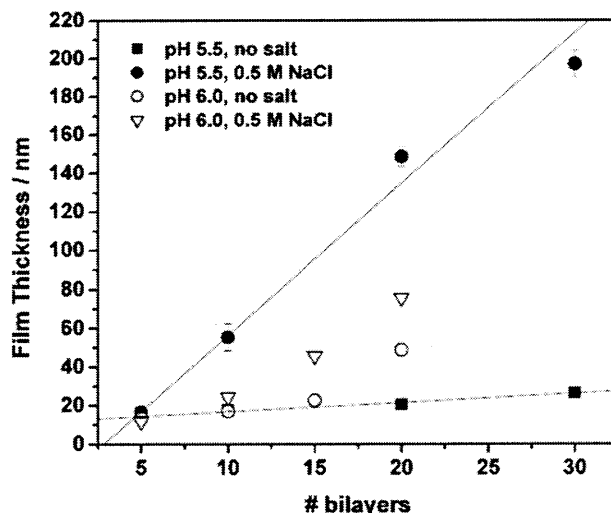


Figure 3.14. Thickness of LPEI(CM β CD/Chi)_n films determined via ellipsometry. Error bars represent \pm one standard deviation from at least $n = 5$ spots on each film. The solid lines represent best fits from linear regression. R^2 values greater than 0.99 were achieved for both linear fits.

The loading of Flurbiprofen, a non-steroidal anti-inflammatory drug (NSAID), into the the LPEI(CM β CD/Chi)₃₀ films assembled at pH 5.0/5.0 was investigated with fluorescence spectroscopy. The drug was pre-complexed with the CD prior to film assembly as described in the Materials and Methods section. Films were assembled on UV-transparent quartz slides for fluorescence measurements. Figure 3.15 below shows the fluorescence spectra of films assembled with no added salt and those with 0.50 M NaCl in both the Chi and CD dipping solutions. The results confirm that Flurbiprofen may be loaded into these films via CD complexation, and that the films assembled with added salt load a significantly greater amount of the drug on account of the increased film thickness.

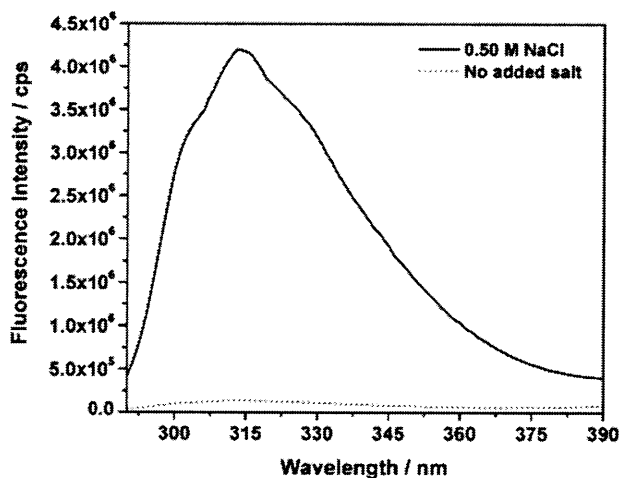


Figure 3.15. Fluorescence spectra of of LPEI(CM β CD/Chi) $_n$ films assembled at pH 5.0/5.0 loaded with Flurbiprofen. The films assembled with 0.50 M NaCl in the polymer dipping baths were thicker and loaded a substantially greater amount of the drug.

Next, Prussian Blue nanoparticles were integrated into the films using a tetralayer architecture: LPEI(PB/Chi/CM β CD/Chi) $_n$. LPEI and PB were deposited at pH 4 with no added salt, while Chi and CM β CD were deposited at pH 5.5 with either no added salt or 0.50 M NaCl in each bath. The thickness of the $n = 20$ tetralayer films initially were 545 ± 8 nm and 372 ± 26 nm with no added salt and with 0.50 M NaCl, respectively. Even though the Chi/CM β CD layers are substantially thicker when salt is present, the tetralayer composite films with PB exhibit a lower film thickness in the presence of salt. After application of +1.25 V (vs. SCE) for 30 min for each film in a 0.10 M KCl electrolyte solution, the film thicknesses were 514 ± 35 nm and 321 ± 21 nm for the films with no added salt and with 0.50 M NaCl respectively. While the film thicknesses decreased slightly, upon application of the voltage, we observed that the films did not change color from blue to yellow as is typically seen with PB-containing films when the PB is oxidized. This result indicates the incomplete electroactivity /

electroaccessibility of the PB in the composite films with Chi and CM β CD. We observed full electroactivity in Chi/PB films (not explicitly shown), which implies that the CM β CD interferes with the redox chemistry of PB in the films. Figure 3.16 shows cyclic voltammograms of LPEI(Chi/PB)₁₀ and LPEI(Chi/PB/Chi/CM β CD)₁₀ films in a 0.1 M KCl electrolyte at a scan rate of 10 mV/s. While the PW/PB and PB/PX redox couples are evident in the LPEI(Chi/PB)₁₀ film, only the PW/PB couple is evident in the LPEI(Chi/PB/Chi/CM β CD)₁₀ film. Apparently, the oxidation of Prussian Blue to the Prussian Yellow oxidation state is stifled by the presence of CM β CD, thus rendering this cyclodextrin system non-promising for electrically triggered drug delivery utilizing PB electrochemical switching.

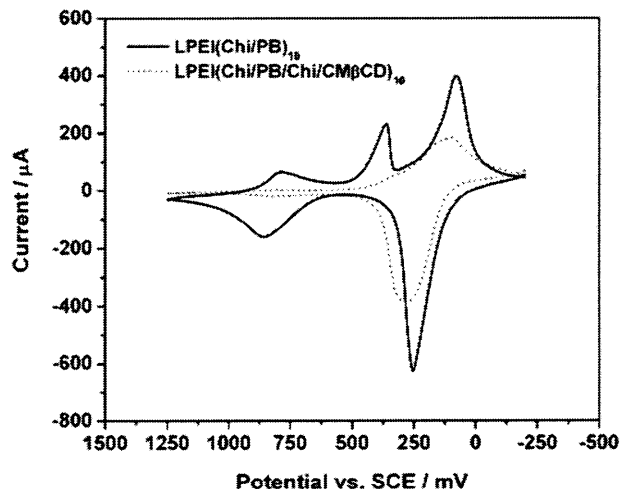


Figure 3.16. Cyclic voltammograms of LPEI(Chi/PB)₁₀ and LPEI(Chi/PB/Chi/CM β CD)₁₀ films in a 0.1 M KCl electrolyte at a scan rate of 10 mV/s. The oxidation of Prussian Blue to the Prussian Yellow oxidation state is apparently stifled by the presence of CM β CD.

3.3.3 Electrostatic Complexation

3.3.3.1 Film Growth and Surface Morphology

The thickness of the $\text{Chi(PB/Chi)}_5(\text{PB/GS})_n$ films was monitored with profilometry (Fig. 3.17). The films were observed to assemble with super-linear growth behavior in contrast to previously reported LbL films containing PB nanoparticles.¹⁴ This growth behavior is common for species that can interdiffuse through the multilayer film instead of depositing only as a single molecular layer on the film surface.⁶⁵ Gentamicin-containing LbL films reported previously by our group also showed super-linear growth behavior.⁴⁵ Indeed, it is not surprising that gentamicin, a small molecule with MW 477 g/mol, can diffuse within the film during assembly. An additional potential source of the super-linear growth behavior is the increased surface roughness of the film,⁶⁶ and thus increased surface area for adsorption with the deposition of additional layers (refer to text below on AFM studies).

An important factor critical to the growth of the films is the use of underlying adhesion or base multilayers. Interestingly, the initial deposition of five (PB/Chi) adhesion layers, while only ~24 nm thick, had a substantial effect on overall film growth (i.e., the thickness per deposited bilayer). As seen in Figure 3.17, Chi(PB/GS)_n films (i.e., without adhesion layers) are ultrathin with a bilayer thickness of less than 1 nm, while $\text{Chi(PB/Chi)}_5(\text{PB/GS})_n$ films grow with bilayer thicknesses ranging from 3.4-5.6 nm. In the absence of the adhesion layers, it is possible that the pentavalent gentamicin is unable to adhere to the substrate in sufficient quantities to reverse the surface charge due to its limited cooperative binding ability compared to a flexible polyelectrolyte. Similarly, the low surface roughness of the substrate without adhesion layers may result in an insufficient number of available adsorption sites. The RMS roughness values, as calculated from AFM height images of films in the dry state (Fig. A2.1 in Appendix 2),

are 2.4 ± 0.2 nm and 4.4 ± 0.4 nm for the bare ITO substrate and the $\text{Chi}(\text{PB}/\text{Chi})_5$ adhesion layers, respectively. Since the difference in surface roughness is not substantial, it seems more likely that the adhesion layers permit interlayer diffusion of gentamicin in sufficient quantities such that it can more easily reverse the surface charge. Since gentamicin and chitosan are both carbohydrates, and thus chemically similar, there is reason to believe that the chitosan-containing adhesion layers could serve as a reservoir for the absorption of gentamicin.

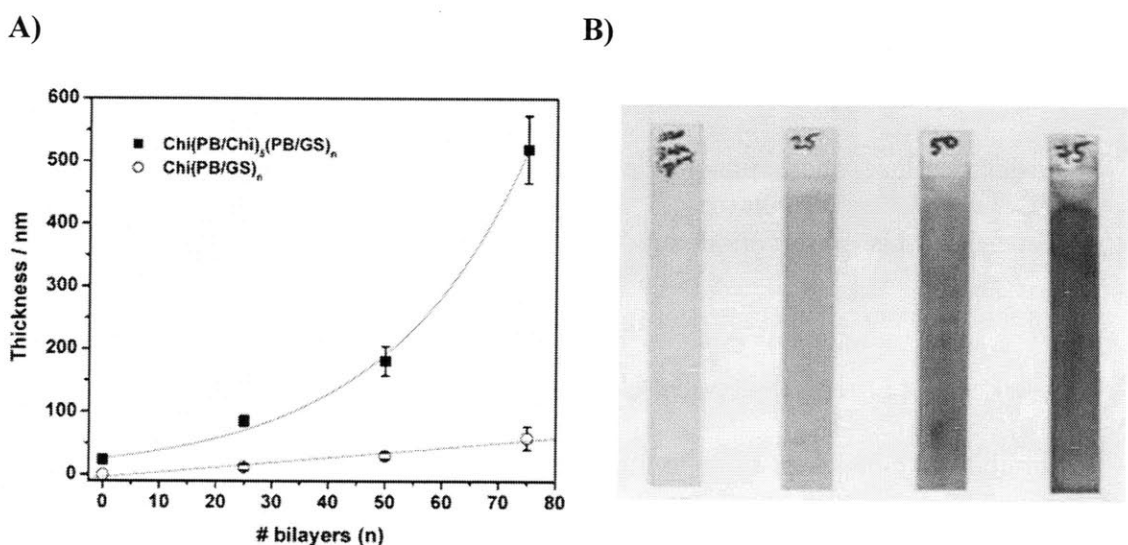


Figure 3.17. A) Growth curve, determined via profilometry, for $\text{Chi}(\text{PB}/\text{Chi})_5(\text{PB}/\text{GS})_n$ and $\text{Chi}(\text{PB}/\text{Chi})_n$ film architectures, revealing accelerated film growth when adhesion layers are deposited. The lines are best fit lines for exponential and linear growth models for films with and without adhesion layers, respectively. Error bars represent \pm one standard deviation in measured thickness values at $n = 5-7$ locations on each film. B) Photographs of $\text{Chi}(\text{PB}/\text{Chi})_5(\text{PB}/\text{GS})_n$ films for $n = 0, 25, 50,$ and 75 .

The surface morphology and roughness of the $\text{Chi}(\text{PB}/\text{Chi})_5(\text{PB}/\text{GS})_n$ films in the dry state were investigated with AFM and optical microscopy (Fig. 3.18). The RMS

roughness of each film surface, as calculated from AFM height images, was 8.9 ± 0.5 nm, 11.2 ± 0.4 nm, and 35.7 ± 1.8 nm for $n = 25$, 50, and 75, respectively. Accordingly, we observed larger features on the film surface for an increasing number of deposited bilayers. Optical microscopy allows visualization of these features for the $n = 75$ film; however, the $n = 25$ and 50 films are featureless when viewed with this microscope due to insufficient resolution. It is likely that these features are regions of clustered Prussian Blue nanoparticles; similar nanoparticle clustering has been observed in other layer-by-layer systems.⁶⁷ Analysis of the AFM height and phase images over the same scan area (Fig. A2.2 in Appendix 2) shows a greater phase angle in the regions containing the clusters. Since phase imaging provides contrast with respect to material mechanical properties, this observation supports the hypothesis that the cluster regions consist primarily of one of the film components, most likely the PB nanoparticles. Besides the presence of clusters, the optical micrograph also shows microscale cracks in the $n = 75$ film that have developed due to internal film stresses during drying.

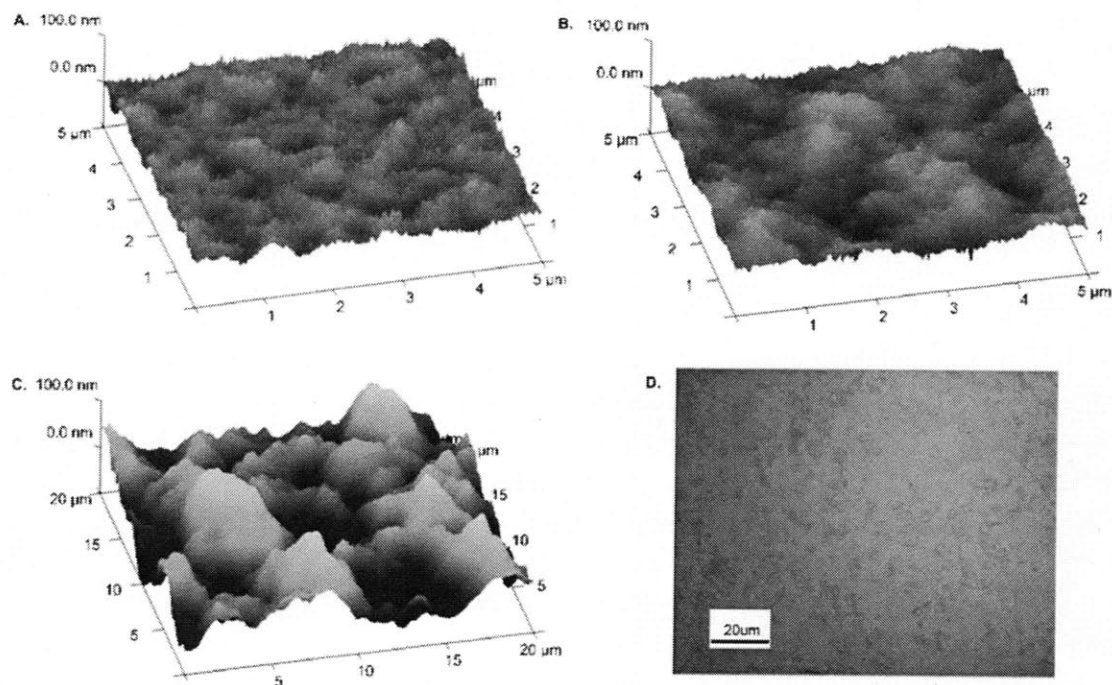


Figure 3.18. Atomic force microscopy 3D height images of A) $n = 25$, B) $n = 50$, and C) $n = 75$ bilayer films and D) an optical micrograph of an $n = 75$ film. Film surface roughness increases and clusters form on the film surface with the deposition of an increasing number of bilayers.

3.3.3.2 Electrochemical Analysis

The electrochemical behavior of $\text{Chi}(\text{PB}/\text{Chi})_5(\text{PB}/\text{GS})_n$ films was investigated with cyclic voltammetry and chronocoulometry. Cyclic voltammetry over the potential range -0.4 V to 1.25 V (vs. Ag/AgCl) in PBS at a scan rate of 50 mV/s shows the full range of Prussian Blue redox states (Fig. 3.19). The fully reduced state is known as Prussian White (PW) ($\text{Fe}^{\text{II}}[\text{Fe}^{\text{II}}(\text{CN})_6]^{2-}$), the mixed valence state is known as Prussian Blue (PB) ($\text{Fe}^{\text{III}}[\text{Fe}^{\text{II}}(\text{CN})_6]^{1-}$), and the fully oxidized state is known as Prussian Yellow or Prussian Brown (PX) ($\text{Fe}^{\text{III}}[\text{Fe}^{\text{III}}(\text{CN})_6]^{0}$) with a partially oxidized Berlin Green state.

The half-peak potentials observed here are $E_{1/2, \text{PW-PB}} = 0.018 \text{ V}$ and $E_{1/2, \text{PB-PX}} = 0.81 \text{ V}$ both versus a Ag/AgCl (3M KCl) reference electrode. These values are shifted to slightly lower values than those reported for inorganic PB films⁶⁸ as well as other PB-containing LbL films.¹⁴ As noted previously by our group,¹⁴ this observation is consistent with the fact that a multivalent counterion in place of potassium, in this case gentamicin, is balancing the charge on the PB exterior sites; similar results have been observed elsewhere.⁶⁹ Upon multiple CV scans over the entire voltage range, the peak heights (and peak areas) continually decrease indicating a loss of Prussian Blue from the film (Fig. 3.19). When switching between the PB and PW states only, the voltammograms for multiple scans overlap exactly (data not shown) indicating no loss of material. Thus, as reported previously by our group,^{9,14} switching to the fully oxidized PX state leads to dissolution of the film. Refer to Fig. A2.3-A2.5 in Appendix 2 for additional details on electrochemical switching kinetics and confirmation that all of the PB nanoparticles in the film are electrochemically accessible.

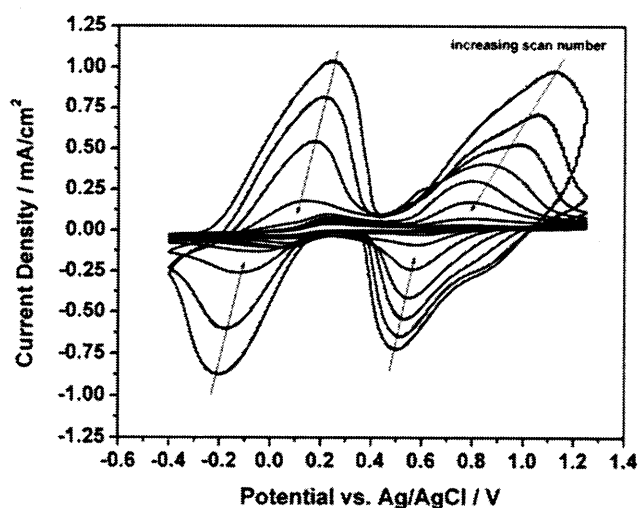


Figure 3.19. Cyclic voltammograms of a $\text{Chi}(\text{PB}/\text{Chi})_5(\text{PB}/\text{GS})_{25}$ film subjected to multiple cycles at a scan rate of 50 mV/s in a PBS, pH 7.4 electrolyte. A decrease in

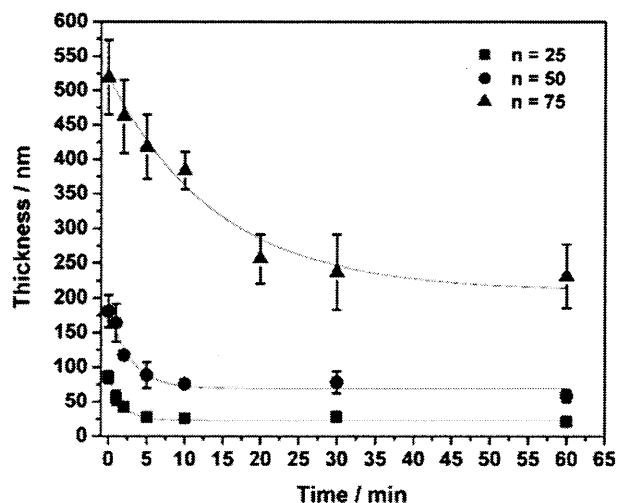
peak height (and peak area) with subsequent scans reveals a loss of the electroactive Prussian Blue from the film.

3.3.3.3 Electrodesolution and Drug Release

The electrochemically triggered dissolution of $\text{Chi(PB/Chi)}_5(\text{PB/GS})_n$ films was investigated by applying an electric potential for different periods of time in PBS buffer and then measuring the resulting film thickness with profilometry (Fig. 3.20). When a potential sufficient to oxidize the PB nanoparticles is applied to the film-coated electrode, electrons flow through the percolative network of nanoparticles in the film as they are removed from the Fe^{II} atoms and transferred to the electrode and then through the external circuit. The result of this process is a change in the net charge of the particles from negative to neutral. The ionic crosslinks binding the PB to the positively charged gentamicin are thus broken, and there is now an excess of positive charge present in the film. To maintain electroneutrality in the film, anions from solution and water (from both solvation of the anions and electroosmotic flux) will enter the film and solubilize the formerly bound gentamicin. The film will then dissolve as gentamicin is solubilized and diffuses into the solution, along with some of the neutralized PB nanoparticles. Application of +1.25 V (vs. Ag/AgCl) induces a clear loss of material from the film. Soaking the films in the PBS buffer for 1 hr with no applied potential, however, does result in some loss of material from the film (an $n = 50$ film decreased in thickness by roughly 9%). Refer to the text below for further discussion on passive dissolution and drug release. During application of a potential, no delamination of the film is observed at the electrode and no precipitates are observed in the release bath; instead, the components of the film are released into the PBS as soluble molecules and/or complexes. As

expected, the thicker films deconstruct more slowly than the thinner films due to the increased diffusion time required for both percolation of charge/current through the film and access of the film components to the surrounding aqueous solution to achieve a given degree of dissolution. The time to 50% dissolution (considering only the dissolvable portion of the film within 60 min) is roughly 1 min 11 sec, 1 min 57 sec, and 10 min 40 sec for the 25, 50, and 75 bilayer films, respectively; the corresponding film thicknesses of these films were 85.3 ± 9.0 nm, 181.0 ± 23.5 nm, and 519.1 ± 54.0 nm. Interestingly, the films are not completely removed from the substrate; instead the thicknesses plateau to approximately 25-45% of the initial film thicknesses. Likely, a portion of the neutral Prussian Yellow nanoparticles, which would not be expected to be readily solubilized or stable as a suspension in the aqueous electrolyte, aggregates irreversibly on the substrate surface along with an amount of trapped drug. The amount of drug released from an $n = 75$ film at +1.25 V for one hour, as discussed below, was compared to the total amount of drug in the film by dissolving an identical film in 0.01 M NaOH, which rapidly dissolves the Prussian Blue nanoparticles to their constituent iron salts. It was found that approximately 88% of the total drug in the film is released by application of the voltage. Therefore, the material remaining on the substrate must consist primarily of oxidized PB, chitosan, and roughly 12% of the initial amount of encapsulated drug.

A)



B)

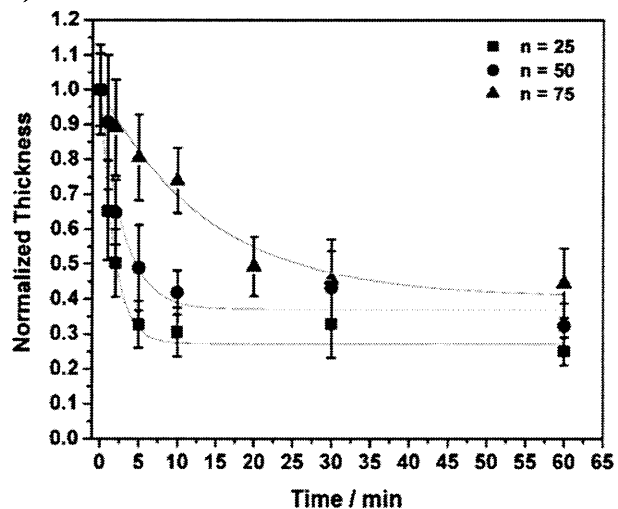


Figure 3.20. A) Absolute and B) normalized thickness of $\text{Chi}(\text{PB}/\text{Chi})_5(\text{PB}/\text{GS})_n$ films over time at an applied potential of +1.25 V vs. Ag/AgCl in a PBS, pH 7.4 electrolyte. The thickest films dissolve more slowly, and all film thicknesses plateau to approximately 25-45% of initial thickness. The lines represent the best fit to a first order exponential decay model. Error bars represent \pm one standard deviation in measured thickness values at $n = 5$ -10 locations on each film.

The total drug loading into the film and drug release kinetics were studied as a function of the number of deposited layers. Films with architecture $\text{Chi}(\text{PB}/\text{Chi})_5(\text{PB}/^3\text{H-GS})_n$ were assembled with radioactively labeled drug ($^3\text{H-GS}$) (see Materials & Methods section), and the amount of drug released in PBS buffer over a duration of 60 min was measured via scintillation counting. Fig. 3.21A shows the release of gentamicin from $n = 25, 50,$ and 75 bilayer films at a constant applied voltage of $+1.25$ V (vs. Ag/AgCl) over 60 minutes, demonstrating that the dosage size can be precisely controlled simply by adjusting the number of deposited layers. At the open circuit potential (OCP), which was roughly $+0.25$ V, a non-negligible amount of drug is released, equating to roughly 10-15% of the total releasable amount of drug in 60 min. Conceivably, this passive drug release is a combination of drug molecules that are weakly bound to the film plus drug molecules that are released from the partial dissolution of the film as mentioned above. While the passive release appears to plateau, drug release studies over a much longer duration reveal that approximately 67% of the total releasable drug in the film (from an $n = 75$ film) is released after 1 month in PBS. Thickness measurements confirm (data not shown) that the film thickness decreases substantially over this time frame as well. We suspect that the chemical instability of the Prussian Blue at high pH⁷⁰ is responsible for the dissolution of these films in the absence of an applied potential. Nonetheless, we are able to precisely control drug release actively in short to moderate timeframes relevant to a range of applications by applying an electric potential.

The active drug release kinetics were well fit by an empirical pseudo-second order model of the form shown in Eqn. 3.3, which was adapted from Ho et al. (Fig. 3.21B).⁷¹ As was also done by Ho et al., we attempted to fit the experimental data to a pseudo-first

order model and a diffusion-based model; however, these fits were poor (not shown). See Appendix 2 for further discussion.

$$\frac{dM(t)}{dt} = k(M_{\infty} - M(t))^2 \quad (3.3)$$

In the pseudo-second order model that we used, $M(t)$ is the total cumulative mass of gentamicin released up to time, t , M_{∞} is the total mass of all releasable drug, and k is a second order rate constant. After integrating from time 0 to time t , Eqn. 3.4 results. Therefore, a plot of $t/M(t)$ versus t should be linear

$$\frac{t}{M(t)} = \frac{1}{kM_{\infty}^2} + \frac{1}{M_{\infty}}t \quad (3.4)$$

with slope $1/M_{\infty}$ and intercept $1/(kM_{\infty}^2)$. The second order rate constants for drug release rate (normalized to the total amount of drug released from each film) were determined to be $0.77 \pm 0.18 \text{ min}^{-1}$, $0.70 \pm 0.12 \text{ min}^{-1}$, and $0.58 \pm 0.05 \text{ min}^{-1}$, for the $n = 25, 50$, and 75 films, respectively. While the number of deposited bilayers has a significant impact on the kinetics of film dissolution versus time at $+1.25 \text{ V}$ (Fig. 3.20), the corresponding time scales of drug release (Fig. 3.21) are much more comparable. Specifically, the time to 50% drug release is roughly 57 sec, 1 min 17 sec, and 1 min 34 sec for the $n = 25, 50$, and 75 films, respectively. The time scales of drug release and film erosion match up relatively well for the $n = 25$ (1 min 11 sec for erosion, 57 sec for drug release) and $n = 50$ films (1 min 57 sec for erosion, 1 min 17 sec for drug release); however, there is a greater discrepancy between those values for the $n = 75$ film (10 min 40 sec for erosion, 1 min 34 sec for drug release). We hypothesize that the difference between the rate of thickness decrease and drug release is indicative of a surface erosion mechanism in which a non-uniform distribution of drug exists within the films (i.e., a higher concentration of

drug toward the top of the film, which is expected for the diffusing component in exponentially growing layer-by-layer systems). A model for exponentially growing LbL films was proposed by Lavallo et al.⁷² and Picart et al.,⁶⁵ in which the diffusing component diffuses throughout the entire film during deposition of that component; then when the film is exposed to the non-diffusing polyelectrolyte solution, the diffusing component will migrate to the outermost regions of the film for charge compensation with the newly deposited material. Thus, thicker films provide a larger reservoir for the diffusing component, allowing for an exponential increase in film growth versus the number of deposited layers. That hypothesis justifies how films could develop a non-uniform distribution of components. Relatedly, our group previously compared the controlled release of heparin, an interdiffusing polyanion, with dextran sulfate, a non-diffusing polyanion, from hydrolytically degradable thin films.^{73,74} For these linearly surface eroding systems, it was found that the release rate of heparin was faster than the rate of film erosion, suggesting that an outer zone of the film is enriched in the diffusing species.^{73,74} AFM surface studies on $\text{Chi}(\text{PB}/\text{Chi})_5(\text{PB}/\text{GS})_n$ films electrochemically dissolved at +1.25 V over time reveal that the surface roughness remains the same or even decreases (Fig. A2.6 in Appendix 2), as opposed to the formation of pits and furrows within the film that would be expected for bulk erosion. This observation suggests that the films do indeed dissolve by a surface erosion mechanism.^{75,76}

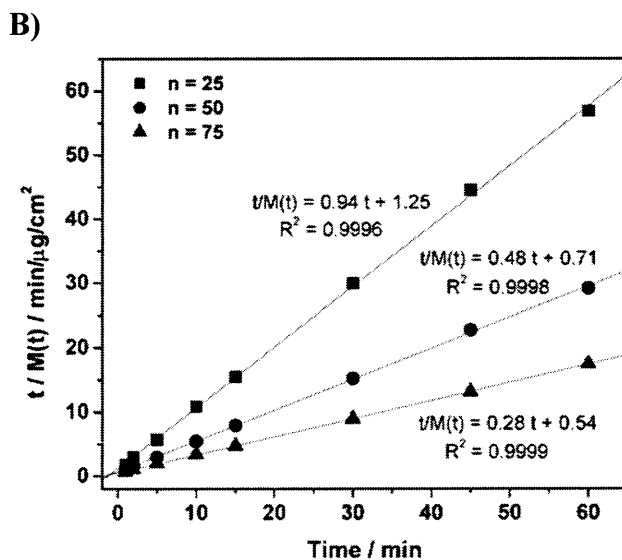
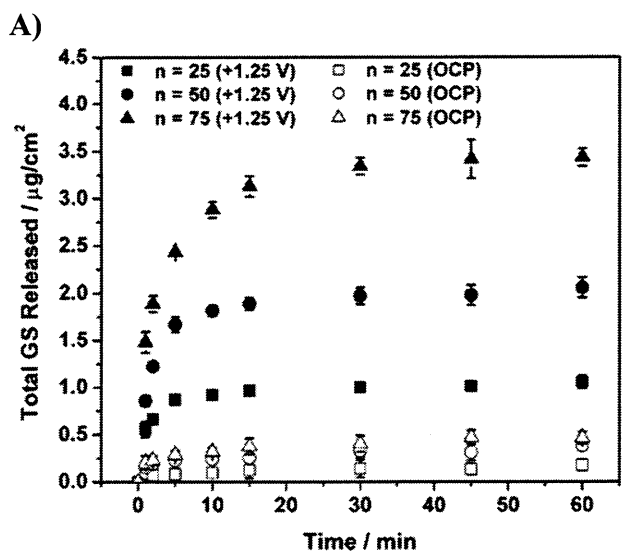
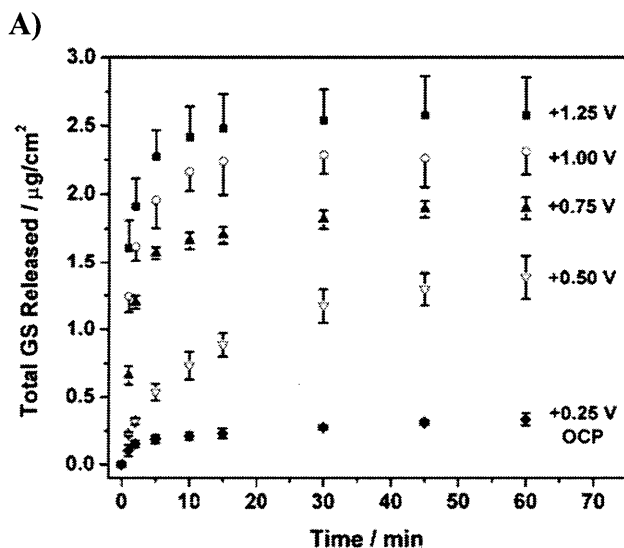


Figure 3.21. (A) Drug release profiles from $\text{Chi}(\text{PB}/\text{Chi})_5(\text{PB}/\text{GS})_n$ films at an applied potential of +1.25 V vs. Ag/AgCl and at the open circuit potential (OCP). The total amount of released drug, or the drug dosage, can be set by tuning the number of deposited layers, n . Error bars represent \pm one standard deviation in measured values from $n = 3$ films. (B) Linear regression best fits for a pseudo-second order drug release kinetics model for $n = 25, 50,$ and 75 films.

Next, the drug release behavior from films at different applied voltages was studied to examine the impact of voltage on the dose (Fig. 3.22) (Table A2.2 in Appendix 2). In the absence of an applied potential (at the open circuit potential, +0.25 V), approximately 10-15% of the drug is released from the film over 1 hour, which was the standard drug release duration used in this study. Upon application of +1.25 V, there is a marked increase in the release rate of the drug as the Prussian Blue is fully oxidized to its neutral state. Application of +1.00 V is also sufficient to fully oxidize PB since this voltage is higher than the measured half-peak potential of +0.81 V. The amount of drug released at +1.25 V after 60 minutes appears greater than that released at +1.00 V; however, the means are not statistically different ($p = 0.15$). At +1.25 V, hydrolysis of water occurs at the electrode interface as evidenced by the fact that the charge removed from the film does not plateau with time (see Fig. A.2.5 in Appendix 2). At +1.00 V, however, the charge does plateau, indicating little to no hydrolysis is occurring; this result further confirms that oxidation of Prussian Blue, and not hydrolysis of water, is the primary mechanism responsible for film dissolution. The application of +0.75 V or +0.50 V also destabilizes the film and results in release of drug. These potentials are below the half-peak potential exhibited by the films, such that not all of the PB in the film will be oxidized and less of the drug will be released. Given the extremely broad peaks in the CV (Fig. 3.19), we hypothesize that non-equivalent electrochemical sites exist within the film due to differences in ionic binding or complexation within the matrix, which are more easily oxidized at these lower potentials, resulting in only partial destabilization of the film. We also observe that the kinetics of charge removal from the

film, measured via chronocoulometry, match up well with the kinetics of drug release at +0.50 V to +1.00 V (see Fig. A2.7 in Appendix 2).

Electrochemically reducing the PB in the film, on reversal of the current, partially at 0 V or fully at -0.25 V, results in the release of a statistically greater amount of drug than at the open circuit potential. As shown in a previous publication by our group, reducing PB in a polymer/nanoparticle LbL film doubles the charge on the PB surface and interior, resulting in film swelling.⁶⁰ It is possible that the charge imbalance created in the film upon reduction of PB induces partial release of the encapsulated drug. Alternatively, it is known that PB in its reduced state can electrocatalyze the reduction of dissolved oxygen,⁷⁷ which can increase the local pH environment. Since PB becomes chemically unstable at elevated pH levels,⁷⁰ partial dissolution of the film may also be occurring through this mechanism. Further studies on the mechanism of drug release upon electrochemical reduction of PB are beyond the scope of this work.



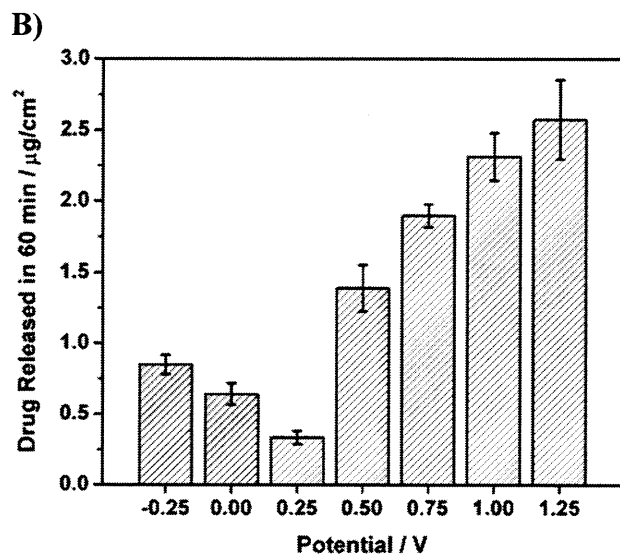


Figure 3.22. A) Total amount of gentamicin released from a $\text{Chi}(\text{PB}/\text{Chi})_5(\text{PB}/\text{GS})_{50}$ film over time at different applied potentials. B) Total amount of gentamicin released from a $\text{Chi}(\text{PB}/\text{Chi})_5(\text{PB}/\text{GS})_{50}$ film in 1 hr at different applied potentials. The smallest amount of drug is released at the open circuit potential of +0.25 V, while increasing amounts of drug are released at both anodic and cathodic potentials, with the greatest amount released during oxidation of the PB. Error bars represent \pm one standard deviation in measured values from $n = 3$ films. All means are statistically different from each other with $p < 0.05$ except for those at +1.00 and +1.25 V, for which $p = 0.15$.

Besides application of a constant potential, the drug release behavior under the influence of short electric potential pulses was investigated. While the results discussed above involved application of a constant potential for one hour, shorter pulse lengths at +1.25 V allow release of smaller doses of drug (Table 3.1). The fact that significant amounts of drug can be released with short pulses is important for device applications because shorter pulse lengths also require less power. Further, compared to the previously reported electrochemically controlled release of a model polymeric species

(dextran sulfate) by Prussian Blue switching,⁹ the drug in the films reported here is released more rapidly at the same applied voltage. We attribute this phenomenon to two possible factors: first, gentamicin is a small molecule with an expected higher diffusivity compared to a polymer; second, there is evidence that the top portion of the films is enriched in gentamicin due to its interdiffusing nature, whereas dextran sulfate is a non-diffusing species in LbL systems. In addition to applying a single short pulse, application of multiple short pulses of 2 seconds each allows the release of gentamicin to be turned on and off on demand for a pulsatile drug release profile (Fig. 3.23). The fact that the application of +1.25 V for only 2 seconds releases some drug, but does not permanently destabilize the film also suggests a surface erosion mechanism; bulk erosion typically involves pitting and roughening of the surface,^{75,78} which would likely lead to an irreversible and rapid increase in the release rate of drug.

Table 3.1. The fraction of total gentamicin released from Chi(PB/Chi)₅(PB/GS)₅₀ films with different pulse lengths at +1.25 V vs. Ag/AgCl. The pulse length may be used to control the total amount of released drug. The standard deviations were determined from n = 3 films.

Pulse length at +1.25 V	Normalized Fraction of GS Released in 30 min¹
0 sec	0.18 ± 0.02
2 sec	0.50 ± 0.04
5 sec	0.58 ± 0.11
30 sec	0.78 ± 0.03

¹Drug release is normalized to the total amount of GS released in 30 min at a constant applied potential of +1.25 V.

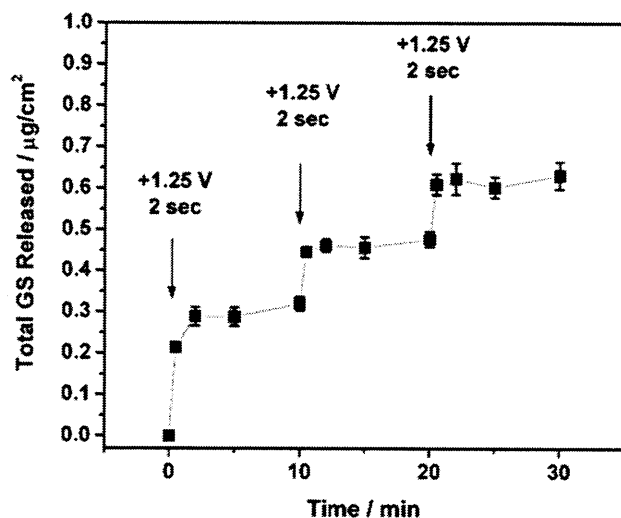


Figure 3.23. Drug release profile from a $\text{Chi}(\text{PB}/\text{Chi})_5(\text{PB}/\text{GS})_{75}$ film with 2 sec pulses of +1.25 V to turn drug release ‘on’, followed by 30 sec pulses at +0.25 V to turn drug release ‘off’. The films are sufficiently stable to allow for on/off, or pulsatile, drug release controlled by the applied potential. Error bars represent \pm one standard deviation in measured values from $n = 3$ films.

3.3.3.4 Efficacy of Released Drug

The *in vitro* efficacy of the gentamicin released from a $\text{Chi}(\text{PB}/\text{Chi})_5(\text{PB}/\text{GS})_{75}$ films against *S. aureus* bacteria was assessed using a microdilution assay. A potential of +1.25 V (vs. Ag/AgCl) was applied to a film in 5 mL of PBS, resulting in a concentration of approximately 4.5 µg/mL gentamicin. Serial microdilutions were made in a 96 well plate (see Methods) and cultured with *S. aureus* at a concentration of 10^5 CFU/mL for 16 h. Normalized bacterial cell density was calculated as $(\text{OD}_{600,\text{sample}} - \text{OD}_{600,\text{negative control}}) / (\text{OD}_{600,\text{positive control}} - \text{OD}_{600,\text{negative control}})$. The minimum inhibitory concentration (MIC) exhibited by the gentamicin released from a $\text{Chi}(\text{PB}/\text{Chi})_5(\text{PB}/\text{GS})_{75}$ film was found to be in the range 0.25-0.50 µg/mL (Fig. 3.24). This value agrees well with the reported literature value of 0.25 µg/mL for the MIC of gentamicin against the same strain of *S.*

aureus.⁷⁹ Thus, it is apparent that the gentamicin released from Chi(PB/Chi)₅(PB/GS)₇₅ films retains a comparable level of bactericidal activity compared to unmodified, commercial gentamicin. While application of an anodic potential can reportedly oxidize gentamicin in the presence of a metal electrocatalyst at very basic pH levels,⁸⁰ there is no evidence that this process occurs in the system reported here. Further, while it is known that gentamicin can form complexes with ferric and ferrous ions,⁸¹ the existence of any such complexes and/or gentamicin-Prussian Blue complexes in the elution medium from the films reported here does not significantly affect the bactericidal activity of the drug.

Evaluation of the *in vivo* efficacy of gentamicin released from Chi(PB/Chi)₅(PB/GS)₇₅ films is beyond the scope of this study, but we can qualitatively assess whether the amount of drug released from our film would be sufficient to prevent or treat an infection based on studies from the literature. In a study by Darouiche et al., the authors simulated introduction of bacteria into a wound site during surgery by inoculating titanium alloy pins with 500 CFU of *S. aureus* (giving a maximum concentration of 2×10^4 CFU/mL at the wound site) and implanting them into rabbits.⁸² They demonstrated that antimicrobial-coated implants had a significantly lower rate of colonization and thus were able to prevent infection. In a separate study by Alvarez et al., the authors established a bone infection in rabbits by introducing *S. aureus* bacteria into a drilled site in the femur at a concentration on the order of 10^8 CFU/mL.⁸³ After two weeks, the affected areas were cleaned, resulting in a bacteria concentration on the order of 10^4 CFU/mL, after which antibiotic-containing implants were inserted into the drill sites. They demonstrated that the implants were able to eliminate the bone infection within 3-4 weeks. Our results described above show that the amount of gentamicin

released from a 75 bilayer film is sufficient to kill *S. aureus* bacteria at a concentration of 10^5 CFU/mL within 16 hr, an order of magnitude greater concentration than that present in the animal studies mentioned above. While the exact area and thickness of our films that would be used in an implant are not known, nor is the extent of dilution of the drug in the wound site over time, the results of our *in vitro* assay show that our films can release gentamicin in amounts sufficient to prevent and treat *S. aureus* infections.

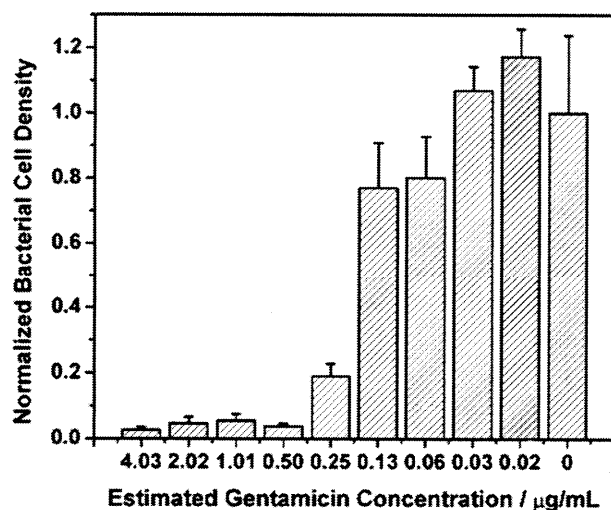


Figure 3.24. Results of a microdilution assay of gentamicin released from a Chi(PB/Chi)₅(PB/GS)₇₅ film against *S. aureus* bacteria. The MIC of the drug released from the film corresponds well with that of the free drug. Error bars represent \pm one standard deviation in measured values from $n = 3$ samples.

3.4 Conclusions

3.4.1 Micelles

Here we have reported the fabrication and characterization of LbL thin films containing PS-b-P4VP micelles and PB nanoparticles. This work is the first report of LbL films containing solely micelles and nanoparticles, however, the films are more stable when layers of

a linear polyelectrolyte are interspersed in the film. A variety of small, hydrophobic dyes were successfully loaded into the micelle cores and subsequently into the films as demonstrated by fluorescence spectroscopy; however, the release of the dyes from the films was not well-controlled by an electric potential. Instead, all of the investigated dyes and film architectures exhibited passive leakage / diffusion of the dye out of the films. Future work could explore different methods of better retaining the dyes in the films such that an external stimulus could be used to control the release. One strategy could be to select micelles with cores that interact more specifically with the dye. Another more general strategy, which has been reported by Taton and co-workers to stabilize hybrid micelles, could be to crosslink the corona of the micelles to decrease the diffusivity of the small molecule dye.⁸⁴⁻⁸⁷ This technique, however, may significantly reduce the charge density on the micelle corona, thereby inhibiting LbL assembly. A related alternative strategy could be to assemble micelles with triblock copolymers and crosslink the middle block to provide a dense crosslinked annulus while maintaining a core to sequester the drugs and a charged corona for electrostatic-based assembly.

3.4.2 Cyclodextrins

In addition to charged micelles, charged cyclodextrins were explored as “carrier” species for the incorporation of small hydrophobic drugs into LbL films and their subsequent electrochemically triggered release. In this thesis I report the fabrication and characterization of LbL thin films containing Chi, CM β CD, and PB nanoparticles. The pH and ionic strength of the polymer baths were varied to optimize film growth, and the incorporation of the drug Flurbiprofen into the film was confirmed with fluorescence spectroscopy. Despite the

successful film growth and drug incorporation, for each set of parameters investigated, the presence of the CM β CD inhibited the electroactivity of the PB and the films were only minimally electrically degradable. Future work could explore alternative charged cyclodextrins or other charge-shifting electroactive materials instead of PB.

3.4.3 Electrostatic Complexation

In this chapter, we have reported the fabrication and characterization of a nanoscale thin film that can release precise quantities of a small molecule drug in response to an applied electric potential. The films are fabricated by LbL assembly on the basis of electrostatic attraction between Prussian Blue nanoparticles and the small molecule antibiotic, gentamicin. Application of a voltage greater than *ca.* +0.50 V (vs. Ag/AgCl) destabilizes the film causing simultaneous release of the drug. We can control the drug loading into the film by tuning the number of deposited layers, and we can control the dose size and drug release kinetics by applying different electric potential profiles. While slow release of drug does occur from the films in the absence of applied potentials, likely due to the inherent instability of PB at alkaline pH,⁷⁰ as reported by Ricci et al., many authors have developed PB-based biosensors for short-term use under physiological conditions, while others have been able to improve the pH stability of PB through various means.⁷⁰ Therefore, the system reported here could potentially be engineered for specific shorter-term medical applications, and/or different methods could be explored to enhance the pH-stability of the films.

In previous work, we controlled the release of a model polymeric species (dextran sulfate) from an LbL film with an applied electric potential.⁹ Here we have improved upon that system by including an active therapeutic molecule and showing that the drug maintains its

efficacy *in vitro*. Furthermore, the therapeutic is a small molecule drug, a class of materials that is difficult to incorporate into LbL films. In fact, this work is the first report of an LbL film comprised primarily of nanoparticles and small molecules, which could lead to interesting fundamental studies on the self-assembly principles of these materials. Since LbL assembly is such a simple and versatile process and can be used to coat substrates of any size or shape and can incorporate many different active pharmaceutical compounds, we believe that the system reported here is promising for controlling release autonomously or remotely in implantable or transdermal controlled drug release devices.

3.5 References

1. Lynn, D. M. Layers of Opportunity: Nanostructured Polymer Assemblies for the Delivery of Macromolecular Therapeutics. *Soft Matter* **2006**, *2*, 269-273.
2. Lynn, D. M. Peeling Back the Layers: Controlled Erosion and Triggered Disassembly of Multilayered Polyelectrolyte Thin Films. *Adv Mater* **2007**, *19*, 4118-4130.
3. Zelikin, A. N. Drug Releasing Polymer Thin Films: New Era of Surface-Mediated Drug Delivery. *Acs Nano* **2010**, *4*, 2494-2509.
4. Boulmedais, F.; Tang, C. S.; Keller, B.; Voros, J. Controlled Electrodisolution of Polyelectrolyte Multilayers: A Platform Technology Towards the Surface-Initiated Delivery of Drugs. *Adv. Funct. Mater.* **2006**, *16*, 63-70.
5. Dieguez, L.; Darwish, N.; Graf, N.; Voros, J.; Zambelli, T. Electrochemical Tuning of the Stability of PLL/DNA Multilayers. *Soft Matter* **2009**, *5*, 2415-2421.
6. Recksiedler, C. L.; Deore, B. A.; Freund, M. S. A Novel Layer-by-Layer Approach for the Fabrication of Conducting Polymer/RNA Multilayer Films for Controlled Release. *Langmuir* **2006**, *22*, 2811-2815.
7. Sato, K.; Kodama, D.; Naka, Y.; Anzai, J. Electrochemically Induced Disintegration of Layer-by-Layer-Assembled Thin Films Composed of 2-Iminobiotin-Labeled Poly(Ethyleneimine) and Avidin. *Biomacromolecules* **2006**, *7*, 3302-3305.
8. Wang, F.; Li, D.; Li, G. P.; Liu, X. Q.; Dong, S. J. Electrodisolution of Inorganic Ions/DNA Multilayer Film for Tunable DNA Release. *Biomacromolecules* **2008**, *9*, 2645-2652.
9. Wood, K. C.; Zacharia, N. S.; Schmidt, D. J.; Wrightman, S. N.; Andaya, B. J.; Hammond, P. T. Electroactive Controlled Release Thin Films. *P Natl Acad Sci USA* **2008**, *105*, 2280-2285.
10. Newman, D. J.; Cragg, G. M.; Snader, K. M. Natural Products as Sources of New Drugs over the Period 1981-2002. *J. Nat. Prod.* **2003**, *66*, 1022-1037.

11. Kim, B. S.; Lee, H.; Min, Y. H.; Poon, Z.; Hammond, P. T. Hydrogen-Bonded Multilayer of pH-Responsive Polymeric Micelles with Tannic Acid for Surface Drug Delivery. *Chem. Commun. (Cambridge, U. K.)* **2009**, 4194-4196.
12. Thierry, B.; Kujawa, P.; Tkaczyk, C.; Winnik, F. M.; Bilodeau, L.; Tabrizian, M. Delivery Platform for Hydrophobic Drugs: Prodrug Approach Combined with Self-Assembled Multilayers. *J. Am. Chem. Soc.* **2005**, *127*, 1626-1627.
13. Berg, M. C.; Zhai, L.; Cohen, R. E.; Rubner, M. F. Controlled Drug Release from Porous Polyelectrolyte Multilayers. *Biomacromolecules* **2006**, *7*, 357-364.
14. DeLongchamp, D. M.; Hammond, P. T. High-Contrast Electrochromism and Controllable Dissolution of Assembled Prussian Blue/Polymer Nanocomposites. *Adv. Funct. Mater.* **2004**, *14*, 224-232.
15. Croy, S. R.; Kwon, G. S. Polymeric Micelles for Drug Delivery. *Curr Pharm Design* **2006**, *12*, 4669-4684.
16. Gaucher, G. Block Copolymer Micelles: Preparation, Characterization and Application in Drug Delivery. *J Control Release* **2005**, *109*, 169-188.
17. Torchilin, V. P. Micellar Nanocarriers: Pharmaceutical Perspectives. *Pharm Res* **2007**, *24*, 1-16.
18. Kim, B. S.; Park, S. W.; Hammond, P. T. Hydrogen-Bonding Layer-by-Layer Assembled Biodegradable Polymeric Micelles as Drug Delivery Vehicles from Surfaces. *Acs Nano* **2008**, *2*, 386-392.
19. Nguyen, P. M.; Zacharia, N. S.; Verploegen, E.; Hammond, P. T. Extended Release Antibacterial Layer-by-Layer Films Incorporating Linear-Dendritic Block Copolymer Micelles. *Chem Mater* **2007**, *19*, 5524-5530.
20. Ma, N.; Zhang, H. Y.; Song, B.; Wang, Z. Q.; Zhang, X. Polymer Micelles as Building Blocks for Layer-by-Layer Assembly: An Approach for Incorporation and Controlled Release of Water-Insoluble Dyes. *Chem Mater* **2005**, *17*, 5065-5069.
21. Addison, T.; Cayre, O. J.; Biggs, S.; Armes, S. P.; York, D. Incorporation of Block Copolymer Micelles into Multilayer Films for Use as Nanodelivery Systems. *Langmuir* **2008**, *24*, 13328-13333.
22. Liu, X. K.; Zhou, L.; Geng, W.; Sun, J. Q. Layer-by-Layer-Assembled Multilayer Films of Polyelectrolyte-Stabilized Surfactant Micelles for the Incorporation of Noncharged Organic Dyes. *Langmuir* **2008**, *24*, 12986-12989.
23. Jiao, Q.; Yi, Z.; Chen, Y. M.; Xi, F. Dendronized Polymer as Building Block for Layer-by-Layer Assembly: Polyelectrolyte Multilayer Films for Incorporation and Controlled Release of Water-Insoluble Dye. *Polymer* **2008**, *49*, 1520-1526.
24. Guyomard, A.; Nysten, B.; Muller, G.; Glinel, K. Loading and Release of Small Hydrophobic Molecules in Multilayer Films Based on Amphiphilic Polysaccharides. *Langmuir* **2006**, *22*, 2281-2287.
25. Manna, U.; Patil, S. Encapsulation of Uncharged Water-Insoluble Organic Substance in Polymeric Membrane Capsules Via Layer-by-Layer Approach. *J Phys Chem B* **2008**, *112*, 13258-13262.
26. Manna, U.; Patil, S. Dual Drug Delivery Microcapsules Via Layer-by-Layer Self-Assembly. *Langmuir* **2009**, *25*, 10515-10522.
27. Cho, J. H.; Hong, J. K.; Char, K.; Caruso, F. Nanoporous Block Copolymer Micelle/Micelle Multilayer Films with Dual Optical Properties. *J Am Chem Soc* **2006**, *128*, 9935-9942.

28. Hong, J.; Bae, W. K.; Lee, H.; Oh, S.; Char, K.; Caruso, F.; Cho, J. Tunable Superhydrophobic and Optical Properties of Colloidal Films Coated with Block-Copolymer-Micelles/Micelle-Multilayers. *Adv Mater* **2007**, *19*, 4364-+.
29. Brewster, M. E.; Loftsson, T. Cyclodextrins as Pharmaceutical Solubilizers. *Adv Drug Deliver Rev* **2007**, *59*, 645-666.
30. Challa, R.; Ahuja, A.; Ali, J.; Khar, R. K. Cyclodextrins in Drug Delivery: An Updated Review. *Aaps Pharmscitech* **2005**, *6*, -.
31. Davis, M. E.; Brewster, M. E. Cyclodextrin-Based Pharmaceuticals: Past, Present and Future. *Nat Rev Drug Discov* **2004**, *3*, 1023-1035.
32. Loftsson, T.; Duchene, D. Cyclodextrins and Their Pharmaceutical Applications. *Int J Pharm* **2007**, *329*, 1-11.
33. Rasheed, A.; Kumar C.K., A.; Sravanthi, V. V. N. S. S. Cyclodextrins as Drug Carrier Molecule: A Review. *Scientia Pharmaceutica* **2008**, *76*, 567-598.
34. Shimpi, S. Cyclodextrins: Application in Different Routes of Drug Administration. *Acta Pharmaceutica* **2005**, *55*, 139-156.
35. Uekama, K.; Hirayama, F.; Irie, T. Cyclodextrin Drug Carrier Systems. *Chem Rev* **1998**, *98*, 2045-2076.
36. Hirayama, F.; Uekama, K. Cyclodextrin-Based Controlled Drug Release System. *Adv Drug Deliver Rev* **1999**, *36*, 125-141.
37. Yang, X.; Johnson, S.; Shi, J.; Holesinger, T.; Swanson, B. Polyelectrolyte and Molecular Host Ion Self-Assembly to Multilayer Thin Films: An Approach to Thin Film Chemical Sensors. *Sensor Actuat B-Chem* **1997**, *45*, 87-92.
38. Fischer, P.; Koetse, M.; Laschewsky, A.; Wischerhoff, E.; Jullien, L.; Persoons, A.; Verbiest, T. Orientation of Nonlinear Optical Active Dyes in Electrostatically Self-Assembled Polymer Films Containing Cyclodextrins. *Macromolecules* **2000**, *33*, 9471-9473.
39. Sato, K.; Suzuki, I.; Anzai, J. Preparation of Polyelectrolyte-Layered Assemblies Containing Cyclodextrin and Their Binding Properties. *Langmuir* **2003**, *19*, 7406-7412.
40. Sato, K.; Suzuki, I.; Anzai, J. Layered Assemblies Composed of Sulfonated Cyclodextrin and Poly(Allylamine). *Colloid Polym Sci* **2004**, *282*, 287-290.
41. Sato, H.; Okuda, R.; Sugiyama, A.; Hamatsu, M.; Anzai, J. Loading and Release of Methyl Orange in Layer-by-Layer Assembled Polyelectrolyte Films. *Mat Sci Eng C-Bio S* **2009**, *29*, 1057-1060.
42. Benkirane-Jessel, N.; Schwinte, P.; Falvey, P.; Darcy, R.; Haikel, Y.; Schaaf, P.; Voegel, J. C.; Ogier, J. Build-up of Polypeptide Multilayer Coatings with Anti-Inflammatory Properties Based on the Embedding of Piroxicam-Cyclodextrin Complexes. *Adv Funct Mater* **2004**, *14*, 174-182.
43. Smith, R. C.; Riollano, M.; Leung, A.; Hammond, P. T. Layer-by-Layer Platform Technology for Small-Molecule Delivery. *Angew Chem Int Edit* **2009**, *48*, 8974-8977.
44. Ariga, K.; Lvov, Y.; Kunitake, T. Assembling Alternate Dye-Polyion Molecular Films by Electrostatic Layer-by-Layer Adsorption. *J Am Chem Soc* **1997**, *119*, 2224-2231.
45. Chuang, H. F.; Smith, R. C.; Hammond, P. T. Polyelectrolyte Multilayers for Tunable Release of Antibiotics. *Biomacromolecules* **2008**, *9*, 1660-1668.
46. Moskowitz, J. S.; Blaisse, M. R.; Samuel, R. E.; Hsu, H.-P.; Harris, M. B.; Martin, S. D.; Lee, J. C.; Spector, M.; Hammond, P. T. The Effectiveness of the Controlled Release of

- Gentamicin from Polyelectrolyte Multilayers in the Treatment of Staphylococcus Aureus Infection in a Rabbit Bone Model *Biomaterials* **2010**, *31*, 6019-6030.
47. Chen, H.; Zeng, G. H.; Wang, Z. Q.; Zhang, X. To Construct "Ion Traps" For Enhancing the Permselectivity and Permeability of Polyelectrolyte Multilayer Films. *Macromolecules* **2007**, *40*, 653-660.
 48. Chung, A. J.; Rubner, M. F. Methods of Loading and Releasing Low Molecular Weight Cationic Molecules in Weak Polyelectrolyte Multilayer Films. *Langmuir* **2002**, *18*, 1176-1183.
 49. Thierry, B.; Winnik, F. M.; Merhi, Y.; Silver, J.; Tabrizian, M. Bioactive Coatings of Endovascular Stents Based on Polyelectrolyte Multilayers. *Biomacromolecules* **2003**, *4*, 1564-1571.
 50. Kharlampieva, E.; Sukhishvili, S. A. Release of a Dye from Hydrogen-Bonded and Electrostatically Assembled Polymer Films Triggered by Adsorption of a Polyelectrolyte. *Langmuir* **2004**, *20*, 9677-9685.
 51. Wang, L.; Wang, X.; Xu, M. F.; Chen, D. D.; Sun, J. Q. Layer-by-Layer Assembled Microgel Films with High Loading Capacity: Reversible Loading and Release of Dyes and Nanoparticles. *Langmuir* **2008**, *24*, 1902-1909.
 52. Schmidmaier, G.; Lucke, M.; Wildemann, B.; Haas, N. P.; Raschke, M. Prophylaxis and Treatment of Implant-Related Infections by Antibiotic-Coated Implants: A Review. *Injury* **2006**, *37*, 105-112.
 53. Newton, D. W.; Kluza, R. B. pKa Values of Medicinal Compounds in Pharmacy Practice. *Drug Intell. Clin. Pharm.* **1978**, *12*, 546-554.
 54. Loftsson, T.; Hreinsdottir, D.; Masson, M. Evaluation of Cyclodextrin Solubilization of Drugs. *Int J Pharm* **2005**, *302*, 18-28.
 55. Smith, R. C. *Toward a Drug Delivery Coating for Intraocular Lenses* Ph.D. thesis. Massachusetts Institute of Technology, 2010.
 56. Beckstead, D. J.; Desmet, D. J.; Ord, J. L. An Ellipsometric Investigation of the Formation and Conversion of Prussian Blue Films. *J Electrochem Soc* **1989**, *136*, 1927-1932.
 57. Cowen, S.; Sambles, J. R.; Glidle, A. A Study of Thin-Films of Prussian Blue on Gold Electrodes, Using Surface-Plasmon Polaritons. *J Electroanal Chem* **1989**, *261*, 455-462.
 58. Hamnett, A.; Higgins, S.; Mortimer, R. S.; Rosseinsky, D. R. A Study of the Electrodeposition and Subsequent Potential Cycling of Prussian Blue Films Using Ellipsometry. *J Electroanal Chem* **1988**, *255*, 315-324.
 59. Gulce, H.; Ozyoruk, H.; Yildiz, A. Electrochemical Oxidation of Anthracenes on Poly(Vinylferrocenium) Coated Pt-Electrodes in Acetonitrile. *Ber Bunsen Phys Chem* **1994**, *98*, 828-832.
 60. Schmidt, D. J.; Cebeci, F. C.; Kalcioğlu, Z. I.; Wyman, S. G.; Ortiz, C.; Van Vliet, K. J.; Hammond, P. T. Electrochemically Controlled Swelling and Mechanical Properties of a Polymer Nanocomposite. *Acs Nano* **2009**, *3*, 2207-2216.
 61. Miller, M. D.; Bruening, M. L. Correlation of the Swelling and Permeability of Polyelectrolyte Multilayer Films. *Chem Mater* **2005**, *17*, 5375-5381.
 62. Salomaki, M.; Kankare, J. Influence of Synthetic Polyelectrolytes on the Growth and Properties of Hyaluronan-Chitosen Multilayers. *Biomacromolecules* **2009**, *10*, 294-301.

63. Richert, L.; Lavalle, P.; Payan, E.; Shu, X. Z.; Prestwich, G. D.; Stoltz, J. F.; Schaaf, P.; Voegel, J. C.; Picart, C. Layer by Layer Buildup of Polysaccharide Films: Physical Chemistry and Cellular Adhesion Aspects. *Langmuir* **2004**, *20*, 448-458.
64. Park, J. W.; Choi, K. H.; Park, K. K. Acid-Base Equilibria and Related Properties of Chitosan. *B Kor Chem Soc* **1983**, *4*, 68-72.
65. Picart, C.; Mutterer, J.; Richert, L.; Luo, Y.; Prestwich, G. D.; Schaaf, P.; Voegel, J. C.; Lavalle, P. Molecular Basis for the Explanation of the Exponential Growth of Polyelectrolyte Multilayers. *P Natl Acad Sci USA* **2002**, *99*, 12531-12535.
66. Ruths, J.; Essler, F.; Decher, G.; Riegler, H. Polyelectrolytes I: Polyanion/Polycation Multilayers at the Air/Monolayer/Water Interface as Elements for Quantitative Polymer Adsorption Studies and Preparation of Hetero-Superlattices on Solid Surfaces. *Langmuir* **2000**, *16*, 8871-8878.
67. Zhang, F. X.; Srinivasan, M. P. Layer-by-Layer Assembled Gold Nanoparticle Films on Amine-Terminated Substrates. *J. Colloid Interface Sci.* **2008**, *319*, 450-456.
68. Ellis, D.; Eckhoff, M.; Neff, V. D. Electrochromism in the Mixed-Valence Hexacyanides. 1. Voltammetric and Spectral Studies of the Oxidation and Reduction of Thin-Films of Prussian Blue. *J. Phys. Chem.* **1981**, *85*, 1225-1231.
69. Chen, S. M. Preparation, Characterization, and Electrocatalytic Oxidation Properties of Iron, Cobalt, Nickel, and Indium Hexacyanoferrate. *J. Electroanal. Chem.* **2002**, *521*, 29-52.
70. Ricci, F.; Palleschi, G. Sensor and Biosensor Preparation, Optimisation and Applications of Prussian Blue Modified Electrodes. *Biosens. Bioelectron.* **2005**, *21*, 389-407.
71. Ho, Y. S.; McKay, G. Comparative Sorption Kinetic Studies of Dye and Aromatic Compounds onto Fly Ash. *J. Environ. Sci. Health, Part A: Toxic/Hazard. Subst. Environ. Eng.* **1999**, *34*, 1179-1204.
72. Lavalle, P.; Gergely, C.; Cuisinier, F. J. G.; Decher, G.; Schaaf, P.; Voegel, J. C.; Picart, C. Comparison of the Structure of Polyelectrolyte Multilayer Films Exhibiting a Linear and an Exponential Growth Regime: An in Situ Atomic Force Microscopy Study. *Macromolecules* **2002**, *35*, 4458-4465.
73. Kim, B. S.; Smith, R. C.; Poon, Z.; Hammond, P. T. MAD (Multiagent Delivery) Nanolayer: Delivering Multiple Therapeutics from Hierarchically Assembled Surface Coatings. *Langmuir* **2009**, *25*, 14086-14092.
74. Wood, K. C.; Chuang, H. F.; Batten, R. D.; Lynn, D. M.; Hammond, P. T. Controlling Interlayer Diffusion to Achieve Sustained, Multiagent Delivery from Layer-by-Layer Thin Films. *Proc. Natl. Acad. Sci. U. S. A.* **2006**, *103*, 10207-10212.
75. Fredin, N. J.; Zhang, J. T.; Lynn, D. M. Surface Analysis of Erodible Multilayered Polyelectrolyte Films: Nanometer-Scale Structure and Erosion Profiles. *Langmuir* **2005**, *21*, 5803-5811.
76. von Burkersroda, F.; Schedl, L.; Gopferich, A. Why Degradable Polymers Undergo Surface Erosion or Bulk Erosion. *Biomaterials* **2002**, *23*, 4221-4231.
77. Itaya, K.; Shoji, N.; Uchida, I. Catalysis of the Reduction of Molecular Oxygen to Water at Prussian Blue Modified Electrodes. *J. Am. Chem. Soc.* **1984**, *106*, 3423-3429.
78. Lu, L.; Garcia, C. A.; Mikos, A. G. In Vitro Degradation of Thin Poly(DL-Lactic-Co-Glycolic Acid) Films. *J. Biomed. Mater. Res., Part A* **1999**, *46*, 236-244.
79. Andrews, J. M. Determination of Minimum Inhibitory Concentrations. *J. Antimicrob. Chemother.* **2001**, *48*, 5-16.

80. Voegel, P. D.; Baldwin, R. P. Evaluation of Copper-Based Electrodes for the Analysis of Aminoglycoside Antibiotics by CE-EC. *Electroanalysis* **1997**, *9*, 1145-1151.
81. Priuska, E. M.; Schacht, J. Formation of Free Radicals by Gentamicin and Iron and Evidence for an Iron Gentamicin Complex. *Biochem. Pharmacol.* **1995**, *50*, 1749-1752.
82. Darouiche, R. O.; Mansouri, M. D.; Zakarevicz, D.; AlSharif, A.; Landon, G. C. In Vivo Efficacy of Antimicrobial-Coated Devices. *J. Bone Jt. Surg. (Am.)* **2007**, *89A*, 792-797.
83. Alvarez, H.; Castro, C.; Moujir, L.; Perera, A.; Delgado, A.; Soriano, I.; Evora, C.; Sanchez, E. Efficacy of Ciprofloxacin Implants in Treating Experimental Osteomyelitis. *J. Biomed. Mater. Res., Part B* **2008**, *85B*, 93-104.
84. Kang, Y. J.; Erickson, K. J.; Taton, T. A. Plasmonic Nanoparticle Chains Via a Morphological, Sphere-to-String Transition. *J Am Chem Soc* **2005**, *127*, 13800-13801.
85. Kang, Y. J.; Taton, T. A. Core/Shell Gold Nanoparticles by Self-Assembly and Crosslinking of Micellar, Block-Copolymer Shells. *Angew Chem Int Edit* **2005**, *44*, 409-412.
86. Kim, B. S.; Qiu, J. M.; Wang, J. P.; Taton, T. A. Magnetomicelles: Composite Nanostructures from Magnetic Nanoparticles and Cross-Linked Amphiphilic Block Copolymers. *Nano Lett* **2005**, *5*, 1987-1991.
87. Kim, B. S.; Taton, T. A. Multicomponent Nanoparticles Via Self-Assembly with Cross-Linked Block Copolymer Surfactants. *Langmuir* **2007**, *23*, 2198-2202.

Chapter 4: Mechanomutable Layer-by-Layer Polymer Nanocomposite Thin Films Utilizing Prussian Blue

*Portions reproduced with permission from “Electrochemically Controlled Swelling and Mechanical Properties of a Polymer Nanocomposite” by Daniel J. Schmidt, Fevzi Ç. Cebeci, Z. Ilke Kalcioglu, Samantha G. Wyman, Christine Ortiz, Krystyn J. Van Vliet, and Paula T. Hammond, *ACS Nano*, 2009, 3(8), 2207-2216. 10.1021/nn900526c, © 2009 American Chemical Society.

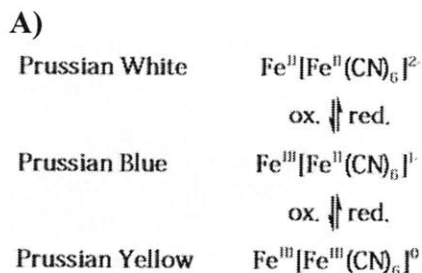
4.1 Introduction

The ability to dynamically control the mechanical properties of a surface could lead to a number of interesting applications. Active modulation of cellular behavior on surfaces is of particular interest, as it is well known that adhesion of cells to surfaces can be modulated via the stiffness of those surfaces.^{1,2} In the area of biomimicry, researchers have recently designed a chemoresponsive polymer nanocomposite to mimic the dermis of the sea cucumber, a marine organism that can reversibly alter its stiffness.³ Stimuli-responsive composite materials open up the possibility of tuning percolative behavior, which can dramatically alter mechanical, electrical, optical, and other composite properties.^{4,5} In this work, we have designed and characterized an electrochemically-responsive polymer nanocomposite thin film with actively-tunable mechanical properties.

Layer-by-layer (LbL) assembly⁶ was employed here for the fabrication of the electroactive thin film composite. While the stiffness of LbL films can be controlled by post-assembly crosslinking,^{7,8} as well as assembly pH and choice of polymer,² these films can also be stimuli-responsive.⁹ It is known that changes in humidity¹⁰ and ionic strength¹¹ can reversibly alter the stiffness of LbL films by changing the degree of film hydration and the degree of ionic crosslinking, respectively. There are only a few examples in the literature of reduction-oxidation

(redox)-driven swelling of LbL films. The Calvo group has studied multilayer films containing a ferrocene-derivatized polyallylamine (PAH-Fc)¹² as well as an osmium complex-derivatized polyallylamine (PAH-Os),¹³ which can swell by 10% of initial film thickness upon oxidation of the Os(II). The Vancso group has layered anionic and cationic polyferrocenylsilanes to form multilayer capsules, which expand and increase their permeability upon chemical oxidation of the ferrocene units.¹⁴ Most recently, Grieshaber et al. reported on a poly(L-glutamic acid)/poly(allylamine hydrochloride) multilayer film that takes up ferrocyanide ions from solution, and can expand and contract by 5-10% in response to electrochemical oxidation and reduction of the ferrocyanide species.¹⁵ None of the above reports on redox-driven swelling quantify the concurrent mechanical changes occurring in the films. Furthermore, in contrast to these three examples, the work presented here utilizes a nanoparticle based assembly, as redox-active Prussian Blue nanoparticles serve as an integral component of a polymer nanocomposite. (Srivastava and Kotov recently reviewed the field of LbL-assembled nanocomposites,¹⁶ though to our knowledge previous LbL nanocomposite systems have not been investigated for reversible swelling properties.) The advantages in using a redox-active nanoparticle include the potential to manipulate particle loading¹⁷ at or near a percolation threshold, thus yielding more dramatic shifts in electrochemical and mechanical properties; the ability to achieve the multiple redox states exhibited by inorganic materials; and the ability to manipulate surface charge and thus directly impact electrostatics within the film with the accompanying redox behavior, independent of a polyelectrolyte conjugate. These properties make this system interesting as a potential mechanomutable material for which stiffness can be altered significantly with a readily controlled external stimulus.

Here we characterize the electrochemically-controlled swelling and mechanical behavior of electroactive LbL thin films containing Prussian Blue nanoparticles as the polyanion and linear polyethyleneimine (LPEI) as the polycation. Specifically, we apply -0.2 V (vs. Ag/AgCl) to reduce the particles from the PB state to the PW state, and $+0.6$ V to oxidize the particles back to the PB state. This negative voltage level is sufficient to fully reduce the PB nanoparticles, and this positive voltage level is sufficient to fully re-oxidize the PB without inducing dissolution that can occur at even higher voltages.¹⁸ Upon electrochemical reduction, the negative charge on the particle surface and interior is doubled as estimated from the valence of the two redox states. In response to the excess negative charge created in the film, cations and water from the electrolyte solution enter the film to maintain electroneutrality (Fig. 4.1B). We have investigated the swelling phenomenon using spectroscopic ellipsometry and electrochemical atomic force microscopy (EC-AFM). Nanoindentation and an electrochemical quartz crystal microbalance with dissipation monitoring (EQCM-D) were used to measure the mechanical properties of films in the oxidized and reduced states. To our knowledge, this is the first direct observation of mechanical property manipulation carried out in an electrochemical cell with a redox-active thin film. We believe that electrochemical control over the swelling and mechanical behavior of polymer nanocomposites could be optimized to have important implications for active manipulation of cell behavior on surfaces, as well as responsive coatings for nanoscale devices in general.



B)

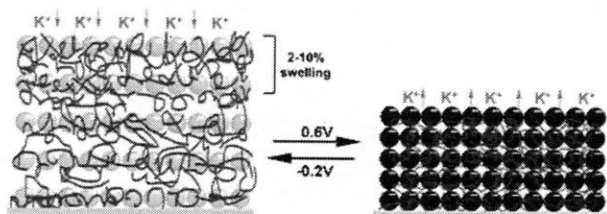


Figure 4.1. (A) Redox states of Prussian Blue. (B) Schematic of an $(\text{LPEI}/\text{PB})_{30}$ film swelling under the influence of an electric potential. Water molecules and positive charges on the polymer are omitted for clarity. The degree of swelling represented in the figure is exaggerated for the reader's convenience.

4.2 Materials and Methods

Materials

Linear polyethyleneimine (LPEI) ($M_n = 25,000$) was purchased from Polysciences. Iron(II) chloride tetrahydrate, potassium ferricyanide, potassium hydrogen phthalate (KHPh), and 3-mercaptopropionic acid (MPS) were purchased from Sigma Aldrich. Potassium chloride was purchased from Mallinckrodt Baker. All chemicals were used as received. Gold-coated silicon wafers (AU.1000.SL1) consisting of a 1000 Å layer of gold with a 50 Å titanium adhesion layer were purchased from Platypus Technologies, LLC. Gold-coated QCM crystals (QSX 301) consisting of a 1000 Å layer of gold with a 50 Å chromium adhesion layer were

purchased from Q-Sense, Inc. Indium tin oxide (ITO)-coated glass slides (CD-50IN-CUV) were purchased from Delta Technologies, Limited.

Synthesis of Prussian Blue Nanoparticles

Synthesis of PB nanoparticles was carried out as described previously.¹⁸ Briefly, 50 mL of aqueous 10 mM FeCl₂•4H₂O was added dropwise to an equivalent volume of aqueous 50 mM K₃[Fe(CN)₆] and 50 mM KCl with vigorous stirring. The dark green mixture was immediately submitted to dialysis against a regenerated cellulose membrane with a 3500 Da molecular weight cutoff to remove excess K₃[Fe(CN)₆] and KCl. The resulting blue nanoparticle suspension was adjusted to pH 4 with potassium hydrogen phthalate (KHPH) (final concentration of 1 mM) and hydrochloric acid.

Assembly of LPEI/PB Films

Films were assembled on gold-coated silicon wafers, gold-coated quartz crystals, or ITO-coated glass slides. The gold coated silicon was cleaned by immersion in Gold Cleaning Solution (Sigma Aldrich) for 1 minute, rinsed copiously with deionized water, and then immersed in an aqueous solution of 20 mM 3-mercapto-1-propanesulfonic acid (MPS) and 16 mM sulfuric acid for 30 minutes to render the surface negatively charged. Thereafter, the substrates were again rinsed thoroughly with deionized water and used for subsequent layer-by-layer assembly. The gold-coated quartz crystals were cleaned by UV/ozone treatment for 10 minutes, immersion in a H₂O:H₂O₂:NH₃ (5:1:1) solution at 75°C for 5 minutes followed by a thorough deionized water rinse, and a second UV/ozone treatment for 10 minutes. Following the cleaning, the crystals were immediately immersed in the MPS solution described above for 30

minutes. ITO-coated slides were cleaned by sonication in a 4% solution of Micro-90 detergent for 15 minutes, following by two 15 minute sonication cycles in deionized water. LPEI solutions were prepared in deionized water at a concentration of 10 mM based on the polymer repeat unit. The solution pH was adjusted to the desired value with HCl and NaOH. (LPEI/PB)_n films, where *n* denotes the number of bilayers, were assembled by dip coating using an automated Zeiss HMS Series programmable slide stainer. Briefly, substrates were immersed in an LPEI solution for 10 minutes followed by three separate deionized water rinse baths (adjusted to pH 4 with KHPH and HCl) for a total of 3 minutes. Next the substrates were immersed in a PB solution for 10 minutes followed by the same cascade rinse cycle. Gold-coated silicon was used for spectroscopic ellipsometry, gold-coated quartz was used for EQCM-D, and ITO-glass was used for EC-AFM. Note that the different substrates did not have an appreciable effect on film thickness, roughness, or the linear growth profile. Slight differences in initial film thickness from sample to sample can be attributed to slight variations in pH of the solutions used for the deposition process. Interparticle distance in the films (in the hydrated state) was approximated assuming spherical particles with a uniform size distribution and dispersion using the equation presented by Hong et al.¹⁹

Atomic Force Microscopy (AFM)

AFM-imaging of (LPEI/PB)₃₀ films on ITO-glass substrates was used for visualization of surface morphology and calculation of the root-mean-squared (RMS) surface roughness of the films. Measurements were made using a Nanoscope IV (IV/IIIa emulation controller) multimode scanning probe microscope (Digital Instruments/Veeco Metrology Group, Santa Barbara, CA) in contact mode. Films were measured in their hydrated state using a fluid cell

(Veeco ECFC) loaded with ca. 20-50 μL of 0.1 M potassium hydrogen phthalate (KHPH) electrolyte solution at pH 4.0. Films were allowed to equilibrate with the solution for 30 minutes before measurement. A silicon nitride (Si_3N_4 , SNL, Veeco Probes, Santa Barbara, CA) cantilever with a nominal spring constant of 0.06 N/m carrying a tip with a nominal diameter of 2 nm was attached to the fluid cell with a gold spring. RMS roughness was calculated from five $3\ \mu\text{m} \times 3\ \mu\text{m}$ height images using Veeco NanoScope v.614r1 software. Tip shape deconvolution of image height and roughness calculations was carried out using SPIP (Scanning Probe Image Processor v4.8.4) software.

Spectroscopic Ellipsometry

Spectroscopic ellipsometry analysis of $(\text{LPEI/PB})_{30}$ films on gold-coated silicon substrates was carried out using a J.A. Woollam M-2000 instrument. Data were fit using J.A. Woollam WVASE32 software. *In situ* measurements were conducted through a custom-made quartz cell with 70° windows (Hellma USA, Inc.). Spectroscopic ellipsometry measures the change in polarization state of light reflected from a surface. Two ellipsometric parameters, ψ and Δ , representing the change in amplitude and phase of the reflected light, respectively, are collected at a number of wavelengths. ψ and Δ are related to the thickness and optical constants of the sample. Briefly, to determine film thickness with spectroscopic ellipsometry, we used a single Gaussian oscillator to model the film absorbance from 620-900 nm. See Appendix 3 for further details on modeling of spectroscopic ellipsometry data. To simultaneously apply a voltage to a film while characterizing the film with spectroscopic ellipsometry, a three-electrode electrochemical cell was set up in the quartz cell with a Ag/AgCl reference electrode (Bioanalytical Systems, Inc.), a Pt coil counter electrode, and a gold-coated silicon wafer

modified with a $(\text{LPEI/PB})_n$ film as the working electrode (Fig. 4.2). The electrolyte was a 0.1 M KHPH solution with pH \sim 4. An AutoLab PGSTAT100 potentiostat was used for electrochemical measurements. Two minutes were allowed to elapse at each applied potential, before taking a measurement. A dynamic scan protocol in the WVASE32 software package with acquisition time of 10 milliseconds was used to capture the kinetics of the redox-induced swelling process.

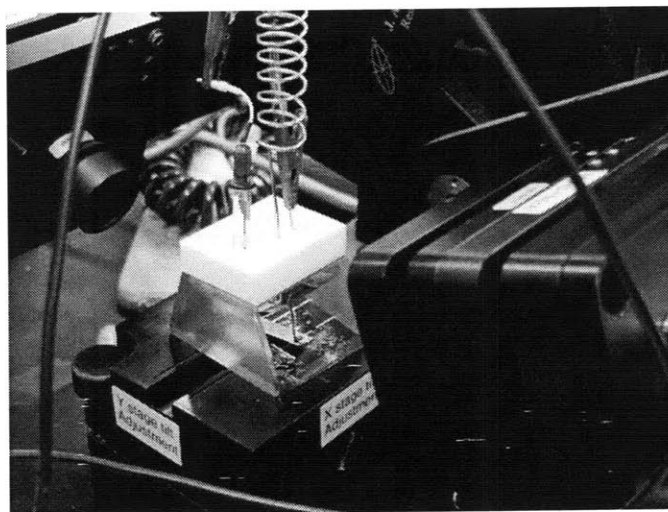


Figure 4.2. Photograph of an electrochemical cell interfaced with a spectroscopic ellipsometer. The three-electrode cell comprises a Ag/AgCl reference electrode, a Pt coil counter electrode, and a gold-coated silicon wafer modified with a $(\text{LPEI/PB})_n$ film as the working electrode. The gold working electrode is connected to the external circuit by a contact connection with a Pt wire.

Electrochemical Atomic Force Microscopy (EC-AFM)

EC-AFM of $(\text{LPEI/PB})_{30}$ films on ITO-glass substrates was performed using a Nanoscope IV (IV/IIIa emulation controller) multimode scanning probe microscope (Digital Instruments/Veeco Metrology Group, Santa Barbara, CA) in contact mode with an integrated multimode EC basic potentiostat. (Note that this platform does not support tapping mode AFM.)

The film sample was attached to the magnetic sample holder using double-sided tape and was placed on the E-type piezo scanner. Electrical contact between the ITO and the sample puck was made with silver paste. A three-electrode type, glass EC fluid cell was used for the contact mode measurements. The cell volume was ca. 20-50 μL and 0.1 M KHPH with pH 4.0 was used as the electrolyte. A silicon nitride (Si_3N_4 , SNL, Veeco Probes, Santa Barbara, CA) cantilever with a nominal spring constant of 0.06 N/m carrying a tip with a nominal diameter of 2 nm was attached to the fluid cell with a gold spring. A silver wire and a platinum wire were used as a pseudo-reference electrode and counter electrode, respectively. An electric potential was applied using the chronoamperometry function, and 2 min were allowed to elapse before surface profiles were captured. Thickness values of the films were calculated as follows. A box was drawn on a flat area of the substrate and a first-order plane fit was applied. A 10 μm scan length was acquired under a nominal contact load of 0.4 nN, traversing the edge of the film, and the average heights of the film and substrate were determined by simple averaging of the individual data points. The same locations at the film/substrate interface were line-scanned before and after redox switching.

Nanoindentation

Nanoindentation on $(\text{LPEI/PB})_{50}$ films on ITO-glass was conducted by a pendulum-based instrumented nanoindenter (NanoTest, Micro Materials Ltd.) with a force resolution of 1 μN and a displacement resolution of 0.1 nm. Films assembled on ITO-coated glass were adhered to an aluminum support with a thin layer of cyanoacrylate and all of the experiments were conducted with the sample fully immersed in 0.1 M KHPH, using a modified platform for *in situ* liquid experiments.²⁰ An electrochemical cell was set up within the liquid cell with the film as the

working electrode, a Pt wire as the counter electrode, and a silver wire as a pseudo-reference electrode (Figure 4.3). The potential was controlled with an EG&G 263A potentiostat/galvanostat. Samples were indented with a spherical ruby indenter of radius $R= 5 \mu\text{m}$, both in the oxidized and reduced states of the film ($n=6$ locations for each condition), with loading, dwell, and unloading times of 10s, 10s, and 2s, respectively. A maximum depth of 40 nm was chosen to induce comparable, low strains on all samples ($\sim 10\%$), and the corresponding maximum loads ranged between 80 and 200 μN . Film Young's elastic modulus inferred from indentation, E_i , was calculated through a finite-thickness correction of Hertzian elastic contact, using the model of Dimitriadis et al.,²¹ in order to account for mechanical contributions from the underlying stiff ITO-glass substrate for the measured film thickness of 224 ± 13 nm (as determined via profilometry). E_i of the film is related directly to the Young's elastic modulus E that is typically measured via uniaxial loading of macroscopic materials, and is theoretically equivalent to E for linear elastic materials. Thicker films (50 bilayers instead of 30 bilayers) were used to improve the accuracy of nanoindentation by allowing for a deeper penetration depth. From spectroscopic ellipsometry analysis, 50-bilayer films were found to swell to the same degree as 30-bilayer films (data not shown).

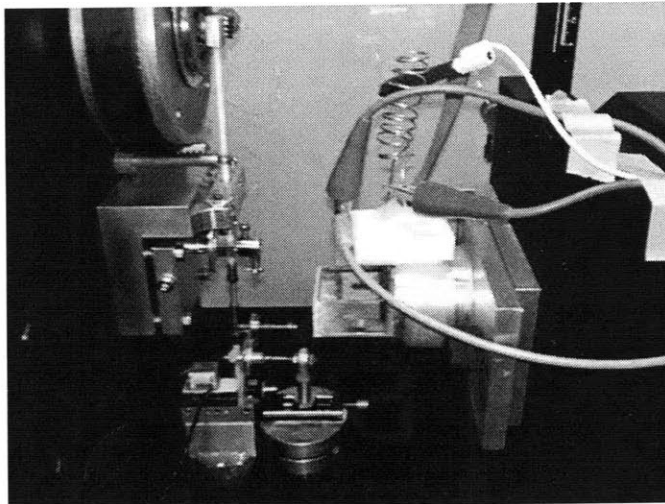


Figure 4.3. Photograph of an electrochemical cell interfaced with a nanoindenter. The three-electrode cell comprises Ag pseudo-reference electrode, a Pt wire counter electrode, and an ITO-coated glass slide modified with a (LPEI/PB)₅₀ film as the working electrode. The substrate, mounted on the aluminum support, is only partially submersed in the liquid, allowing for direct connection to the external circuit with an alligator clip.

Electrochemical Quartz Crystal Microbalance with Dissipation (EQCM-D)

EQCM-D analysis of (LPEI/PB)₃₀ films on gold-coated quartz was carried out using a Q-Sense E1 system along with the Electrochemistry Module (QEM 401). Frequency changes are directly proportional to mass changes according to the Sauerbrey equation.²² (LPEI/PB)₃₀ films were assembled on gold-coated QCM crystals (Q-Sense QSX 301) as described above, and the film was removed from the backside of the crystals using a cotton swab soaked in 1 M NaOH, following by a deionized water rinse. The QCM chamber served as a three-electrode electrochemical cell with a Ag/AgCl reference electrode (Cypress Systems), a built-in Pt counter electrode, and the Au-coated QCM crystal modified with an (LPEI/PB)₃₀ film as the working

electrode. The electrolyte was a 0.1 M KHPH solution with pH 4.0. A VoltaLab 21 potentiostat was used for electrochemical measurements.

4.3 Results and Discussion

4.3.1 Dry Film Characterization

Synthesis of Prussian Blue (PB) nanoparticles, as reported by Delongchamp and Hammond, gives an electrostatically stabilized suspension of negatively charged nanoparticles with a median diameter of 4-5 nm as measured by transmission electron microscopy.¹⁸ Layer-by-layer assembly of the PB nanoparticles with linear polyethyleneimine was also characterized previously by our group.¹⁸ This system exhibits linear growth with an average thickness of ~4.1 nm/bilayer in the dry state both on an indium tin oxide (ITO)-coated glass substrate and a gold (Au)-coated silicon substrate. The volume fraction of PB in the films (dry state) is 0.68, calculated from film thickness and Faradaic charge uptake.¹⁸ An approximation of the interparticle distance indicates that the particles are interlocking (see Methods). The root-mean-squared (RMS) surface roughness of the films assembled on ITO-glass, as calculated from AFM height images, was 3.48 ± 0.16 nm, comparable to the PB nanoparticle diameter (Fig. 4.4).

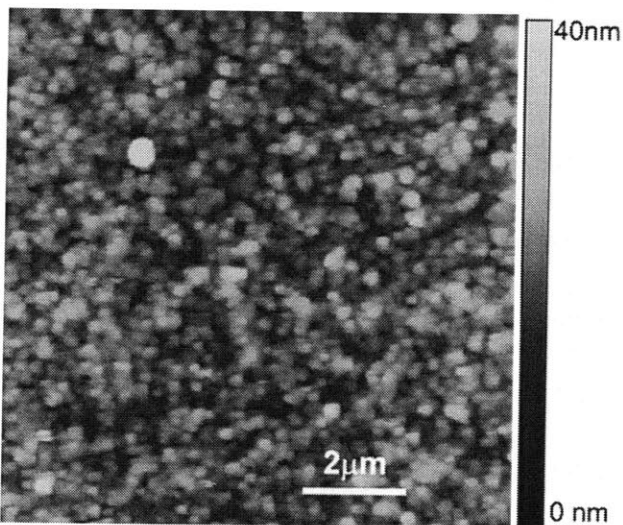


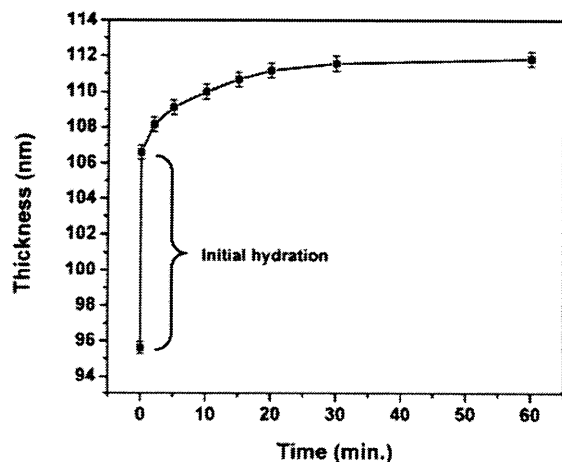
Figure 4.4. AFM height image of an (LPEI/PB)₃₀ film surface assembled on ITO-glass, acquired via contact-mode imaging in an aqueous 0.1 M potassium hydrogen phthalate solution. RMS roughness is 3.48 ± 0.16 nm.

4.3.2 Passive Swelling

Passive swelling of (LPEI/PB)₃₀ films on Au-coated silicon was measured with spectroscopic ellipsometry (see Methods and Appendix 3 for further details). We define passive swelling as swelling of a film from the dry state to the hydrated state, in the absence of an applied potential. A typical (LPEI/PB)₃₀ film had a dry thickness of ~ 100 nm, which agreed well with thickness measured by profilometry (data not shown). To measure the timescale of passive swelling, an (LPEI/PB)₃₀ film was immersed in a potassium hydrogen phthalate (KHPH) electrolyte solution at pH 4.0 for one hour. A typical (LPEI/PB)₃₀ film swelled by $\sim 12\%$ of its initial dry thickness immediately upon immersion in the electrolyte. Over the course of an hour, the film thickness increased to a final degree of swelling (with respect to the initial dry state) of $\sim 17\%$ (Fig. 4.5A). An identical film allowed to swell passively in electrolyte over 2 days reached a final degree of swelling of 30%. It should be noted that the degree of passive swelling varies depending on the ambient humidity since the “dry” film is

equilibrated with vapor in the air.¹⁰ The effect of ionic strength of the electrolyte on degree of passive swelling was also investigated. Identical (LPEI/PB)₃₀ films were swollen passively overnight in 1 mM, 10 mM, and 100 mM KHPH solutions each adjusted to pH 4.0 exactly. The films exhibited degrees of swelling of 21.4% ± 1.7%, 24.7% ± 0.6%, and 26.8% ± 2.2%, respectively, showing that a greater degree of passive swelling resulted for higher ionic strength. In contrast to covalently-crosslinked polyelectrolyte hydrogels, this trend is expected for electrostatically-assembled layer-by-layer films, since mobile ions can compete with the polycation-polyanion linkages in the film. Breakage of some of the cohesive ionic crosslinks in the film then results in loosening of the network and additional swelling.²³

A)



B)

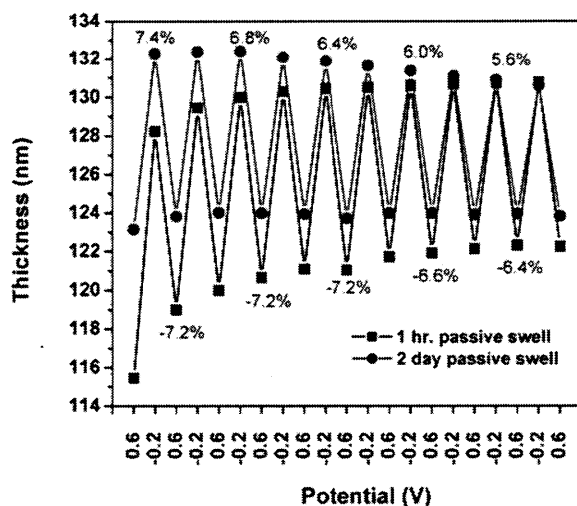


Figure 4.5. (A) Passive swelling of an $(\text{LPEI/PB})_{30}$ film in a 0.1 M KHPH electrolyte solution over one hour. All of the error bars represent 95% confidence intervals based on the ellipsometry model fit. (B) Active swelling of two $(\text{LPEI/PB})_{30}$ films subjected to ten redox cycles. Error bars representing 95% confidence intervals based on the ellipsometry model fit are approximately the size of the data points. Selected swelling percentage values (calculated relative to thickness in the preceding redox state) are next to the corresponding data points; negative values represent shrinking.

4.3.3 Active Swelling

Active swelling of $(\text{LPEI/PB})_{30}$ films on Au-coated silicon was first measured with spectroscopic ellipsometry. We define active swelling as swelling of a hydrated film under the influence of an applied electric potential. Film thicknesses were determined for films subjected to -0.2 V (reduced, or PW, state) and +0.6 V (oxidized, or PB, state), alternately. Ellipsometry measurements are complicated by the fact that the film optical constants differ substantially at the two applied potentials. In the PB state, there was a large absorbance peak centered at $\sim 730\text{-}740$ nm (1.68 eV) stemming from intervalence charge transfer, while in the

PW state there was a much smaller absorbance peak centered at ~ 850 nm (1.45 eV). The model and experimental ellipsometric parameter (ψ and Δ) values for an (LPEI/PB)₃₀ film at +0.6 V and -0.2 V, along with the model fit results, can be found in Appendix 3 (Figure A3.1). At both applied potentials, we observe excellent agreement between our ellipsometric model fit and the data. Measurements were taken after 2 minutes at each specified potential. Two minutes were sufficient for the film to attain a stable thickness following redox-induced swelling. Using spectroscopic ellipsometry, a dynamic scan protocol was employed to take measurements every 10 milliseconds while the film underwent electrochemical switching. This experiment revealed that active film swelling is completed within approximately 100 milliseconds, following the application of -0.2 V (Figure A3.2 in Appendix 3). Figure 4.5B shows the thickness evolution of two (LPEI/PB)₃₀ films submitted to ten reduction/oxidation cycles, as measured via spectroscopic ellipsometry. We observed swelling and shrinking on the order of 5-10% of initial film thickness upon redox switching, with an average of 6.2% ($\pm 0.6\%$) for the film swollen passively for two days (Fig. 4.5B). For the film swollen passively in solution for 1 hour, the swelling was not completely reversible in the timescale of our experiment. Specifically, the degree of swelling decreased slightly with successive redox cycles, and film thickness increases, as the film continues to equilibrate with the electrolyte. For the film swollen passively in solution for 2 days, swelling was much more reversible, although there is a slight decrease in degree of swelling after the first few cycles. This cycle-dependent decrease in swelling may be attributable to desorption of a small number of nanoparticles from the film upon early redox cycles, or to diffusion of polymers and nanoparticles within the film that change the swellability of the film over time.

Electrochemical AFM (EC-AFM) was used as a complementary technique to directly investigate electrochemically-triggered (active) swelling *in situ*. EC-AFM integrates a potentiostat with AFM, allowing simultaneous application of an electric potential and AFM surface measurements. (LPEI/PB)₃₀ films assembled on ITO-glass were allowed to equilibrate with the electrolyte, an electric potential was then applied to reduce or oxidize the film, and two minutes were allowed to elapse before thickness measurements were carried out. In agreement with spectroscopic ellipsometry, when films were allowed to swell passively for only 30 minutes, a gradual increase in film thickness was observed with successive redox cycles (data not shown), indicating that the film was not completely equilibrated with the electrolyte in that time scale. When films were allowed to swell passively for two days, we observed reversible swelling with a more stable baseline film thickness, also in agreement with spectroscopic ellipsometry (Fig. 4.5B). EC-AFM indicates that (LPEI/PB)₃₀ films swell and shrink by 2-4% (with an average of 2.8% ($\pm 1.0\%$)) of initial, hydrated film thickness when the PB is electrochemically reduced and oxidized, respectively (Fig. 4.6), compared to the 6.2% ($\pm 0.6\%$) swelling observed with spectroscopic ellipsometry (Fig. 4.5B). The results from spectroscopic ellipsometry and EC-AFM measurements agree well qualitatively, showing that the films swell when reduced and shrink when oxidized, and that swelling is reversible. The large errors in the EC-AFM measurements result from the fact that film surface roughness is on the same order of magnitude as height changes associated with reversible swelling. Furthermore, the EC-AFM likely underestimates the degree of swelling since the AFM tip in contact mode presses on the film surface (average imaging force = 0.4 nN), which can lead to film compression.

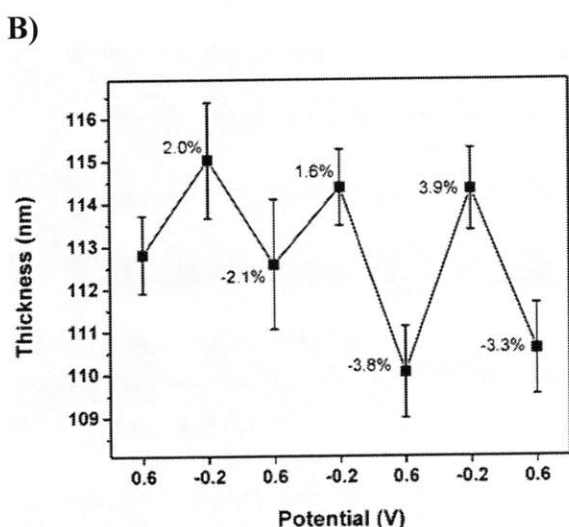
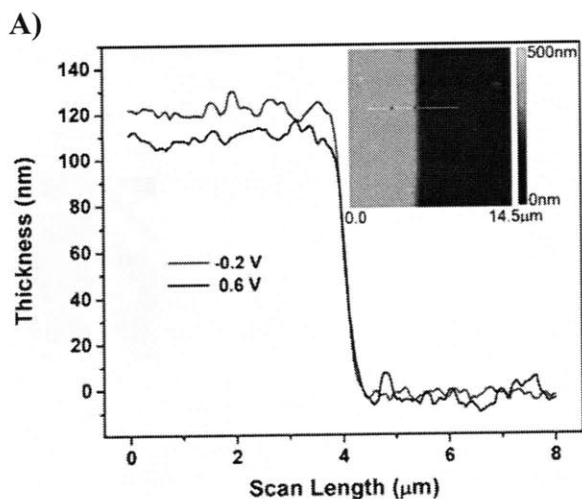


Figure 4.6. (A) Surface profile of an (LPEI/PB)₃₀ film measured with EC-AFM at applied potentials of -0.2 V and +0.6 V. The inset shows a height image of the film/substrate boundary with a demarcation denoting the location of the surface profile measurement. (B) Evolution of film thickness with successive potential cycling. The error bars represent the standard deviation from n=5 measurements taken at different locations on the film. Swelling percentage values (calculated relative to thickness in the preceding redox state) are next to the data points; negative values represent shrinking.

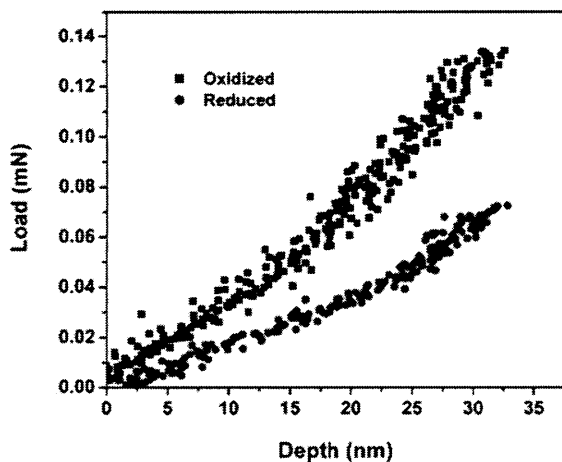
It is reasonably anticipated that the (LPEI/PB)₃₀ films would swell upon reduction and shrink upon oxidation. When PB is fully reduced to PW, all of the Fe(III) centers are switched to the Fe(II) oxidation state, and the negative charge on each unit cell is theoretically doubled. To maintain electroneutrality, potassium ions (and solvating water molecules) enter the film. The excess of potassium ions in the film relative to the surrounding electrolyte will generate an osmotic pressure, bringing additional water into the film. Film swelling ceases when the elastic forces in the film are balanced by osmotic pressure forces. The forced swelling of redox-active thin films to maintain electroneutrality has been observed by a number of other authors.²⁴⁻²⁷ The phenomenon of a continual increase in film thickness with successive redox cycles was also observed by Grumelli et al. for the case of (PAH-Os/PSS) multilayer films.²⁵ They attribute this occurrence to “break in” of the electrolyte, where polycation-polyanion electrostatic interactions are broken by mobile cations and anions, resulting in irreversible solvent uptake and partially “extrinsic” charge compensation in the film. Similarly, we suspect that an influx of ions induced by PB reduction can break ionic crosslinks in the film leading to further reduction in the mechanical stiffness of the composite material, beyond that which would be caused by swelling alone.

4.3.4 Mechanical Measurements

The mechanical behavior of the (LPEI/PB) composite films on ITO-glass, in response to electrochemical redox of PB within the films, was analyzed with instrumented nanoindentation in aqueous conditions, and with EQCM-D. Instrumented, spherical nanoindentation enabled determination of the effective Young’s elastic modulus of the composite films, fully immersed in 0.1 M KHPH at room temperature (see Methods). Fig. 4.7A shows typical load-depth

responses for an (LPEI/PB)₅₀ film in the oxidized state (+0.6 V) and the reduced state (-0.2 V). Clearly the film is more compliant in the reduced state, consistent with an increase in hydration upon film swelling. An effective Young's elastic modulus, E_i , was determined from these indentation responses of the hydrated composite film, correcting for the finite thickness of each film and the stiffness of the underlying ITO-glass substrate (see Methods). Fig. 4.7B shows E_i of a film subjected to two redox cycles. After allowing the film to swell in the electrolyte solution for 2 hours, E_i was measured to be 3.40 ± 1.03 GPa. Subsequent electrochemical reduction of the film reduced E_i further to 1.75 ± 0.26 GPa, a decrease of nearly 50%. Upon re-oxidation of the film, E_i returned to 3.54 ± 0.64 GPa; subsequent electrochemical reduction then reduced E_i to 2.14 ± 0.6 GPa. Measurements at each potential were taken over the course of 1 hour and exhibited excellent repeatability, attesting to the stability of the films and the reversibility of the switching. As expected, the indentation elastic modulus of the film in the absence of an applied potential (i.e., at the open circuit potential) is equal to that at +0.6 V, since the PB redox state is largely unchanged between the open circuit potential (typically +0.3 V to +0.4 V) and +0.6 V (Fig. 4.7). For reference, an (LPEI/PB)₅₀ film in the dry state exhibited $E_i = 6.92 \pm 1.03$ GPa (data not shown). Note that, although these elastic moduli exceed expected Young's elastic moduli of fully hydrated polyelectrolyte-based hydrogels,² these (LPEI/PB)₅₀ nanocomposites comprise 68 vol% of the stiff, inorganic crystalline PB phase.

(A)



(B)

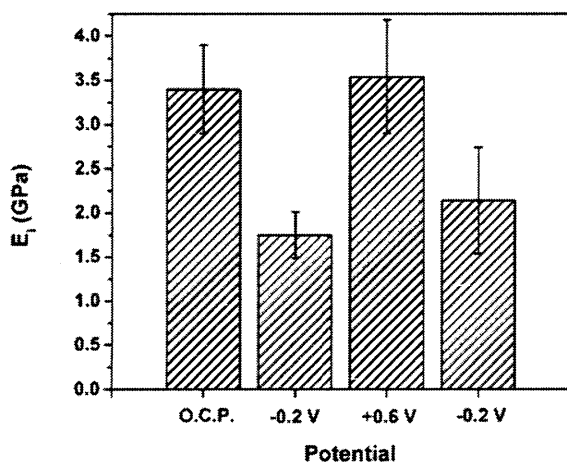


Figure 4.7. Instrumented nanoindentation results for an (LPEI/PB)₅₀ film immersed in aqueous 0.1 M KHP. (A) Loading portion of the load-depth response for a film in the oxidized (black, +0.6 V) and reduced (red, -0.2 V) state. (B) Effective Young's elastic moduli E_1 of the film subjected to two redox cycles, corrected for finite thickness as described in Methods. O.C.P. stands for open circuit potential. Error bars represent the standard deviation from $n=6$ measurements at different locations on the film for each condition.

As expected, the elastic modulus of the film decreases upon immersion in the electrolyte solution, and then decreases further upon electrochemical reduction of the film. Specifically, a ca. 50% reduction in E_i accompanies swelling of the hydrated film upon redox (ca. 5-10% as measured via spectroscopic ellipsometry in Figure 4.5B and 2-4% as measured via EC-AFM in Fig. 4.6B). During swelling, the incoming water and ions serve as plasticizers to reduce cohesive interactions in the film. Furthermore, incoming ions can break ionic crosslinks in the film, thereby giving polymer segments additional degrees of translational freedom and rendering the film less stiff. The extent of decrease in the elastic modulus as a function of swelling observed here is similar in magnitude to that observed for other LbL films in the Schlenoff group^{11,23} and the Van Vliet and Rubner groups^{28,29} (see Appendix 3 for a quantitative comparison). Jaber and Schlenoff recently showed that the elastic modulus of other LbL films can be decreased substantially (for relatively small degrees of swelling)²³ by increasing the ionic strength of the surrounding solution, which decreases the ionic crosslink density in the film.¹¹ Here we maintain the ionic strength of the electrolyte constant, but instead induce increased ionic strength within the film by exploiting PB redox chemistry.

To access the shear and viscous components of mechanical behavior in these films, EQCM-D was employed. In addition to following frequency changes of the quartz crystal oscillator, EQCM-D records the dissipation or damping of the crystal oscillations when the driving voltage is shut off. A change in dissipation can be related to the shear (storage) elastic modulus and shear viscosity of a viscoelastic film adhered to the crystal.³⁰ When (LPEI/PB)₃₀ films assembled on Au-coated quartz were switched from a potential of +0.6 V to -0.2 V (vs. Ag/AgCl), the resonant frequency of the quartz crystal decreased, and the oscillation dissipation of the crystal increased (Fig. 4.8). These results indicate mass uptake by the film

and a qualitative increase in the viscous component of a viscoelastic response, respectively. However, the change in dissipation relative to the change in frequency was too small to allow for viscoelastic modeling of the film with the Voigt model. Furthermore, the frequency responses of the third through thirteenth overtones (normalized by overtone number) overlapped exactly, indicating the rigidity of the film and applicability of the Sauerbrey equation.³¹ Therefore, despite changes in dissipation, we were limited to only qualitative conclusions regarding viscoelasticity of the film.

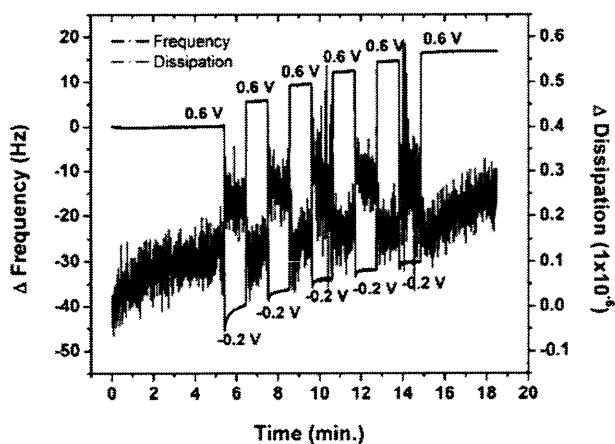


Figure 4.8. Change in frequency and dissipation (13th overtone) of a Au-coated QCM crystal modified with an (LPEI/PB)₃₀ film upon alternate application of -0.2 V and +0.6 V (versus Ag/AgCl). Signal-to-noise of dissipation at the lower frequency overtones was insufficient to identify changes upon voltage switching.

4.3.5 Mechanistic Discussion

As described earlier, the proposed trigger for swelling of the (LPEI/PB) nanocomposite is the electrochemical reduction of PB. To discern whether this is the case, EQCM was used to measure mass uptake at intermediate applied potentials between the oxidized and reduced film states (Fig. 4.9). There is minimal hysteresis, and the inflection in mass uptake, which occurs

at 0.127 V (reduction cycle) and 0.134 V (oxidation cycle), corresponds well with the measured half-wave potential ($E_{1/2}$) of the PB-PW redox couple (0.138 V). This result suggests that electrochemical reduction of PB is responsible for the film swelling phenomenon, as opposed to other possible mechanisms such as double-layer charging effects. As the charge on each PB unit cell is increased, swelling occurs via the influx of counterions to maintain electroneutrality in the film, along with osmotic-driven flow of water into the film. This mechanism is similar to that proposed by other authors for redox-active LbL films.¹³ The trend of decreased stiffness with increased charge in the film is clearly dependent on the fact that ionic crosslinks hold the film together. The opposite trend is observed in certain biological tissues, such as cartilage, where increased effective charge density (attained by minimizing shielding) results in stronger electrostatic repulsions between charged groups, which stiffen the material.³²

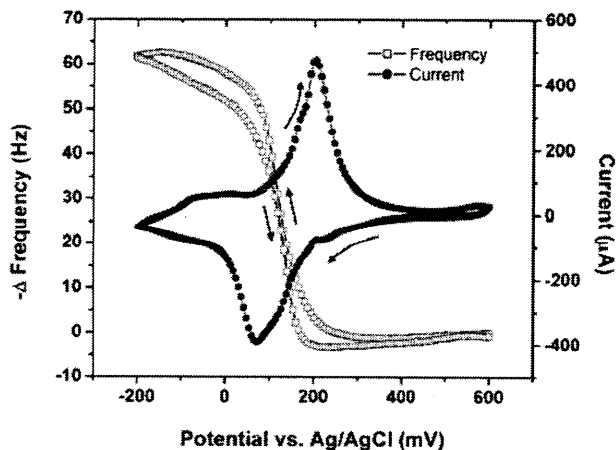


Figure 4.9. Overlay of a cyclic voltammogram and EQCM frequency data (3rd overtone) for an (LPEI/PB)₃₀ film. Scan rate is 10 mV/s. The inflection in frequency (mass change) corresponds with the potential of the Prussian Blue-Prussian White redox couple.

4.4 Conclusions

The electrochemically-triggered swelling behavior and elastic modulus reduction of a polymer nanocomposite film containing Prussian Blue nanoparticles and linear polyethyleneimine has been described. Reduction of the Prussian Blue (PB) in the films to Prussian White doubles the negative charge on the nanoparticle surface and interior. An influx of ions and water from the surrounding solution occurs to maintain electroneutrality in the film and results in film swelling and decreased mechanical stiffness of the composite. Subsequent oxidation back to the PB state causes the film to deswell and return to its original stiffness. The swelling phenomenon, characterized using spectroscopic ellipsometry and EC-AFM, is concurrent with a decrease in the film elastic modulus as measured via instrumented nanoindentation in aqueous conditions.

The system described here is distinct from existing electrochemically-active multilayer systems in several ways. The electroactive species in our films is an integral and structural component of the film, thus requiring only that the film be immersed in an electrolyte solution containing potassium ions for PB switching. On the other hand, the PB in our system exists as nanoparticles and, as such, the polyethyleneimine-Prussian Blue system is a polymer nanocomposite that can exhibit percolative mechanical behavior. While the stiffness of typical polymer-based layer-by-layer assemblies can be changed by an influx of water and ions, the stiffness of a polymer nanocomposite LbL assembly could be further affected by interactions between adjacent filler particles. We posit that the ability to electrochemically modulate the thickness of a polymer-based nanocomposite could lead to interesting control over the mechanical properties of the composite as the particle percolation threshold is approached. We are currently designing electroactive composites at the mechanical percolation threshold, which

is the critical fraction of filler above which the filler particles interact with each other with the potential to significantly stiffen the composite in the initial redox state. Assembly of composite films at or near the percolation threshold could facilitate dramatic mechanical and swelling changes upon redox, as the influx of ions and water could disrupt the percolation network and thus decrease the composite stiffness.

A future system that could be engineered to achieve rapid, dramatic mechanical changes with only slight changes in degree of swelling could be applied to the control of cellular behavior on surfaces. For example, on/off switching of cell adhesion could allow cells to be guided to particular locations within microfluidic devices, or cells could be triggered to differentiate for tissue engineering applications or fundamental studies. The system reported here, however, is likely too stiff to modulate cellular behavior. Previous reports on the tunability of cellular adhesion, locomotion, and differentiation with substrata stiffness utilize substrates with elastic modulus values in the range of 1 kPa up to 100 MPa, and generally consider one to two order-of-magnitude changes in elastic moduli.^{1,2,7,33} Therefore, the stiffness and mutability of a future electroactive mechanomutable surface must be engineered to access most cell-based applications. Nonetheless, we have introduced a new framework for electrically modulating the stiffness of a composite. Further, the fact that our system is a composite opens up the possibility of investigating disruptable percolative networks in which interactions between nanoparticles are turned on and off with an electrochemical trigger. This area represents a new direction in biomimicry, since a number of marine organisms can rapidly alter their stiffness through percolative behavior. This work can thus serve as a starting point for further studies on mechanomutable coatings with potential future applications in micro- and nanoscale devices.

4.5 References

1. Discher, D. E.; Janmey, P.; Wang, Y. L. Tissue Cells Feel and Respond to the Stiffness of Their Substrate. *Science* **2005**, *310*, 1139-1143.
2. Thompson, M. T.; Berg, M. C.; Tobias, I. S.; Rubner, M. F.; Van Vliet, K. J. Tuning Compliance of Nanoscale Polyelectrolyte Multilayers to Modulate Cell Adhesion. *Biomaterials* **2005**, *26*, 6836-6845.
3. Capadona, J. R.; Shanmuganathan, K.; Tyler, D. J.; Rowan, S. J.; Weder, C. Stimuli-Responsive Polymer Nanocomposites Inspired by the Sea Cucumber Dermis. *Science* **2008**, *319*, 1370-1374.
4. Favier, V.; Canova, G. R.; Shrivastava, S. C.; Cavaille, J. Y. Mechanical Percolation in Cellulose Whisker Nanocomposites. *Polym. Eng. Sci.* **1997**, *37*, 1732-1739.
5. Flandin, L.; Bidan, G.; Brechet, Y.; Cavaille, J. Y. New Nanocomposite Materials Made of an Insulating Matrix and Conducting Fillers: Processing and Properties. *Polym. Compos.* **2000**, *21*, 165-174.
6. Decher, G. Fuzzy Nanoassemblies: Toward Layered Polymeric Multicomposites. *Science* **1997**, *277*, 1232-1237.
7. Ren, K. F.; Crouzier, T.; Roy, C.; Picart, C. Polyelectrolyte Multilayer Films of Controlled Stiffness Modulate Myoblast Cell Differentiation. *Adv. Funct. Mater.* **2008**, *18*, 1378-1389.
8. Thompson, M. T.; Berg, M. C.; Tobias, I. S.; Lichter, J. A.; Rubner, M. F.; Van Vliet, K. J. Biochemical Functionalization of Polymeric Cell Substrata Can Alter Mechanical Compliance. *Biomacromolecules* **2006**, *7*, 1990-1995.
9. Sukhishvili, S. A. Responsive Polymer Films and Capsules Via Layer-by-Layer Assembly. *Curr. Opin. Colloid Interface Sci.* **2005**, *10*, 37-44.
10. Nolte, A. J.; Treat, N. D.; Cohen, R. E.; Rubner, M. F. Effect of Relative Humidity on the Young's Modulus of Polyelectrolyte Multilayer Films and Related Nonionic Polymers. *Macromolecules* **2008**, *41*, 5793-5798.
11. Jaber, J. A.; Schlenoff, J. B. Mechanical Properties of Reversibly Cross-Linked Ultrathin Polyelectrolyte Complexes. *J. Am. Chem. Soc.* **2006**, *128*, 2940-2947.
12. Hodak, J.; Ethenique, R.; Calvo, E. J.; Singhal, K.; Bartlett, P. N. Layer-by-Layer Self-Assembly of Glucose Oxidase with a Poly(Allylamine)Ferrocene Redox Mediator. *Langmuir* **1997**, *13*, 2708-2716.
13. Forzani, E. S.; Perez, M. A.; Teijelo, M. L.; Calvo, E. J. Redox Driven Swelling of Layer-by-Layer Enzyme-Polyelectrolyte Multilayers. *Langmuir* **2002**, *18*, 9867-9873.
14. Ma, Y. J.; Dong, W. F.; Hempenius, M. A.; Mohwald, H.; Vancso, G. J. Redox-Controlled Molecular Permeability of Composite-Wall Microcapsules. *Nat. Mater.* **2006**, *5*, 724-729.
15. Grieshaber, D.; Voros, J.; Zambelli, T.; Ball, V.; Schaaf, P.; Voegel, J. C.; Boulmedais, F. Swelling and Contraction of Ferrocyanide-Containing Polyelectrolyte Multilayers Upon Application of an Electric Potential. *Langmuir* **2008**, *24*, 13668-13676.
16. Srivastava, S.; Kotov, N. A. Composite Layer-by-Layer (LBL) Assembly with Inorganic Nanoparticles and Nanowires. *Acc. Chem. Res.* **2008**, *41*, 1831-1841.
17. Particle loading in LbL assemblies can be altered by changing film architecture (e.g., adding extra polymer layers to space apart nanoparticle layers) or by changing film assembly conditions (e.g., deposition time, pH, or ionic strength).

18. DeLongchamp, D. M.; Hammond, P. T. High-Contrast Electrochromism and Controllable Dissolution of Assembled Prussian Blue/Polymer Nanocomposites. *Adv. Funct. Mater.* **2004**, *14*, 224-232.
19. Hong, J. I.; Schadler, L. S.; Siegel, R. W.; Martensson, E. Rescaled Electrical Properties of ZnO/Low Density Polyethylene Nanocomposites. *Appl. Phys. Lett.* **2003**, *82*, 1956-1958.
20. Constantinides, G.; Kalcioğlu, Z. I.; McFarland, M.; Smith, J. F.; Van Vliet, K. J. Probing Mechanical Properties of Fully Hydrated Gels and Biological Tissues. *J. Biomech.* **2008**, *41*, 3285-3289.
21. Dimitriadis, E. K.; Horkay, F.; Maresca, J.; Kachar, B.; Chadwick, R. S. Determination of Elastic Moduli of Thin Layers of Soft Material Using the Atomic Force Microscope. *Biophys. J.* **2002**, *82*, 2798-2810.
22. Sauerbrey, G. Verwendung von Schwingquarzen zur Waegung duenner Schichten und zur Microwaegung. *Z. Phys.* **1959**, *155*, 206-222.
23. Dubas, S. T.; Schlenoff, J. B. Swelling and Smoothing of Polyelectrolyte Multilayers by Salt. *Langmuir* **2001**, *17*, 7725-7727.
24. Barbero, C.; Calvo, E. J.; Etchenique, R.; Morales, G. M.; Otero, M. An EQCM Electroacoustic Study of Poly(Vinylferrocene) Modified Electrodes in Different Aqueous Electrolytes. *Electrochim. Acta* **2000**, *45*, 3895-3906.
25. Grumelli, D.; Bonazzola, C.; Calvo, E. J. Hydration Cycling in Redox Active LBL Self-Assembled Polyelectrolyte Multilayers. *Electrochem. Commun.* **2006**, *8*, 1353-1357.
26. Hillman, A. R.; Mohamoud, M. A. Ion, Solvent and Polymer Dynamics in Polyaniline Conducting Polymer Films. *Electrochim. Acta* **2006**, *51*, 6018-6024.
27. Tagliazucchi, M.; Grumelli, D.; Calvo, E. J. Nanostructured Modified Electrodes: Role of Ions and Solvent Flux in Redox Active Polyelectrolyte Multilayer Films. *Phys. Chem. Chem. Phys.* **2006**, *8*, 5086-5095.
28. Lichter, J. A.; Thompson, M. T.; Delgadillo, M.; Nishikawa, T.; Rubner, M. F.; Van Vliet, K. J. Substrata Mechanical Stiffness Can Regulate Adhesion of Viable Bacteria. *Biomacromolecules* **2008**, *9*, 1571-1578.
29. Mendelsohn, J. D.; Yang, S. Y.; Hiller, J.; Hochbaum, A. I.; Rubner, M. F. Rational Design of Cytophilic and Cytophobic Polyelectrolyte Multilayer Thin Films. *Biomacromolecules* **2003**, *4*, 96-106.
30. Voinova, M. V.; Rodahl, M.; Jonson, M.; Kasemo, B. Viscoelastic Acoustic Response of Layered Polymer Films at Fluid-Solid Interfaces: Continuum Mechanics Approach. *Phys. Scr.* **1999**, *59*, 391-396.
31. Johannsmann, D. Viscoelastic, Mechanical, and Dielectric Measurements on Complex Samples with the Quartz Crystal Microbalance. *Phys. Chem. Chem. Phys.* **2008**, *10*, 4516-4534.
32. Dean, D.; Han, L.; Ortiz, C.; Grodzinsky, A. J. Nanoscale Conformation and Compressibility of Cartilage Aggrecan Using Microcontact Printing and Atomic Force Microscopy. *Macromolecules* **2005**, *38*, 4047-4049.
33. Levental, I.; Georges, P. C.; Janmey, P. A. Soft Biological Materials and Their Impact on Cell Function. *Soft Matter* **2007**, *3*, 299-306.

Chapter 5: Electrochemically Erasable Hydrogen-Bonded Thin Films

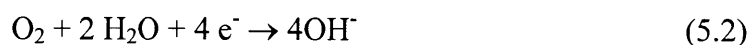
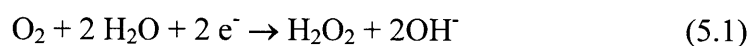
*Portions reproduced by permission of The Royal Society of Chemistry from “Electrochemically Erasable Hydrogen-Bonded Thin Films” by Daniel J. Schmidt and Paula T. Hammond, *Chem. Comm.*, 2010, 46, 7358-7360. 10.1039/c0cc02346a, © 2010 Royal Society of Chemistry.

5.1 Introduction

The ability to dynamically control the properties of a surface, thin film, or hydrogel lends itself to a number of biomedical applications, including controlled drug delivery, biosensing, separations, and cell sheet engineering, among others.^{1,2} Of the various available external stimuli, electrochemical stimuli are particularly advantageous because they can be applied rapidly, reversibly, locally, remotely, and under mild conditions at constant bulk pH and temperature. Our group and others have used electrochemical triggers to manipulate functional surfaces ranging from alkanethiol monolayers on gold³ to polyelectrolyte brushes⁴ and multilayers.⁵⁻¹⁰ Multilayered thin films constructed through layer-by-layer (LbL) assembly¹¹ represent a unique class of polymeric materials given the simplicity of fabrication, nanoscale control over composition and morphology, and variety of responsive and functional materials that can be incorporated.^{12,13} While these films are typically assembled on the basis of electrostatic interactions, a number of hydrogen (H)-bonded systems have also been studied.¹⁴ These H-bonded films have been shown to be pH-erasable since they contain a weak polyacid that will become substantially ionized at elevated pH values above the pK_a and thereby result in dissolution of the film.¹⁵ Of great importance for biomedical applications, Erel-Unal and Sukhishvili recently demonstrated the construction of H-bonded films stable under physiological conditions using tannic acid ($pK_a \sim 8.25$), a polyphenol, as the H-bond donor.¹⁶ The pH-

triggered dissolution of these films is initiated at pH 8-9.5 depending on the H-bond acceptor. While these materials are promising for a number of applications, including drug encapsulation,¹⁷ the need to elevate the bulk pH may limit their use in an *in vivo* environment.

In this manuscript, we present a strategy to electrochemically induce the dissolution of an H-bonded thin film at constant bulk pH. A cathodic potential is applied to films on conductive substrates, causing the reduction of dissolved oxygen, which generates OH⁻ ions (Reactions 5.1-5.2) and increases the local pH, resulting in the dissolution of the film (Fig. 5.1). This



electrochemically induced local pH increase was previously utilized by Kwon et al. to trigger the dissolution of a hydrogen-bonded hydrogel for the controlled release of insulin.¹⁸ Tam et al. used the reduction of oxygen to reversibly open and close an electrode interface functionalized with a polymer brush,⁴ while a number of other authors have used this phenomenon to electrochemically precipitate metal salts and oxides for various applications, including desalination of water¹⁹ and synthesis of corrosion-resistant ceramic coatings²⁰. Further, other authors including Boulmedais et al.,⁵ Dieguez et al.,⁶ and Sato et al.⁷ have used an electrochemically induced local pH *decrease* via hydrolysis of water to dissolve LbL films for applications in drug delivery. Lastly, many other authors have used electrically triggered pH gradients to swell or actuate hydrogels.²¹ Utilizing an alternative strategy, that is the electrochemical switching of redox-active nanoparticles or transition metal ions incorporated in polymer thin films, both our group^{10,22} and Wang et al.⁹ have triggered dissolution of layer-by-layer films through the charge neutralization or charge shifting of one film component, respectively.

While H-bonded LbL films have been shown to be responsive to a variety of stimuli including pH and temperature,¹⁴ this work is the first demonstration of the use of electrochemistry to manipulate these H-bonded, nanoscale thin films, greatly enhancing the prospects of these materials for applications that require mild, physiologically relevant conditions. For a model H-bonded LbL film we chose the poly(vinylpyrrolidone) (PVPON) / tannic acid (TA) system reported earlier by Sukhishvili.¹⁶ Films are denoted as (PVPON/TA)_n where *n* is the number of deposited bilayers. The films were deposited on gold-coated silicon substrates, and electric potentials were applied to the gold electrodes in a three-electrode electrochemical cell to induce film dissolution. The effects of the magnitude of the applied potential and the concentration of dissolved oxygen on film dissolution kinetics were investigated. Furthermore, we demonstrate the electrically-triggered release of an ultrathin free-standing film, using the H-bonded film as a sacrificial layer.

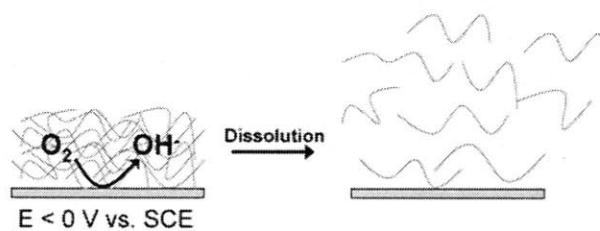


Figure 5.1. Schematic of electrochemically induced oxygen reduction at a film-coated gold electrode inducing dissolution of the film.

5.2 Materials and Methods

Materials

Polyvinylpyrrolidone (PVPON) (MW = 1.3 million), tannic acid (TA), polyallylamine hydrochloride (PAH) (MW = 70K), poly(4-styrenesulfonic acid) (SPS) (MW = 75K), sodium

sulfate (Na_2SO_4), ammonium hydroxide (NH_4OH) (25%), hydrogen peroxide (H_2O_2) (30%), and sulfuric acid were purchased from Sigma Aldrich (St. Louis, MO). Hydrochloric acid (HCl) was purchased from VWR Scientific (Edison, NJ). Polyethyleneimine, branched (BPEI) (MW = 70K) was purchased from PolySciences, Inc. All chemicals were used as received. Gold-coated silicon wafers (AU.1000.SL1) comprising a 1000 Å layer of gold with a 50 Å titanium adhesion layer were purchased from Platypus Technologies (Madison, WI).

Preparation of polymer solutions

PVPON and TA solutions were prepared at concentrations of 0.5 mg/mL with 10 mM phosphoric acid. The pH of each solution was adjusted down to 2.0 with HCl. BPEI solutions were prepared at a concentration of 0.5 mg/mL with 10 mM phosphate buffer at pH 7.5. PAH and SPS solutions were prepared at concentrations of 10 mM with respect to the repeat units with 0.5 M NaCl and were adjusted to pH 2.0. Rinse water contained 10 mM phosphoric acid and was adjusted to pH 2.0 with HCl. Deionized (DI) water (18.2 MΩ-cm, Milli-Q Ultrapure Water System, Millipore) was used to prepare all solutions.

Assembly of films

The gold-coated silicon wafers (typically 1 cm x 3 cm) were first immersed in a solution of $\text{H}_2\text{O}/\text{H}_2\text{O}_2(30\%)/\text{NH}_4\text{OH}(25\%)$ (5:1:1) solution at 75-80°C for 5 min (*Caution: cleaning solution is highly reactive and caustic*), rinsed thoroughly with DI water, and then dried under a stream of nitrogen. Next, each substrate was electrochemically cycled in 0.5 M H_2SO_4 (~20 mL) from 0.2 V to 1.6 V (vs. a saturated calomel electrode (SCE)) with a Pt wire counter electrode in a three-electrode cell. This cyclic voltammetry (CV) procedure was carried out at scan rate of 1

V/s for 100 cycles, sufficient to give a stable CV curve. This process activates the gold surface by forming and reducing a gold oxide layer on the surface. Next, the substrates were rinsed thoroughly with DI water and then immersed in a BPEI solution (0.5 mg/mL, 10 mM phosphate buffer, pH 7.5) overnight.

Subsequently, the substrates were rinsed with DI water and coated with (PVPON/TA)₂₀ films using a StratoSequence VI dip coater (nanoStrata, Inc.). This process included a 5 min immersion in the PVPON solution, followed by three 1 min rinse steps. Next, the substrate was immersed in the TA solution for 5 min, followed by three additional 1 min rinse steps. This cycle was repeated to construct films comprising the desired number of layers. After assembly, films were rinsed with DI water and dried under a stream of nitrogen.

Film thickness and morphology measurements

Film thickness was measured with spectroscopic ellipsometry using a J.A. Woollam (Lincoln, NE) M-2000 instrument. Data were fit using J.A. Woollam WVASE32 software. Since the Au layer on the Au-coated Si substrates is optically thick, only a two-layer model was required to fit the data; specifically, one layer for the gold substrate and one layer for the overlying polymer film. The optical constants of the gold were obtained through a point-by-point fit for refractive index (n) and extinction coefficient (k). The transparent polymer film ($k = 0$) was modeled as a Cauchy layer (two-term only: $n(\lambda) = A_n + B_n/\lambda$) in which the fitted parameters were film thickness, A_n , and B_n over the wavelength range 300-1000 nm. For films that exhibited a microporous morphology with a cloudy appearance, ellipsometric fits were improved by including Urbach absorption as part of the Cauchy model using WVASE32 software. An incident angle of 70° was used for all measurements. Film thickness was also checked with a

Veeco Dektak 150 Surface Profiler with a stylus tip radius of 2.5 μm and an applied stylus force of 2 mg.

Film surface morphology was investigated with atomic force microscopy (AFM) using a Dimension 3100 Scanning Probe Microscope (Veeco Instruments, Plainview, NY) in tapping mode. PointProbe Plus AFM probes (Nanosensors, Neuchatel, Switzerland) with a nominal tip radius of less than 7 nm were used. Images were flattened and the root-mean-squared (RMS) surface roughness (R_q) was determined using Veeco Nanoscope version 6.13R1 software.

Electrochemical dissolution studies and pH control studies

Electrochemical experiments were carried out with a Princeton Applied Research EG&G 263A potentiostat/galvanostat in a three-electrode cell. The electrolyte was ~ 20 mL of 10 mM Na_2SO_4 , the working electrode was a conducting Au-coated silicon substrate (10 x 30 x 0.5 mm) coated with the polymer thin film, the reference electrode was an SCE (sat. KCl), and the counter electrode was a Pt wire. Three different dissolved oxygen concentrations were investigated. Saturated O_2 levels (~ 40 ppm) were attained by bubbling pure O_2 through the electrolyte for 30 min, while ambient O_2 levels (~ 8 ppm) were attained by aerating the solution through shaking. Oxygen was eliminated from solutions (< 1 ppm) by bubbling pure N_2 through the solution for 30 min. Linear scan voltammetry, carried out at a scan rate of 50 mV/s, was executed to assess the current response at different voltages and for different dissolved oxygen levels. Potentiostatic experiments were carried out to induce film dissolution; current flow was measured over time (chronoamperometry), integrated to charge versus time (chronocoulometry), and normalized by the film area. After each experiment, films were rinsed with DI water and dried under a stream of nitrogen.

As a control, the pH-triggered dissolution of the films was studied by raising the *bulk* pH of the solution. Solutions containing 10 mM Na₂SO₄ were adjusted to pH 9, 9.5, and 10.0 by addition of dilute NaOH. Utilizing the procedure previously reported by Erel-Unal and Sukhishvili,¹⁶ films were immersed in the high pH solution and intermittently removed and dried with nitrogen gas for a thickness measurement using spectroscopic ellipsometry.

Free-standing film release

First, a (PVPON/TA)₂₀ film was assembled as described above. Next, a (PAH/SPS)₈₀ film was assembled atop the (PVPON/TA)₂₀ film using 10 min dips in the PAH and SPS baths, each followed by three, 1 minute rinses. A razor blade was then used to scratch the edges of the substrate to ensure that the film did not wrap around to the backside (not Au-coated) of the substrate. Next, an electric potential of -1.0 V (vs. SCE) was applied to the substrate in a 10 mM Na₂SO₄ electrolyte (8 ppm O₂) for 2 min with no stirring, at which point the electrolyte was gently stirred with a magnetic stirrer to facilitate release of the free-standing film.

5.3 Results and Discussion

5.3.1 Electrochemical Response of a Gold-Coated Silicon Electrode

Linear scan voltammetry was used to observe the electrochemical response of a gold electrode to a potential sweep in a 10 mM Na₂SO₄ electrolyte (pH ~5.8) in a three-electrode cell with an SCE reference electrode and Pt wire counter electrode (Fig. 5.2). Below a potential of roughly 0 V, an increase in current flow occurred due to oxygen reduction. This voltage is not as large (less negative) as that reported by Tam et al.⁴ owing to the different electrode material (Au versus ITO); indeed, gold is known to be an electrocatalyst for oxygen

reduction.²³ Below a potential of roughly -1.0 V, an abrupt increase in current flow indicates onset of the reduction of water, which also increases pH at the electrode interface. At moderately higher (anodic) voltages, only capacitive behavior was observed, which is not expected to affect local pH. Starting at +1.3 V, hydrolysis of water occurred, which lowers the pH at the interface between the electrode and the film. Therefore, the oxygen reduction potential region is roughly 0 V to -1.0 V.

Besides establishing the relevant potential window, we also observed that the magnitude of the voltage and the concentration of dissolved oxygen in the electrolyte greatly affect the current response. Deoxygenation of the electrolyte by N₂ bubbling for 30 min (<1 ppm O₂) nearly eliminates the current flow between 0 V and -1.0 V where only oxygen reduction takes place, while saturating the solution with oxygen (40 ppm O₂) increases the current flow, and thus the rate of oxygen reduction, in that range. Fig. 5.1B shows the same data displayed in Fig. 5.1A, but only in the oxygen reduction region down to -1.0 V to emphasize the impact of dissolved oxygen concentration on the current flow. The first wave in the voltage range of approximately 0 V to -0.50 V (with dependence on oxygen concentration) is attributed to reduction of oxygen to hydrogen peroxide (Reaction 5.1), while the wave at more negative voltages is attributed to the direct reduction of oxygen to water (Reaction 5.2). Clearly, in the oxygen reduction potential window, the current flow is a function of both oxygen concentration and the applied voltage. Since current flow is directly proportional to the rate of oxygen reduction, and thus the rate of generation of hydroxide ions at the electrode surface, we anticipated that the dissolution rate of hydrogen-bonded thin films can be tuned using these variables.

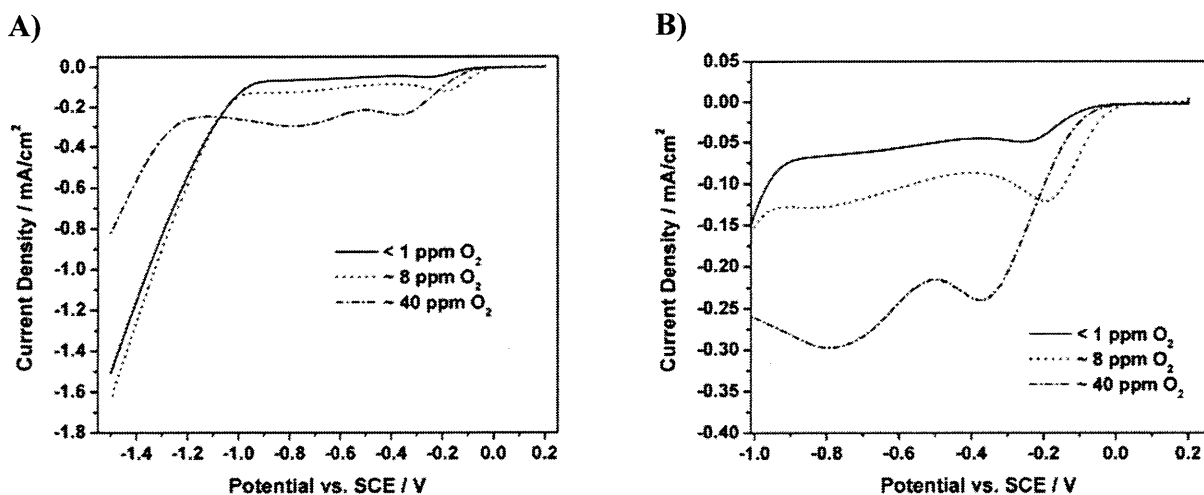


Figure 5.2. Linear scan voltammograms (A) including the reduction of water (below -1 V) and (B) including only the oxygen reduction region (0 V to -1 V) of a gold-coated Si substrate at a scan rate of 50 mV/s in 10 mM Na₂SO₄ with different concentrations of dissolved oxygen.

5.3.2 Electrochemical Dissolution – Effect of Applied Voltage

The (PVPON/TA)₂₀ films assembled on gold-coated silicon were found to have a dry thickness of 158 ± 16 nm via spectroscopic ellipsometry. Figure 5.3 shows the decrease in film thickness (Note: normalized thickness is presented instead of absolute thickness for clarity) at different applied potentials at an ambient dissolved O₂ concentration of 8 ppm. Since film dissolution proceeded within the oxygen reduction region (-0.25 V to -1.0 V), but not at more positive voltages, it appears that reduction of dissolved oxygen plays an important role in film dissolution. Specifically, analogous to the mechanism proposed by Sukhishvili and Granick for bulk pH changes,¹⁵ the OH⁻ generated by the reduction of dissolved oxygen deprotonates the phenolic hydroxyl groups in the tannic acid, thereby breaking the cohesive hydrogen bonds in the film. In addition to the absence of hydrogen bonds, the excess of negative charge generated in the film will cause an influx of counterions to maintain

electroneutrality and electroosmotic influx of water, a phenomenon reported by our group and others.^{8,24} This influx of water will then solubilize the film components.

We also observed a voltage dependence on the rate of film dissolution; in particular, a faster rate of dissolution is observed when a greater (more negative) voltage is applied. The time to 50% dissolution ranges from roughly 24 sec at -1.0 V to 5 min 50 sec at -0.25 V. From chronocoulometry, we found that the rate of charge injection into the film, which corresponds to the rate of the electrode reaction, was strongly dependent on the applied voltage (Fig. 5.3). When water was reduced (and hydrogen gas evolved) at -1.5 V, dissolution of the film occurred much faster (within 2 sec) (data not shown) since this additional electrochemical reaction rapidly generated hydroxide ions, and hydrogen bubbles may mechanically disrupt the film. Application of 0 V, where little to no oxygen reduction takes place, as well as application of +2.0 V, where oxidation of water to H^+ and O_2 takes place, did not destabilize the film. A decrease in local pH via the electrochemical generation of H^+ ions would not be expected to disrupt the stability of these films since the H-bonds are not sensitive to a pH decrease assuming that all of the H-bond donor groups in the film are already protonated. In contrast, certain layer-by-layer films of weak polyelectrolytes assembled via electrostatics have been shown to dissolve when the local pH is decreased via hydrolysis of water.^{5,6}

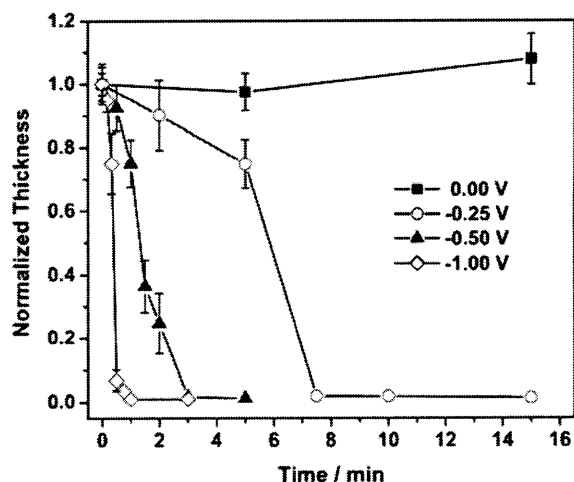


Figure 5.3. Effect of different applied voltages (at ~8 ppm dissolved O₂) on the thickness of (PVPON/TA)₂₀ films over time in 10 mM Na₂SO₄. Error bars represent ± one standard deviation from measurements taken at five different locations on each film.

To further assess the effect of the voltage magnitude, the cumulative amount of charge injected into the submerged gold electrodes was measured over time during the application of different voltages (at 8 ppm O₂) (Fig. 5.4). The magnitude of the current at each time corresponds to the rate of the reaction occurring at the electrodes, while the total amount of charge injected up to a certain time is representative of the cumulative extent of reaction. Fig. 5.4 shows charge injected versus time for (PVPON/TA)₂₀ films subjected to voltages in the range -0.25 V to -1.5 V (vs. SCE). The time to 50% dissolution of the films (determined from linear interpolation between points in Fig. 5.3) and the corresponding total charge injected at that time are listed in Table 5.1. Quantitative assessment of these results is complicated by the fact that oxygen reduction occurs through a complex reaction mechanism involving different pathways that are favored at different applied voltages and pH values.²⁵ At -0.50 V and -1.0 V, the total charge required to dissolve the film by 50% is very similar. At -0.25 V, significantly

more charge is required to dissolve the film to the same extent, while at -1.5 V, reduction of water rapidly produces OH⁻ and significantly less charge is required to dissolve the film.

Future modeling work might consider how the rate of OH⁻ generation and the influence of diffusion affect the time scale of local pH changes and the time scale for film dissolution.

Electrochemically triggered dissolution was also attempted in an electrolyte with higher ionic strength and buffering capacity, namely a phosphate buffered saline (PBS) solution at pH 7.4 and ionic strength of 0.15 M, consistent with biological pH and ion content. Despite the buffering capacity of the electrolyte, an applied potential of -1.0 V was sufficient to completely dissolve a (PVPON/TA)₂₀ film in less than 5 min. Further studies could probe the effect of electrolyte ionic strength and buffer strength on film dissolution kinetics.

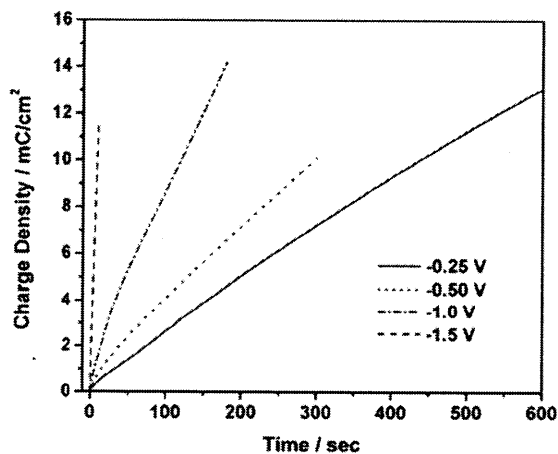


Fig. 5.4. Cumulative charge injected over time into gold electrodes coated with (PVPON/TA)₂₀ films at different applied voltages. The slope of each line corresponds to the current, that is, the rate of reaction (O₂ and/or H₂O reduction to OH⁻).

Table 5.1: Comparison of the time to 50% dissolution and the total cumulative charge injected up to that time for (PVPON/TA)₂₀ films subjected to different voltages.

Potential (V)	Time to 50% Dissolution (sec)	Total Charge Required (mC/cm²)
-0.25	351	8.28
-0.50	79.4	3.41
-1.0	23.7	3.08
-1.5	1.01	1.33

5.3.3 Electrochemical Dissolution – Effect of Oxygen Concentration

Figure 5.5 shows the decrease of film thickness for different dissolved oxygen concentrations at a constant applied potential of -0.50 V. The film did not dissolve in the deoxygenated electrolyte solution, while increasing the dissolved oxygen concentration from ambient (8 ppm) to saturated (40 ppm) resulted in an increase in film dissolution rate. These results further confirm that reduction of dissolved oxygen is the stimulating factor for electrochemically triggered film dissolution in the oxygen reduction region. Moreover, the faster rates of dissolution correspond with greater currents, that is, greater rates of oxygen reduction, as discussed above.

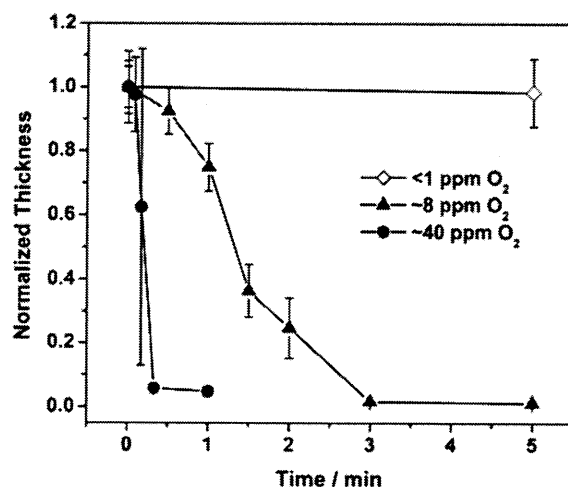


Figure 5.5. Effect of different oxygen concentrations (at -0.50 V vs. SCE) on the thickness of (PVPON/TA)₂₀ films over time in 10 mM Na₂SO₄. Error bars represent \pm one standard deviation from measurements taken at five different locations on each film.

5.3.4 Surface Morphology during Dissolution

The surface morphology of the (PVPON/TA)₂₀ films during the electrochemically triggered dissolution was studied with atomic force microscopy (AFM). Specifically, the surface morphology of the (PVPON/TA)₂₀ films was measured in the dry state for films as a function of time and applied potential. For reference, the AFM height images of the bare gold and the initial film are displayed in Fig. 5.6 and 5.7, respectively, at both height scales used in the subsequent figures. At applied potentials of -0.25 V and -0.50 V (with 8 ppm O₂) (Fig. 5.8) the film surface remains smooth ($R_q < 4$ nm) throughout the dissolution process. This observation is indicative of a top-down, or surface erosion mechanism.^{26,27} In contrast, at applied voltages of -1.0 V (with 8 ppm O₂) (Fig. 5.9) and -0.50 V (at 30 ppm O₂) (Fig. 5.10), the films develop a pitted morphology during the dissolution process. This observation is consistent with a bulk erosion mechanism, instead of a surface erosion mechanism.^{26,28} At more negative voltages,

and at higher oxygen concentrations, the rate of oxygen reduction, and thus the rate of hydroxide ion generation is increased, as shown above. Therefore, it appears that a faster onset of increased local pH and/or possibly a higher local pH results in both a more rapid decrease in film thickness and a rapid destabilization of the film structure.

The formation of pores indicates a thermodynamic instability, possibly a spinodal decomposition, as proposed by other authors for pH-induced porosity transitions in layer-by-layer films,²⁹ or a different “dewetting” mechanism involving the nucleation of holes in the film.^{30,31} In either case, when a locally high pH causes the deprotonation of the phenol groups in tannic acid, the cohesive hydrogen bonds in the film are broken. The polymer chains and tannic acid molecules are then free to explore the energy landscape and rearrange into a minimal energy conformation that results in the formation of pores. It appears that the pores grow with time and merge to form a “cellular” structure, as has been previously observed by Reiter for polystyrene films,³² before the material dissolves into solution. The bumps or ridges observed around the edges of the pores have also been observed by others,^{30,31,33} and are thought to comprise material formerly present in the interior of the pores. As an aside, the pores do reach the substrate. The average pore depth for a (PVPON/TA)₂₀ film subjected to 1.00 V for 20 sec was found to be 127 ± 18 nm (average from the measurement of 24 pores), determined via AFM. The thickness of the same film was measured to be 127 ± 10 nm with profilometry and 123 ± 14 nm with ellipsometry, identical to the pore depth.

The above observations suggest that films subjected to faster oxygen reduction undergo a phase change to a porous morphology that results in a bulk erosion mechanism, while films subjected to slower rates of oxygen reduction undergo surface erosion. The ability to tune the

erosion mechanism and erosion kinetics has important implications for controlled release applications in particular.

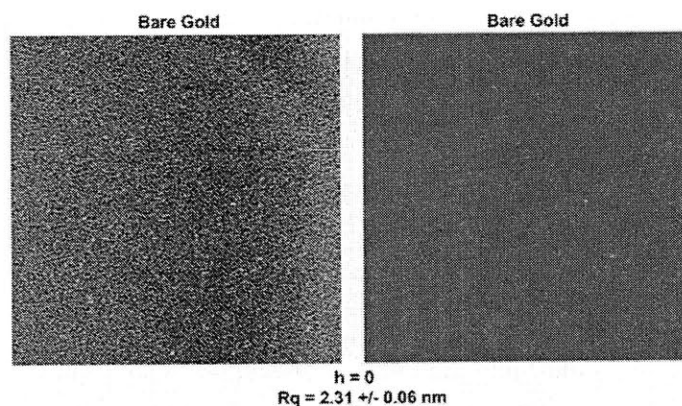


Fig. 5.6. AFM height images with scale $20\ \mu\text{m} \times 20\ \mu\text{m} \times 20\ \text{nm}$ (left) and $20\ \mu\text{m} \times 20\ \mu\text{m} \times 200\ \text{nm}$ (right) of bare, freshly cleaned gold-coated silicon slides in the dry state. The normalized film thickness (h) and RMS roughness (Rq) are reported with \pm one standard deviation from $n = 5-7$ measurements.

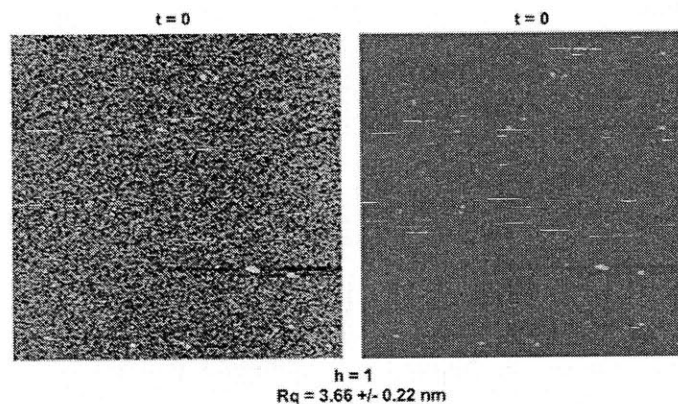


Fig. 5.7. AFM height images with scale $20\ \mu\text{m} \times 20\ \mu\text{m} \times 20\ \text{nm}$ (left) and $20\ \mu\text{m} \times 20\ \mu\text{m} \times 200\ \text{nm}$ (right) of initial $(\text{PVPON/TA})_{20}$ films in the dry state. The normalized film thickness (h) and RMS roughness (Rq) are reported with \pm one standard deviation from $n = 5-7$ measurements.

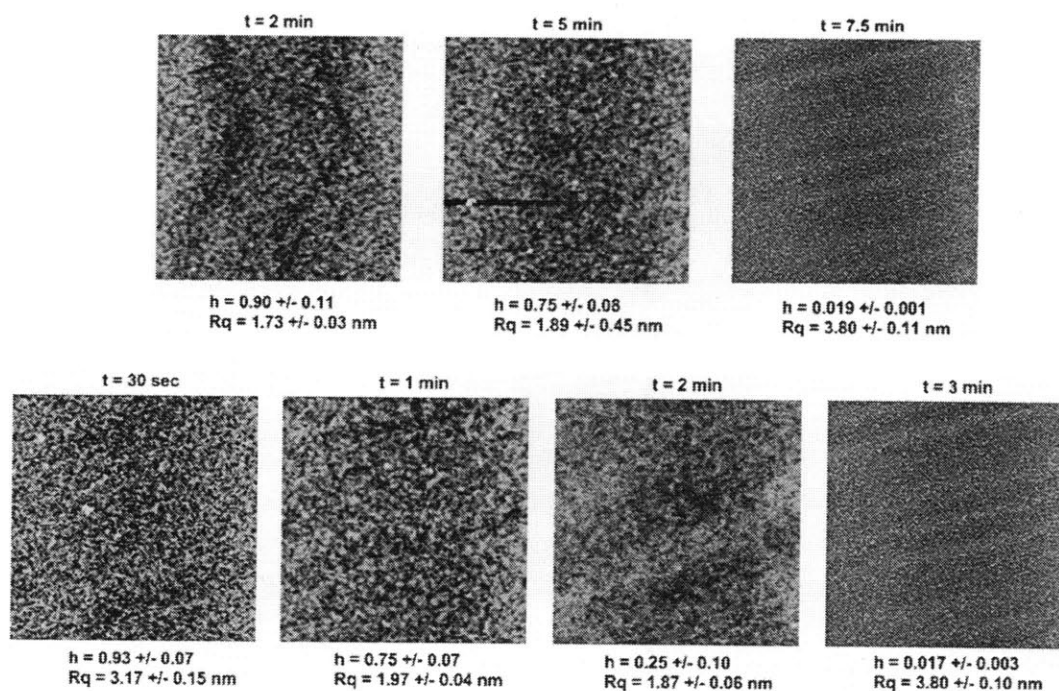


Fig. 5.8. AFM height images (scale 20 μm x 20 μm x 20 nm) of (PVPON/TA)₂₀ films in the dry state after application of -0.25 V (top row) and -0.50 V (bottom row) in a 10 mM Na₂SO₄ solution (8 ppm O₂) for the specified amounts of time. The normalized film thickness (h) and RMS roughness (Rq) are reported for each image. Values are reported with \pm one standard deviation from $n = 5-7$ measurements. At these mild voltages, the films appear to degrade by a homogeneous, top-down surface erosion mechanism.

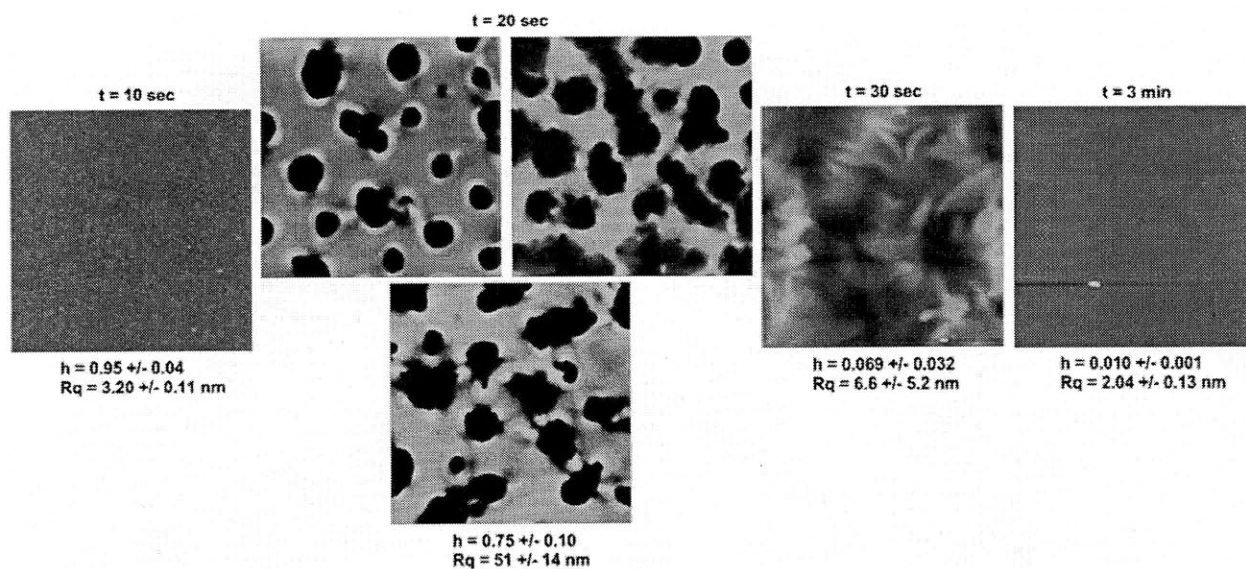


Fig. 5.9. AFM height images (scale 20 μm x 20 μm x 200 nm) of (PVPO/TA)₂₀ films in the dry state after application of -1.00 V in a 10 mM Na₂SO₄ solution (8 ppm O₂) for the specified amounts of time. The normalized film thickness (h) and RMS roughness (Rq) are reported for each image. Values are reported with \pm one standard deviation from $n = 5-7$ measurements. At this more negative voltage, the films develop a porous morphology indicative of a phase separation and they appear to degrade by a heterogeneous bulk erosion mechanism. At $t = 20$ sec, the films were not spatially homogenous; thus, images from different locations on the film are provided.

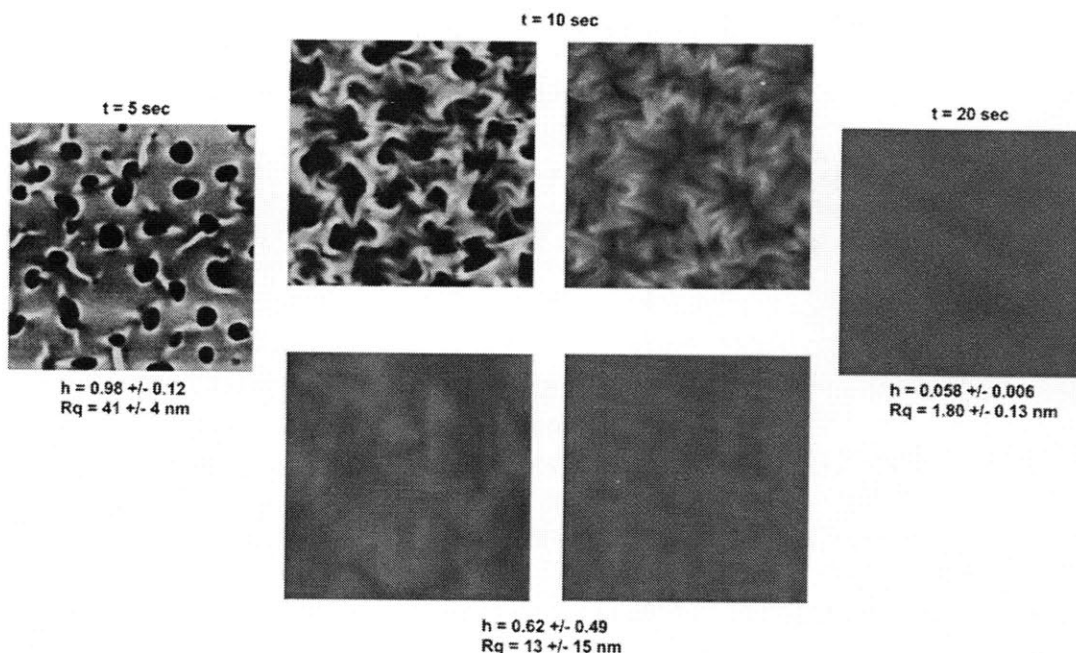


Fig. 5.10. AFM height images (scale 20 μm x 20 μm x 200 nm) of (PVPO/TA)₂₀ films in the dry state after application of -0.50 V in a 10 mM Na₂SO₄ solution (30 ppm O₂) for the specified amounts of time. The normalized film thickness (*h*) and RMS roughness (*Rq*) are reported for each image. Values are reported with \pm one standard deviation from $n = 5-7$ measurements. At this elevated concentration of dissolved oxygen, a potential of -0.50 V more rapidly increases local pH and leads to a different film erosion mechanism. As at -1.00 V with 8 ppm O₂, the films develop a porous morphology indicative of a phase separation and they appear to degrade by a heterogeneous bulk erosion mechanism. At $t = 10$ sec, the films were not spatially homogenous; thus, images from different locations on the film are provided.

5.3.5 Ultrathin Free-Standing Film Release

One important application of stimuli-responsive surfaces is the release of ultrathin free-standing films, which is especially relevant to cell sheet engineering³⁴ and to allow isolation of films for mechanical and thermal analysis.³⁵ Researchers have typically used either sacrificial substrates that can be dissolved generally w/ harsh chemicals (e.g. HF or organic solvents) or

responsive underlayers that release an overlying film in response to a stimulus.³⁶ Previously, Ono and Decher demonstrated the pH-triggered release of polyallylamine hydrochloride (PAH) / polystyrene sulfonate (PSS) multilayer films using a sacrificial H-bonded layer.³⁷ Guillaume-Gentil et al. reported the release of cell sheets from polyelectrolyte platforms by application of anodic potentials that hydrolyze water.³⁸

Here we demonstrate the electrochemically triggered release of (PAH/PSS)₈₀ films assembled atop (PVPON/TA)₂₀ films, where a potential of -1.0 V is applied to dissolve the underlying H-bonded layer. As was also observed by Ono and Decher, scratching the film was necessary to facilitate penetration of water to the film-substrate interface to assist lift off. Here we scratched the edges of the substrates, which allowed the film to release as one single sheet (Fig. 5.11). After application of -1.0 V (vs. SCE) for 2 min, however, the film would not release from the substrate without mechanical agitation. Therefore, gentle magnetic stirring was initiated, which caused the film to peel off the substrate. While the film did have a tendency to fold upon itself, it was possible to capture the film on a microscope slide and to measure the thickness of a single film layer (and multiple layers with integral multiples of thickness) with profilometry (Fig. 5.11). The thickness of the (PAH/SPS)₈₀ free-standing film was measured to be 238 ± 17 nm, while the thickness of the sacrificial (PVPON/TA)₂₀ layers before deposition of the overlying (PAH/SPS)₈₀ film was measured to be 149 ± 14 nm. Considering the thickness of the composite (PVPON/TA)₂₀(PAH/SPS)₈₀ film (i.e., 397 ± 11 nm with profilometry and 412 ± 13 nm with spectroscopic ellipsometry), the expected thickness for the free-standing film, assuming complete dissolution of the sacrificial layers would be 263 ± 20 nm. This value matches well with the actual measured thickness of the

free-standing film, which implies complete or nearly complete dissolution of the sacrificial layers.

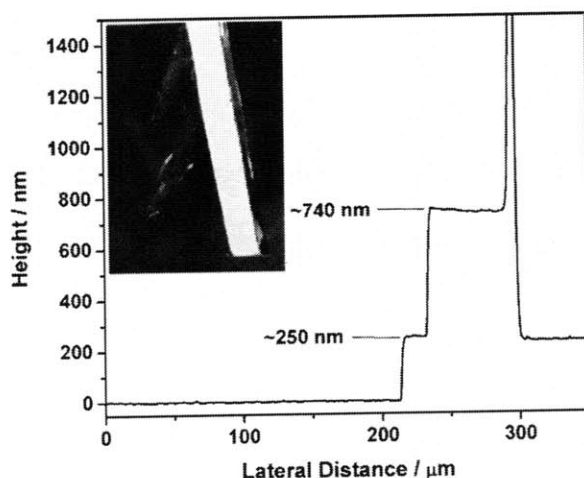


Fig. 5.11. Profilometry scan of a free-standing ultrathin (PAH/SPS)₈₀ film detached from a gold-coated silicon substrate through electrochemical dissolution of an underlying sacrificial (PVPON/TA)₂₀ film at -1.0 V (vs. SCE). Regions of a single sheet (~250 nm thick) and regions of the film folded upon itself giving integral multiples of the single sheet thickness were observed. The inset shows a photograph of the film partially detached from the substrate.

5.3.6 Control – Bulk pH-Triggered Dissolution

Dissolution of the (PVPON/TA)₂₀ films induced by raising the *bulk* pH instead of the *local* pH confirmed that the film stability is indeed compromised by an increase in pH, as has been previously shown by Erel-Unal and Sukhishvili for (PVPON/TA)₆ films on silicon.¹⁶ Fig. 5.12 shows the normalized thickness of identical (PVPON/TA)₂₀ films on gold-coated silicon over time after submersion in 10 mM Na₂SO₄ solutions of pH 9, 9.5, and 10. While Erel-Unal and Sukhishvili found the critical disintegration pH (defined as the pH that causes ~50% of the film to dissolve after 20 min) to be 9.0, we observe a slightly higher critical dissolution pH between

9.0 and 9.5. It is possible that the difference in film thickness (~25 nm for 6 bilayer films and ~160 nm for 20 bilayer films), PVPON molecular weight (360K used by Erel-Unal compared to 1.3 million used by us), supporting electrolyte (phosphate buffer used by Erel-Unal compared to sodium sulfate used by us), and/or substrate effects (silicon versus gold) may result in a slight shift in critical disintegration pH. Regardless, the electrochemical reduction of dissolved oxygen evidently raises the local pH above the critical disintegration pH for (PVPON/TA)₂₀ on gold, resulting in film dissolution. Deslouis et al. previously showed that reduction of dissolved oxygen on a gold mesh electrode in a 0.5 M K₂SO₄ solution resulted in an interfacial pH of 10.4-10.7,³⁹ well above the critical disintegration pH for the (PVPON/TA)_n system.

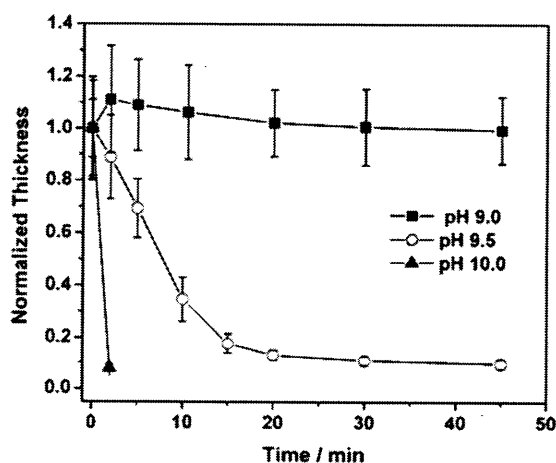


Figure 5.12. Normalized thickness of three identical (PVPON/TA)₂₀ films exposed to different bulk pH conditions over time. Error bars represent \pm one standard deviation from measurements taken at five different locations on each film.

5.4 Conclusions

In summary, we have reported here a method to electrochemically trigger the dissolution of an H-bonded layer-by-layer film comprising polyvinylpyrrolidone and tannic acid. This strategy can be achieved without the need to raise bulk pH, rather by increasing the local (interfacial) pH induced by the reduction of dissolved oxygen. Furthermore, this strategy may be extrapolated to other H-bonded films besides the system studied here. We maintain that this technique has important implications for future biomedical applications of hydrogen bonded materials. In particular, one promising application area is electrically triggered drug delivery as part of an implantable “pharmacy-on-a-chip” or transdermal device. The Sukushvili group⁴⁰ and the Caruso group⁴¹ have both demonstrated incorporation of model drugs into H-bonded films and have controlled their release through raising the pH or temperature. Further, as shown by our group, water insoluble, small molecule therapeutics can be incorporated into LbL H-bonded films by encapsulation in micelles⁴² or through covalent bonding to H-bonding species (i.e., a prodrug approach)¹⁷. Therefore, electrochemically controlled release of both H-bonding and non-H-bonding drugs seems promising.

Future work on electrically triggered dissolution of H-bonded LbL films should include modeling of the pH gradients and further study on the effects of different variables including film thickness, pH and ionic strength during film assembly and dissolution, and the effect of stirring. In addition, utilization of covalent cross-linking of H-bonded films⁴³ to allow for electrochemically triggered film swelling (and dynamic mechanical changes) instead of dissolution, analogous to work done by Elsner et al. using a pH stimulus,⁴⁴ is an interesting new direction. The ability to precisely tune the covalent crosslink density and dynamic hydrogen-

bond crosslink density within a thin film could have important implications for the study of stimuli-responsive mechanical phenomena in polymer thin films.

5.5 References

1. Roy, D.; Cambre, J. N.; Sumerlin, B. S. Future Perspectives and Recent Advances in Stimuli-Responsive Materials. *Prog. Polym. Sci.* **2010**, *35*, 278-301.
2. Tokarev, I.; Minko, S. Stimuli-Responsive Hydrogel Thin Films. *Soft Matter* **2009**, *5*, 511-524.
3. Lahann, J.; Mitragotri, S.; Tran, T. N.; Kaido, H.; Sundaram, J.; Choi, I. S.; Hoffer, S.; Somorjai, G. A.; Langer, R. A Reversibly Switching Surface. *Science* **2003**, *299*, 371-374.
4. Tam, T. K.; Pita, M.; Trotsenko, O.; Motornov, M.; Tokarev, I.; Halamek, J.; Minko, S.; Katz, E. Reversible "Closing" Of an Electrode Interface Functionalized with a Polymer Brush by an Electrochemical Signal. *Langmuir* **2010**, *26*, 4506-4513.
5. Boulmedais, F.; Tang, C. S.; Keller, B.; Vörös, J. Controlled Electrodissolution of Polyelectrolyte Multilayers: A Platform Technology Towards the Surface-Initiated Delivery of Drugs. *Adv. Funct. Mater.* **2006**, *16*, 63-70.
6. Dieguez, L.; Darwish, N.; Graf, N.; Voros, J.; Zambelli, T. Electrochemical Tuning of the Stability of PLL/DNA Multilayers. *Soft Matter* **2009**, *5*, 2415-2421.
7. Sato, K.; Kodama, D.; Naka, Y.; Anzai, J. Electrochemically Induced Disintegration of Layer-by-Layer-Assembled Thin Films Composed of 2-Iminobiotin-Labeled Poly(Ethyleneimine) and Avidin. *Biomacromolecules* **2006**, *7*, 3302-3305.
8. Schmidt, D. J.; Cebeci, F. Ç.; Kalcioglu, Z. I.; Wyman, S. G.; Ortiz, C.; Van Vliet, K. J.; Hammond, P. T. Electrochemically Controlled Swelling and Mechanical Properties of a Polymer Nanocomposite. *ACS Nano* **2009**, *3*, 2207-2216.
9. Wang, F.; Li, D.; Li, G. P.; Liu, X. Q.; Dong, S. J. Electrodissolution of Inorganic Ions/DNA Multilayer Film for Tunable DNA Release. *Biomacromolecules* **2008**, *9*, 2645-2652.
10. Wood, K. C.; Zacharia, N. S.; Schmidt, D. J.; Wrightman, S. N.; Andaya, B. J.; Hammond, P. T. Electroactive Controlled Release Thin Films. *Proc. Natl. Acad. Sci. U. S. A.* **2008**, *105*, 2280-2285.
11. Decher, G. Fuzzy Nanoassemblies: Toward Layered Polymeric Multicomposites. *Science* **1997**, *277*, 1232-1237.
12. Bertrand, P.; Jonas, A.; Laschewsky, A.; Legras, R. Ultrathin Polymer Coatings by Complexation of Polyelectrolytes at Interfaces: Suitable Materials, Structure and Properties. *Macromol. Rapid Commun.* **2000**, *21*, 319-348.
13. Hammond, P. T. Form and Function in Multilayer Assembly: New Applications at the Nanoscale. *Adv. Mater.* **2004**, *16*, 1271-1293.
14. Kharlampieva, E.; Kozlovskaya, V.; Sukhishvili, S. A. Layer-by-Layer Hydrogen-Bonded Polymer Films: From Fundamentals to Applications. *Adv. Mater.* **2009**, *21*, 3053-3065.
15. Sukhishvili, S. A.; Granick, S. Layered, Erasable, Ultrathin Polymer Films. *J. Am. Chem. Soc.* **2000**, *122*, 9550-9551.

16. Erel-Unal, I.; Sukhishvili, S. A. Hydrogen-Bonded Multilayers of a Neutral Polymer and a Polyphenol. *Macromolecules* **2008**, *41*, 3962-3970.
17. Kim, B. S.; Lee, H.; Min, Y. H.; Poon, Z.; Hammond, P. T. Hydrogen-Bonded Multilayer of pH-Responsive Polymeric Micelles with Tannic Acid for Surface Drug Delivery. *Chem. Commun.* **2009**, 4194-4196.
18. Kwon, I. C.; Bae, Y. H.; Kim, S. W. Electrically Erodible Polymer Gel for Controlled Release of Drugs. *Nature* **1991**, *354*, 291-293.
19. Gabrielli, C.; Maurin, G.; Francy-Chausson, H.; They, P.; Tran, T. T. M.; Tlili, M. Electrochemical Water Softening: Principle and Application. *Desalination* **2006**, *201*, 150-163.
20. Galor, L.; Silberman, I.; Chaim, R. Electrolytic ZrO₂ Coatings .1. Electrochemical Aspects. *J. Electrochem. Soc.* **1991**, *138*, 1939-1942.
21. Calvert, P.; Carpi, F., Smela, E., Eds.; John Wiley & Sons: Chichester, UK, 2009, p 7-33.
22. DeLongchamp, D. M.; Hammond, P. T. High-Contrast Electrochromism and Controllable Dissolution of Assembled Prussian Blue/Polymer Nanocomposites. *Adv. Funct. Mater.* **2004**, *14*, 224-232.
23. Jena, B. K.; Raj, C. R. Synthesis of Flower-Like Gold Nanoparticles and Their Electrocatalytic Activity Towards the Oxidation of Methanol and the Reduction of Oxygen. *Langmuir* **2007**, *23*, 4064-4070.
24. Tagliacruzchi, M.; Grumelli, D.; Calvo, E. J. Nanostructured Modified Electrodes: Role of Ions and Solvent Flux in Redox Active Polyelectrolyte Multilayer Films. *Phys. Chem. Chem. Phys.* **2006**, *8*, 5086-5095.
25. Hoare, J. P. *The Electrochemistry of Oxygen*; Interscience Publishers: New York, 1968.
26. Fredin, N. J.; Zhang, J. T.; Lynn, D. M. Surface Analysis of Erodible Multilayered Polyelectrolyte Films: Nanometer-Scale Structure and Erosion Profiles. *Langmuir* **2005**, *21*, 5803-5811.
27. von Burkersroda, F.; Schedl, L.; Gopferich, A. Why Degradable Polymers Undergo Surface Erosion or Bulk Erosion. *Biomaterials* **2002**, *23*, 4221-4231.
28. Lu, L.; Garcia, C. A.; Mikos, A. G. In Vitro Degradation of Thin Poly(DL-Lactic-Co-Glycolic Acid) Films. *J. Biomed. Mater. Res., Part A* **1999**, *46*, 236-244.
29. Mendelsohn, J. D.; Barrett, C. J.; Chan, V. V.; Pal, A. J.; Mayes, A. M.; Rubner, M. F. Fabrication of Microporous Thin Films from Polyelectrolyte Multilayers. *Langmuir* **2000**, *16*, 5017-5023.
30. Seemann, R.; Herminghaus, S.; Jacobs, K. Dewetting Patterns and Molecular Forces: A Reconciliation. *Phys. Rev. Lett.* **2001**, *86*, 5534-5537.
31. Xie, R.; Karim, A.; Douglas, J. F.; Han, C. C.; Weiss, R. A. Spinodal Dewetting of Thin Polymer Films. *Phys. Rev. Lett.* **1998**, *81*, 1251-1254.
32. Reiter, G. Dewetting of Thin Polymer-Films. *Phys. Rev. Lett.* **1992**, *68*, 75-78.
33. Lutkenhaus, J. L.; McEnnis, K.; Hammond, P. T. Nano- and Microporous Layer-by-Layer Assemblies Containing Linear Poly(Ethylenimine) and Poly(Acrylic Acid). *Macromolecules* **2008**, *41*, 6047-6054.
34. Matsuda, N.; Shimizu, T.; Yamato, M.; Okano, T. Tissue Engineering Based on Cell Sheet Technology. *Adv. Mater.* **2007**, *19*, 3089-3099.
35. Lutkenhaus, J. L.; Hrabak, K. D.; McEnnis, K.; Hammond, P. T. Elastomeric Flexible Free-Standing Hydrogen-Bonded Nanoscale Assemblies. *J. Am. Chem. Soc.* **2005**, *127*, 17228-17234.

36. Jiang, C. Y.; Tsukruk, V. V. Freestanding Nanostructures Via Layer-by-Layer Assembly. *Adv. Mater.* **2006**, *18*, 829-840.
37. Ono, S. S.; Decher, G. Preparation of Ultrathin Self-Standing Polyelectrolyte Multilayer Membranes at Physiological Conditions Using pH-Responsive Film Segments as Sacrificial Layers. *Nano Lett.* **2006**, *6*, 592-598.
38. Guillaume-Gentil, O.; Akiyama, Y.; Schuler, M.; Tang, C.; Textor, M.; Yamato, M.; Okano, T.; Voros, J. Polyelectrolyte Coatings with a Potential for Electronic Control and Cell Sheet Engineering. *Adv. Mater.* **2008**, *20*, 560-565.
39. Deslouis, C.; Frateur, I.; Maurin, G.; Tribollet, B. Interfacial pH Measurement During the Reduction of Dissolved Oxygen in a Submerged Impinging Jet Cell. *J. Appl. Electrochem.* **1997**, *27*, 482-492.
40. Kharlampieva, E.; Erel-Unal, I.; Sukhishvili, S. A. Amphoteric Surface Hydrogels Derived from Hydrogen-Bonded Multilayers: Reversible Loading of Dyes and Macromolecules. *Langmuir* **2007**, *23*, 175-181.
41. Quinn, J. F.; Caruso, F. Facile Tailoring of Film Morphology and Release Properties Using Layer-by-Layer Assembly of Thermoresponsive Materials. *Langmuir* **2004**, *20*, 20-22.
42. Kim, B. S.; Park, S. W.; Hammond, P. T. Hydrogen-Bonding Layer-by-Layer Assembled Biodegradable Polymeric Micelles as Drug Delivery Vehicles from Surfaces. *ACS Nano* **2008**, *2*, 386-392.
43. Yang, S. Y.; Rubner, M. F. Micropatterning of Polymer Thin Films with pH-Sensitive and Cross-Linkable Hydrogen-Bonded Polyelectrolyte Multilayers. *J. Am. Chem. Soc.* **2002**, *124*, 2100-2101.
44. Elsner, N.; Kozlovskaya, V.; Sukhishvili, S. A.; Fery, A. pH-Triggered Softening of Crosslinked Hydrogen-Bonded Capsules. *Soft Matter* **2006**, *2*, 966-972.

Chapter 6: Mechanomutable Polyelectrolyte Thin Films Controlled by Electrochemically Induced pH Gradients

*Portions reproduced from “Mechanomutable Polyelectrolyte Thin Films Controlled by Electrochemically Induced pH Gradients” by Daniel J. Schmidt, Younjin Min, and Paula T. Hammond, *In preparation*.

6.1 Introduction

As described in the previous chapter, control over the local pH at an electrode interface is a viable strategy to manipulate pH-responsive thin films. Previously, in the field of LbL assembly, electrochemically triggered local pH gradients have only been used to dissolve thin films. Here, for the first time, that strategy is employed to reversibly swell and deswell a polymer film and concomitantly induce large mechanical changes of much greater magnitude than has been reported for other LbL films. The films comprise polyallylamine hydrochloride (PAH) and sulfonated polystyrene (SPS) assembled at pH 9.3, and will be denoted as (PAH/SPS)_n where *n* is the number of deposited bilayers. As previously reported by the Rubner group, these films exhibit a pH-switchable, discontinuous swelling/deswelling transition with a large hysteresis loop.¹⁻³ When exposed to a pH ≤ 4, the films swell to 400-800% of their initial thickness; when exposed to pH ≥ 10.5, the films deswell to their original thickness. The film swelling state is dictated by the degree of ionization of the PAH. Here, instead of changing *bulk* pH, we control the film swelling state by manipulating only the *local* pH. In solutions with bulk pH in the range of 3 to 4, we apply electric potentials that reduce dissolved oxygen by Reactions 6.1 and 6.2 below. At more negative potentials, water can be reduced by Reaction 6.3 below.



The generation of hydroxide ions raises the pH in the vicinity of the electrode, allowing for film deswelling (Fig. 6.1). Switching the voltage off causes the pH gradient to dissipate and the film to reswell. We study the influence of different variables (film thickness, magnitude of the applied voltage, and bulk pH) on the magnitude, kinetics, and reversibility of the electrochemically controlled swelling/deswelling transition utilizing *in situ* electrochemical spectroscopic ellipsometry. To probe film mechanical properties, we utilize an electrochemical quartz crystal microbalance with dissipation monitoring (EQCM-D).

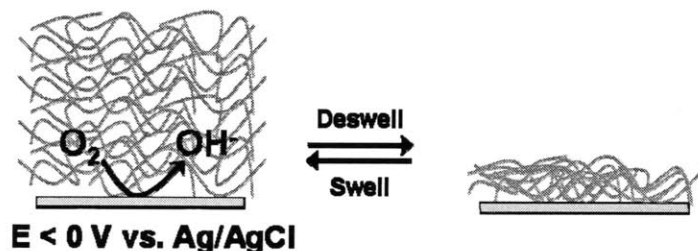


Figure 6.1. Schematic of electrochemically induced deswelling of a $(\text{PAH/SPS})_n$ film through an increase in local pH.

6.2 Materials and Methods

Materials

Poly(allylamine hydrochloride) (PAH) ($M_w = 70,000$), poly(sodium 4-styrenesulfonate) (SPS) ($M_w = 75,000$), hydrogen peroxide (30 wt% solution in water), and ammonium hydroxide (28-30 wt% in water) were purchased from Sigma Aldrich and used as received. Sodium carbonate and sodium bicarbonate were purchased from Mallinckrodt Chemicals. Hydrochloric acid (1 M

solution) and sodium hydroxide (1 M solution) were purchased from VWR. Deionized water ($>18.2 \text{ M}\Omega\cdot\text{cm}$ resistivity), obtained using a Milli-Q Plus system (Millipore, Bedford, MA), was used to make all solutions. Gold-coated silicon wafers (AU.1000.SL1) consisting of a 1000 Å layer of gold with a 50 Å titanium adhesion layer were purchased from Platypus Technologies, LLC. Gold-coated QCM crystals (QSX 301) consisting of a 1000 Å layer of gold with a 50 Å chromium adhesion layer were purchased from Q-Sense, Inc.

Assembly of PAH/SPS Films

Films were assembled on gold-coated silicon wafers or gold-coated AT-cut quartz crystals. Both substrates were cleaned with an RCA cleaning solution (5:1:1 $\text{H}_2\text{O}:\text{H}_2\text{O}_2$ (30%): NH_3 (25%)) at 75°C for 5 minutes, rinsed copiously with deionized water, and dried under a stream of nitrogen gas. Next, each substrate was electrochemically cycled in 0.5 M H_2SO_4 (~20 mL) from 0.2 V to 1.6 V (vs. Ag/AgCl (3 M NaCl)) with a Pt wire counter electrode in a three-electrode cell. This cyclic voltammetry (CV) procedure was carried out at scan rate of 1 V/s for 100 cycles, sufficient to give a stable CV curve. This process activates the gold surface by forming and reducing a gold oxide layer on the surface. Next, the substrates were rinsed thoroughly with DI water and then immersed in a PAH solution. PAH and SPS solutions were prepared in deionized water at a concentration of 10 mM based on the polymer repeat unit. The pH of the PAH solution was adjusted to pH 9.3 with 1 M NaOH, while the pH of the SPS solution was set to pH 9.3 with a 10 mM carbonate buffer to eliminate pH drift. $(\text{PAH/SPS})_n$ films, where n denotes the number of bilayers, were assembled by dip coating using an automated Zeiss HMS Series programmable slide stainer. The positively-charged substrates (owing to the layer of PAH) were immersed in an SPS solution for 10 min followed by three separate deionized water rinse baths

(adjusted to pH 9.3 with 10 mM carbonate buffer) for a total of three minutes. Next, the substrates were immersed in PAH solution for 10 minutes followed by the same cascade rinse cycle. This alternating deposition process was repeated until films were assembled with the desired number of bilayers. Gold-coated silicon substrates were used for spectroscopic ellipsometry, while gold-coated quartz was used for EQCM-D.

Spectroscopic Ellipsometry

Film thickness was measured both dry and *in situ* at room temperature (25 °C) with spectroscopic ellipsometry using a J.A. Woollam (Lincoln, NE) M-2000 instrument at an incident angle of 70°. *In situ* measurements were conducted through a custom-made quartz cell with 70° windows (Hellma USA, Inc.). Data were modeled using J.A. Woollam WVASE32 software. Since the Au layer on the Au-coated Si substrates is optically thick, only a two-layer model was required to fit the data; specifically, one layer for the gold substrate and one layer for the overlying polymer film. The optical constants of the gold were obtained through a point-by-point fit for refractive index (n) and extinction coefficient (k). The transparent polymer film ($k = 0$) was modeled as a Cauchy layer (two-term only: $n(\lambda) = A_n + B_n / \lambda$) in which the fitted parameters were film thickness, A_n , and B_n over the wavelength range 300-1000 nm. To simultaneously apply a voltage to a film-coated electrode while characterizing the film with spectroscopic ellipsometry, a three-electrode electrochemical cell was set up in the quartz cell with a Ag/AgCl (3 M NaCl) reference electrode (Bioanalytical Systems, Inc.), a Pt coil counter electrode, and a Au-coated Si wafer modified with a (PAH/SPS)_n film as the working electrode. The electrolyte was an NaCl solution with pH 3-4 and total ionic strength of 3.6 mM (combination of HCl and NaCl). An AutoLab PGSTAT100 potentiostat was used for

electrochemical measurements. A dynamic scan protocol in the WVASE32 software package with acquisition time of ~10 milliseconds was used to capture the kinetics of the redox-induced swelling process.

Quartz Crystal Microbalance with Dissipation Monitoring

EQCM-D analysis of (PAH/SPS)_{5.5} films on gold-coated quartz was carried out using a Q-Sense E1 system along with the Electrochemistry Module (QEM 401). The quartz crystals were cleaned as described above, and (PAH/SPS)_{5.5} films were assembled in the QCM chamber by the following procedure. A PAH solution was pumped into the chamber and the polymer was allowed to adsorb for 10 min under static conditions. Next, rinse water was pumped through the chamber for ~3 min at a flow rate of ~1 $\mu\text{L}/\text{min}$. Then an SPS solution was pumped through the chamber, adsorption allowed for 10 min, and rinse water flowed through for ~3 min. The cycle was repeated 5.5 times. Film swelling was then induced by flowing through a pH 4.0 solution (3.6 mM ionic strength adjusted with NaCl). A voltage could then be applied to the film directly in the QCM chamber, which served as a three-electrode electrochemical cell with a Ag/AgCl (3 M NaCl) reference electrode (Cypress Systems), a built-in Pt counter electrode, and the Au-coated QCM crystal modified with a (PAH/SPS)_{5.5} film as the working electrode. A PG580 potentiostat/galvanostat (Uniscan Instruments) was used for electrochemical measurements. Experiments were carried out at room temperature (25 °C).

6.3 Results and Discussion

6.3.1 Film Assembly and Swelling

The thickness of (PAH/SPS)_n films assembled at pH 9.3/9.3 on Au-coated Si was measured with spectroscopic ellipsometry. Fig. 6.2 shows the film thickness as a function of number of deposited bilayers, *n*, for films in the dry state, immersed in DI water for 5 min, and immersed in pH 4 electrolyte solution for 15 min. These films exhibit linear growth, meaning that thickness increases linearly with *n*, with a thickness per bilayer of roughly 6-8 nm based on dry thickness. The bilayer thickness we measured is higher than that reported by the Rubner group (4.9 nm) on account of the 10 mM carbonate buffer we added to the SPS solution and rinse baths to stabilize the pH. Indeed, it is well known that addition of salt to polyelectrolyte solutions increases the thickness of each layer.⁴

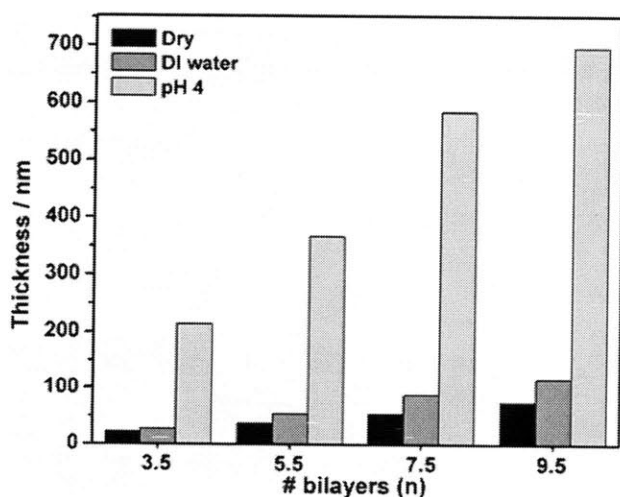


Figure 6.2. Thickness of (PAH/SPS)_n films in the dry state, immersed in DI water for 1 min, and immersed in pH 4 water for 15 min, as determined with spectroscopic ellipsometry.

Table 6.1. Percent swelling (relative to dry thickness) of (PAH/SPS)_n films in DI water and in pH 4 water.

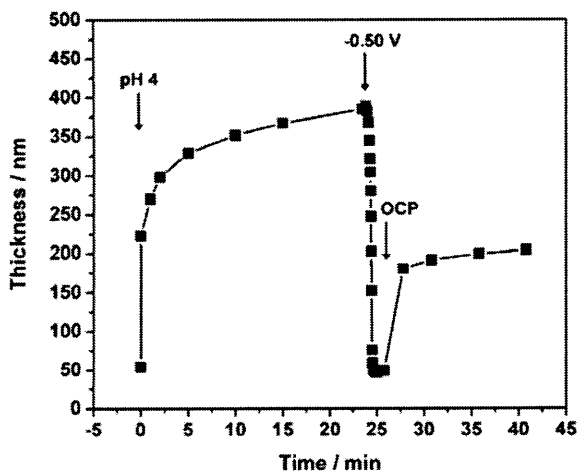
<i>n</i>	% Swelling (DI water)	% Swelling (pH 4 water)
3.5	24.4	876
5.5	43.5	876
7.5	63.2	983
9.5	56.3	833

The swelling behavior of the films is summarized in Table 6.1. In DI water (pH 5.5-6) the films swell moderately by roughly 24-63% of dry thickness, reaching a plateau swollen thickness within 1 min. When exposed to $\text{pH} \leq 4$, the films swell dramatically to 833-983% of their dry thickness and 500-685% of their hydrated thickness in DI water within 15 min. These swelling results are in accordance with previous reports from the Rubner group, who showed that $\text{pH} \sim 4$ is the onset swelling pH corresponding roughly to the pK_a of the PAH in the assembled film.^{1,2} Note that the pK_a is shifted to more acidic values compared to that of free PAH (~ 8.5) in solution due to the hydrophobic microenvironment in the film.^{1,5} At the effective film pK_a , the degree of ionization of PAH changes from about 70% to above 95% as measured via FTIR by the Rubner group.² In response to the excess positive charges introduced in the film as well as the local acidic environment, counterions (*e.g.* OH^- , Cl^-), to maintain electroneutrality, and water, via electroosmotic flux, enter the film and disrupt hydrophobic interactions resulting in a dramatic swelling transition. With the film in the swollen state, the pK_a of the PAH is shifted back to higher pH values;^{1,2} at a pH of 10.5, the film deswells back to its original thickness, forming a large hysteresis loop.

6.3.2 Electrochemically Triggered Deswelling

While it is well established that the swelling state of PAH/SPS films may be controlled with *bulk* pH, here we demonstrate control over the swelling state at a constant bulk pH using an electrochemically induced *local* pH change. A three-electrode electrochemical cell was then set up on the stage of a spectroscopic ellipsometer inside a quartz cell (see Experimental Section), which allowed simultaneous application of an electric potential to the film-coated electrode plus measurement of film thickness. As shown in a previous publication from our group, application of voltages in the range -0.25 V to -1.00 V (vs. Ag/AgCl (3M NaCl)) to gold substrates results in the reduction of dissolved oxygen at the electrode surface.⁶ That reaction generates hydroxide ions, which raise the local/interfacial pH near the electrode surface.⁷ As an initial proof of concept, we immersed a (PAH/SPS)_{5.5} film in a pH 4 electrolyte solution, such that the film underwent a swelling transition from ~54 nm thick in DI water to ~390 nm thick in the pH 4 solution. When a potential of -0.50 V was applied, the film underwent a deswelling transition to a thickness of 49 nm, near its original thickness in DI water, within 1 min (Fig 6.3A). When the potential was turned off and the open circuit potential was restored (~-0.20 V), the film gradually reswelled to ~195 nm (Fig 6.3A) as the local pH gradient was “erased” by diffusion of the hydroxide ions into the bulk solution. Multiple swell/deswell cycles were performed to assess the reversibility of the transition (Fig 6.3B). It is apparent

A)



B)

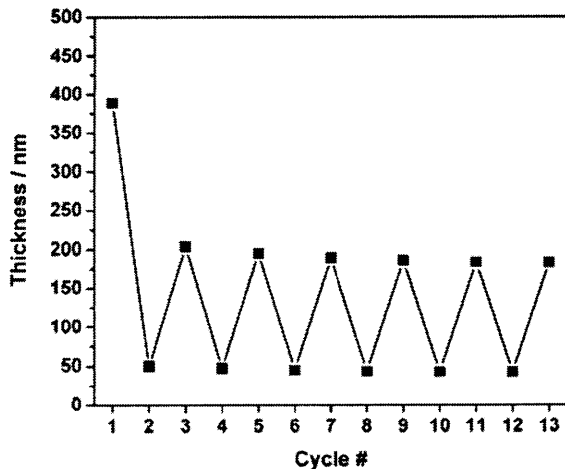


Figure 6.3. (A) Thickness of (PAH/SPS)_{5.5} swollen at pH 4, deswollen at -0.50 V, and reswollen at the open circuit potential (OCP). (B) Thickness of (PAH/SPS)_{5.5} after multiple swell (at pH 4) and deswell (-0.50 V) cycles. Odd numbered cycle numbers correspond to the OCP, while even numbered cycles correspond to application of -0.50 V.

that after the first deswelling transition, the film does not reswell to its original thickness.

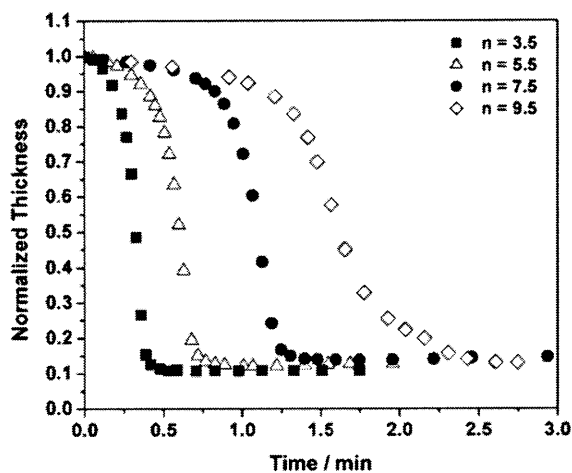
Rather, it only attains approximately 50% of its original thickness. Subsequent swell/deswell

cycles exhibit relatively reversible behavior with only a slight decrease in film thickness over time. Similar trends were observed for all films studied regardless of film thickness, bulk pH, and the applied potential. Hiller et al. commented on incomplete reversibility during reswelling at acidic pH for the same system. They report that immersion of the film for extended periods of time at $\text{pH} > 6$, or at elevated temperatures, strengthens the hydrophobic interactions in the film irreversibly, limiting the ability of the film to swell. They also note the possibility that the film has entered a different hysteresis loop.⁸ Alternatively, we believe it is likely that some more weakly bound material is lost from the film during the first swell/deswell cycle. If film densification were occurring, we would expect the films to exhibit higher indices of refraction and greater shear elastic moduli following any densification. We observed, however, that these values are equivalent for films before and after multiple swell/deswell cycles. We also carried out control experiments in which films were deswollen by raising the bulk pH instead of through electrochemistry; in this case, we also observed a decrease in swellability following the first cycle (data not shown). Therefore, the observed loss of reversibility is not due to the electrochemical induction of local pH changes.

6.3.3 Effect of Film Thickness on Deswelling Kinetics

Since film swelling and deswelling rely on the diffusion of water into and out of the film, respectively, we expected the swelling/deswelling kinetics to vary with the film thickness. To study this variable, we investigated $(\text{PAH/SPS})_n$ films with $n = 3.5, 5.5, 7.5,$ and 9.5 . Figure 6.4A shows the kinetics of electrically triggered deswelling at an applied potential of -0.50 V at pH 4. Qualitatively,

A)



B)

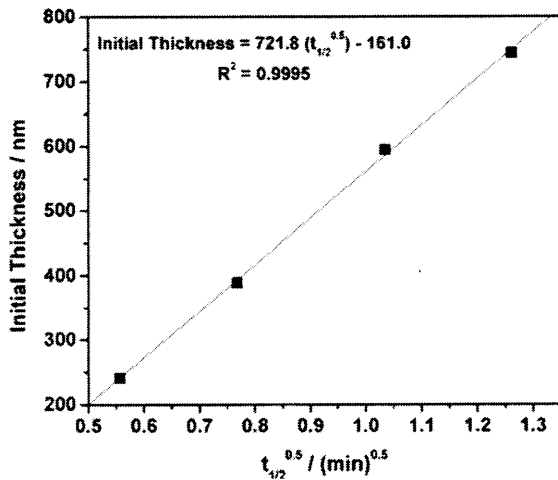


Figure 6.4. (A) Thickness of (PAH/SPS)_n at an applied potential of -0.50 V in a pH 4 electrolyte solution. The thickness was normalized to the initial swollen thickness in pH 4, which can be found in Fig. 1. The data shown are for the first deswell cycle. (B) Linear relationship between the initial film thickness and the square root of the deswelling time indicates that diffusion of water out of the film controls the rate of film deswelling.

it is clear that thicker films deswell more slowly than thinner films given the greater distance required for the diffusion of water to reach the same degree of swelling. Quantitatively, we found that the square root of the half deswelling time scales linearly with the initial thickness of the film (Fig. 6.4B). The half deswelling time ($t_{1/2}$) was quantified based on a Boltzmann sigmoidal fit to the thickness versus time data (Equation 6.4) where h is the film thickness as a function of time, $h_{deswollen}$ is the film thickness in the deswollen state from the model fit (right, horizontal asymptote), $h_{swollen}$ is the film thickness in the swollen state from the model fit (left, horizontal asymptote), t is time, $t_{1/2}$ is the time at the point of inflection, and t_{width} is the sigmoid width from the model fit. The Boltzmann sigmoid fit all of the deswelling data very well giving R^2 values of at least 0.996. The deswelling time scale was taken as the $t_{1/2}$ value. The square root dependence of deswell time with thickness implies that diffusion is the rate controlling step for film deswelling; however, poroelasticity may also play a role in controlling water transport. If we assume that diffusion of water out of the film is the rate limiting step for film deswelling, then the order of magnitude of the diffusivity of water in the polymer film may then estimated by Equation 6.5 (for Fickian diffusion), which gives values in the range of 3×10^{-11} to 6×10^{-11} cm^2/s . These values are within the range reported for water diffusivity in hydrophilic polymers⁹ and within an order of magnitude of values reported by us for another layer-by-layer film.¹⁰

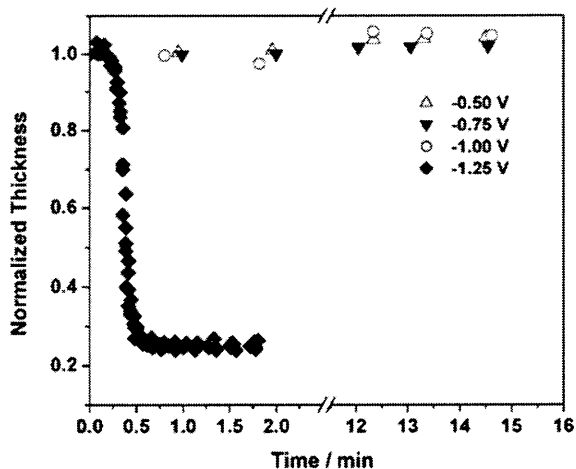
$$h(t) = h_{deswollen} + \frac{h_{swollen} - h_{deswollen}}{1 + \exp\left[\frac{(t - t_{1/2})}{t_{width}}\right]} \quad (6.4)$$

$$D_{H_2O} \approx \frac{(h_{swollen})^2}{t_{1/2}} \quad (6.5)$$

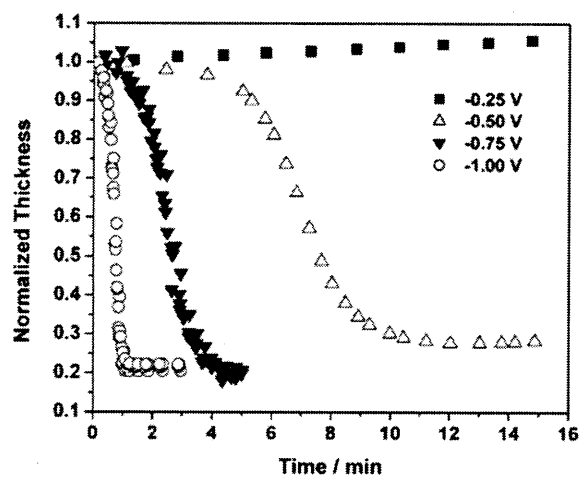
6.3.4 Effect of Magnitude of Applied Potential on Deswell Kinetics

A key variable to tune the rate of electrochemically induced film deswelling is the magnitude of the applied potential. Since oxygen reduction is a mass-transfer limited process, a current “plateau” (i.e., a constant rate of oxygen reduction) is generally observed in the oxygen reduction potential range.⁷ However, as shown by us in a previous publication, application of a more negative potential does modestly increase the rate of oxygen reduction, which speeds up the response of polymer films sensitive to elevated pH.⁶ In agreement with these past results, we observe that more negative voltages induce a faster rate of electrochemically triggered deswelling of (PAH/SPS)_n films (Fig. 6.5). At a bulk pH of 4, the half deswelling time can be tuned from 9 sec at -1.00 V to 1 min 42 sec at -0.25 V. An applied potential of 0 V does not raise the local pH sufficiently to deswell the film, while a more negative voltage of -1.00 V induces the reduction of water (i.e., decomposition of the solvent) (Reaction 6.3), which evolves hydrogen gas and also generates hydroxide ions that raise the local pH. Deswelling can be triggered even faster at these more negative voltages (data not shown); however, solvent decomposition and hydrogen evolution may be undesired for an end application.

A)



B)



C)

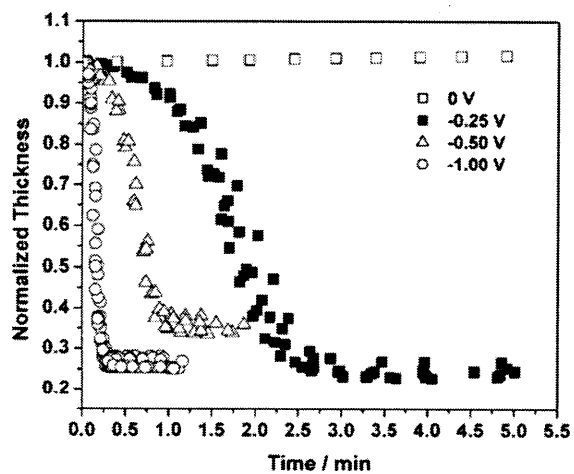


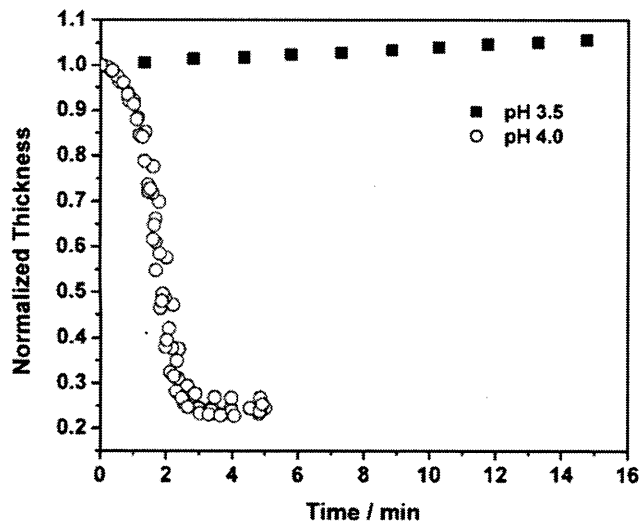
Figure 6.5. Normalized thickness versus time of (PAH/SPS)_{5.5} films at bulk pH values of (A) 3.0, (B) 3.5, and (C) 4.0. The minimum electric potential required to deswell the film depends strongly on the bulk pH. Thickness is normalized to the swollen film thickness at the open circuit potential after the first swell/deswell cycle. Data for multiple cycles are reported to show reproducibility.

6.3.5 Effect of Bulk pH on Deswell Kinetics

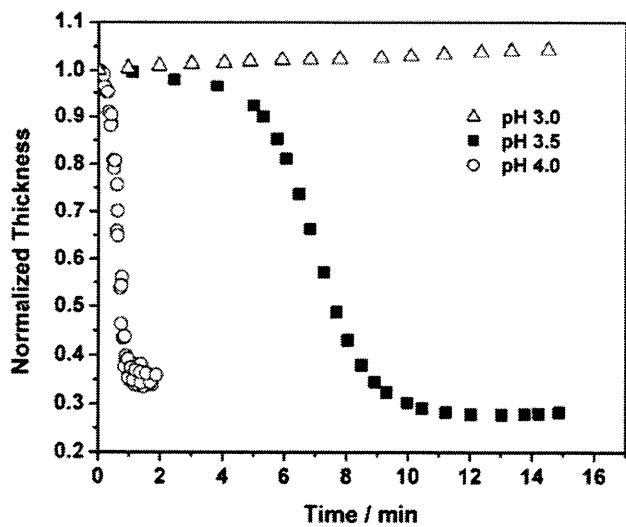
Above, we described the effect of the magnitude of the applied voltage at a bulk pH of 4, which is roughly the highest pH at which the films exist in a superswollen state.² At lower bulk pH values, the same voltage may induce slower deswelling kinetics or may not induce deswelling at all (Fig. 6.6). In effect, each bulk pH has a different critical voltage that is required to induce film deswelling. The value of the bulk pH evidently affects how high of a local pH may be attained by any given applied potential. In Deslouis et al., the authors neglect the concentration of OH⁻ ions in the bulk (i.e., the bulk pH) relative to the concentration at the electrode surface for their derivation of the interfacial pH; however, the pH profile (i.e., the concentration of OH⁻ that extends from the electrode interface into the bulk) seemingly depends upon the bulk pH, given the results of our experiments. While reversible swell/deswell cycles controlled by an electrochemical trigger are only possible at pH < 4, it is possible to deswell the film one time under milder pH conditions. As shown by Hiller et al., the PAH/SPS system exhibits a large swelling hysteresis with so-called “molecular memory”.¹ If a film is swollen below pH 4 and then transferred to a pH 7.4 solution, it will remain in the swollen state. Therefore, to demonstrate the electrochemically triggered deswelling phenomenon at milder conditions, we pre-swelled a film at pH < 4, transferred the film to a pH 7.4 solution with equivalent ionic strength, and applied -0.25 V (Fig. 6.7). When the potential is turned off, however, the film will not reswell unless transferred back to a solution with pH < 4 (Fig. 6.7). While the ability to deswell the film under milder conditions is promising for biomedical applications, there is also an ionic strength dependence on the film swelling state that is not systematically explored in this manuscript. When a film pre-swollen at pH 4 is

immersed in a PBS solution (pH 7.4, 0.15 M ionic strength), representative of physiological conditions, the film immediately deswells due to the decrease in the osmotic pressure force to swell the film. That is, the difference in salt concentration between the film and surrounding solution is no longer sufficient to maintain the film in a superswollen state.

A)



B)



C)

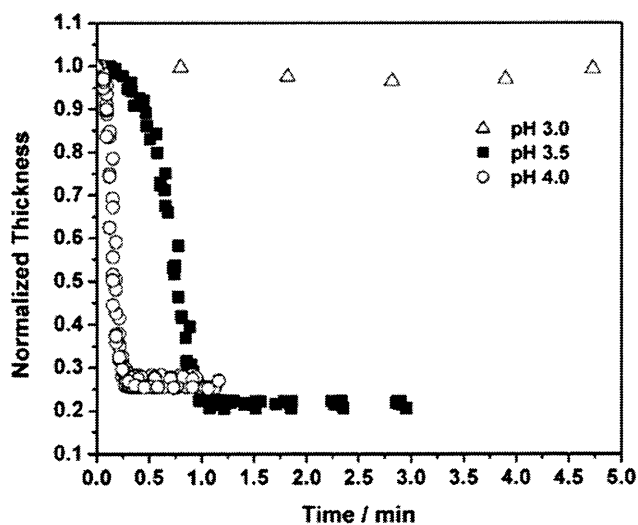


Figure 6.6. Normalized thickness versus time of (PAH/SPS)_{5.5} films at (A) -0.25 V, (B) -0.50 V, and (C) -1.0 V. Thickness is normalized to the swollen film thickness at the open circuit potential after the first swell/deswell cycle. Data for multiple cycles are reported to show reproducibility.

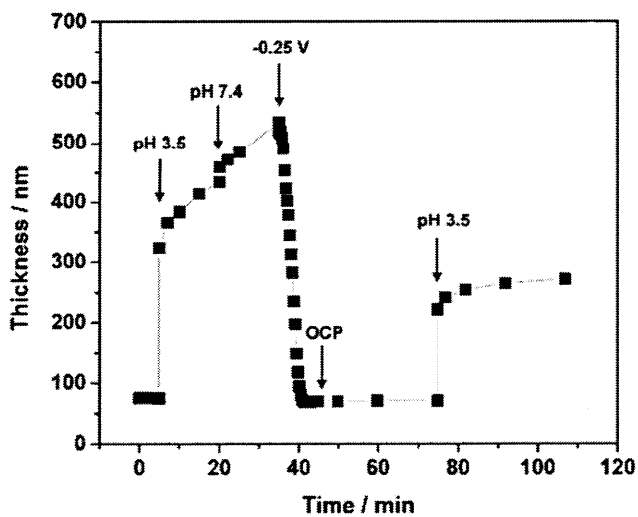


Figure 6.7. Thickness of a (PAH/SPS)_{5.5} film initially immersed in DI water, swollen after immersion in pH 3.5 solution, transferred to a pH 7.4 solution, electrochemically deswollen

during application of -0.25 V (vs. Ag/AgCl (3 M NaCl)), and then reswollen after re-immersion in a pH 3.5 solution. Returning to the open circuit potential (OCP) alone does not cause the film to reswell in the pH 7.4 solution, since that pH is above the critical pH for film swelling.

6.3.6 QCM-D

Film growth, swelling, and electrochemically triggered deswelling were also studied using QCM-D. Fig. 6.8 shows the growth of a (PAH/SPS)_{5.5} film on the QCM crystal. Before swelling, the film was rigid and obeyed the Sauerbrey relationship (Equation 6.6), which relates the change in the quartz resonator frequency (Δf) to the change in mass adsorbed to the crystal (Δm), where C (17.7 ng/Hz/cm²) is a constant related to the physical properties of the quartz and n is the overtone number.

$$\Delta m = -C \left(\frac{\Delta f}{n} \right) \quad (6.6)$$

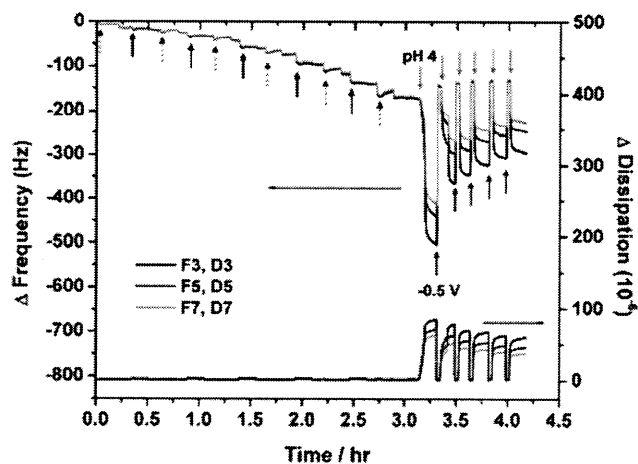


Figure 6.8. Change in frequency (F) and dissipation (D) of a QCM crystal during *in situ* build up of a (PAH/SPS)_{5.5} film at pH 9.3/9.3, film swelling at pH 4, electrochemically triggered deswelling at -0.50 V, and reswelling at the open circuit potential (OCP). Dashed arrows

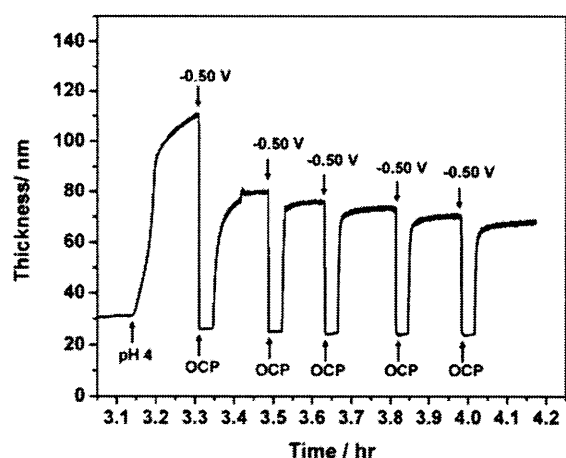
indicate injection of the PAH, while solid arrows indicate injection of the SPS. The blue arrows indicate application of -0.50 V, and the orange arrows indicate a return to the OCP. Data are presented for the 3rd (F3, D3), 5th (F5, D5), and 7th (F5, D7) overtones corresponding to resonance frequencies of approximately 15 MHz, 25 MHz, and 35 MHz, respectively.

The Sauerbrey relationship is valid when all of the frequency overtones overlap.¹¹ When water with pH = 4 was pumped into the QCM chamber, the resonance frequencies all dropped substantially, indicating uptake of water into the film. Concomitantly, the dissipation values all rose substantially, indicating that the film became more compliant. The large increase in dissipation and the fact that the different frequency overtones do not overlap when the film is in the swollen state, necessitates the consideration of the viscoelastic properties of the film for accurate determination of film thickness.¹¹ As described by Voinova et al. for thin polymer films in liquid, the polymer film may be considered as a Voigt element to characterize the viscoelasticity of the film.¹² The Voigt element is defined as a spring (representing elastic behavior) and a dashpot (representing viscous behavior) arranged in parallel. Using QTools software, we set the variable parameters in the model to be the film thickness, film shear (storage) elastic modulus, and film shear viscosity. The fixed parameters were fluid density (1000 kg/m³), fluid viscosity (1 cP), and film density, which we assumed was equal to that of the density of water. Fig. 8 shows film thickness, shear modulus, and shear viscosity over time for film growth and for multiple swell/deswell cycles achieved by injection of pH 4 water at the open circuit potential and by application of -0.50 V to the gold electrode, respectively. The hydrated film thickness for an $n = 5.5$ film was determined to be roughly 38 nm with QCM-D. That value is less than the hydrated thickness of films made on gold-coated Si wafers using standard dip coating (~54 nm). As has been demonstrated previously by Cho et al. for spin-

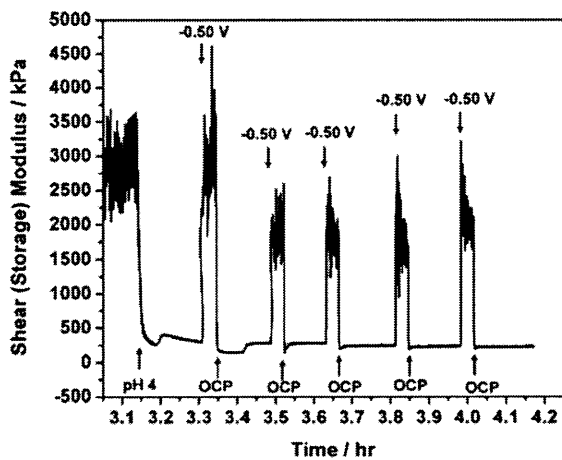
assembled films, shear forces, which were present during assembly on the QCM crystal, can result in a thinner film.¹³ Qualitatively, the QCM-D shows the same film swelling/deswelling behavior as was observed with spectroscopic ellipsometry. Specifically, the films swell substantially at pH 4 and then may be deswelled by application of -0.50 V, which raises the local pH at the electrode surface. Furthermore, QCM shows the same trend with multiple cycles. That is that films reswelled at the OCP do not return to their originally superswollen thickness. Besides determination of film thickness (Fig. 6.9A), the Voigt model also provides mechanical information for films in the swollen and deswollen state (Fig 6.9B and 6.9C). From Eqn. 6.7 below, one may calculate the shear (storage) modulus (G'), loss modulus (G''), and complex shear modulus ($|G^*|$) obtained at a shear rate corresponding to the fundamental quartz oscillation frequency of 5 MHz. Using the electrochemical trigger, we are able to reversibly switch the stiffness of the film over roughly an order of magnitude.

$$G^* = G' + iG'' = \mu_f + 2\pi f\eta_f \quad (6.7)$$

A)



B)



C)

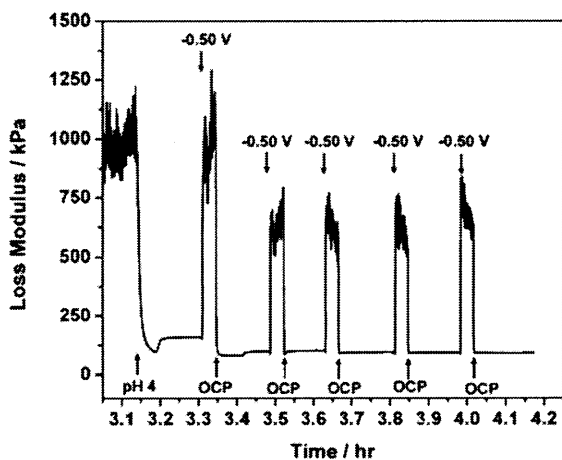


Figure 6.9. (A) Thickness of a (PAH/SPS)_{5.5} film swollen upon exposure to pH 4 water, deswollen upon application of -0.50 V, and reswollen at the open circuit potential. (B) Shear (storage) modulus and (C) loss modulus of (PAH/SPS)_{5.5} films during multiple swell (at pH 4, OCP) / deswell (-0.50 V) cycles.

6.4 Conclusions

The electrochemically controlled swelling and mechanical properties of a polyelectrolyte multilayer thin film containing polyallylamine hydrochloride (PAH) and sulfonated polystyrene (SPS) has been described. Application of cathodic electric potentials in the range of -0.25 V to -1.25 V (vs. Ag/AgCl (3 M NaCl)) to gold electrodes coated with the films induces reduction of dissolved oxygen, which generates hydroxide ions and raises the local (interfacial) pH. Starting in a superswollen state between pH 3 and 4, the films are deswollen when the potential is applied, which raises the local pH to at least 10.5. The increase in pH deprotonates the primary amines of PAH and reforms hydrophobic interactions causing the film to return to a more compact state.² Turning off the voltage then “erases” the local pH, allowing it to return to the bulk pH value, which induces reswelling of the thin film. While the first cycle exhibits incomplete reversibility with regard to the reswelling thickness, subsequent cycles are reversible. Overall, we have attained reversible 300% volume changes (e.g. between roughly 50 nm and 200 nm for $n = 5.5$ bilayer films) in the polymer thin films, and have reversibly altered the viscoelastic properties over nearly an order of magnitude (shear modulus between 1.9 MPa and 230 kPa and loss modulus between 620 kPa and 90 kPa). The kinetics of electrically triggered deswelling were found to vary depending upon the film thickness, magnitude of the applied potential, and the bulk pH. Film thickness dictates the timescale for diffusion of water into and out of the film, the magnitude of the potential controls the rate of oxygen reduction, and the bulk pH affects how high of a local pH can be attained.

The degree of electrochemically triggered swelling and the magnitude of mechanical changes presented in this work are greater than those reported by us and by others for other polymer thin film systems. We previously reported layer-by-layer systems that undergo 2-10% volume

changes and 50% changes in mechanical stiffness,¹⁴ while Grieshaber et al. reported 5-10% volume transitions,¹⁵ and Forzani et al. reported ~10% volume transitions¹⁶ all utilizing the redox switching of transition metal compounds within the polymer films. A number of other authors have measured up to 30% volume transitions and stiffness changes in the range of 20-300% for different polyaniline and polypyrrole conducting polymer films upon redox cycling.¹⁷⁻²³ These systems tend to undergo smooth, continuous changes driven by motion of ions and changes in polymer backbone stiffness. In contrast, as reported first by Hiller et al., the (PAH/SPS)_n system examined in this work exists in a “frustrated” state and can thereby undergo discontinuous swelling transitions between two energy minima, which are formed by competition between attractive and repulsive interactions.¹

We maintain that achieving such drastic, discontinuous changes in the swelling and mechanical properties of a surface coating could be particularly useful for such applications as controlling adhesion of proteins or cells on surfaces, drug delivery, and controlling flow in microfluidic systems. The material system presented in this work will only undergo a reversible electrically triggered deswelling transition at a pH < 4, which is not a pH value that is compatible with typical biological systems; however, if the film is first swollen at pH < 4 and then transferred to a milder pH (e.g. pH 7.0-7.4), then it will remain in the swollen state and be capable of electrochemically induced deswelling. In that case, however, the film will not reswell when the electric potential is turned off unless the film is transferred back to pH < 4. Overall, we have introduced a powerful strategy that allows control over classic pH-responsive polymer thin films by only changing the *local* pH. We believe that this strategy could be extrapolated to other material systems and improve the practical applicability of pH-responsive materials for applications in which altering the *bulk* pH is not an option.

6.5 References

1. Hiller, J.; Rubner, M. F. Reversible Molecular Memory and pH-Switchable Swelling Transitions in Polyelectrolyte Multilayers. *Macromolecules* **2003**, *36*, 4078-4083.
2. Itano, K.; Choi, J. Y.; Rubner, M. F. Mechanism of the pH-Induced Discontinuous Swelling/Deswelling Transitions of Poly(Allylamine Hydrochloride)-Containing Polyelectrolyte Multilayer Films. *Macromolecules* **2005**, *38*, 3450-3460.
3. Lee, D.; Nolte, A. J.; Kunz, A. L.; Rubner, M. F.; Cohen, R. E. pH-Induced Hysteretic Gating of Track-Etched Polycarbonate Membranes: Swelling/Deswelling Behavior of Polyelectrolyte Multilayers in Confined Geometry. *J. Am. Chem. Soc.* **2006**, *128*, 8521-8529.
4. Dubas, S. T.; Schlenoff, J. B. Factors Controlling the Growth of Polyelectrolyte Multilayers. *Macromolecules* **1999**, *32*, 8153-8160.
5. Choi, J.; Rubner, M. F. Influence of the Degree of Ionization on Weak Polyelectrolyte Multilayer Assembly. *Macromolecules* **2005**, *38*, 116-124.
6. Schmidt, D. J.; Hammond, P. T. Electrochemically Erasable Hydrogen-Bonded Thin Films. *Chemical Communications* **2010**, *46*, 7358-7360.
7. Deslouis, C.; Frateur, I.; Maurin, G.; Tribollet, B. Interfacial pH Measurement During the Reduction of Dissolved Oxygen in a Submerged Impinging Jet Cell. *J. Appl. Electrochem.* **1997**, *27*, 482-492.
8. Annaka, M.; Tanaka, T. Multiple Phases of Polymer Gels. *Nature* **1992**, *355*, 430-432.
9. Zaikov, G. i. E.; Iordanskii, A. L.; Markin, V. S. In *New concepts in polymer science*; First English edition. ed.; VSP: Utrecht, Netherlands, 1988, p 63.
10. Smith, A. L.; Ashcraft, J. N.; Hammond, P. T. Sorption Isotherms, Sorption Enthalpies, Diffusion Coefficients and Permeabilities of Water in a Multilayer PEO/PAA Polymer Film Using the Quartz Crystal Microbalance/Heat Conduction Calorimeter. *Thermochim. Acta* **2006**, *450*, 118-125.
11. Johannsmann, D. Viscoelastic, Mechanical, and Dielectric Measurements on Complex Samples with the Quartz Crystal Microbalance. *Phys. Chem. Chem. Phys.* **2008**, *10*, 4516-4534.
12. Voinova, M. V.; Rodahl, M.; Jonson, M.; Kasemo, B. Viscoelastic Acoustic Response of Layered Polymer Films at Fluid-Solid Interfaces: Continuum Mechanics Approach. *Phys. Scr.* **1999**, *59*, 391-396.
13. Cho, J.; Char, K.; Hong, J. D.; Lee, K. B. Fabrication of Highly Ordered Multilayer Films Using a Spin Self-Assembly Method. *Adv. Mater.* **2001**, *13*, 1076-+.
14. Schmidt, D. J.; Cebeci, F. C.; Kalcioglu, Z. I.; Wyman, S. G.; Ortiz, C.; Van Vliet, K. J.; Hammond, P. T. Electrochemically Controlled Swelling and Mechanical Properties of a Polymer Nanocomposite. *ACS Nano* **2009**, *3*, 2207-2216.
15. Grieshaber, D.; Voros, J.; Zambelli, T.; Ball, V.; Schaaf, P.; Voegel, J. C.; Boulmedais, F. Swelling and Contraction of Ferrocyanide-Containing Polyelectrolyte Multilayers Upon Application of an Electric Potential. *Langmuir* **2008**, *24*, 13668-13676.
16. Forzani, E. S.; Perez, M. A.; Teijelo, M. L.; Calvo, E. J. Redox Driven Swelling of Layer-by-Layer Enzyme-Polyelectrolyte Multilayers. *Langmuir* **2002**, *18*, 9867-9873.

17. Bahrami-Samani, M.; Cook, C. D.; Madden, J. D.; Spinks, G. M.; Whitten, P. G. Quartz Crystal Microbalance Study of Volume Changes and Modulus Shift in Electrochemically Switched Polypyrrole. *Thin Solid Films* **2008**, *516*, 2800-2807.
18. Barbero, C.; Kotz, R. Nanoscale Dimensional Changes and Optical-Properties of Polyaniline Measured by in-Situ Spectroscopic Ellipsometry. *J. Electrochem. Soc.* **1994**, *141*, 859-865.
19. Lizarraga, L.; Andrade, E. M.; Molina, F. V. Swelling and Volume Changes of Polyaniline Upon Redox Switching. *J. Electroanal. Chem.* **2004**, *561*, 127-135.
20. Mohamoud, M. A.; Hillman, A. R. The Effect of Anion Identity on the Viscoelastic Properties of Polyaniline Films During Electrochemical Film Deposition and Redox Cycling. *Electrochim. Acta* **2007**, *53*, 1206-1216.
21. Pytel, R. Z.; Thomas, E. L.; Hunter, I. W. In Situ Observation of Dynamic Elastic Modulus in Polypyrrole Actuators. *Polymer* **2008**, *49*, 2008-2013.
22. Singh, P. R.; Mahajan, S.; Raiwadec, S.; Contractor, A. Q. EC-AFM Investigation of Reversible Volume Changes with Electrode Potential in Polyaniline. *J. Electroanal. Chem.* **2009**, *625*, 16-26.
23. Smela, E.; Gadegaard, N. Volume Change in Polypyrrole Studied by Atomic Force Microscopy. *J. Phys. Chem. B* **2001**, *105*, 9395-9405.

Chapter 7: Layer-by-Layer Films for Education – Assembly of a pH-Responsive and Electrochromic Thin Film

*Portions reproduced with permission from “Layer-by-Layer Assembly of a pH-Responsive and Electrochromic Thin Film” by Daniel J. Schmidt, Eric M. Pridgen, Paula T. Hammond, and J. Christopher Love, *Journal of Chemical Education*, 2010, 87(2), 208-211. 10.1021/ed800045r, © 2010 American Chemical Society and Division of Chemical Education.

7.1 Introduction

This chapter describes an experiment that demonstrates both the process for fabricating thin films of polymers using layer-by-layer (LbL) assembly, and some of the properties of the resulting films, for use as an education tool. Many strategies exist for coating a substrate with a thin film including physical vapor deposition, chemical vapor deposition, electrodeposition, and spin coating, among others. Most of these techniques require complex and expensive equipment. In contrast, LbL assembly is a simple yet powerful technique, and is therefore particularly suitable to implement in an undergraduate lab. While a number of papers have been published in the *Journal of Chemical Education* on the fabrication and analysis of various thin films,¹⁻¹² the utility of LbL assembly for teaching concepts related to self-assembly and polymeric thin films has not been reported. The experiments outlined here were designed for and carried out in an upper-level undergraduate laboratory course in polymer science at the Massachusetts Institute of Technology. Through this exciting and visually appealing experiment, students gain exposure to the growing area of functional polymeric coatings.

Layer-by-layer assembly, first reported by Decher,^{13,14} is a method for fabricating thin films of polymers by the sequential adsorption of two or more polymers with complementary functional groups. Typically, positively and negatively charged species are used (Fig. 7.1), but

LbL assembly can also be accomplished by hydrogen bonding, covalent bonding, as well as other specific interactions. Besides natural and synthetic polymers, a number of other species including metallic and inorganic nanoparticles, micelles, and even small molecules can be included in LbL films. Assembly can be carried out by dip coating, spin coating, or spray coating to coat conformally virtually any substrate of any shape or size.^{15,16} In this paper, we employ dip coating since this process can be easily accomplished by hand. LbL assembly is extremely simple and versatile, making it possible to control thickness, morphology, and functionality of thin films with excellent precision.

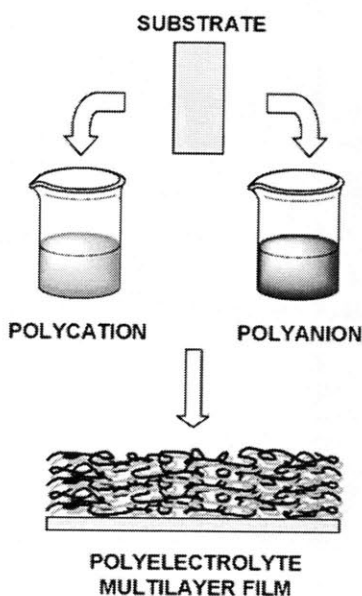


Figure 7.1. Schematic representation of the layer-by-layer assembly of a polycation and a polyanion to form a polyelectrolyte multilayer thin film.

Conducting polymers are one class of functional materials that can be incorporated into LbL assemblies. Discovered in 1970, conducting polymers remain an area of interest as responsive materials.¹⁷⁻¹⁹ These polymers usually possess a conjugated backbone and must be “doped” through partial oxidation or reduction of the polymer backbone to generate a

delocalized π -electron network with free charge carriers. Conducting polymers can possess an interesting combination of properties: the conductivity of metals along with the processability of polymers.¹⁸ This combination makes them useful for biological and chemical sensors, displays, batteries, antistatic coatings, and artificial muscles.^{20,21} The experiments described here use polyaniline (PANi), a conducting polymer, and sulfonated polystyrene (SPS) to assemble LbL films (Fig. 7.2). The assembly and conductivity of this system was first reported by Cheung et al.²² and further characterized by Ram et al.²³ Since then, LbL films containing PANi and other electroactive polymers have been used as optical pH sensors²⁴ and electrochromic displays.²⁵

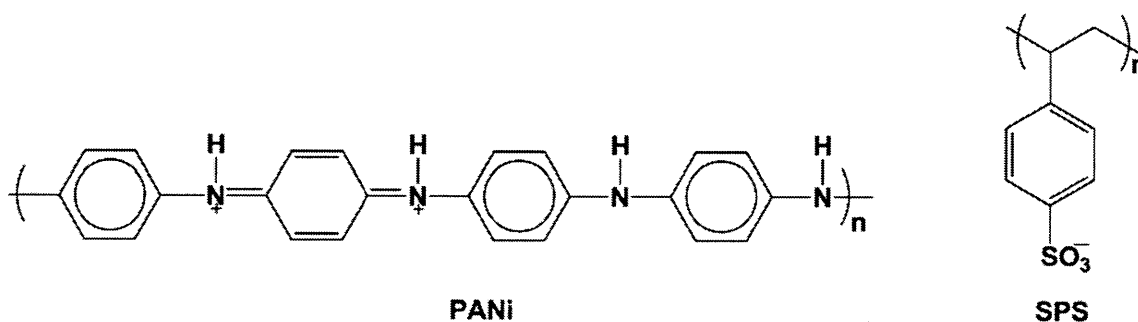
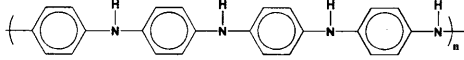
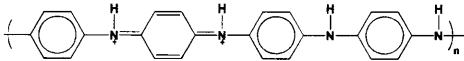
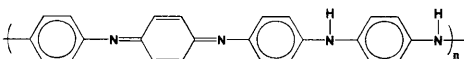
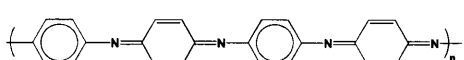


Figure 7.2. Molecular structures of polyaniline (acid-doped, conducting emeraldine salt form) (left) and sulfonated polystyrene (right).

PANi can exist in four different oxidation states termed leucoemeraldine, emeraldine salt, emeraldine base, and pernigraniline (in order of increasing oxidation state) (Table 7.1). The different oxidation states possess four different colors (clear, green, blue, and purple). Only the emeraldine salt is conducting and charged, and is the form used to assemble LbL films. PANi can be switched between oxidation states by acid/base chemistry (which changes the electronic energy levels) or by electrochemistry (which injects or removes electrons from the polymer backbone).¹⁸ Given the visual appeal and versatile functions of PANi films, other

undergraduate-level experiments investigating electropolymerized PANi thin films have been described.^{5,10-12}

Table 7.1. The four oxidation states of polyaniline.

Name	Structure	Color	Notes
Leucoemeraldine		Clear	Fully reduced Insulating
Emeraldine salt		Green	Partially oxidized Conducting
Emeraldine base		Blue	Partially oxidized Insulating
Pernigraniline		Purple	Fully oxidized Insulating

In the experiment described in this paper, students prepare (SPS/PANi)_n films by hand (where *n* is the number of deposited bilayers). They monitor the assembly of the films by visual inspection, UV/Vis spectroscopy, and conductance measurements. The pH-dependent optical properties of the films are observed, and the electrochromic properties of the films are demonstrated using a potentiostat to modify the oxidation state of PANi in the films. Students executing this experiment are exposed to a versatile technique for preparing thin films by self-assembly. An instructor can place LbL assembly in context with other methods for producing polymeric thin films, and provide examples demonstrating the prevalence and many functions of coatings in everyday life. Furthermore, an instructor can use LbL assembly as a model system to discuss the thermodynamics of self-assembly.²⁶

7.2 Materials and Methods

Materials

Polyaniline (PANi) (emeraldine base) (MW 50K), poly(4-styrenesulfonic acid) (SPS) (18% wt in water) (MW 75K), and N,N-dimethylacetamide were purchased from Sigma Aldrich

(St. Louis, MO). Hydrochloric acid (1 N), sulfuric acid (1 N), sodium hydroxide (1 N), ethanol (190 proof) and glass microscope slides were purchased from VWR Scientific (Edison, NJ). Linear polyethylenimine (LPEI) (MW 25K) was purchased from PolySciences, Inc. (Warrington, PA). Indium tin oxide (ITO)-coated glass slides (CD-50IN-CUV) were purchased from Delta Technologies, Limited (Stillwater, MN). All chemicals were used as received.

Preparation of Polyelectrolyte Solutions

The PANi solution should be made according to the method from Cheung et al.²² PANi was dissolved in N,N-dimethylacetamide at a concentration of 20 mg/mL and stirred vigorously overnight. The solution was then filtered to remove un-dissolved solids, and then diluted into deionized water (at a ratio of 1:9 v/v) that had been previously adjusted to pH 3.0 using HCl. The resulting aqueous solution of PANi was then be adjusted to pH 2.5 with HCl and then filtered again to remove any un-dissolved solids. Note that the PANi solution has a finite lifetime as it is prone to precipitation. It can be used for up to 1-2 weeks. If the pH is adjusted below 2.5, the polymer will precipitate out of solution; the pH adjustment should therefore be done gradually. Filtration must be carried out using a filter material compatible with the N,N-dimethylacetamide. The SPS solution should be made by diluting the 18 wt% SPS with deionized water to a concentration of 10 mM based on the repeat unit and addition of NaCl to a concentration of 0.5 M. The pH of this solution should then be adjusted to pH 2.5 with HCl. The deionized water used to prepare the solutions had a resistivity of 18.2 M Ω -cm (Milli-Q Ultrapure Water System, Millipore).

Film Assembly

Glass microscope slides (cut into 1 x 2 cm pieces) and ITO-coated glass slides were cleaned by rinsing with ethanol and DI water, followed by drying under nitrogen gas. The substrates were then subjected to 5 min of O₂ plasma using a Harrick PDC-32G plasma cleaner on high RF power to remove any remaining organic contaminants and to increase the negative charge density on the surface. After removal from the plasma cleaner, the slides were placed in an LPEI solution (10 mM, pH 4.0) overnight to form a positively charged adhesion layer on the surface. After rinsing with DI water, the substrates were then dip coated by hand (by students) to build up a (SPS/PANi)_n film. Substrates were immersed in the SPS solution for 3 min followed by at least three pH 2.5 water rinse baths. Next substrates were immersed in the PANi solution for 3 min followed by at least three pH 2.5 water rinse baths. This cycle was repeated to build up the desired number of bilayers. Once film deposition was complete, the films were dried under a stream of nitrogen gas.

Film Characterization

The optical, electrical, and electrochemical properties of the resulting films were then characterized. The color of the films with increasing numbers of layers was assessed visually and with UV/Vis spectroscopy (StellarNet EPP2000C). A handheld multimeter (Fluke 189 True RMS multimeter) was used to measure the electrical conductivity of the films. For conductivity measurements, films were first doped with HCl (by immersion in a 1 M HCl solution for 30 sec) and dried with nitrogen. Two pieces of conducting copper tape were then affixed to a film a known distance apart. The conductance (or resistance) of the film was then measured with the multimeter and converted to conductivity (or resistivity) by dividing by the distance between the pieces of copper tape. Lastly, a potentiostat (EG&G Princeton Applied Sciences 263A) was used

to apply electric potentials to the films on ITO-coated glass electrodes in a three-electrode electrochemical cell with a saturated calomel (SCE) reference electrode (sat. KCl) and a Pt coil counter electrode in a 0.05 M H₂SO₄ / 0.1 M KCl electrolyte. Spectroelectrochemical measurements were carried out by setting up the three-electrode cell in a UV/Vis cuvette and simultaneously monitoring film absorbance while applying an electric potential.

7.3 Results and Discussion

7.3.1. Module #1 - Fabrication and characterization of (SPS/PANi)_n thin film growth

A green-colored film was apparent after two bilayers. As additional bilayers were deposited the students noticed that the color intensity of the film increased proportionately (Fig. 7.3). The incremental increase in color can be quantified using a UV/Vis spectrometer. For the most accurate absorbance measurement, the PANi in the films should be deprotonated to the blue emeraldine base form by immersion in a 0.1 M NaOH solution for 10 seconds. The height of the absorbance peak at ~620 nm increased linearly with the number of deposited bilayers (Fig. 7.4). This measurement indicates that the assembly process occurred in a stepwise fashion, and that an equivalent amount of PANi was adsorbed at each step. Furthermore, students observed here that the color of the films is sensitive to pH. The students were required to consider how they would characterize these films as potential pH sensors, and what properties an ideal pH sensor would possess (i.e., sensitivity and selectivity).

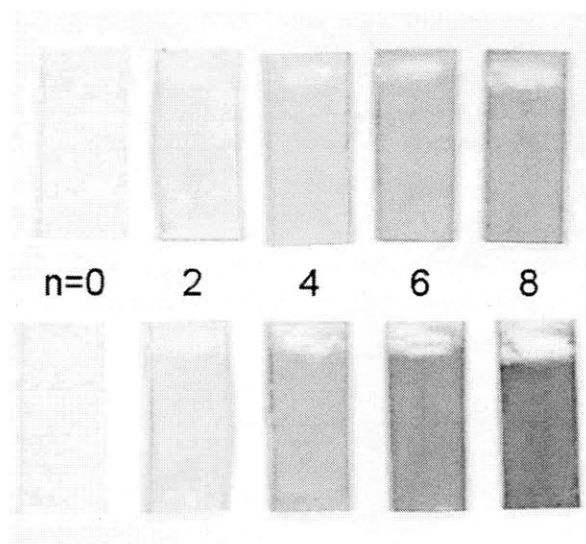
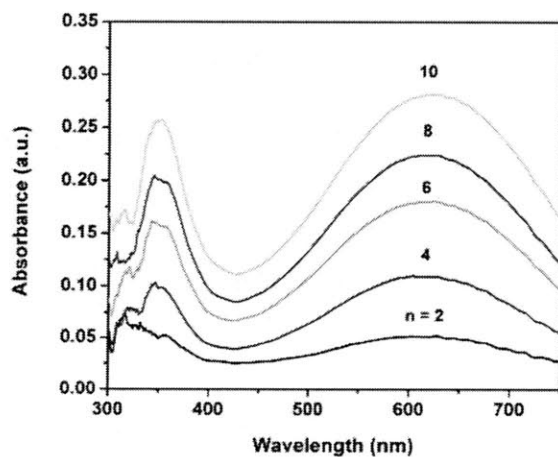


Figure 7.3. Photograph of $(\text{SPS/PANi})_{n=0, 2, 4, 6, 8}$ films in the acid-doped emeraldine salt form (top) and de-doped emeraldine base form (bottom) on glass microscope slides (1 cm x 2 cm).

A)



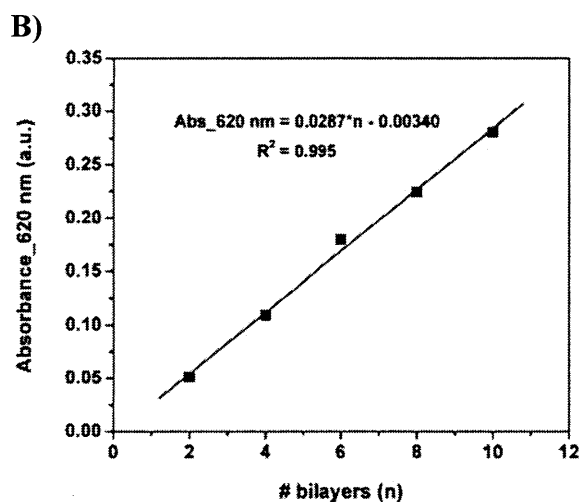
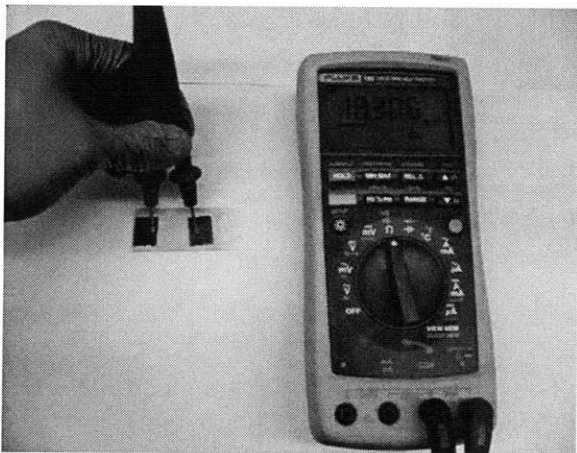


Figure 7.4. (A) UV/Vis absorbance spectrum of (SPS/PANi)_n films for $n = 2, 4, 6, 8, 10$ and (B) linear regression of absorbance at 620 nm versus the number of deposited bilayers, n .

Besides being colored, PANi is also a conducting polymer. Students measured the conductivity of their (SPS/PANi)_n films using a handheld multimeter. First, the PANi in the films was protonated to the emeraldine salt by immersion of the films in 1 M HCl for 30 sec., and then drying with nitrogen. Next, two pieces of conducting copper tape were be affixed to a film to measure its in-plane conductance (Fig. 7.5A). The conductivity may then be estimated by dividing the conductance by the distance between the pieces of copper tape. Pieces of tape with equal areas, and good adhesion between the tape and film, are necessary to compare the conductivity of films with different numbers of layers quantitatively. The conductivity of (SPS/PANi)_n films should increase linearly to a limiting value for films with fewer than 10 bilayers.²² Students observed a non-linear induction period for films with 2 bilayers or less, likely due to a lack of a completely interconnected PANi network; a linear trend in the conductivity was observed for films comprising 4 to 8 bilayers (Fig. 7.5B).

A)



B)

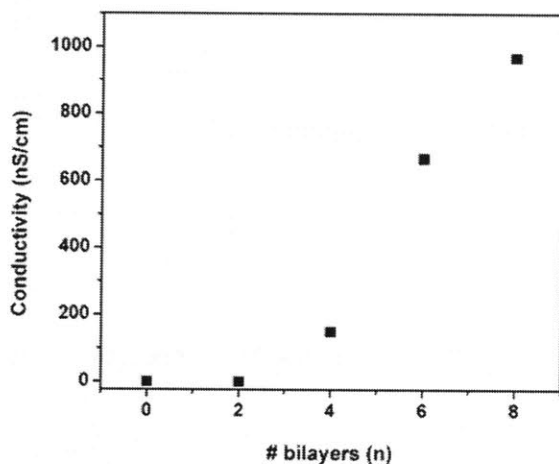


Figure 7.5. (A) Photograph showing measurement of in-plane conductivity using a handheld multimeter. (B) Student-collected data showing conductivity versus number of bilayers for (SPS/PANi)_n films.

7.3.1. Module #2 - Electrochromic properties of (SPS/PANi)₈ films

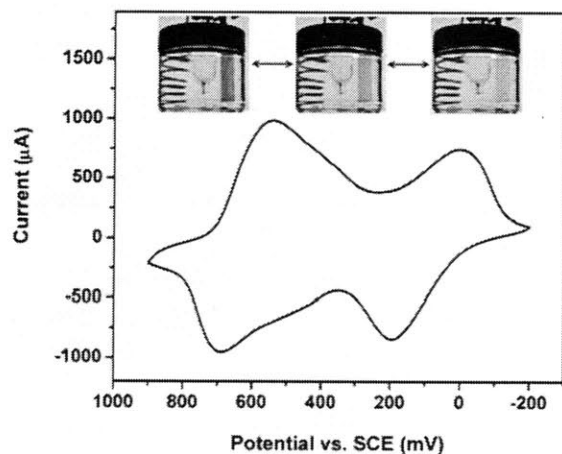
The second module of this experiment demonstrates the electrochromic properties of (SPS/PANi)_n layer-by-layer films. As reported by Sherman et al. for an electropolymerized PANi film, electrochromism may be observed using a simple one- or two-battery electrochemical cell.¹⁰ This strategy may be employed for the (SPS/PANi)_n LbL films

prepared here as well. One modification we suggest is to use a potentiostat if available to control the applied voltage precisely and to give the ability to sweep the voltage.

For this module, the students prepared one (SPS/PANi)₈ film on an ITO-coated glass slide. Next, with the help of the instructor, a three-electrode cell was prepared with a reference electrode (saturated calomel (SCE) or Ag/AgCl), a Pt wire counter electrode, and the (SPS/PANi)₈ film on ITO-glass as the working electrode. The electrolyte was an aqueous solution of 0.05 M H₂SO₄ with 0.1 M KCl. The potential at the working electrode was controlled with an EG&G Princeton Applied Sciences 263A potentiostat/galvanostat.

After an introduction to the potentiostat, the students evaluated the electrochromic response of the films by a cyclic voltammetry experiment where the potential was swept between -0.2 V and +0.9 V with respect to the SCE reference electrode at a scan rate of 50 mV/s. This protocol allowed visualization of three to four of the PANi oxidation states (Fig. 7.6A).^{Note 1} Students also carried out spectroelectrochemistry wherein an electrochemical cell was set up directly in a UV/Vis cuvette for simultaneously monitoring absorbance while changing the applied voltage. The absorbance at 620 nm of a (SPS/PANi)₈ film changed over time when square wave potentials of -0.2V and 0.9 V were applied (Fig. 7.6B). From these data, students determined the contrast and response time of the electrochromic film. Contrast is defined as the change in percent transmittance between two states; the response time is the time required to achieve 90% of the maximum contrast. Students were asked to think practically about these values in terms of the suitability of these films for displays, electrochromic windows, or other applications.

A)



B)

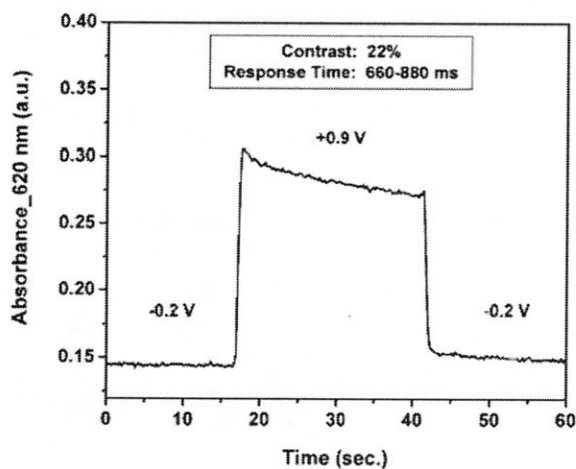


Figure 7.6 (A) A cyclic voltammogram and photos showing the electrochromism of a (SPS/PANi)₈ film on ITO-glass. The colors of three PANi oxidation states, leucoemeraldine, emeraldine salt, and pernigraniline, are apparent in the photographs from right to left. (B) Student-collected data showing spectroelectrochemistry of (SPS/PANi)₈ subject to square waves at -0.2 V and 0.9 V (with respect to a Ag/AgCl reference electrode).

7.4 Conclusions

With the prevalence of polymeric coatings in many common products, it is important for students in the areas of chemistry, chemical engineering, materials science, and related fields to

be familiar with the various techniques used to make these thin films. Through the experiments described here, students are able to explore an emerging method for preparing and characterizing a visible polymeric coating used as an electrochromic material. This experiment has been successfully integrated into an undergraduate polymer laboratory course; it is simple to execute and does not require expensive or sophisticated equipment. The results obtained by students were repeatable and consistent with those reported here. Students found this experiment interesting and exciting, given its visual appeal and its connection to cutting edge research; multiple students have inquired about pursuing undergraduate research on layer-by-layer assembly following execution of this experiment in the laboratory class.

Note

1. The leucoemeraldine (clear), emeraldine salt (green), and pernigraniline (purple) oxidation states will all be visibly apparent. The emeraldine base (blue) form may be visible at 0.5-0.6 V (versus SCE) between the green and purple colored states.

7.5 References

1. Bunting, R. K.; Swarat, K.; Yan, D. J.; Finello, D. Synthesis and Characterization of a Conducting Polymer - an Electrochemical Experiment for General Chemistry. *J. Chem. Educ.* **1997**, *74*, 421-423.
2. Chakraborty, M.; Chowdhury, D.; Chattopadhyay, A. Spin-Coating of Polystyrene Thin Films as an Advanced Undergraduate Experiment. *J. Chem. Educ.* **2003**, *80*, 806-809.
3. Cortes, M. T.; Moreno, J. C. Electropolymerized Conducting Polymer as Actuator and Sensor Device - an Undergraduate Electrochemical Laboratory Experiment. *J. Chem. Educ.* **2005**, *82*, 1372-1373.
4. Dagostino, A. T. A Multitechnique Approach for Materials Characterization - Using X-Ray-Diffractometry, Visible Spectroscopy, and Atomic-Absorption Analysis to Determine Thin Metal-Film Thickness. *J. Chem. Educ.* **1994**, *71*, 892-896.
5. Goto, H.; Yoneyama, H.; Togashi, F.; Ohta, R.; Tsujimoto, A.; Kita, E.; Ohshima, K. Preparation of Conducting Polymers by Electrochemical Methods and Demonstration of a Polymer Battery. *J. Chem. Educ.* **2008**, *85*, 1067-1070.

6. Ibanez, J. G.; Solorza, O.; Gomezdelcampo, E. Preparation of Semiconducting Materials in the Laboratory - Production of Cds Thin-Films and Estimation of Their Band-Gap Energy. *J. Chem. Educ.* **1991**, *68*, 872-875.
7. Mathias, L. J.; Hankins, M. G.; Bertolucci, C. M.; Grubb, T. L.; Muthiah, J. Quantitative-Analysis by Ftir - Thin-Films of Copolymers of Ethylene and Vinyl-Acetate. *J. Chem. Educ.* **1992**, *69*, A217-A219.
8. Ramanaviciene, A.; Finkelsteinas, A.; Ramanavicius, A. Basic Electrochemistry Meets Nanotechnology: Electrochemical Preparation of Artificial Receptors Based on a Nanostructured Conducting Polymer, Polypyrrole. *J. Chem. Educ.* **2006**, *83*, 1212-1214.
9. Sadik, O. A.; Brenda, S.; Joasil, P.; Lord, J. Electropolymerized Conducting Polymers as Glucose Sensors - an Undergraduate Analytical Chemistry Laboratory Experiment. *J. Chem. Educ.* **1999**, *76*, 967-970.
10. Sherman, B. C.; Euler, W. B.; Force, R. R. Polyaniline - a Conducting Polymer - Electrochemical Synthesis and Electrochromic Properties. *J. Chem. Educ.* **1994**, *71*, A94-A96.
11. Virji, S.; Weiller, B. H.; Huang, J. X.; Blair, R.; Shepherd, H.; Faltens, T.; Haussmann, P. C.; Kaner, R. B.; Tolbert, S. H. Construction of a Polyaniline Nanofiber Gas Sensor. *J. Chem. Educ.* **2008**, *85*, 1102-1104.
12. Xie, Q.; Li, Z.; Deng, C.; Liu, M.; Zhang, Y.; Ma, M.; Xia, S.; Xiao, X.; Yin, D.; Yao, S. Electrochemical Quartz Crystal Microbalance Monitoring of the Cyclic Voltammetric Deposition of Polyaniline - a Laboratory Experiment for Undergraduates. *J. Chem. Educ.* **2007**, *84*, 681-684.
13. Decher, G. Fuzzy Nanoassemblies: Toward Layered Polymeric Multicomposites. *Science* **1997**, *277*, 1232-1237.
14. Decher, G.; Hong, J. D.; Schmitt, J. Buildup of Ultrathin Multilayer Films by a Self-Assembly Process .3. Consecutively Alternating Adsorption of Anionic and Cationic Polyelectrolytes on Charged Surfaces. *Thin Solid Films* **1992**, *210*, 831-835.
15. *Multilayer Thin Films: Sequential Assembly of Nanocomposite Materials*; Decher, G.; Schlenoff, J. B., Eds.; Wiley-VCH: Weinheim, 2003.
16. Hammond, P. T. Form and Function in Multilayer Assembly: New Applications at the Nanoscale. *Adv. Mater.* **2004**, *16*, 1271-1293.
17. Heeger, A. J. Semiconducting and Metallic Polymers: The Fourth Generation of Polymeric Materials (Nobel Lecture). *Angew. Chem., Int. Ed.* **2001**, *40*, 2591-2611.
18. MacDiarmid, A. G. "Synthetic Metals": A Novel Role for Organic Polymers (Nobel Lecture). *Angew. Chem., Int. Ed.* **2001**, *40*, 2581-2590.
19. Shirakawa, H. The Discovery of Polyacetylene Film: The Dawning of an Era of Conducting Polymers (Nobel Lecture). *Angew. Chem., Int. Ed.* **2001**, *40*, 2575-2580.
20. Kumar, D.; Sharma, R. C. Advances in Conductive Polymers. *Eur. Polym. J.* **1998**, *34*, 1053-1060.
21. *Handbook of Conducting Polymers*; 3rd ed. ed.; Skotheim, T. A.; Reynolds, J. R., Eds.; CRC: Boca Raton, Fla., 2007.
22. Cheung, J. H.; Stockton, W. B.; Rubner, M. F. Molecular-Level Processing of Conjugated Polymers .3. Layer-by-Layer Manipulation of Polyaniline Via Electrostatic Interactions. *Macromolecules* **1997**, *30*, 2712-2716.

23. Ram, M. K.; Salerno, M.; Adami, M.; Faraci, P.; Nicolini, C. Physical Properties of Polyaniline Films: Assembled by the Layer-by-Layer Technique. *Langmuir* **1999**, *15*, 1252-1259.
24. Ge, C. H.; Armstrong, N. R.; Saavedra, S. S. Ph-Sensing Properties of Poly(Aniline) Ultrathin Films Self-Assembled on Indium-Tin Oxide. *Anal. Chem.* **2007**, *79*, 1401-1410.
25. DeLongchamp, D.; Hammond, P. T. Layer-by-Layer Assembly of PEDOT/Polyaniline Electrochromic Devices. *Adv. Mater.* **2001**, *13*, 1455-1459.
26. Bucur, C. B.; Sui, Z.; Schlenoff, J. B. Ideal Mixing in Polyelectrolyte Complexes and Multilayers: Entropy Driven Assembly. *J. Am. Chem. Soc.* **2006**, *128*, 13690-13691.

Chapter 8: Conclusions and Recommendations

In summary, this thesis investigated how the stability and swelling state of various layer-by-layer (LbL) thin films could be manipulated with electrochemical stimuli. LbL technology represents an attractive option for the development of stimuli-responsive surface coatings due to the simplicity and versatility of the fabrication technique as well as the plethora of incorporable functional and responsive materials. Two strategies were used to electrochemically trigger film dissolution or swelling/deswelling: the use of redox-active, charge-shifting, Prussian Blue nanoparticles and the increase in local pH through electrochemical reduction of dissolved oxygen. Through the application of these two strategies to multiple different materials systems, this thesis contributes to the understanding of how both electrostatic and hydrogen bonding interactions in thin films can be disrupted to actuate dramatic film responses, which could be exploited for applications in electrically triggered drug delivery and “mechanomutable” surfaces.

Prussian Blue nanoparticle-containing films may be dissolved when an applied potential oxidizes the PB from a negatively-charged to a neutral state, which disrupts the electrostatic bonding in the film. This phenomenon could potentially be used for the development of an electrically triggered drug releasing implant or transdermal device that would allow for active and remote control of drug delivery. Three classes of model agents/drugs were successfully incorporated into films along with PB: polyanions/polycations (i.e., dextran sulfate, linear polyethyleneimine, and chitosan), small hydrophobic dyes/drugs (i.e., coumarin 30, 9,10-diphenylanthracene, and flurbiprofen), and a small hydrophilic drug (i.e., gentamicin sulfate). Successful electrically controlled release was achieved in the case of the model polyanion, dextran sulfate, and the small, hydrophilic, charged molecule, gentamicin sulfate. Drug loading

into the films could be tuned with the number of deposited layers, and the amount and kinetics of drug release could be tuned with the magnitude of the applied voltage. Further, the drug release profile (burst versus pulsatile release) could be tuned with the applied electric potential profile (potentiostatic versus pulsed potentials). Finally, it was demonstrated that, in the case of gentamicin release, the drug maintains its antibiotic efficacy *in vitro* following electrically triggered release from a film.

The PB-based drug delivery concept does, however, possess some limitations. While the release of polymeric species and small, charged species could be well controlled electrochemically, that was not the case for small, hydrophobic dyes/drugs. These species leaked out of films passively when sequestered in charged, block copolymer micelles (i.e., polystyrene-block-poly-4-vinylpyridine micelles); when a cyclodextrin (i.e., polymeric carboxymethyl- β -cyclodextrin) was explored as alternative charged “carrier” species for hydrophobic drugs, it interfered with the PB electrochemical switching. Future work on the encapsulation and electrically triggered release of small, hydrophobic molecules from these films could include a larger sampling of micelle-drug combinations and potentially cross-linking the micelles to restrict passive diffusion. In the case where PB switching is disrupted, it would be informative to carry out fundamental studies as to the nature of this disruption, that is, whether the cyclodextrin interferes with ionic or electronic conductivity in the films. Electrochemical impedance spectroscopy could be used as a tool to investigate these phenomena more thoroughly. Besides current limitations in the controlled release of small, hydrophobic drugs, the chemical instability of PB at basic pH values results in slow leakage of drug from films at typical physiological conditions (pH 7.4, ionic strength 0.15 M). Therefore, PB-based drug delivery could be used for

shorter term applications, or an alternative charge-shifting material with better pH stability might be considered.

Prussian Blue nanoparticle-containing films may alternatively be swollen/deswollen and softened/stiffened reversibly when an applied potential reduces the PB, doubling its negative charge, and re-oxidizes the PB, returning to its original charge state, respectively. When the charge density in the film is altered, but ionic crosslinks remain intact, counterions will enter the film to maintain electroneutrality, and osmotic pressure will bring water into the film, causing film swelling and an increased compliance. In this work, the magnitude and reversibility of the swelling response of a linear polyethyleneimine/Prussian Blue nanoparticle film was measured in real-time with spectroscopic ellipsometry. Since film thickness and optical properties change simultaneously during PB redox-shifting, electrochemical AFM was used to corroborate the swelling results. For the first time, instrumented nanoindentation was used in concert with an electrochemical cell to measure the elastic modulus of thin films at different applied potentials. Further, an electrochemical quartz crystal microbalance with dissipation monitoring was used to confirm film swelling and mechanical transitions qualitatively. Overall, the magnitude of the swelling and mechanical responses was relatively small. Films swelled/deswelled reversibly by 5-10% of their hydrated thickness, and they exhibited changes in elastic modulus on the order of 50% (between 3.40 GPa and 1.75 GPa). Nonetheless, this work laid an important foundation by first establishing a multitude of techniques to study electrically controlled, “mechanomutable” thin films, and also by suggesting further study on mechanical percolation. Since these films are polymer nanocomposites, containing a nanoparticles and polymer, it is principle possible to tune the mechanical interaction between the nanoparticle fillers by tuning their volume fraction. We hypothesize that the assembly of films at or near the mechanical percolation threshold (i.e., the

volume fraction of filler particles at which filler-filler interactions persist through the entire network), and subsequent formation/disruption of percolation with an electrochemical stimulus via film swelling changes or through other means, could result in much more dramatic mechanical changes in polymer nanocomposite thin films. We recommend the pursuit of various other nano-sized filler materials toward the precise control of filler loading and distribution within LbL films for the study of mechanical percolation.

The charge density within LbL films may be indirectly altered by manipulation of the local pH via reduction of dissolved oxygen. The manipulation of *local* pH and a constant, mild *bulk* pH may improve the applicability of many pH-responsive material systems for sensitive biomedical applications. Hydrogen-bonded LbL films comprising polyvinylpyrrolidone and tannic acid were controllably dissolved at applied potentials between -0.25 V and -1.00 V (vs. Ag/AgCl) at a rate dependent upon the magnitude of the applied voltage and the concentration of dissolved oxygen. AFM revealed interesting morphological changes including the formation of microporous films at the more negative voltages and/or higher oxygen concentrations. It seems that the mechanism of film dissolution, that is surface erosion or bulk erosion, may be controlled with the aforementioned variables. It was also demonstrated that these electrochemically erasable H-bonded films could be used as sacrificial surface coatings to trigger the release of ultrathin free-standing LbL assemblies, which could be used for cell sheet engineering applications or for fundamental study of the free-standing LbL film properties. We recommend further study of the effects of ionic strength and film thickness on film stability and dissolution kinetics and the pursuit of applications in electrically triggered release of H-bonding drugs.

Besides film dissolution, the swelling and deswelling of pH-responsive films can be triggered by raising the local pH. Films comprising polyallylamine hydrochloride and sulfonated

polystyrene undergo a dramatic swelling transition (by 400-800 vol%) below pH 4 when the PAH becomes substantially more charged, and will deswell to their original state at pH >10.5. Using spectroscopic ellipsometry, film thickness was followed in real-time in response to an applied electric potential. Film deswelling was successfully triggered at bulk pH values ranging from 3.0 to 7.4 with kinetics depending upon the magnitude of the applied voltage, the bulk pH, and the film thickness. Reversible thickness changes on the order of 300% were observed after the first cycle in bulk pH 3.0 to 4.0. Electrochemical QCM-D corroborated the swelling results and further allowed quantification of film mechanical properties using the Voigt viscoelastic model. The shear (storage) modulus and the loss modulus of the films were found to vary reversibly by nearly an order of magnitude between 1.9 MPa and 230 kPa for the storage modulus and 620 kPa and 90 kPa for the loss modulus. Given the large magnitude of swelling and mechanical changes at constant bulk pH, this material system may be promising for biomedical applications; however, reversible changes are only achievable at bulk pH values less than 4.0. Further, the swelling transition is stifled at elevated ionic strength values comparable to physiological levels (i.e., 0.15 M). We recommend further study on the effect of ionic strength on film swelling, as well as further modeling work in concert with experimental work under controlled hydrodynamic conditions to fully elucidate the timescale and magnitude of the local pH changes, as well as the “persistence length” of the local pH elevation both within the polymer film and surrounding solution. We further recommend the study of mechanical percolation in all-polymer material systems in which percolation is established by a critical number of crosslinks. We believe that precisely controlling the number of permanent and dynamic crosslinks in a film, along with electrochemical control of the formation/breakage of the dynamic crosslinks could lead to fruitful results and further understanding.

Finally, the use of LbL assembly for educational purposes was demonstrated through an experiment in which students in an undergraduate polymer science laboratory class fabricate LbL films containing a conducting polymer by dip coating. The use of the conducting polymer, polyaniline, allows visible films to be created after just a few dip cycles; furthermore, the polymer is conducting and is optically responsive to both pH and an applied electric potential, which allows students to readily observe and measure properties of a self-made coating. The students followed film assembly with UV/Vis spectroscopy and conductance measurements. Subsequently, the students characterized the electrochromic properties of the films (i.e. switching speed and contrast) using a spectroelectrochemical set up. Given the simplicity and versatility of LbL assembly, the fabrication and properties of the resulting films are an ideal model system for students to study both the fundamentals of self-assembly and the many applications of both responsive and non-responsive surface coatings.

In conclusion, LbL films are a promising platform for the engineering and development of electroresponsive surface coatings. Given the wide variety of redox-responsive materials and pH-responsive materials that may be incorporated into such films, the structure and stability of LbL films may be manipulated through multiple different mechanisms and engineered toward future applications.

Appendix 1: Supplemental Materials for Chapter 2

Effect of the Applied Potential on Total Film Thickness

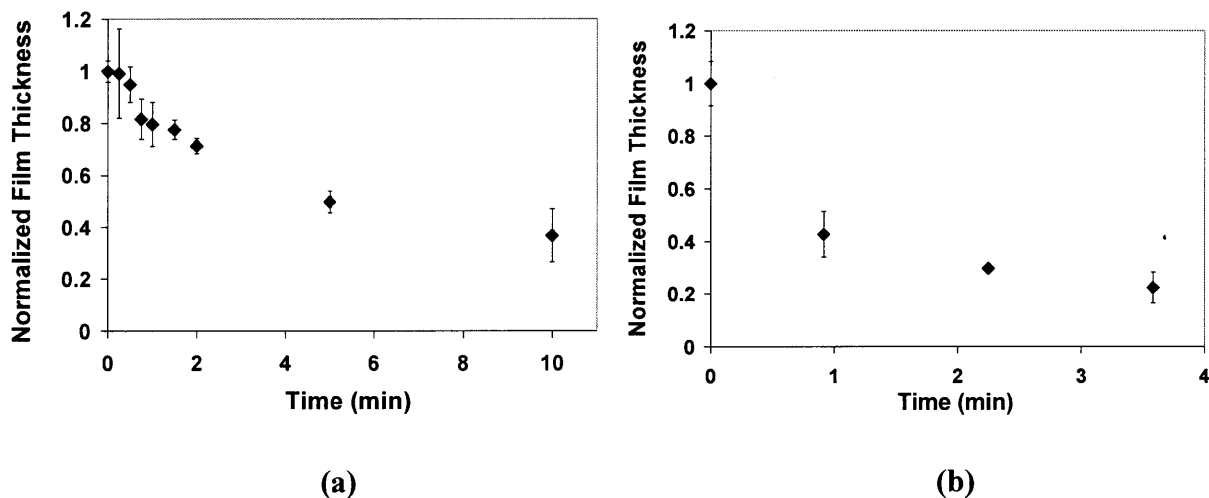


Figure A1.1. Normalized thickness of PB-containing films versus time at a constant potential of +1.25 V (by profilometry). (a) (LPEI/PB/LPEI/¹⁴C-DS)₃₀ films; (b) (LPEI/PB)₂₀ films. Error bars represent one standard deviation of the measured thickness values at five predetermined locations on the surface of the film.

To measure the effect of an applied potential on film thickness, and specifically to determine if PB loss correlated with deconstruction of the entire film, PB-containing films were exposed to a constant potential of +1.25 V and thickness was measured with respect to time using profilometry (Fig. A1.1). For all PB-containing films, film thickness was observed to decrease rapidly at early times (1-5 min) followed by a more gradual decrease at later times (5 – 60 min), kinetics which reflect the time scales for PB loss described in Figure 2. Further, in all systems, thickness was observed to decay until reaching 10-20% of the original film thickness, suggesting that some residual material was remaining on the surface of the substrate. In keeping with this observation, we also observed that 50-70% of the film's incorporated ¹⁴C-DS is released actively, leaving behind a fraction which is likely bound within this portion of the film structure. The amount of material bound at the surface (relative to the total quantity of material in the film) may vary with changes in film composition, deposition conditions, and total film thickness. In (LPEI/PB/LPEI/¹⁴C-DS)₃₀ tetralayer films, thickness decayed to 80% of that of the original film after 1 min at 1.25 V, 50% after 5 min, and 20% after 60 min. In (LPEI/PB)₂₀ systems, destabilization occurred on a more rapid time scale, reaching 43% in under 1 min and 20% in under 4 min. The shorter time scales required for destabilization in (LPEI/PB)₂₀ systems likely reflects the fact that these films lose all cohesive electrostatic interactions following the PB to PX transition, resulting in rapid deconstruction relative to (LPEI/PB/LPEI/DS)₃₀ systems, which retain some stable electrostatic interactions (from LPEI and DS) in the presence of an applied potential.

Effect of Applied Potentials Less Than +1.25 V on Film Stability and ^{14}C -DS Release

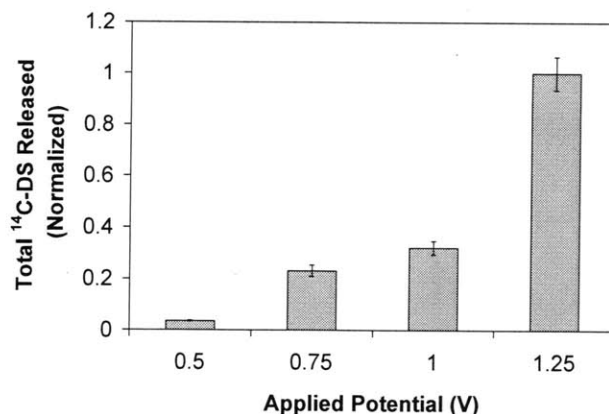


Figure A1.2. Release of ^{14}C -DS from PB-containing films held at the indicated constant potential for 10 min. All films are $(\text{LPEI}/\text{PB}/\text{LPEI}/^{14}\text{C}\text{-DS})_{30}$ and ^{14}C -DS release is normalized to the total ^{14}C -DS release from films held at +1.25 V. In all cases, error bars represent one standard deviation in measured values.

Figure A1.2 shows voltage dependent release of ^{14}C -DS after 10 minutes at the indicated square wave voltage. As expected, the amount of ^{14}C -DS released from the film increases with an increase in applied voltage. The formal potential for the PB/PX redox pair is roughly +0.85 V with a relatively broad peak (by cyclic voltammetry; nearly complete conversion to the PX state occurs at voltages exceeding +1.2 V).¹ At +0.5 V, all the nanoparticles are in the fully charged PB state and minimal ^{14}C -DS release is observed. At +0.75 V, a fraction of the Fe(II) centers have been oxidized to Fe(III). Therefore, the surface charge density of the nanoparticles has decreased, inducing partial film destabilization and ^{14}C -DS release. Likewise, at +1.00 V, even more of the Fe(II) centers have been oxidized to Fe(III) and further film destabilization and ^{14}C -DS release occurs. Finally at +1.25 V, essentially all the iron centers are in the Fe(III) oxidation state, corresponding to the Prussian Brown (PX) state, at which complete film destabilization and ^{14}C -DS release occurs.

Chronoamperometry and Power Requirements of Thin Films

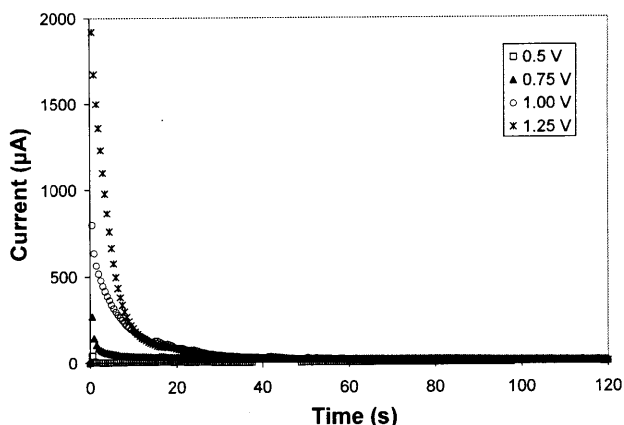


Figure A1.3. Chronoamperometric response of a (LPEI/PB/LPEI/¹⁴C-DS)₃₀ film subjected to various potentials ranging from 0.5 V to 1.25 V vs. SCE.

Figure A1.3 shows the chronoamperometric response of (LPEI/PB/LPEI/¹⁴C-DS)₃₀ films subjected to various potentials ranging from +0.5 V to +1.25 V vs. SCE for 30 min. In all cases, the current decays rapidly to approximately 0 within 30 sec. The total capacity, or the total amount of charge withdrawn from the film (representing the number of redox centers oxidized), can be calculated by integrating under the current versus time curve (Figure A1.3). We calculated a total capacity of 24,000 µA-s for (LPEI/PB/LPEI/¹⁴C-DS)₃₀ films subjected to a constant potential of 1.25 V (vs. SCE) for 30 minutes.

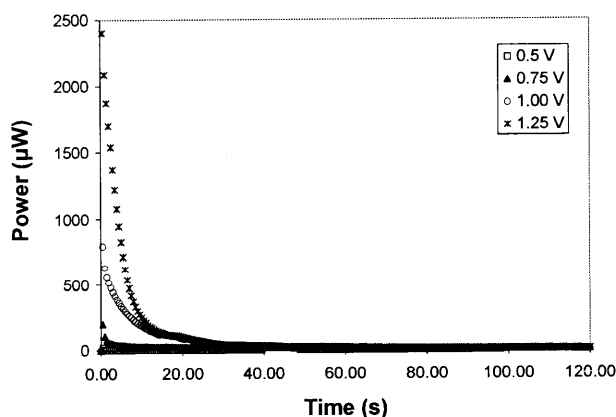


Figure A1.4. Dynamic power requirements of (LPEI/PB/LPEI/¹⁴C-DS)₃₀ films subjected to various potentials (relative to SCE).

Figure A1.4 shows the power requirements of (LPEI/PB/LPEI/¹⁴C-DS)₃₀ films subjected to various potentials (relative to SCE). Power was calculated by multiplying current response (Fig. A1.3) by the applied potential at each time. As expected, application of a higher oxidative potential has the greatest power requirement. The total energy requirement for electrochemical switching can be calculated by integrating under the power versus time curve. We found a total

energy requirement of 30,000 $\mu\text{W}\cdot\text{s}$ for $(\text{LPEI}/\text{PB}/\text{LPEI}/^{14}\text{C}\text{-DS})_{30}$ films subjected to a constant potential of 1.25 V (vs. SCE) for 30 minutes.

Comparison of Power Requirements for Electroactive Thin Films with Other Common

Implantable Systems

The following section serves to compare power requirements for the PB-based systems described in this study with those for other implantable devices such as pacemakers. The capacity of a pacemaker battery is typically in the range of 1 to 1.5 Amp-hours.² To apply +1.25 V to a $(\text{LPEI}/\text{PB}/\text{LPEI}/^{14}\text{C}\text{-DS})_{30}$ film for 30 min requires a capacity of 6.67×10^{-6} Amp-hours, well below the capacity of implanted pacemaker batteries. We can also compare the energy required for typical pacemaker output with that required for dissolution of our films. A typical pacemaker applies a voltage of 1-5 V over a resistance of 500 – 1000 Ohms for a duration of 0.3 to 1 ms.² Using these values, the range of energy requirements is 0.3 to 50 μJ . This range is in relatively close agreement with Mallela et al.³ Mallela et al. also report the typical energy requirement of implantable cardioverter defibrillators as 15-40 J. From the chronoamperometry data above, applying 1.25 V to a $(\text{LPEI}/\text{PB}/\text{LPEI}/^{14}\text{C}\text{-DS})_{30}$ film for 30 min requires 0.03 J of energy. This is 2.5 to 5 orders of magnitude greater than the energy needed for a pacemaker pulse, but it is 1.5 to 3 orders of magnitude less than the energy needed for an implantable defibrillator. Again using typical values for pacemakers to give a conservative estimate, the maximum power requirement (1 V over 1000 Ohm resistance) is 1 mW. Typical power requirements for implantable blood pumps range from 3-15 W⁴. In applying +1.25 V to a $(\text{LPEI}/\text{PB}/\text{LPEI}/^{14}\text{C}\text{-DS})_{30}$ film, the maximum power requirement is 2.4 μW ; this is about three orders of magnitude less than that for a pacemaker and six to seven orders of magnitude less than that for implantable blood pumps.

Calculation of Film Drug Loading Capacity

Drug or chemical agent loading in the electroactive LbL thin films described in this work can vary based on factors such as the choice of drug species, film deposition conditions (namely salt concentration and pH), film surface area, and the number of deposited layers. We estimate that films used in the present study, which are deposited onto flat, conducting substrates with a surface area of 2.45 cm^2 and contain ^{14}C -dextran sulfate (DS), can be loaded with between 50-300 ng DS / ($\text{cm}^2 \cdot \text{tetralayer}$). Thus, we estimate that a single, 100 nm-thick film (24 tetralayers at 4.2 nm per tetralayer) deposited onto a surface area of 1 cm^2 can load and release 1.2-7.2 μg of ^{14}C -DS. Further, in many cases it may be possible to substantially increase loading beyond this degree by increasing the surface area of the deposited film, its thickness, and/or deposition conditions.

Methodology Regarding PB Toxicity Studies

The toxicity assays reported in the manuscript were conducted on PB nanoparticles suspended in solution instead of the film's entire set of constituents (DS, LPEI, and PB). We elected to perform toxicity studies in this way because PB is the electroactive, functional component in these systems, and as such, it is the only essential component that will be present in any electroactive thin film of this type (regardless of drug choice and other architectural components). DS and LPEI, on the other hand, were used in these films only to demonstrate the concept of electroactive controlled release: DS was chosen as a model biomolecule that can be obtained in pure, radiolabeled form, and LPEI was chosen as a counter polyion. Therefore, while next generation electroactive films will contain PB, they are unlikely to contain LPEI or DS, which will instead be replaced by an active system (for example, a therapeutic molecule). Therefore, toxicity measurements on DS and LPEI were omitted from the present study so as not to obfuscate the more clinically relevant findings regarding the toxicity of PB.

References

1. DeLongchamp, D. M.; Hammond, P. T. High-Contrast Electrochromism and Controllable Dissolution of Assembled Prussian Blue/Polymer Nanocomposites. *Adv Func Mater* **2004**, *14*, 224-232.
2. Schmidt, D. J., Personal Communication with Medtronic, Inc. 2007.
3. Mallela, V. S.; Ilankumaran, V.; Rao, N. S. *Indian Pacing Electrophysiol J* **2004**, *4*, 201-212.
4. Geertsma, R. E.; deBruijn, A. C. P.; Hilbers-Modderman, E. S. M.; Hollestelle, M. L.; Bakker, G.; Roszek, B. *New and Emerging Medical Technologies: A Horizon Scan of Opportunities and Risks*, National Institute for Public Health and the Environment (RIVM), 2007.

Appendix 2: Supplemental Materials for Chapter 3

Surface Morphology of Bare Substrate versus Substrate with Adhesion Layers

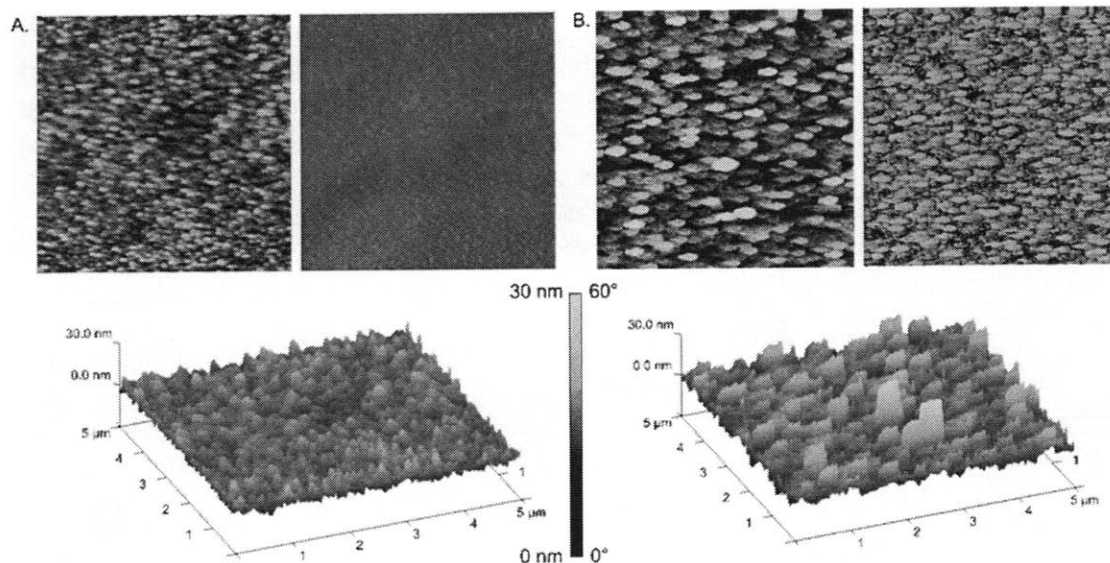


Figure A2.1. Atomic force microscopy height (top, left), phase (top, right), and 3D height (bottom) images in the dry state of A) a bare ITO substrate and B) an ITO substrate with Chi(PB/Chi)₅ adhesion layers. The RMS roughness values, as calculated from the AFM height images, are 2.4 ± 0.2 nm and 4.4 ± 0.4 nm for the bare ITO substrate and the Chi(PB/Chi)₅ adhesion layers, respectively. The scan sizes are all $5 \mu\text{m} \times 5 \mu\text{m}$.

Comparison of Height and Phase Images for a Chi(PB/Chi)₅(PB/GS)₇₅ Film

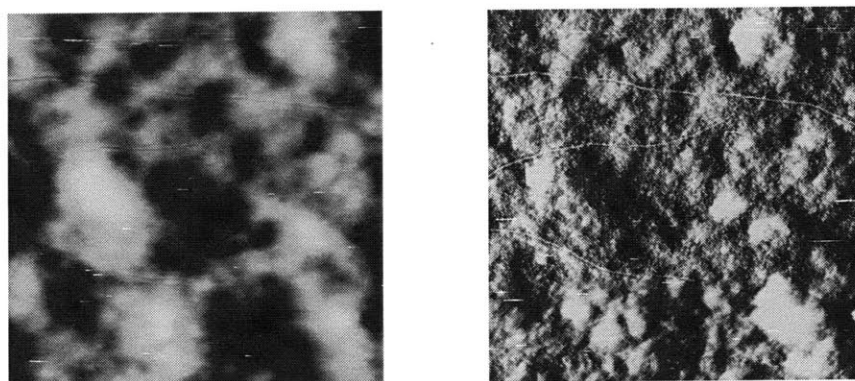
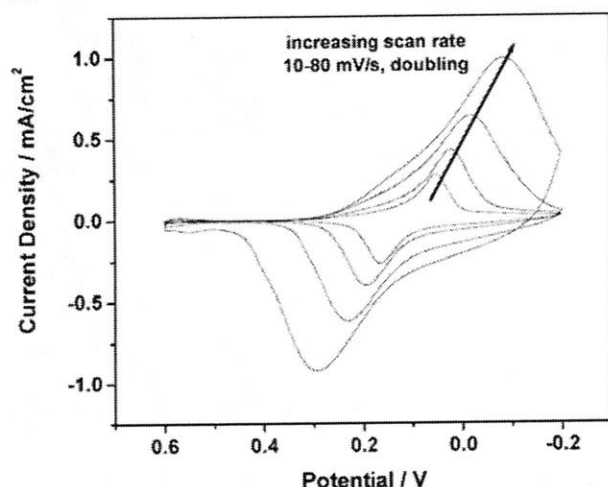


Figure A2.2. An AFM height image (left) and phase image (right) of a Chi(PB/Chi)₅(PB/GS)₇₅ film (in the dry state) over identical areas. The scans are $20 \mu\text{m} \times 20 \mu\text{m}$ in size and the scales are 200 nm and 50° for the height and phase images, respectively. Comparison of the images reveals that the locations of a higher phase angle correspond to the locations of the clusters,

implying that the clusters are enriched in one of the film materials, most likely the PB nanoparticles.

Electrochemical Behavior of Chi(PB/Chi)₅(PB/GS)_n Films

A.



B.

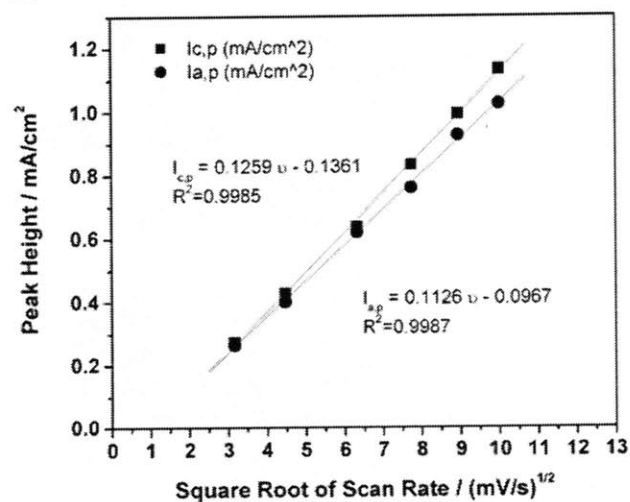
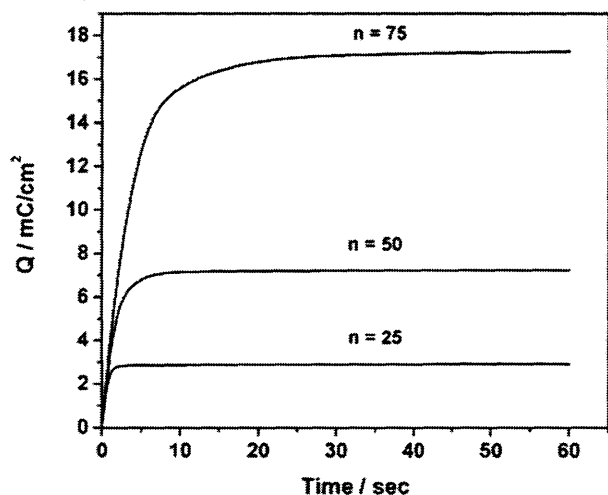


Figure A2.3. A) Cyclic voltammograms of a Chi(PB/Chi)₅(PB/GS)₂₅ film with increasing scan rate in a potassium hydrogen phthalate (KHPH) 0.1 M electrolyte at pH 4.0 with a Ag/AgCl (3M NaCl) reference electrode and Pt counter electrode. The large peak separation implies sluggish electrochemical switching kinetics. B) The cathodic peak height, I_{c,p}, and anodic peak height, I_{a,p}, vary linearly with the square root of the scan rate. This relationship implies that the redox switching is controlled by diffusion (of counterions) instead of electron transfer, for which peak height would vary linearly with scan rate.

Assessment of PB Electroactivity in $\text{Chi}(\text{PB}/\text{Chi})_5(\text{PB}/\text{GS})_n$ Films

A.



B.

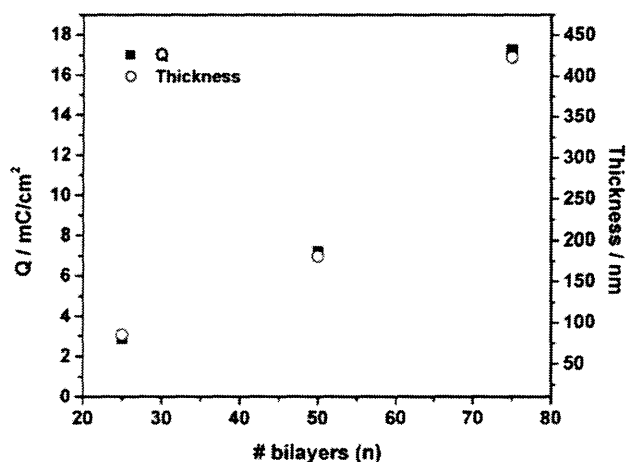


Figure A2.4. A) Chronocoulometry results showing the amount of electric charge removed from $\text{Chi}(\text{PB}/\text{Chi})_5(\text{PB}/\text{GS})_n$ films during the transition from the fully reduced PW state to the mixed valence PB state by application of -0.2 V (vs. Ag/AgCl) for 60 sec following the application of $+0.6$ V (vs. Ag/AgCl) for 60 sec. The electrolyte is 0.1 M KHPH with pH 4.0. B) Overlay of total electric charge (from PB electrochemical switching) and film thickness with the number of bilayers. The fact that these quantities scale proportionately implies that all or nearly all PB nanoparticles within the film are electrochemically accessible.

Charge Removed (via PB oxidation) Over Time at Different Applied Voltages

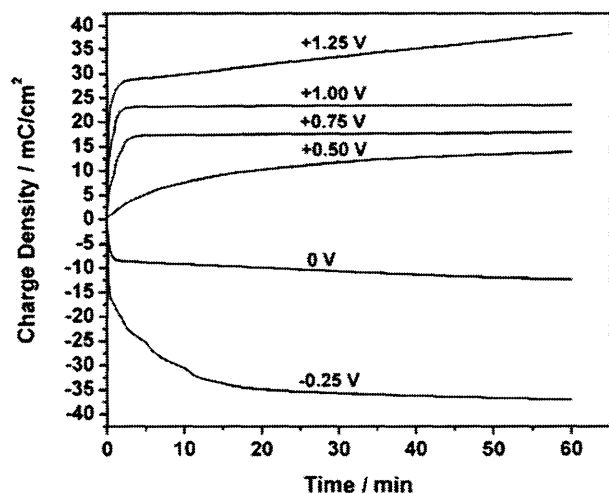


Figure A2.5. Chronocoulometry results showing charge injected/removed from a Chi(PB/Chi)₅(PB/GS)₇₅ film during electrochemical reduction/oxidation of the Prussian Blue. At an applied voltage of +1.00 V (vs. Ag/AgCl) the charge plateaus with time, whereas at +1.25 V the charge continually increases indicating reaction of the solvent, specifically hydrolysis of water.

Drug Release Kinetics Modeling

The release rate of gentamicin from the Chi(PB/Chi)₅(PB/GS)_n films was fit well by a pseudo-second order model of the form:

$$\frac{dM(t)}{dt} = k(M_{\infty} - M(t))^2$$

where $M(t)$ is the total mass of gentamicin released as a function of time, M_{∞} is the total mass of releasable gentamicin, and k is a second order rate constant. After integrating from time 0 to time t , the following equation results:

$$\frac{t}{M(t)} = \frac{t}{M_{\infty}} + \frac{1}{kM_{\infty}^2}$$

Therefore, a plot of $t/M(t)$ versus t should be linear with slope $1/M_{\infty}$ and intercept $\frac{1}{kM_{\infty}^2}$. Before

fitting the drug release data to the model, the data for each film were normalized to the total amount released in 60 min (assumed to be the total amount of releasable gentamicin). Therefore, the rate constants have units of min^{-1} only. Table 1 below reports the fit results for $n = 25, 50,$ and 75 films at a constant applied voltage of +1.25 V (vs. Ag/AgCl) in PBS. The release rates for $n = 25$ and 50 films are not statistically different ($p = 0.33$). The release rate for the $n = 75$ film is apparently lower than for the thinner films; however, given the spread in the data, the means are not statistically different ($p = 0.12$, comparing $n = 25$ to $n = 75$ and $n = 50$ to $n = 75$). Table 2 below reports the fit results for $n = 50$ films at different applied potentials in PBS to test the effect of the magnitude of the applied voltage on the drug release rate. Together with Fig. 6 in the main manuscript, it is evident that both the total amount of drug released from a film, and

the drug release kinetics can be modulated by the magnitude of the applied voltage. Furthermore, since the pseudo-second order model fit the data better than a pseudo-first order model ($R^2 = 0.75, 0.77, \text{ and } 0.98$ for $n = 25, 50, 75$ films, respectively) or a diffusion model ($R^2 = 0.64, 0.68, \text{ and } 0.75$ for $n = 25, 50, 75$ films, respectively), the rate-limiting step of gentamicin release from the films may involve a chemical desorption / chemical reaction mechanism, which is the proposed absorption/desorption mechanism for pseudo-second order kinetic behavior.¹ In fact, gentamicin is known to form 2:1 gentamicin:Fe²⁺ complexes in solution;² thus, pseudo-second order behavior could imply that absorption/desorption from the film involves complexation/decomplexation of two gentamicin molecules, similar to the mechanism proposed by Ho et al. for absorption of dye molecules to peat as dimers.³

Table A2.1. Second order rate constants and correlation coefficients from a fit of gentamicin release rate from Chi(PB/Chi)₅(PB/GS)_n films at a constant applied potential of +1.25 V (Ag/AgCl).

n	k / min ⁻¹	R ²
25	0.77 ± 0.18	0.9993
50	0.70 ± 0.12	0.9996
75	0.58 ± 0.05	0.9998

Table A2.2 Second order rate constants and correlation coefficients from a fit of gentamicin release rate from Chi(PB/Chi)₅(PB/GS)₅₀ films at different applied potentials.

E (vs. Ag/AgCl)	k / min ⁻¹	R ²
1.25 ¹	1.43 ± 0.10	1.0000
1.00	1.22 ± 0.22	0.9998
0.75	0.65 ± 0.08	0.9997
0.50	0.16 ± 0.02	0.9922
0.25 (OCP)	0.23 ± 0.06	0.9891
0	0.19 ± 0.04	0.9881
-0.25	0.58 ± 0.09	0.9995

¹Note that the rate constant in Table 2 for an $n = 50$ film at 1.25 V does not match the value in Table 1 for a film of the same architecture. We observe some variation in films made with different batches of nanoparticles and at different times; however, direct comparisons are always made between identical films made with the same batch of nanoparticles and at the same time.

Surface Morphology of $\text{Chi}(\text{PB}/\text{Chi})_5(\text{PB}/\text{GS})_n$ Films During Electrochemical Dissolution

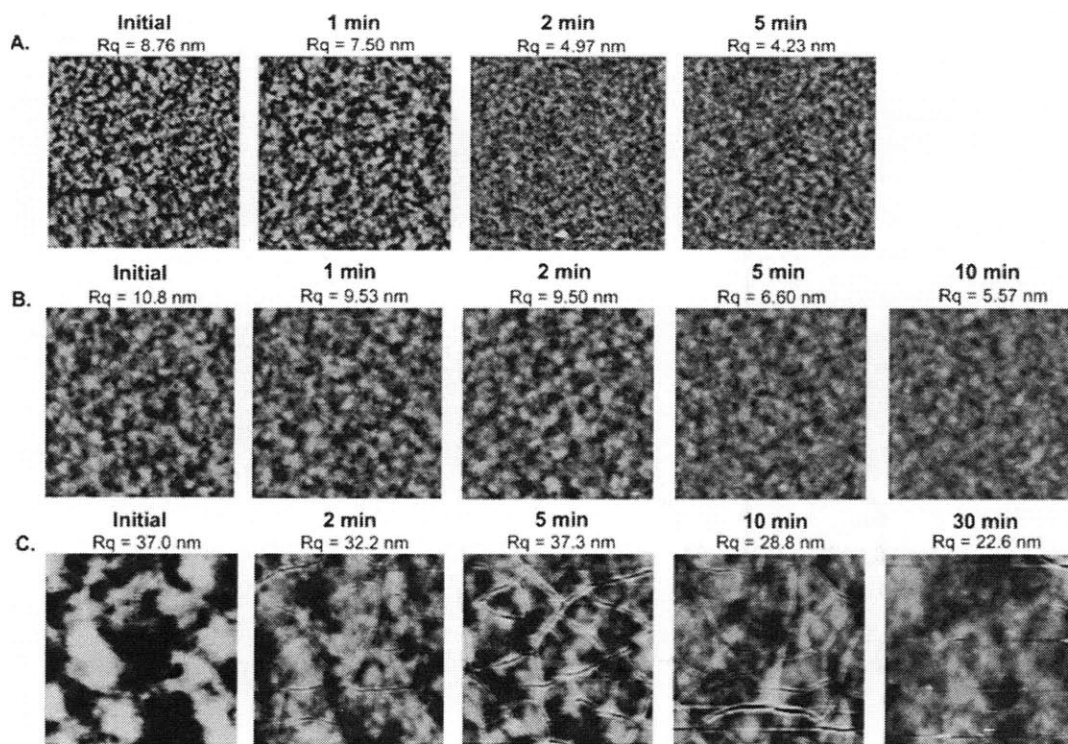


Figure A2.6. AFM height images of $\text{Chi}(\text{PB}/\text{Chi})_5(\text{PB}/\text{GS})_n$ films in the dry state after application of +1.25 V (vs. Ag/AgCl) for the specified amounts of time for A) $n = 25$ with scale $20\ \mu\text{m} \times 20\ \mu\text{m} \times 50\ \text{nm}$, B) $n = 50$ with scale $20\ \mu\text{m} \times 20\ \mu\text{m} \times 100\ \text{nm}$, and C) $n = 75$ with scale $20\ \mu\text{m} \times 20\ \mu\text{m} \times 200\ \text{nm}$. The RMS roughness values (Rq) decrease or stay about the same during dissolution, which is indicative of surface (instead of bulk) erosion. The one deviation from this trend is seen for the $n = 75$ film from 2 min to 5 min; however, this discrepancy may be due to the presence of cracks.

Comparison of PB Oxidation Kinetics and Drug Release Kinetics

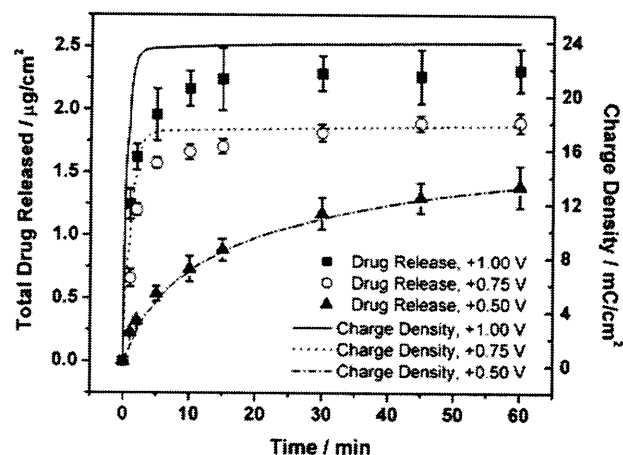


Figure A2.7. Comparison of the kinetics of drug release from a $\text{Chi}(\text{PB}/\text{Chi})_5(\text{PB}/\text{GS})_{50}$ film with the kinetics of charge removal from the film, measured via chronocoulometry. The relatively good overlap shows that drug release occurs concomitantly with PB oxidation and that kinetics of both oxidation and drug release can be modulated at potentials below the half-peak potential. The displayed charge density values at each voltage are the average from $n = 3$ films. The error bars on the drug release data represent \pm one standard deviation in measured values from $n = 3$ films.

References

1. Ho, Y. S.; McKay, G. Comparative Sorption Kinetic Studies of Dye and Aromatic Compounds onto Fly Ash. *J. Environ. Sci. Health, Part A: Toxic/Hazard. Subst. Environ. Eng.* **1999**, *34*, 1179-1204.
2. Priuska, E. M.; Clark-Baldwin, K.; Pecoraro, V. L.; Schacht, J. NMR Studies of Iron-Gentamicin Complexes and the Implications for Aminoglycoside Toxicity. *Inorg. Chim. Acta* **1998**, *273*, 85-91.
3. Ho, Y. S.; McKay, G. The Kinetics of Sorption of Basic Dyes from Aqueous Solution by Sphagnum Moss Peat. *Can. J. Chem. Eng.* **1998**, *76*, 822-827.

Appendix 3: Supplemental Materials for Chapter 4

Spectroscopic Ellipsometry – Background and Modeling Strategy

Spectroscopic ellipsometry (SE) was used to measure film thickness dry and in liquid electrolyte solution. SE measurements give the ellipsometric parameters ψ and Δ at multiple wavelengths. ψ and Δ are related to r_p and r_s , the Fresnel reflection coefficients for light polarized parallel and perpendicular to the plane of incidence, respectively, which are in turn related to the thickness and optical constants of a thin film sample (Equation A3.1). From these data, an optical layer model of the sample plus a dielectric function model of the sample components is necessary to interpret the data. More specifically, one must specify the discrete material layers that affect the reflected light, and one must define how the optical constants (refractive index (n) and extinction coefficient (k))¹ of these materials vary with wavelength.

$$\rho = \tan(\psi) \exp(i\Delta) = \frac{r_p}{r_s} \quad (\text{A3.1})$$

Our films were deposited on gold-coated silicon: we used a three-layer optical model consisting of a gold substrate layer, a homogenous film layer, and an ambient water layer. The gold surface onto which our films were deposited was optically thick, so the underlying silicon substrate could be ignored. To determine the optical constants of the bare gold, we obtained ψ and Δ data on freshly cleaned gold, and then conducted a fit for n and k at each wavelength from 350-1000 nm using J.A. Woollam's WVASE32 software package. Data collected on 3-mercaptopropylsulfonic acid (MPS)-modified gold were identical to that of bare gold and attempts to fit the thickness of the MPS layer gave a zero thickness (data not shown). Therefore, MPS was ignored in our optical model.

Now that n and k for the gold substrate were known, we modeled ψ and Δ data obtained from a (LPEI/PB)_n film assembled on MPS-modified gold. These films exhibit a broad absorbance centered at ~730-740 nm, giving them their blue color. One or more oscillators can be used to model the absorbing region; however, approximate film optical constants are needed in order to set realistic starting values for the oscillator parameters. Therefore, we first considered the wavelength range 450-500 nm, where the film is relatively transparent. Here we used a Cauchy dispersion model (Equation A3.2) to describe the refractive index, assuming $k = 0$. This model yielded only an approximate thickness, as k was small but nonzero in this region. The wavelength range was then expanded to 350-1000 nm. With thickness fixed at the value obtained from the Cauchy model, a point-by-point fit was conducted for n and k at each wavelength to give approximate optical constants of the film. These optical constants were then loaded as a reference material into a generalized oscillator (GenOsc) layer in the WVASE32

$$n(\lambda) = A\lambda + \frac{B}{\lambda^2} + \frac{C}{\lambda^4} \quad \text{for } k = 0 \quad (\text{A3.2})$$

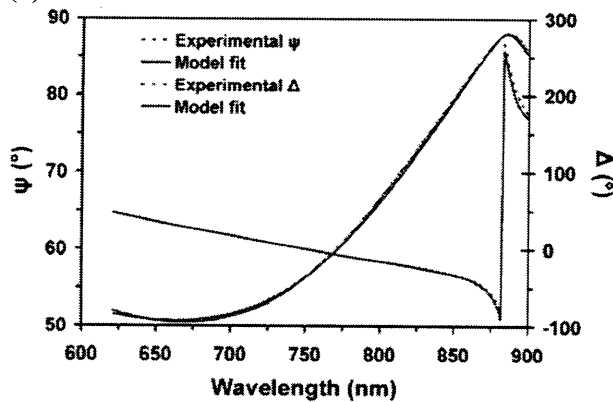
¹ The optical constants of a material can be equivalently discussed in terms of refractive index (n) and extinction coefficient (k) or the real and imaginary parts of the dielectric function, ϵ_1 and ϵ_2 , respectively, where $\epsilon_1 = n^2 + k^2$ and $\epsilon_2 = 2nk$.

software. A GenOsc layer allows a user to model ε_2 (the imaginary part of the dielectric function) with any number and type of oscillators and ε_1 (the real part of the dielectric function) with poles and/or offset. To limit the number of oscillators and number of fit parameters, we narrowed the wavelength range to 620-900 nm to focus on the metal-to-metal charge transfer band at ~ 730 nm. This absorbance was modeled with a single Gaussian oscillator of the form given in Equation A3.3 below. While the shape of the refractive index, n , is dictated by the shape of k according to Kramers-Kronig relations, often there is some additional curvature or offset in n from absorbance outside the considered wavelength range. This effect on n was modeled with a simple offset in the real part of the dielectric constant, ε_1 . Our model had a total of five parameters: film thickness, ε_1 offset, oscillator central energy (E_n), oscillator amplitude (A), and oscillator broadening (B_r). The WVASE 32 software varies the model parameters to

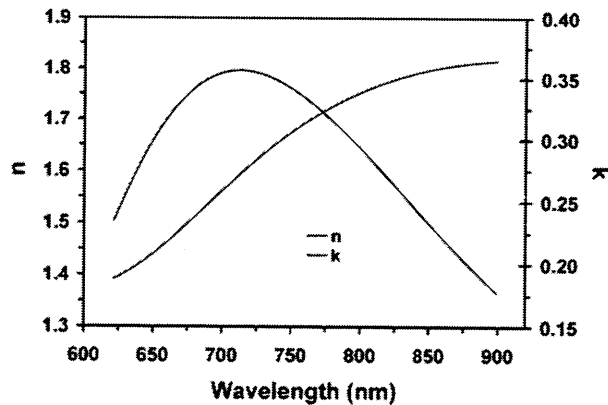
$$\varepsilon_2(E) = Ae^{-\left(\frac{E-E_n}{B_r}\right)^2} - Ae^{-\left(\frac{E+E_n}{B_r}\right)^2} \quad (\text{A3.3})$$

minimize the difference between the experimental and calculated model data, or the mean squared error (MSE). Figure A3.1 below shows the excellent fit to the data achieved for (LPEI/PB)₃₀ films in the oxidized and reduced states.

(a)



Fit results	
Thickness	153.31 ± 0.72 nm
ε_1 offset	2.4921 ± 0.0078
A	1.1543 ± 0.0065 eV
E_n	1.6891 ± 0.0003 eV
B_r	0.6753 ± 0.0011 eV
MSE	13.91



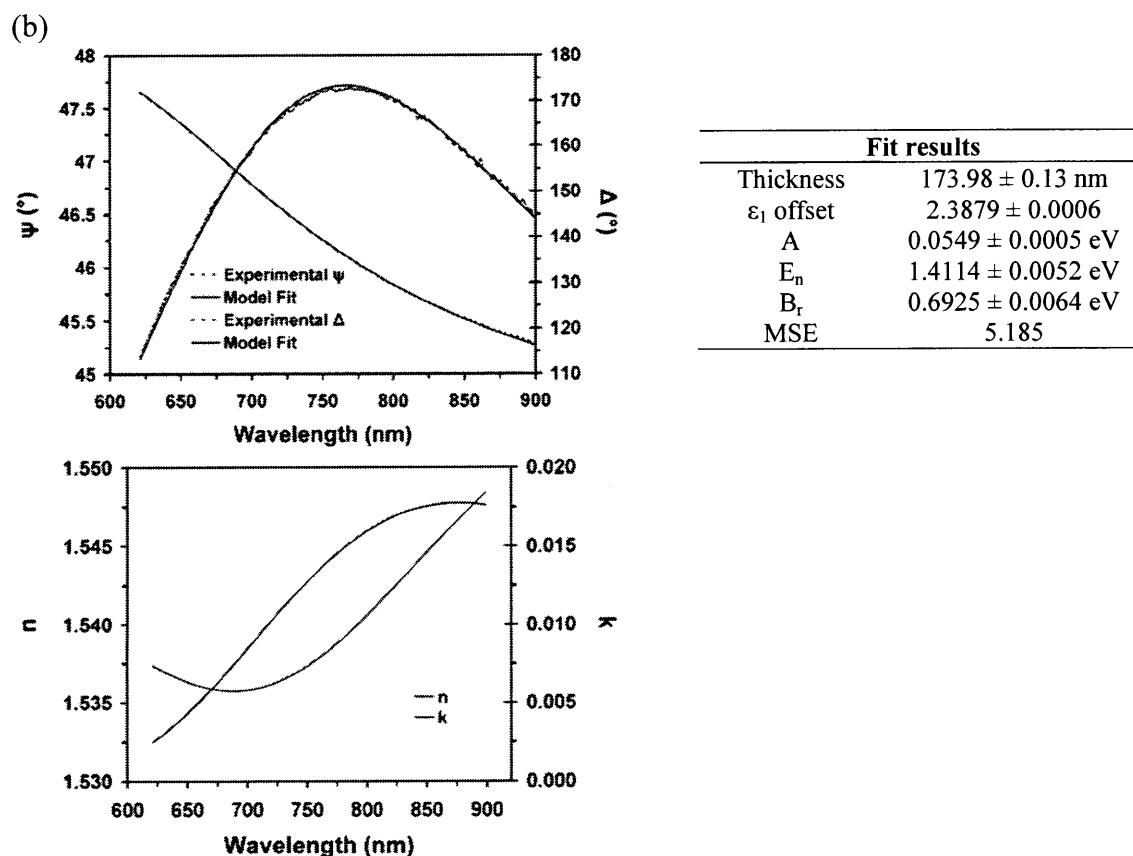
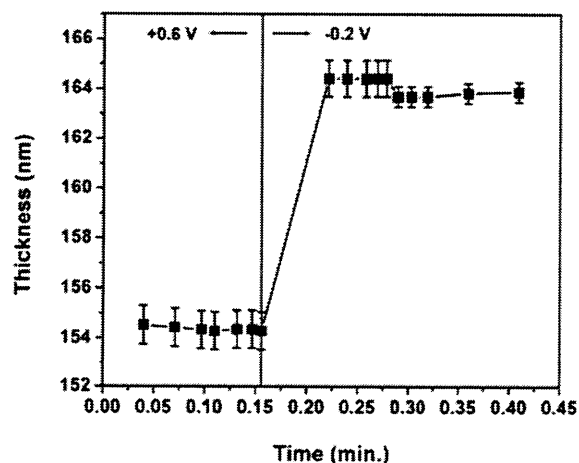


Figure A3.1. Ellipsometric parameters ψ and Δ with model fits and refractive index n and extinction coefficient k versus wavelength for (LPEI/PB)₃₀ films at applied potentials of (a) +0.6 V (oxidized state) and (b) -0.2 V (reduced state).

Spectroscopic Ellipsometry – Dynamic Scan Results

A dynamic scan protocol in the WVASE32 software package was used to capture the kinetics of the redox-induced swelling process. The data acquisition rate was maximized, which resulted in data points being collected approximately every 10 milliseconds. A selection of those data points were fit as described above resulting in a plot of film thickness versus time (Fig. A3.2A). For reference, the change in ψ and Δ at 850 nm over time is also displayed (Fig. A3.2B).

a)



b)

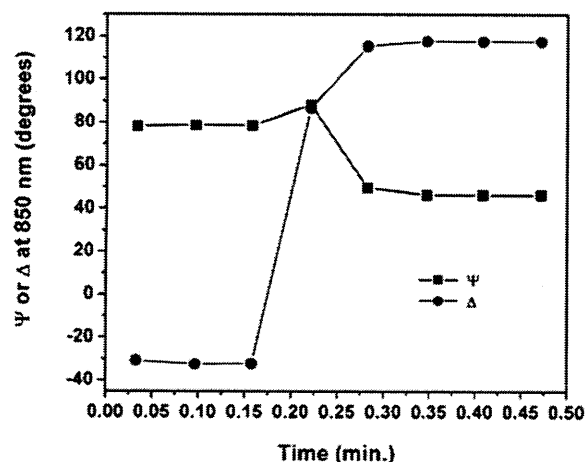


Figure A3.2. (a) Thickness of an (LPEI/PB)₃₀ film on Au-coated silicon over time, subjected to an applied electric potential of 0.6 V (vs. Ag/AgCl) switched to -0.2 V vs. Ag/AgCl starting shortly after the 0.15 minute time point. (b) Values of the ellipsometric parameters (ψ and Δ) over time.

Mechanical Analysis – Modulus vs. Degree of Swelling

The Young's elastic modulus E versus degree of swelling for the (LPEI/PB)_n films reported here was compared to two sets of films from literature: poly(styrene sulfonate) (PSS) / poly(diallyldimethylammonium) (PDADMA) films reported by the Schlenoff group^{1,2} and poly(acrylic acid) (PAA) / poly(allylamine hydrochloride) (PAH) reported by the Rubner and Van Vliet groups.^{3,4} Table A3.1 below shows a compilation of E and swelling data from this paper and the manuscripts referred to above.

Table A3.1: Compilation of elastic modulus and degree of swelling data for LbL films from literature.

Film	Condition	Q_{swell}^a	$\log(Q_{\text{swell}})$	E (MPa)	$\log(E)$
LPEI/PB	Dry	1.00	0	6920	3.84
	In situ – O.C.P. (1 hr.)	1.17	0.0682	3400	3.53
	-0.2 V	1.29	0.110	1750	3.24
PSS/PDADMA ^b	0.2 M NaCl	1.91	0.281	13	1.11
	0.4 M NaCl	1.93	0.285	9	0.954
	0.6 M NaCl	1.99	0.299	5.5	0.740
	0.8 M NaCl	2.09	0.320	3	0.477
	1.0 M NaCl	2.18	0.339	1	0
PAA/PAH ^c	pH 6.5/6.5	1.15	0.0607	80.4	1.91
	pH 3.5/7.5	1.30	0.114	36.6	1.56
	pH 2.0/2.0	4.00	0.602	0.75	-0.125

^aThe swelling ratio Q_{swell} is defined as swollen thickness/dry thickness.

^bSwelling data were approximated and/or interpolated from data presented by Dubas et al.¹ Mechanical data were approximated from Jaber et al.² The listed ionic strength conditions refer to treatment of identical films with different NaCl concentrations after film assembly.

^cSwelling data were borrowed from Lichter et al.³ Mechanical data were borrowed from Mendelsohn et al.⁴ The listed pH conditions refer to the assembly pH for the PAA and PAH, respectively. Films were swollen in PBS buffer at pH 7.4.

In 1946, using the classical theory of rubber elasticity and Flory-Huggins theory, Flory predicted that a double logarithmic plot of elastic modulus versus swelling ratio for crosslinked polymers should be linear with a slope of $-5/3$ for a high degree of swelling.⁵ He verified this prediction using a series of differently crosslinked butyl rubbers. Fig. A3.3 below shows this double logarithmic plot applied to the data presented in Table A3.1. The linearity of the data for all three systems shows that these LbL assemblies behave in a qualitatively similar fashion to other crosslinked polymer systems; however, the slopes are all more negative than $-5/3$, while the degrees of swelling for the LbL systems shown here are less than those investigated by Flory. Comparing the LbL systems to each other, the extent of Young's elastic modulus decrease versus swelling ratio for the LPEI/PB system presented here is close in magnitude to that of the PAA/PAH films, whereas the PSS/PDADMA films exhibit a more drastic drop in modulus with degree of swelling. It must be noted that these LbL films are all ionically-crosslinked, as distinct from the covalently crosslinked butyl rubbers investigated by Flory. It is likely that ionic crosslink density, degree of swelling, and elastic moduli are interrelated differently for ionically crosslinked systems (i.e., with crosslinks that dynamically change in local density or position). Jaber and Schlenoff noted that the ionic crosslinking in LbL systems is under thermodynamic control, resulting in a non-Gaussian distribution of chain lengths at high cross-link density.²

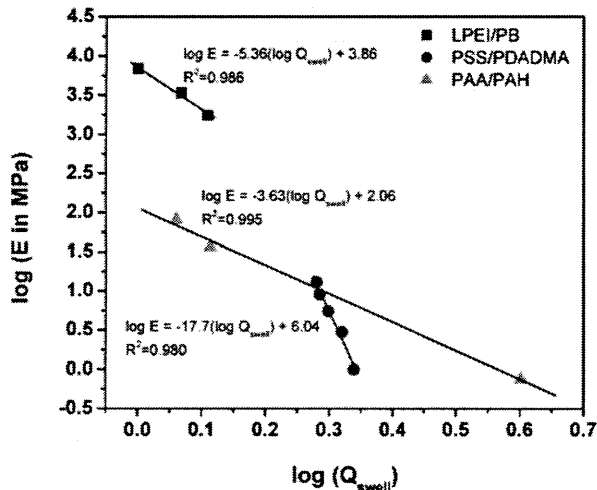


Figure A3.3 Correlation of Young's elastic moduli E with degree of swelling in the current system and other swellable polymers. Here, $\log(E \text{ in MPa})$ versus $\log(Q_{\text{swell}})$ compares the LPEI/PB films reported in this manuscript to the PSS/PDADMA films reported by Dubas et al.¹ and Jaber et al.² and the PAA/PAH films reported by Lichter et al.³ and Mendelsohn et al.⁴

References

1. Dubas, S. T.; Schlenoff, J. B. Swelling and Smoothing of Polyelectrolyte Multilayers by Salt. *Langmuir* 2001, *17*, 7725-7727.
2. Jaber, J. A.; Schlenoff, J. B. Mechanical Properties of Reversibly Cross-Linked Ultrathin Polyelectrolyte Complexes. *J Am Chem Soc* 2006, *128*, 2940-2947.
3. Lichter, J. A.; Thompson, M. T.; Delgadillo, M.; Nishikawa, T.; Rubner, M. F.; Van Vliet, K. J. Substrata Mechanical Stiffness Can Regulate Adhesion of Viable Bacteria. *Biomacromolecules* 2008, *9*, 1571-1578.
4. Mendelsohn, J. D.; Yang, S. Y.; Hiller, J.; Hochbaum, A. I.; Rubner, M. F. Rational Design of Cytophilic and Cytophobic Polyelectrolyte Multilayer Thin Films. *Biomacromolecules* 2003, *4*, 96-106.
5. Treloar, L. R. G. *The Physics of Rubber Elasticity*, 3d; Clarendon Press: Oxford, 1975.